Technische Universität München
Institut für Energietechnik

Lehrstuhl für Thermodynamik

Determination of the Heat Release Distribution in Turbulent Flames by Chemiluminescence Imaging

Martin Rolf Werner Lauer

Vollständiger Abdruck der von der Fakultät für Maschinenwesen der Technischen Universität München zur Erlangung des akademischen Grades eines

DOKTOR-INGENIEURS

genehmigten Dissertation.

Vorsitzender:
>Univ.-Prof. Dr.-Ing. Harald Klein

Prüfer der Dissertation:
>1. Univ.-Prof. Dr.-Ing. Thomas Sattelmayer
>2. Univ.-Prof. Dr. rer. nat. habil. Rainer Suntz,
>   Karlsruher Institut für Technologie

Die Dissertation wurde am 21.03.2011 bei der Technischen Universität München eingereicht und durch die Fakultät für Maschinenwesen am 01.06.2011 angenommen.

Für Alfred

Danksagung / Acknowledgment

Abstract

Imaging of OH^* or CH^* chemiluminescence with intensified cameras is often used for the determination of heat release in turbulent flames. Proportionality is commonly assumed, but was never proven. This study investigates which information about turbulent flame heat release rate can be obtained from chemiluminescence. It is found that although the integral heat release rate can be obtained from the integral chemiluminescence intensity, no information about the local heat release rate is provided by chemiluminescence due to turbulence-chemistry interactions.

A model based correction method is introduced to obtain a better approximation of the spatially resolved heat release rate of lean turbulent flames from OH^* measurements. The correction method uses a statistical strain rate model to account for the turbulence influence. The strain rate model is evaluated with time-resolved velocity measurements of the turbulent flow, and is linked with one-dimensional simulations of strained counterflow flames. In this way the non-linear effect of turbulence on chemiluminescence intensities and heat release rate is taken into account and corrected, heat release rate proportional OH^* intensities are obtained.

For all investigated flames in the lean, partially premixed regime the corrected OH^* intensities are in very good agreement with the heat release rate distributions of the flames.

Kurzfassung

OH* und CH* Chemilumineszenz wird oft zur Charakterisierung der Wärmefreisetzung in turbulenten Flammen verwendet. Meist wird ein linearer Zusammenhang angenommen, was jedoch nicht gerechtfertigt ist. Die Studie untersucht die Verwendung von OH* als Maß für die Wärmefreisetzung in mageren turbulenten Flammen. Es wird gezeigt, dass lediglich die integrale Wärmefreisetzung durch OH* abgebildet wird. Die lokale Wärmefreisetzung wird aufgrund der Turbulenz-Chemie-Interaktion in der Flamme nicht durch OH* charakterisiert.

Eine modellbasierte Korrekturmethode wird vorgestellt, um eine bessere Abbildung der lokalen Wärmefreisetzung durch OH* zu erhalten. Die Korrekturmethode basiert auf einem statistischen Modell der durch Turbulenz verursachten Flammenstreckung und Simulationen von Gegenstromflammen, um die nichtlinearen Zusammenhänge zwischen Turbulenz, OH* Intensität und Wärmefreisetzung zu modellieren.

Für alle untersuchten Flammen im mageren vorgemischten Regime zeigt die korrigierte OH* Chemilumineszenz eine gute Übereinstimmung mit der Wärmefreisetzungsverteilung.

Contents

Nomenclature

Latin characters

a	thermal diffusivity [m^2 s^{-1}]
a_t	tangential strain rate [s^{-1}]
a_q	quenching strain rate [s^{-1}]
c	reaction progress of combustion [$-$]
c	speed of light [m s^{-1}]
c_p	isobaric heat capacity [J (kg K)$^{-1}$]
d	center body diamater [m]
e	error [$-$]
$\vec{e}_i$	unit vector [$-$]
h	Planck constant [J s]
h	specific enthalpy [J kg^{-1}]
i	imaginary unit [$-$]
i	chemiluminescence intensity [photons s^{-1}]
$\vec{j}$	single electron total angular momentum vector [J s]
k	Boltzmann constant [J K^{-1}]
k	reaction rate coefficient [mol (m^3 s)$^{-1}$]
l	single electron azimuthal quantum number [$-$]
l	turbulent length scale [m]
$\vec{l}$	single electron orbital angular momentum [J s]
l_f	thickness of preheat zone [m]
l_t	integral length scale of turbulence [m]
l_δ	thickness of inner layer [m]
l_ε	thickness of oxidation layer [m]
l_λ	Taylor length scale [m]
l_η	Kolmogorov length scale [m]
m	mass [kg]
$\dot{m}$	mass flow [kg s^{-1}]
m_l	single electron magnetic quantum number [$-$]
m_s	single electron spin quantum number [$-$]
n	single electron principal quantum number [$-$]
$\vec{n}$	flame front normal vector [$-$]

p	pressure [N m^{-2}]
$p(a_t)$	strain rate probability density function [$-$]
$\dot{q}$	volumetric heat release rate [J (m^3 s)$^{-1}$]
r	radial coordinate [m]
r_i	arbitrary spatial coordinate [m]
s	stretch rate [s^{-1}]
$\vec{s}$	single electron spin vector [J s]
s_l	flame front propagation speed [m s^{-1}]
t	time [s]
u	velocity [m s^{-1}]
$\vec{u}$	velocity vector [m s^{-1}]
$\vec{u}_f$	flame front velocity vector [m s^{-1}]
u_l	laminar flame speed [m s^{-1}]
v'	vibrational state within electronically excited state [$-$]
v''	vibrational state within electronic ground state [$-$]
v	turbulent velocity scale [m s^{-1}]
v_η	Kolmogorov velocity [m s^{-1}]
w	surface propagation speed [m s^{-1}]
x	coordinate
$\vec{x}$	position vector [m]
y	flame coordinate [m]
z	distance [m]
A	area [m^2]
A	pre-exponential factor [mol (cm^3 s)$^{-1}$]
$A_{i \to j}$	Einstein coefficient of spontaneous emission from state i to j [s^{-1}]
C	proportionality constant [-]
D	burner nozzle diameter [m]
E	energy [J]
F	self similar function [$-$]
$\vec{J}$	resulting multi-electron total angular momentum vector (atom) [J s]
J'	rotational state within electronically exited state [$-$]
J''	rotational state within electronic ground state [$-$]
L	resulting multi-electron orbital angular momentum quantum number (atom) [$-$]
L	characteristic flow length scale [m]
$\vec{L}$	resulting multi-electron orbital angular momentum vector (atom) [J s]
N	temperature exponent [$-$]
N_i	relative amount of radicals in state i [$-$]

$\dot{N}_{i,\text{source}}$	production rate of radicals in state i [s^{-1}]
P_i	predissociation rate of state i [s^{-1}]
P_{th}	thermal power [W]
Q_i	quenching rate of state i [s^{-1}]
$\dot{Q}_l$	heat loss [J s^{-1}]
$\dot{Q}_R$	integral heat release rate [J s^{-1}]
R	two point correlation function
R	universal gas constant [kJ (mol K)$^{-1}$]
$\vec{S}$	resulting multi-electron spin vector (atom) [J s]
S_{BP}	bandpass filtered chemiluminescence signal [$-$]
S_{ij}	fluid dynamic strain rate tensor [s^{-1}]
T	temperature [K]
T_{BP}	bandpass filter transmittance [$-$]
T_{ad}	adiabatic flame temperature [K]
U	potential [V]
V	volume [m^3]
$V_{i \rightarrow j}$	vibrational transfer rate from state i to j [s^{-1}]
X	mole fraction [$-$]
Y	mass fraction [$-$]

Greek characters

α_t	tangential strain rate [s^{-1}]
δA_f	flame surface element [m^2]
δ_{ij}	Kronecker delta [$-$]
ε	dissipation rate of turbulent kinetic energy [m^2 s^{-3}]
κ	wavenumber [m^{-1}]
κ_c	curvature rate [s^{-1}]
λ	molecule electron orbital angular momentum quantum number [$-$]
λ	wavelength [m]
μ	dynamic viscosity [kg (s m)$^{-1}$]
ν	kinematic viscosity [m^2 s^{-1}]
ρ	density [kg m^{-3}]
σ_a	standart deviation of strain rate distribution [$-$]
σ_α	standart deviation of strain rate distribution [$-$]
τ	turbulent time scale [s]
τ_η	Kolmogorov time scale [s]

| ϕ | equivalence ratio $[-]$ |
| ψ | amplitude of wave function |

ΔE_A	activation energy [kJ mol^{-1}]
$\Delta E_{i \to j}$	energy difference between state i and j [J]
Δh_R^0	specific chemical reaction enthalpy [J kg^{-1}]
$\Delta \vec{s}$	displacement vector [m]
Δt	time difference / time step size [s]
Δv	difference in vibrational state [-]
Λ	resulting multi-electron orbital angular momentum quantum number (molecule) $[-]$
$\vec{\Lambda}$	resulting multi-electron orbital angular momentum vector (molecule) [J s]
$\vec{\Sigma}$	resulting multi-electron spin vector (molecule) [J s]
χ_0	scalar dissipation rate [s^{-1}]
Ψ	time-dependent wave function
$\vec{\Omega}$	resulting multi-electron total angular momentum vector (molecule) [J s]
Ω_{ij}	rotation rate tensor [s^{-1}]

Subscripts

ad	adiabat
bp	balance point
BP	bandpass
f	flame
norm	normalized to maximum value
r	radial
ref	reference
x	axial
y	local value in counterflow simulations
max	maximum
min	minimum
burner	burner exit plane

Superscripts

| 0 | reference |
| + | symmetric wave function |

$^-$	anti-symmetric wave function
$*$	electronically excited state
$'$	turbulent fluctuation

Symbols

$\langle\rangle$	mean value
$\langle\rangle_a$	strain-averaged value
$\langle\rangle_{a,\chi}$	strain and scalar dissipation rate averaged value
$\langle\rangle_t$	time-averaged value
$\vec{\nabla}$	Nabla operator

Non-dimensional numbers

Re	Reynolds number	$\mathrm{Re} = uL/\nu$
Re_t	turbulent Reynolds number	$\mathrm{Re}_t = ul_t/\nu$
Re_λ	Taylor length scale Reynolds number	$\mathrm{Re}_\lambda = ul_\lambda/\nu$

Abbreviations

CMOS	complementary metal oxide semiconductor
CTA	constant temperature anemometry
DNS	direct numerical simulation
FWHM	full width at half maximum
LDV	laser doppler velocimetry
LED	light emitting diode
Nd:YAG	neodymium-doped yttrium aluminum garnet
Nd:YLF	neodymium-doped yttrium lithium fluoride
pdf	probability density function
PIV	particle image velocimetry
PLIF	planar laser induced fluorescence
rms	root mean square

1 Introduction

The world wide consumption of energy is increasing steadily. With growing public awareness for environmental protection, the amount of electric power produced from renewable sources like wind, water, or solar technologies is increasing but approximately 85% of electric power is still generated by burning fossil fuels. According to the *World Energy Outlook* of the *International Energy Agency* combustion of fossil fuels will remain an important cornerstone for the power generation throughout the next decades [2] even though the accessible amount of fossil fuels is limited, and the exploitation of new sources is becoming increasingly expensive. Thus, new combustion systems, such as gas turbines, have to be highly efficient and low in emissions at the same time.

These contradicting goals cannot be achieved with diffusion flames, which have been commonly utilized in gas turbines in the last decades. Lean premixed combustion is an auspicious technology to improve efficiency and to meet actual legal regulations to reduce emissions. Fuel and air are mixed and homogenized upstream of the burner in lean premixed combustion systems. This results in lower combustion temperatures and thus a significant reduction of emissions of nitrogen oxides. Additionally, the amount of unburnt hydrocarbon in the exhaust gases are reduced. However, lean premixed combustors are prone to combustion instabilities, such as thermoacoustic instabilities [51, 4, 5, 26] and flame flashback [49, 87, 50, 48]. These instabilities are strongly influenced by the local heat release rate or heat release fluctuations.

1.1 Background of this study

The utilization of potentially unstable combustion technologies, like lean premixed combustion, requires that the desired combustion states can be stabilized by the layout of the combustor based on simulations during the development process, or by active control of unsteady combustion states based on predictive simulations (e.g. [62]). In both cases the heat release rate of the flame has to be measured, either to validate the simulations or as input parameter for active control mechanisms. However, the heat release rate of technical flames is hardly accessible by

measurement. Dependable time resolved measurement techniques which provide the local heat release rate, like heat release imaging[1] [29], are so complex in terms of experimental effort that they can be applied to laboratory flames only [7]. In general, the application of such measurement techniques to technical combustion systems is not possible.

Therefore, the heat release rate is measured indirectly in most applications. A common quantity for such indirect measurements is the light emission of the flame, the so-called chemiluminescence. Chemiluminescence is light emitted from electronically excited atoms or molecules formed by chemical reactions. Chemiluminescence can be measured without external excitation by optical means and thus non-invasively. Since chemiluminescence originates from the reaction zone of the flame, it is commonly assumed to characterize the heat release rate of flames.

The first studies on chemiluminescence date back to the 19th century. Since the middle of the last century it is studied systematically in combustion research. It is shown in several studies that the integral emissions of specific chemiluminescent species can be used to measure the integral heat release rate of flames [17, 43, 40, 76, 32]. Furthermore, it is shown that the spatially resolved chemiluminescence from the hydroxyl radical is a measure for the spatially resolved heat release rate in laminar flames [33, 6].

Generally, these results cannot be transferred to turbulent flames. Flame parameters such as turbulence intensity, strain rate, and curvature have a strong impact on the chemiluminescence intensity [40, 61, 55, 6]. Since these quantities may vary substantially in turbulent flames, a direct proportionality between the spatially resolved chemiluminescence and heat release rate cannot be expected for the turbulent case.

Nevertheless, chemiluminescence is often used in turbulent flame studies to characterize the heat release rate. This is contrary to the studies described before, but especially for confined and adiabatic turbulent flames the integral chemiluminescence intensity is successfully used to monitor the integral heat release of the flame in many studies, e.g. [4, 26, 24]. The correlation between heat release and chemiluminescence is determined empirically in these studies. This approach is not based on an understanding of the underlying processes but rather sanctified by

---

1 Heat release rate imaging is the convolution of planar laser induced fluorescence signals from hydroxyl and formaldehyde. If both signals are quantified the convoluted signal correlates well with the local heat release rate [29]. Two synchronized laser systems with high pulse energies at 355nm and 283nm, and two image intensified cameras are necessary for heat release rate imaging. Additionally, the flame must be optically accessible from at least two sides.

the results. In any case, local heat release information of turbulent flames obtained from chemiluminescence seems highly questionable.

1.2 Context of this study

The current knowledge about chemiluminescence is fragmentary at the best. Especially in turbulent flame studies chemiluminescence is commonly used as an indicator for heat release rate based on empirical studies. A fundamental understanding of the basic relationships between chemiluminescence and heat release is missing.

Since 2006 the interdisciplinary research project *Chemiluminescence and Heat Release* funded by the *German Research Council*[2] works on improving the understanding of chemiluminescence. Seven institutes have systematically investigated chemiluminescence to develop a basic understanding of the underlying mechanisms and a reliable measurement technique for the heat release rate based on chemiluminescence, which can be applied to a wide range of flames.

The present study is part of the contribution of the *Lehrstuhl für Thermodynamik* at the *Technische Universität München* to the DFG-funded research project. In particular, lean premixed turbulent flames close to technical application have been investigated. The two scientific aspects of this study are:

- To investigate which information can be (reliably) determined from chemiluminescence measurements in turbulent flames. The commonly assumed direct proportionality between chemiluminescence and heat release rate is based on studies of laminar flames. These results cannot be transferred to turbulent flames in general, since several studies indicate that the results from laminar lames are not valid for turbulent flames.

- The development of a correction method, allowing to determine heat release rate from chemiluminescence by taking all non-linear effects into account that have been identified before to be important in turbulent flames.

An important precondition to tackle these aspects is the ability to measure representative chemiluminescence signals. This is non-trivial problem, because of the complex spectral characteristics of chemiluminescence. Additionally, a recorded

---

2 *Deutsche Forschungsgemeinschaft*, DFG

chemiluminescence signal is not proportional to the incident light intensity in general. All elements of the optical measurement setup have certain wavelength dependent transmittances which distort measured intensities. As a consequence, two measurement signals of the same intensity, but recorded in different wavelength ranges, do not necessarily indicate identical incident light intensities. Another distorting effect on measured intensities is the non-linear characteristic of certain elements in the measurement setup, such as CMOS sensors and image intensifiers of cameras. Such non-linear characteristics cause that the measurement signal is not proportional to the incident light intensity.

As a consequence, commonly used bandpass filtered measurement signals usually are not representative for the number or electronically excited molecules or radicals in a flame. Thus, in addition to the two scientific aspects of this study introduced before, the development of a measurement and data evaluation procedure to obtain representative chemiluminescence measurements is an important aspect in this study. This measurement aspect can be divided into the following tasks:

- To identify which parts of the chemiluminescence spectrum of a flame are representative for the different chemiluminescence species.

- To develop a measurement and data evaluation procedure to recover the previously identified parts of the chemiluminescence spectrum from measurement signals with high spatial and temporal resolution.

- To account for all non-linear characteristics of the measurement hardware.

1.3 Outline

In the following chapters the theoretical background is presented. The main focus will be on chemiluminescence in Ch. 2. In this chapter the basics of the spectral characteristics of flame chemiluminescence and a literature review on chemiluminescence studies are presented. Additionally, basic considerations on how a representative chemiluminescence signal can be measured are introduced here.

The fundamentals of turbulence and turbulence-chemistry interaction, as far as they are of importance for this study, are introduced in Ch. 3.

Thereafter, the experimental rig and the measurement techniques, which are used in this study, are described in Ch. 4. This chapter introduces a convenient measurement and data evaluation procedure to obtain representative chemiluminescence measurements, based on the basic considerations described in Ch. 2.

This is followed by an introduction to a newly developed reference technique for heat release rate measurements in Ch. 5. This reference technique is used to determine the information about heat release rate that can be obtained from chemiluminescence in turbulent flames. Additionally, the error made when assuming a direct proportionality between chemiluminescence and heat release in turbulent flames is quantified.

In Ch. 6 data from the comparison of heat release rate and chemiluminescence are used to develop a model based correction method, which allows for a reliable determination of spatially resolved heat release rate from a turbulent flame's chemiluminescence. The model description is given in two parts: Firstly, the fluid mechanical part, a statistical strain rate model proposed by Pope and co-workers, which describes the statistics of flame straining caused by turbulence, is given. Secondly, one-dimensional simulations of counter flow flames with detailed chemistry, which describe the effect of straining on heat release rate and chemiluminescence intensity, are presented. Then both parts of the model are combined to describe the effect of turbulence on chemiluminescence. The model is then used to correct measured hydroxyl radical chemiluminescence in a way to reliably exhibit heat release rate proportional intensities. Additionally, counterflow simulations are presented to investigate the impact of pressure, preheating, and fuel composition on the chemiluminescence of turbulent flames. Also the applicability of the presented method for diffusion flames is briefly discussed.

The study is concluded with a summary in Ch. 7.

2 Chemiluminescence

The term *chemiluminescence* refers to light emitted from atoms, molecules, or radicals, returning from an electronically excited state to ground state. The prefix *'chemi'* indicates that the excitation energy comes from a chemical reaction. Chemiluminescence can be found in many processes which involve unstable and energetic intermediate species, such as combustion processes[1]. Figure 2.1 shows a typical chemiluminescence spectrum of a non-preheated, turbulent methane-air flame at atmospheric pressure.
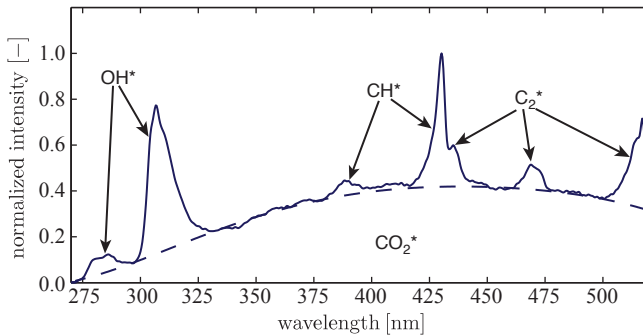

Figure 2.1: Typical chemiluminescence spectrum of a methane-air flame at atmospheric pressure. The spectral resolution is 1nm.

The spectrum is a superposition of the emissions from four electronically excited species: The radicals OH^*, CH^*, and C_2^*, and the molecule carbon dioxide CO_2^*[2]. The diatomic radicals emit light in narrow spectral bands whereas the emissions from CO_2^* are broadband in the wavelength range from approximately 270nm

---

1   It is important to note that although the chemiluminescence light investigated in this study is generated by combustion processes, the origin of the chemiluminescence lies not in the temperature rise caused by combustion. Thus, a direct proportionality between chemiluminescence and heat release cannot be expected a priori.

2   Throughout this study the asterisk is used to indicate electronically excited molecules or radicals.

to 550nm. In a hydrogen flame, OH* is the only chemiluminescence emitter (Fig. 2.2).
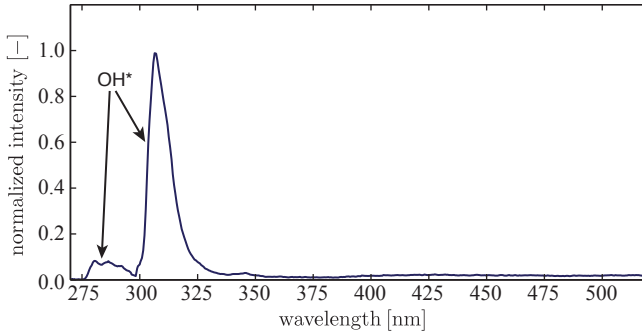
Figure 2.2: Typical chemiluminescence spectrum of an atmospheric hydrogen-air flame. OH* is the only chemiluminescence emitter.

In combustion research most studies use OH* chemiluminescence as a marker for the heat release rate. OH* is emitted by all flames burning gaseous fuels. Therefore, this study will focus on OH* chemiluminescence.

This chapter introduces the relevant fundamentals of chemiluminescence. Firstly, the spectral characteristics of OH* chemiluminescence and the underlying quantum mechanical background will be presented. Secondly, a literature review of chemiluminescence studies will be shown. The last section of this chapter introduces experimental considerations on how to measure OH* chemiluminescence. These considerations are the basis for the measurement and data evaluation procedure described in Sec. 4.3.2, which aims for a representative measurement of the number of electronically excited radicals. This measurement and data evaluation procedure is one of the main aspects of this study and the basis for the scientific aspects sketched in the introduction (Sec. 1.2).

2.1 Spectral characteristics of OH*

The chemiluminescence spectrum of a diatomic radical or molecule is considerably more complicated than the discrete emission lines from single atoms [23]. As

an example, Fig. 2.3 shows a 2200K hydrogen flame chemiluminescence spectrum between 305nm and 320nm.
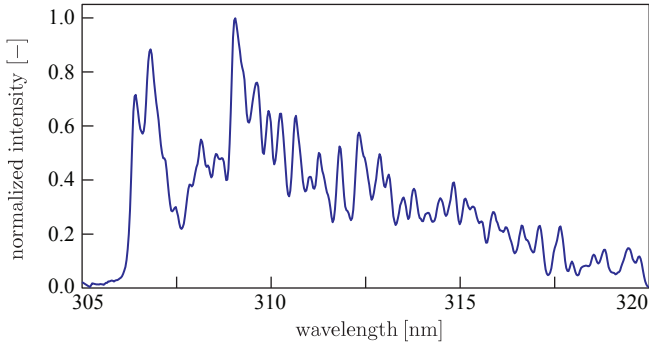

Figure 2.3: Spectrum of the OH* chemiluminescence between 305nm and 320nm. The observed structure is caused by the complex energetic structure of the OH* radical introduced below. The spectral resolution is 0.06nm.

The observed emission spectrum of the hydroxyl radical results from its energetic structure. In the following, the quantum mechanical model describing the energetic states of its electrons will be introduced. The energetic states of the electrons couple with the rotational and vibrational states of the radical. This causes the electronic states to be split and is explained thereafter. The corresponding nomenclature commonly used in chemiluminescence studies is introduced. The overview presented here follows closely the more detailed descriptions of Eckbreth [23], Tipler [84], Vogel [86], and Mayer-Kuckuk [59]. It is followed by an explanation of the OH* emission spectrum.

The fundamentals of chemiluminescence are introduced using the example of OH*, because it is the most important chemiluminescence species in this study. Other chemiluminescence molecules or radicals can be described analogous.

2.1.1 Schrödinger equation and electronic quantum numbers

An electron in a potential field $U(\vec{x},t)$, which is caused for example by the nucleus of an atom or the nuclei of a molecule, is described by the time-dependent Schrödinger equation [59]:

$$\vec{\nabla}^2\Psi(\vec{x},t) - \frac{2m}{h^2}U(\vec{x},t)\Psi(\vec{x},t) + \frac{2m}{h}i\frac{\partial\Psi(\vec{x},t)}{\partial t} = 0 \qquad (2.1)$$

Here, $\Psi(\vec{x},t)$ is the time-dependent wave function characterizing the electron. m is the electron mass, and h is the Planck constant. i is the imaginary unit. Equation 2.1 is called time-dependent Schrödinger equation, because the potential field $U(\vec{x},t)$ is time-dependent. For the stationary case, i.e. a time-independent potential field $U(\vec{x})$, the wave function $\Psi(\vec{x},t)$ can be split into a spatial amplitude function $\psi(\vec{x})$ and a time dependent part:

$$\Psi(\vec{x},t) = \psi(\vec{x})\exp\left(-i\frac{E}{h}t\right) \qquad (2.2)$$

E is the total energy of the electron. Substituting Eq. (2.2) in Eq. (2.1) gives the time-independent Schrödinger equation [84]:

$$\vec{\nabla}^2\psi(\vec{x}) + \frac{2m}{h^2}\left(E - U(\vec{x})\right)\psi(\vec{x}) = 0 \qquad (2.3)$$

Atoms and molecules, which do not absorb or emit light, have a time-independent potential field. Thus, the electrons of such atoms and molecules can be described by the time-independent Schrödinger equation [86]. The squared magnitude of the wave function $|\psi(\vec{x})|^2$ can be interpreted as the probability density function of the position of the electron. Thus, the volume integral of the squared magnitude of the wave function must equal unity. This so-called normalization condition is a constraint for possible solutions of the Schrödinger equation. [84]:

$$\int\limits_V |\psi(\vec{x})|^2 \, dV = 1 \qquad (2.4)$$

Only certain discrete pairs of E and $\psi(\vec{x})$ satisfy the Schrödinger eqiation (Eq. (2.3)) and the normalization condition (Eq. (2.4)). These are eigenvalues and

eigenfunctions of the Schrödinger equation and can be interpreted as possible energy levels and associated wave functions of the electron[3]. Due to this quantization of the possible energy levels, a single electron in the potential field of an atom or molecule is unambiguously characterized by four quantum numbers [23]:

- Principal quantum number n. n characterizes the average distance between electron and nucleus, and represents the so-called shell or orbital. Only discrete orbitals can occur, namely those which satisfy $\vec{l} = n \cdot h/2\pi$, with $\vec{l}$ being the orbital angular momentum of the electron. n is a positive integer value, $n = 1, 2, 3, ...$

- Azimuthal quantum number l. l characterizes the orbital angular momentum $\vec{l}$ or subshell of the electron and can be interpreted as the basic shape of the orbital. l is an integer, $0 \leq l \leq n$. Commonly, $l = 0, 1, 2, 3, 4$ orbitals are denoted by the lower case (roman) letters s, p, d, f, and g.

- Magnetic quantum number m_l. Each electronic orbital has a specific magnetic momentum. Thus, in an magnetic field the orbital of the electron is subject to a torque which tends to align the orbital angular momentum $\vec{l}$ parallel to the magnetic field. The magnetic quantum number m_l characterizes the projection of the angular momentum on a reference plane, and can be interpreted as the direction the angular momentum $\vec{l}$ is pointing to. m_l is an integer, $-l \leq m_l \leq l$.

- Spin quantum number m_s. m_s characterizes the spin $\vec{s}$ of an electron. m_s is either $-1/2$ (counter-clockwise spin) or $1/2$ (clockwise spin).

The three quantum numbers n, l, and m_l define the orbital angular momentum $\vec{l}$ of the electron. The spin quantum number m_s defines the spin vector $\vec{s}$ of the electron. The total angular momentum $\vec{j}$ of an electron is the vector sum of the orbital angular momentum and spin, $\vec{j} = \vec{l} + \vec{s}$.

In contrast to atoms, the orbital angular momentum of molecules can only have distinct orientations with respect to the internuclear axis of the molecule. In order to distinguish the energetic states for given n and l in a molecule, a new quantum number, λ, is introduced[4]. The magnitude of λ is defined by $\lambda \equiv |m_l|$. Since

---

3 The only atomic system, for which an exact solution of the Schrödinger equation can be obtained without any approximations, is the hydrogen atom. For all other atoms and molecules the potential field $U(\vec{x})$ is too complex to obtain a self-contained solution of the Schrödinger equation.

4 Commonly, roman letters are used in spectroscopy for atoms, greek letters for molecules. Single electrons are characterized by lower case letters. Capital letters are used to characterize electron configurations consisting of several electrons.

states of $\lambda \neq 0$ correspond to two values of m_l, either positive or negative, these states are split. This effect is called lambda-doubling. Electrons with $\lambda = 0, 1, 2, 3$ are commonly denoted $\sigma, \pi, \delta, \phi$. To identify a specific electron orbital one writes $nl\lambda$, with a succeeding superscript to identify the number of electrons in this state, such as $(2p\sigma)^1$ or $(4d\pi)^2$.

In multi electron systems like atoms or molecules, the various orbital angular momenta of the electrons form a resulting orbital angular momentum ($\vec{L}$ for atoms, $\vec{\Lambda}$ for molecules) of the electron configuration. It is characterized by the quantum number L (in case of a atom) or Λ (in case of a molecule). Analogously to the nomenclature of single electrons the electron configurations corresponding to $L = 0, 1, 2, 3$ and $\Lambda = 0, 1, 2, 3$ are denoted by capital letters S, P, D, F and Σ, Π, Δ, Φ.

Similar to the lambda-doubling effect of a single molecule electron, also the electron configuration of a molecule is double-degenerated for states other than $\Lambda = 0$ because of the opposing directions $\vec{\Lambda}$ can point to. $\Lambda = 0$ states split into two states whose electronic wave functions are either symmetric or anti-symmetric to any plane through the internuclear axis of the molecule. The symmetric case is indicated with a trailing superscript $^+$, the anti-symmetric case with a trailing superscript $^-$.

In multi electron systems also the electron spins form a resulting spin vector. $\vec{S}$ is the resulting total electron spin vector of an atom. In a molecule $\vec{\Sigma}$ denotes the component of the resulting spin vector $\vec{S}$ along the internuclear axis of the molecule. Consequently, the total (orbital + spin) angular momentum of an atom's electron configuration is calculated as $\vec{J} = \vec{L} + \vec{S}$, of a molecule's electron configuration as $\vec{\Omega} = \vec{\Lambda} + \vec{\Sigma}$. The value of $\vec{J}$ or $\vec{\Omega}$ is usually written as trailing subscript of the capital letter which identifies the electron configuration.

In general, the total angular momentum vectors $\vec{J}$ and $\vec{\Omega}$ are split into $2S + 1$ components by the so-called spin-orbit coupling. The number $2S + 1$ is called multiplicity and is usually written as leading superscript of the capital letter which identifies the electron configuration.

For example, the denotation $^2\Pi_{3/2}$ identifies a molecule with quantum number $\Lambda = 1$, multiplicity 2, and total angular momentum $\vec{\Lambda} + \vec{\Sigma} = 3/2$.

2.1.2 Energy levels of the hydroxyl radical

The electron configuration of ground state OH is $(1s\sigma)^2 (2s\sigma)^2 (2p\sigma)^2 (2p\pi)^3$ or $^2\Pi_{3/2,1/2}$. The two possible values of the total angular momentum, 3/2 and 1/2,

arise from the two possible alignments of the orbital angular momentum and spin vector. 3/2 corresponds to a parallel alignment, 1/2 to an anti-parallel alignment. In general[5], ground states, which are also referred to as electronically non-excited states, are indicated with an preceding X. The complete description of the ground state OH radical electron configuration is $X^2\Pi_{3/2,1/2}$. For simplicity, the ground state of OH is usually written as $X^2\Pi_i$ [23].

The excited state of OH is obtained when one of the $2p\sigma$ electrons is transfered to $2p\pi$. The remaining $2p\sigma$ electron determines the excited state, which is $^2\Sigma^+$ [23]. The first excited state is denoted with a preceding A. Thus, the electron configuration of OH* is $A^2\Sigma^+$. Further excited states would be denominated B, C, etc.

The energy levels of the radical are divided into more sub-levels because of the vibration and rotation of the radical, which are independent from the electron configuration. Comparably to the discrete electronic states, only discrete rotational and vibrational states can occur. Figure 2.4 shows a simplified scheme for the energetic levels of the hydroxyl radical.

The figure shows the two potentials for the ground state and the first excited state of the OH radical. The potential curves describe the energy of the radical as a function of the average nuclei distance. For very low distances the potential is very high. At larger distances the radical dissociates into the atoms O and H with electron configurations shown in Fig. 2.4. Between these extrema lies a region with lower energies in which the radical is stable.

For each potential curve also the vibrational states are shown. In ground state the vibrational level is denominated v'', the excited state vibrational level is denominated v'. The vibrational states are numbered consecutively starting with 0 for the lowest energetic level. Each vibrational state is split into several rotational states denominated by J'' (ground state) and J' (excited state). Furthermore, the rotational states are split due to the spins of the nuclei (not shown in the figure) [23].

2.1.3 Emission spectrum of OH*

In general, electronically excited states are unstable. An OH* radical tends to return to the stable ground state. One possible transition from excited state to

---

5 The only exception from this rule is C_2, where a lower energy level was discovered after a marginally higher energy level was denominated X [23].
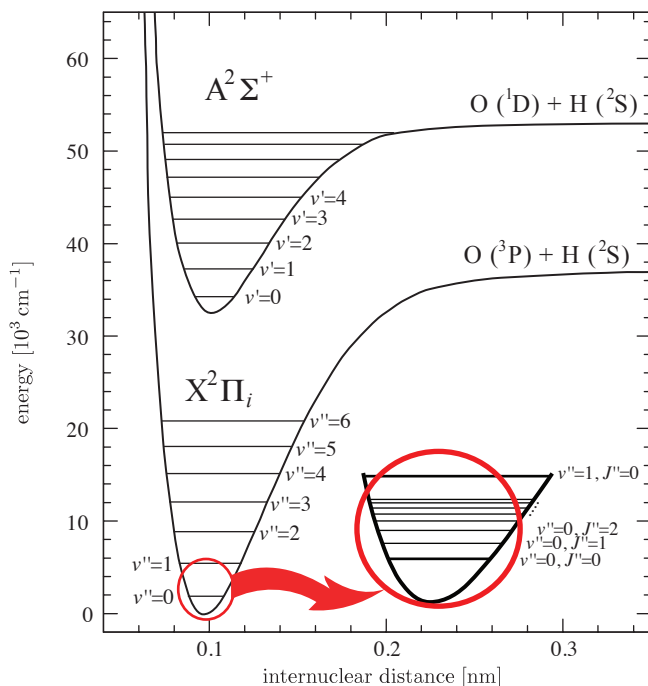
Figure 2.4: Simplified sketch of the OH radical's energy levels [57]. The potential curves are divided into several vibrational states. Each vibrational state is split in several rotational states.

ground state is fluorescence - the spontaneous emission of the energy difference as a photon. The average lifetime of an electronically excited hydroxyl radical before a photon is emitted, if the excitation energy is not dissipated by any other means, is in the order of 700ns [10, 8, 39]. However, most excited radicals return to ground state without emission of light. The dominant deactivation mechanism is the energy transfer by collision, the so-called quenching [27].

Not all collisions return the electronically excited radicals to electronic ground state. Collisions can also change the vibrational or rotational state of the excited

radical. Both, transfer to higher and lower energy levels can occur. The ratio between upward and downward energy transfer is a function of temperature [19]. Thus, after a sufficient number of collisions, the shares of radicals in the different rotational and vibrational states of the electronically excited state reach an equilibrium distribution, which can be described by a steady state rate balance [19]. The derivation of an equation describing the equilibrium distribution of OH* radicals to the different vibrational states will be discussed in detail in Sec. 2.3.1.

Quantum mechanically, transitions from each electronically excited rotational and vibrational state to each rotational and vibrational ground state can occur. However, fluorescence transitions only occur between states which have the same multiplicity [23]. But since the states $A^2\Sigma^+$ and $X^2\Pi_i$ both have multiplicity 2, there is no constraint for the possible fluorescence transitions. The emission spectrum of OH* is determined by the equilibrium distributions of the vibrational and rotational states and the Einstein coefficients for spontaneous emission. The resulting chemiluminescence spectrum shows characteristic bands which represent the different rotational and vibrational transitions.
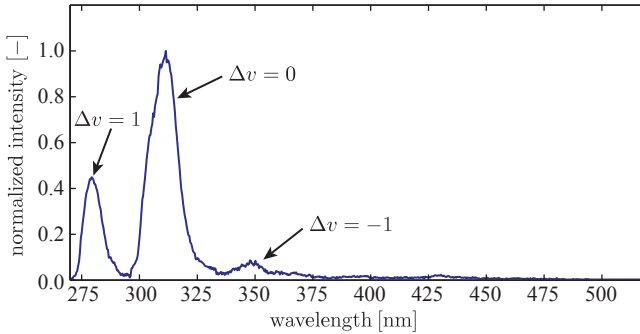
Figure 2.5: Emission spectrum of OH* at approximately 2200K and atmospheric pressure. Three vibrational bands from $\Delta v = 1$, $\Delta v = 0$, and $\Delta v = -1$ can be seen.

Figure 2.5 shows a hydroxyl radical emission spectrum after 283nm laser excitation at approximately 2200K and atmospheric pressure. Three vibrational bands can be seen at 280nm, 309nm, and 345nm. The emission band around 280nm originates from transitions with $\Delta v = v' - v'' = 1$. The strongest emission band at

around 309nm originates from transitions with $\Delta v = 0$. Additionally, an emission band from transitions with $\Delta v = -1$ can be seen around 345nm. Rotational energy levels are not resolved in this measurement.

Each vibrational band is divided into several rotational bands. Figure 2.6 shows the OH* $\Delta v = 0$ band. The different peaks correspond to different rotational transitions.
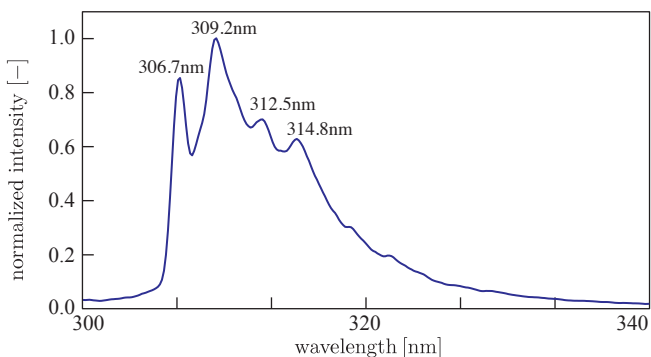
Figure 2.6: Rotational bands within the $\Delta v = 0$ vibrational band of OH*.

It is important to notice that this chemiluminescence band is the superposition of the $X^2\Pi_i(v'' = 0) \leftarrow A^2\Sigma^+(v' = 0)$ and the $X^2\Pi_i(v'' = 1) \leftarrow A^2\Sigma^+(v' = 1)$ transitions. Figure 2.7 shows a computed emission spectrum in the same wavelength range in which both transitions are shown distinctively [58]. The spectrum is computed with the software *LIFBASE* [56]. It can be seen that the rotational peaks at 306.7nm and 309.2nm in Fig. 2.6 originate from the $X^2\Pi_i(v'' = 0) \leftarrow A^2\Sigma^+(v' = 0)$ transition, the two peaks at 312.5nm and 314.8nm from the $X^2\Pi_i(v'' = 1) \leftarrow A^2\Sigma^+(v' = 1)$ transition.

The fine structure within the rotational bands as seen in in Fig. 2.3 is caused by the nuclei spins discussed in Sec. 2.1.2. Throughout the rest of this study, only vibrational states will be considered. The splitting of the vibrational states into rotational states and the fine structure of the rotational states are not relevant in this study and therefore not further considered.
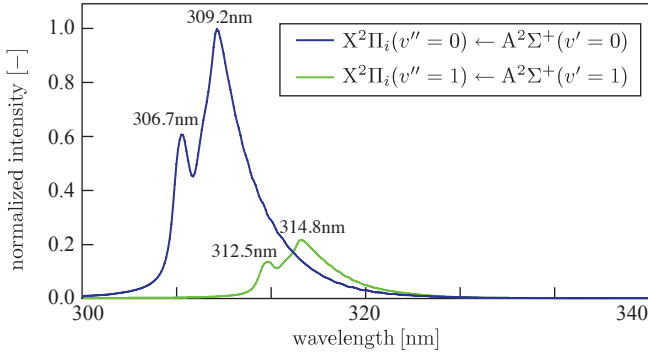
Figure 2.7: Computed emission spectrum of the $\Delta v = 0$ band. OH* chemiluminescence in the wavelength range between 300nm and 340nm is a superposition of the $X^2\Pi_i(v''=0) \leftarrow A^2\Sigma^+(v'=0)$ and the $X^2\Pi_i(v''=1) \leftarrow A^2\Sigma^+(v'=1)$ transitions. The spectrum is computed with the software *LIFBASE* [56].

2.2 Literature review

In this section a brief overview of the previous studies on chemiluminescence is given. The literature review is divided into three parts. The first part is on chemiluminescence as an indicator for the heat release rate. The second part of the literature review outlines equivalence ratio[6] measurements via the ratio of different chemiluminescence emissions. The last part describes the modeling of the reaction kinetics of OH*.

The first part of the literature review is further divided. Firstly, the early studies of the 1950s and 1960s are presented, which investigate the integral chemiluminescence of laminar and turbulent flames. These rather phenomenological studies show that turbulence strongly affects chemiluminescence intensities. Secondly, the most important recent studies are presented, which investigate the use of chemiluminescence as a measure for the local heat release rate as well as the underlying mechanisms forming chemiluminescence. Also the influence of pressure on chemiluminescence intensities is presented in this part of the literature review.

---

6 The equivalence ratio is the ratio of the oxygen mole fraction necessary for stoichiometric combustion and the actual oxygen mole fraction of the air-fuel mixture.

The section is concluded with a short summary of the actual state of knowledge and an evaluation of the reliability of OH* as an indirect heat release rate and equivalence ratio indicator in combustion research. Although not all chemiluminescence studies can be discussed in this literature review, the presented studies give a complete picture of the actual state of knowledge.

2.2.1 Heat release rate

Early studies

The first systematic experimental investigations on the correlation between chemiluminescence and integral heat release rate of a flame date back to the 1950s. In 1954 Clark and Bittker [17] investigated the integral chemiluminescence of laminar and weakly turbulent propane-air bunsen type flames with fuel flow rate and equivalence ratio as flame parameters. They investigated flames with Reynolds numbers[7] up to 6,000. The chemiluminescence was measured in two wavelength ranges, 360nm to 500nm, and 460nm to 600nm. Clark and Bittker found a linear dependency of both measured chemiluminescence signals on fuel-flow rate at constant equivalence ratios as well as a decrease of the intensity with decreasing equivalence ratio. No difference in the chemiluminescence spectra of laminar and turbulent flames was observed. From this, Clark and Bittker [17] concluded that the reaction kinetics of chemiluminescence are identical for laminar and turbulent flames.

The work of Clark and Bittker [17] was continued in 1958 by Clark [16]. OH*, CH*, CO$_2^*$, and C$_2^*$ were investigated in flames with Reynolds numbers up to 18,000. The results of the former study for Reynolds numbers up to 6,000 were confirmed. However, for Reynolds numbers higher than 6,000 lower chemiluminescence intensities were observed than those predicted by a linear extrapolation from the lower Reynolds number range.

The results of Clark [16] were confirmed by Hurle et al. ten years later [40]. Hurle et al. investigated the emissions from C$_2^*$ and CH* in ethylene-air flames. For Reynolds numbers up to 10,000 a linear dependency of chemiluminescence intensity on fuel-flow rate and heat release rate was observed. The slope of the correlation was found to be a function of the equivalence ratio. For Reynolds numbers in the range from 10,000 to 13,000 lower intensities were observed than

---

7 The Reynolds number is the ratio of inertia and viscous forces of the flow and characterizes the turbulence of the flow. The definition and interpretation of the Reynolds number is given in Sec. 3.1.

those expected from linear extrapolation from smaller Reynolds numbers. For Reynolds numbers higher than 17,000 decreasing intensities with increasing fuel-flow rate were observed.

Another study on the effect of turbulence on chemiluminescence intensities was published in 1957 by John and Summerfield [43]. They investigated the light emissions from CO_2^*, C_2^*, and CH^* in highly turbulent propane flames with Reynolds numbers up to 100,000. For all investigated chemiluminescent species turbulence was found to reduce the specific intensity of the chemiluminescence with the intensity reduction being stronger for CO_2^* than for C_2^* or CH^*. According to John and Summerfield these results indicate that sufficiently high turbulence breaks up the laminar flame sheet. This modifies the chemical reactions and transport processes in the flame.

Recent studies

In 1995 Samaniego et al. studied the emissions from CO_2^* in laminar and turbulent premixed methane-air and propane-air flames with a numerical model [76]. They found CO_2^* chemiluminescence to be a good indicator for fuel consumption in flames with varying dilution, strain rate, and equivalence ratio. However, in the investigation of Najm et al. [61], a complex dependency of CO_2^* chemiluminescence on flame curvature and flow history is reported. This leads to an ambiguous correlation of the chemiluminescence with burning rate and heat release. Furthermore, Najm et al. showed a detailed analysis of the reaction mechanism of the methane oxidation. The fractions of carbon in the different reaction paths were quantified. Najm et al. concluded that only a small fraction of the carbon follows side reaction paths forming the chemiluminescence radicals OH^*, CH^*, and C_2^*. Most of the carbon follows the main reaction path which produces only CO_2^* (Fig. 2.8).

Moreover, it was shown that for stoichiometric and lean flames carbon is transferred from the side paths to the main reaction path, reducing the chemiluminescence intensity from the OH^*, CH^*, and C_2^* radicals. This mechanism explains the observed reduction in chemiluminescence intensities for leaner flames as already shown by the experiments of Clark and Bittker [17], Clark [16], and Hurle et al. [40]. Najm et al. concluded that OH^*, CH^*, and C_2^* are no reliable markers for the turbulent flame front, burning rate, or heat release rate because their appearance in the flame is no indicator for the pathway of carbon oxidation for the major fraction of carbon.
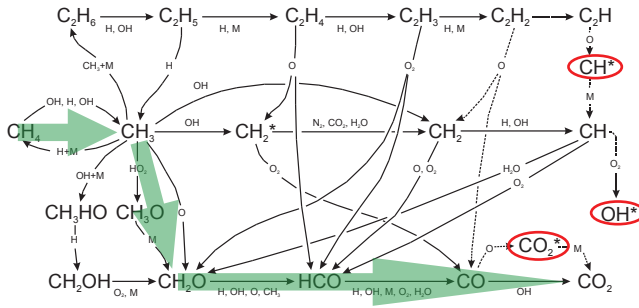
Figure 2.8: The simplified reaction mechanism for methane oxidation [61]. The main fraction of the carbon follows the reaction path depicted with the bold arrows. Only a small fraction of carbon follows the side paths producing OH^*, CH^*, and C_2^*.

In 2003 Lee and Santavicca investigated the integral visible chemiluminescence emission from a turbulent swirled flame [55]. They reported a linear dependency of the chemiluminescence signal on fuel-flow rate, and an exponentially decreasing signal with decreasing equivalence ratio. Moreover, they reported a strong influence of premix level, flame curvature, and flame stretch on the chemiluminescence signal.

In 2004 Hardalupas and Orain [33] investigated the chemiluminescence of counterflow flames with Reynolds numbers up to 10,000. They found that OH^*, CH^*, and CO_2^* chemiluminescence are good markers for the spatially resolved heat release rate in this Reynolds number range. This is a milestone compared with the results of the earlier studies, which only correlate integral quantities. However, a study of Ayoola et al. in 2006 showed that the results of Hardalupas and Orain [33] are not applicable for highly turbulent flames [6]. Ayoola et al. used heat release rate imaging to characterize OH^* chemiluminescence as a measure for spatially resolved heat release rate[8]. Several turbulent, premixed, ethylene-fueled flames with Reynolds numbers in the range from 19,000 to 29,000 were investigated. OH^* was

---

8 Heat release rate imaging aims at the measurement of the formyl radical concentration, which correlates very well with the spatially resolved heat release rate [67, 61]. Since the formyl radical is very difficult to detect, the formyl precursor species hydroxyl and formaldehyde are detected by planar laser induced fluorescence. It was shown that the convolution of the OH and CH_2O LIF signals correlates well with the forward reaction rate of the reaction forming formyl, and thus is a good indicator for the local heat release rate [67, 61].

found to be very sensitive to strain and turbulence. It was observed that strong OH*
chemiluminescence signals emerged from regions within the flame with relatively
low heat release rate. It was also observed that in bluff-body stabilized flames
the equivalence ratio dependency of the OH* chemiluminescence is different for
different positions in the flame brush. Ayoola et al. concluded that OH* chemilu-
minescence is no reliable indicator for the local heat release rate in moderately to
highly turbulent flames.

The influence of pressure on chemiluminescence intensities was systematically
investigated by Higgins et al. [36]. The integral OH* chemiluminescence of a
laminar methane-air flame was measured for varying pressure, equivalence ratio,
and fuel mass flows. Figure 2.9 shows the obtained results. From their experimen-
tal data Higgins et al. defined a empiric correlation between OH* intensity, fuel
mass flow, equivalence ratio, and pressure [36]:

$$i_{\mathrm{OH}^*} \sim \dot{m}_{\mathrm{CH}_4}\, \phi^{5.23}\, p^{-0.86} \tag{2.5}$$

The results of Higgins et al. show that the fuel mass flow normalized OH* inten-
sities are decreasing with increasing pressure. However, since the fuel mass flow is
increasing linearly with pressure in most applications, slightly increasing absolute
OH* intensities with increasing pressure have to be expected.
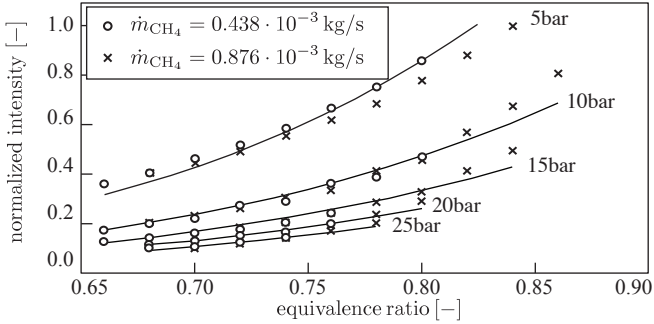
Figure 2.9: Results for the dependence of OH* intensity on pressure, equivalence ratio, and
fuel mass flow rate obtained by Higgins et al. [36]. The chemiluminescence
intensities are normalized with the maximum values at 5bar. Symbols indicate
measurements, the lines are obtained from the correlation defined in Eq. (2.5).

2.2.2 Equivalence ratio

Despite the shortcomings in determining the heat release rate from the chemiluminescence of a single chemiluminescent species as pointed out before, the equivalence ratio of a flame can be determined from the ratio of different chemiluminescence signals. This effect was first investigated by Clark in 1958 [16]. Clark found that the C_2^*/CH* ratio is characteristic for the equivalence ratio. However, the correlation between the chemiluminescence ratio and the equivalence ratio was not universal but fuel specific.

In later studies the OH*/CH* ratio was used for equivalence ratio measurements. In 2000 Haber [31] investigated this ratio in methane fueled Bunsen type flames and flat flames. In the equivalence ratio range from 0.6 to 1.1 a monotonically decreasing OH*/CH* ratio was observed for increasing equivalence ratios. Similar results were also reported for natural gas and propane fueled premixed counterflow flames by Hardalupas and Orain [33, 64], and for propane-air and methane-air fueled bunsen type flames by Ikeda et al. [41]. Nori and Seitzman [63] and Wäsle et al. [89] used the OH*/CH* ratio to measure the equivalence ratio in turbulent methane fueled swirl flames.

In 2009 a study of Panoutsos et al. [65] also investigated the OH*/CH* ratio. Numerical simulations of counterflow flames with detailed chemistry were compared with experimental data. The used reaction mechanisms were extended by elementary reactions, accounting for the formation and deactivation of OH* and CH*. This study showed that the OH*/CH* ratio is a monotonic function of the equivalence ratio. Additionally, it was shown that this function does not depend on the straining of the flame, although the single intensities of OH* and CH* are strongly dependent on the strain rate. The numerical results were in good agreement with the experimental data. Furthermore, it was shown that the OH*/CH* ratio of a diffusion flame is significantly lower than the ratio of a stoichiometric premixed flame. This difference can be used to distinguish between non-premixed and premixed combustion in turbulent flames.

The strain rate range of the investigation of Panoutsos et al. [65] was limited by the operation range of counterflow diffusion flames which is significantly lower than the strain rates of technical flames. However, Guyot et al. [30] showed that the OH*/CH* chemiluminescence ratio can also be utilized in swirl-stabilized flames with much higher strain rates close to technical application.

2.2.3 Modeling of OH* reaction kinetics

The reaction kinetics of OH* formation and deactivation were investigated in many theoretical and experimental studies. An overview on the reaction kinetics of OH* is given, for example, by Kathortia et al. [44]. Three important OH* formation reactions are known [44]:

$$CH + O_2 \rightarrow OH^* + CO \tag{2.6}$$

$$CHO + O \rightarrow OH^* + CO \tag{2.7}$$

$$H + O + M \rightarrow OH^* + M \tag{2.8}$$

The predominant deactivation reaction of OH* is the collisional quenching [81] (Reaction (2.9)). Only a small fraction of electronically excited OH* returns to ground state by the emission of a photon (Reaction (2.10)):

$$OH^* + M \rightarrow OH + M \tag{2.9}$$

$$OH^* \rightarrow OH + \frac{hc}{\lambda} \tag{2.10}$$

Reaction (2.6) is the dominant OH* formation reaction in hydrocarbon combustion [44]. Thus, the ability of a reaction mechanism to predict the concentration of OH* correctly is not only dependent on the correct reaction rate coefficients of the OH* formation and deactivation reactions, but also on the ability of the mechanism to predict the concentrations of CH and the species responsible for collisional quenching of OH* accurately.

In general, the reaction rate coefficient k of a chemical reaction is calculated as [85]:

$$k = A T^N \exp\left(-\frac{\Delta E_A}{RT}\right) \tag{2.11}$$

A is the so-called pre-exponential factor, T the temperature, N the temperature exponent, ΔE_A the activation energy of the reaction, and R the universal gas constant. The known rate coefficients of the OH* formation and deactivation reactions are summarized in Tab. 2.1.

Number	Reaction	A	N	ΔE_A
(2.6)	$CH + O_2 \rightarrow OH^* + CO$	3.24E+14	-0.4	17
(2.7)	$CHO + O \rightarrow OH^* + CO$	2.89E+11	0.0	1.93
(2.8)	$H + O + M \rightarrow OH^* + M$	1.20E+13	0.0	29
(2.9)	$OH^* + M \rightarrow OH + M$			
	M = O_2	2.10E+12	0.5	-2.0
	M = H_2O	5.93E+12	0.5	-3.6
	M = H_2	2.95E+12	0.5	-1.9
	M = CO_2	2.76E+12	0.5	-4.1
	M = N_2	1.08E+11	0.5	-5.2
	M = CO	3.23E+12	0.5	-3.3
	M = CH_4	3.36E+12	0.5	-2.7
	M = OH	6.01E+12	0.5	-3.2
	M = H	1.31E+13	0.5	-0.7
(2.10)	$OH^* \rightarrow OH + hc/\lambda$	1.45E+06	0.0	0.0

Table 2.1: Known reaction rate coefficients of the OH* formation and deactivation reactions [44].

2.2.4 Summary

The studies of Clark [16], Hurle et al. [40], Najm et al. [61], Lee and Santavicca [55], and Ayoola et al. [6] summarize the problems of heat release measurements via chemiluminescence in turbulent flames. The chemiluminescence signal of all emitting species are strongly affected by turbulence intensity, strain rate, curvature, fuel-flow rate, degree of premixing, and equivalence ratio. But these quantities are not necessarily spatially or temporally constant in turbulent flames. Thus, the local chemiluminescence intensity of any species is not a reliable measure for the local heat release rate of a turbulent flame.

However, the equivalence ratio can be determined reliably from the OH*/CH* chemiluminescence ratio of a methane or propane fueled flame, as shown by Haber [31], Panoutsos et al. [65], and Guyot et al. [30][9]. Since the variation of the OH*/CH* ratio is approximately one order of magnitude stronger than the corre-

---

9 Orain and Hardalupas [64] also investigated the OH*/CH* ratio of methanol, ethanol, and isooctane fueled flames. For these fuels the OH*/CH* ratio was found to be a function of the strain rate.

sponding equivalence ratio variation, the OH*/CH* ratio is a very robust measure for the equivalence ratio [31].

The modeling of the OH* reaction kinetics is summarized in the work of Karthotia et al. [44]. A complete set of reaction rate coefficients for the most important OH* formation and deactivation reactions is given. However, the rate coefficients presented by Kathrotia et al. [44] and shown in Tab. 2.1 are validated for low pressure and atmospheric pressure flames only. The rate coefficients for higher pressures are generally unknown. The determination of the pressure influence on the reaction rates of OH* reactions is subject of actual research, e.g. [70].

2.3 Experimental considerations

In a stationary flame the formation and deactivation of electronically excited radicals are in equilibrium. Thus, at each time a specific amount of electronically excited radicals is present. This number of radicals is the desired measure and is proportional to the chemiluminescence intensity with the Einstein coefficient of spontaneous emission as proportionality factor [18]. In this section it is discussed how the number of electronically excited radicals can be obtained from a chemiluminescence measurement. This is a non trivial problem because the emission spectrum of OH* is a superposition of different OH* transitions (Sec. 2.1.3). Thus, a wavelength range of the chemiluminescence spectrum must be identified, which is representative for the number of electronically excited radicals. Furthermore, the OH* emissions are superimposed with the emissions of CO_2^*. This superposition also has to be taken into account.

2.3.1 Representative OH* measurements

In the following an equation describing the share of OH* radicals in the different vibrational states is derived. Based on this description it will be shown that the integral intensity of the $\Delta v = 0$ emission band of OH* is a representative measure for the number of OH* radicals.

Vibrational equilibrium

As discussed before in Sec. 2.1.3, the OH* radicals are distributed to different vibrational states. A steady state balance for the number of OH* radicals N_i in vibrational state $v' = i$ reads [23]:

$$\frac{dN_i}{dt} = 0$$

$$= \dot{N}_{i,\text{source}} + \sum_j \left(N_j V_{j \to i} \right) - N_i \left(\sum_j V_{i \to j} + \sum_k Q_{i \to k} + \sum_k A_{i \to k} + P_i \right) \quad (2.12)$$

Here, the subscripts i and j denote vibrational states within the electronically excited state ($i \neq j$), the subscript k denotes vibrational states in the electronic ground state. N_i and N_j denote the number of OH* radicals in a vibrational states i and j, $\dot{N}_{i,\text{source}}$ is the production rate of OH* radicals in state i by the chemical reactions. V, Q, A, and P are the rate constants which describe the change of the vibrational state within the electronically excited state, the collisional quenching of electronically excited states to ground state, the spontaneous emission of photons, and predissociation.

The following assumptions and simplifications are made:

- Only vibrational states are considered. The effect of rotational states on the rate constants is neglected [19].

- The share of radicals in vibrational states $v' \geq 2$ is small compared to the share in vibrational states $v' = 0$ and $v' = 1$. Although the exact amount of radicals in vibrational states $v' \geq 2$ is unknown at this point, an estimation based on a Boltzmann distribution shows that for temperatures lower than 2500K more than 96% of the radicals are in vibrational states $v' = 0$ and $v' = 1$ [58, 56]. Thus, vibrational states $v' \geq 2$ will be neglected.

- For vibrational states $v' = 0$ and $v' = 1$ predissociation does not occur [23].

- The Einstein coefficient for spontaneous emission A is much smaller than the vibrational transfer rate constant V and the quenching rate constant Q. Thus, also A is neglected [19].

- Based on the work of Paul [66] the quenching rate constants Q_i are assumed to be approximately identical for vibrational states $v' = 0$ and $v' = 1$:

$$Q_0 \approx Q_1 \tag{2.13}$$

- The upward vibrational transfer rate constant $V_{0 \to 1}$ can be related to the downward vibrational transfer rate constant $V_{1 \to 0}$ by detailed balancing [19]:

$$\frac{V_{0 \to 1}}{V_{1 \to 0}} = \exp\left(-\frac{\Delta E_{1 \to 0}}{kT}\right) \tag{2.14}$$

$\Delta E_{1 \to 0}$ is the energy difference between state $v' = 1$ and $v' = 0$, k the Boltzmann constant, and T the temperature.

- It is assumed that the production rates $\dot{N}_{0,\text{source}}$ and $\dot{N}_{1,\text{source}}$ can be described by a yet to be defined function of temperature:

$$\frac{\dot{N}_{1,\text{source}}}{\dot{N}_{0,\text{source}}} = f(T) \tag{2.15}$$

With the above made simplifications and assumptions, the rate equation (Eq. (2.12)) for vibrational state $v' = 1$ reads:

$$
\begin{aligned}
\frac{dN_1}{dt} &= 0 \\
&= \dot{N}_{1,\text{source}} + N_0 V_{0 \to 1} - N_1 V_{1 \to 0} - N_1 Q \\
&= \dot{N}_{0,\text{source}} f(T) + N_0 V_{1 \to 0} \exp\left(-\frac{\Delta E_{1 \to 0}}{kT}\right) - N_1 V_{1 \to 0} - N_1 Q
\end{aligned} \tag{2.16}
$$

Solved for the ratio N_1/N_0 Eq. (2.16) reads:

$$\frac{N_1}{N_0} = \frac{\dot{N}_{0,\text{source}}}{N_0 V_{1 \to 0}} \frac{f(T)}{1 + \frac{Q}{V_{1 \to 0}}} + \frac{\exp\left(-\frac{\Delta E_{1 \to 0}}{kT}\right)}{1 + \frac{Q}{V_{1 \to 0}}} \tag{2.17}$$

The rate equation for the vibrational state $v' = 0$ reads:

$$\frac{dN_0}{dt} = 0$$

$$= \dot{N}_{0,\text{source}} + N_1 V_{1\rightarrow0} - N_0 V_{0\rightarrow1} - N_0 Q \tag{2.18}$$

$$= \dot{N}_{0,\text{source}} + N_1 V_{1\rightarrow0} - N_0 V_{1\rightarrow0} \exp\left(-\frac{\Delta E_{1\rightarrow0}}{kT}\right) - N_0 Q$$

By rearranging Eq. (2.18) the following expression can be obtained:

$$\frac{\dot{N}_{0,\text{source}}}{N_0 V_{1\rightarrow0}} = \frac{Q}{V_{1\rightarrow0}} + \exp\left(-\frac{\Delta E_{1\rightarrow0}}{kT}\right) - \frac{N_1}{N_0} \tag{2.19}$$

Substituting Eq. (2.19) in Eq. (2.17) and solving for N_1/N_0 gives:

$$\frac{N_1}{N_0} = \frac{\frac{Q}{V_{1\rightarrow0}} f(T) + \exp\left(-\frac{\Delta E_{1\rightarrow0}}{kT}\right) f(T) + \exp\left(-\frac{\Delta E_{1\rightarrow0}}{kT}\right)}{1 + \frac{Q}{V_{1\rightarrow0}} + f(T)} \tag{2.20}$$

The ratio of the quenching rate constant and the vibrational transfer rate constant $Q/V_{1\rightarrow0}$ is a function of the gas composition, and thus fuel and equivalence ratio. Moreover, Q and $V_{1\rightarrow0}$ are also dependent on temperature. However, as shown by Copeland et al. [18], the ratio can be approximated with a constant value of 0.59.

Unfortunately, no information on the function $f(T)$, defining the ratio of the production rates $\dot{N}_{0,\text{source}}/\dot{N}_{1,\text{source}}$, is available in literature. Thus, lacking any better information, it is assumed that the ratio can be described with the Boltzmann distribution[10]:

$$f(T) = \frac{\dot{N}_{1,\text{source}}}{\dot{N}_{0,\text{source}}} = \exp\left(-\frac{\Delta E_{1\rightarrow0}}{kT}\right) \tag{2.21}$$

By substituting Eq. (2.21) in Eq. (2.20) it can be seen that with the above made simplifications and assumptions the shares of OH* radicals in the different vibrational states are also described by the Boltzmann distribution:

$$\frac{N_1}{N_0} = \exp\left(-\frac{\Delta E_{1\rightarrow0}}{kT}\right) \tag{2.22}$$

---

10 This assumption will be verified at the end of this subsection.

Figure 2.10 shows the distribution of the OH* radicals to the different vibrational states, assuming that also states $v' \geq 2$ follow the Boltzmann distribution [58, 56].
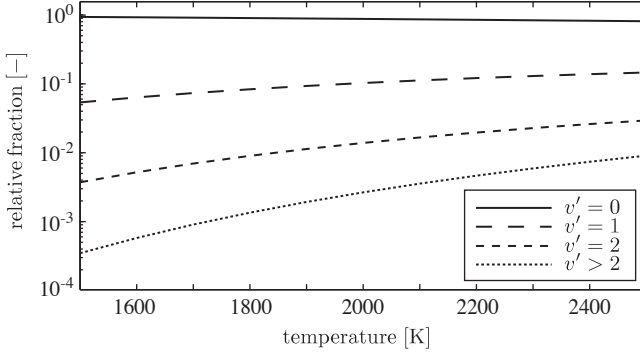
Figure 2.10: Distribution of the OH* radicals to different vibrational states, computed with the software *LIFBASE* [58, 56]. States of $v' = 2$ and higher only account for less than 4% of the radicals and are neglected in this study.

Characteristic spectral range for OH* measurements

Based on the above obtained result for the distribution of the OH* radicals to the different vibrational states it now will shown that the integral chemiluminescence intensity of the $\Delta v = 0$ band is a representative measure for the number OH* radicals.

A steady state balance of all OH* radicals reads:

$$\frac{dN}{dt} = 0 = \sum_i \left(\dot{N}_{i,\text{source}} + \sum_j \left(N_j V_{j \to i} \right) - N_i \left(\sum_j V_{i \to j} + \sum_k Q_{i \to k} + \sum_k A_{i \to k} \right) \right)$$

$$(2.23)$$

The integral chemiluminescence intensity i_{OH^*} of all vibrational transitions is obtained by rearranging Eq. (2.23):

$$i_{OH^*} = \sum_i \left(N_i \sum_k A_{i \to k} \right)$$

$$= \sum_i \left(\dot{N}_{i,\text{source}} + \sum_j \left(N_j V_{j \to i} \right) - N_i \left(\sum_j V_{i \to j} + \sum_k Q_{i \to k} \right) \right)$$

(2.24)

It can be seen from Eq. 2.24 that the chemiluminescence intensity only depends on the number of radicals N_i and the Einstein coefficient of spontaneous emission $A_{i \to j}$. The Einstein coefficient can be considered to be constant [57], however, the number of radicals N_i is strongly affected by collisional quenching. The quenching rate constant is in general a function of gas composition and temperature. Thus, the dependency of the quenching rate constant on equivalence ratio, which defines gas composition and temperature, has to be investigated. Figure 2.11 shows the quenching rate constant as function of the equivalence ratio of the mixture. The values for Q are calculated from the gas composition in the reaction zone of the flame, obtained from one-dimensional counterflow simulations with detailed chemistry (Sec. 6.3), and temperature dependent values of the quenching rate constants for different collisional species published by Garland and Crosley [27].
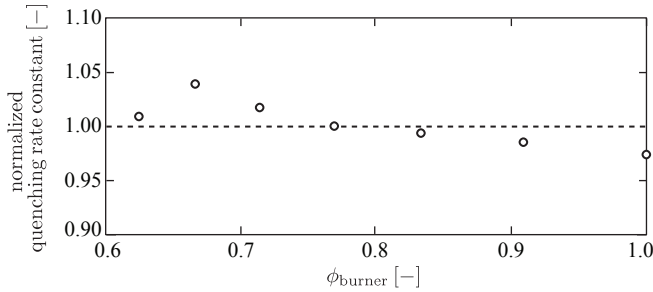
Figure 2.11: Dependency of the quenching rate constant on equivalence ratio. The values of Q are normalized with the value for $\phi = 0.77$.

It can be seen that the quenching rate in the lean regime can be approximated with a constant value with an accuracy of $\pm 5\%$. This means that independent

from the equivalence ratio a constant share of OH* radicals is quenched before a photon is emitted. As a consequence, the share of radicals which emit photons is also independent from equivalence ratio. Thus, even in non-constant equivalence ratio flames the influence of quenching on chemiluminescence intensities is approximately constant and thus it does not need to be explicitly considered in this study.

Since for flame temperatures below 2500K more than 96% of the OH* radicals are in vibrational states $v' = 0$ and $v' = 1$ (Fig. 2.10), vibrational states $v' = 2$ and higher are neglected. The vibrational state $v' = 1$ accounts for up to 15% of the radicals and must be considered. By neglecting the higher vibrational states Eq. (2.24) reads:

$$i_{\text{OH}^*} = N_0 \sum_j A_{0 \to j} + N_1 \sum_j A_{1 \to j} \tag{2.25}$$

With the above introduced simplification of neglecting the higher vibrational states, the $\Delta v = 0$ emission band can be assumed to consist only of the $v'' = 0 \leftarrow v' = 0$ and $v'' = 1 \leftarrow v' = 1$ transitions (Fig. 2.12).
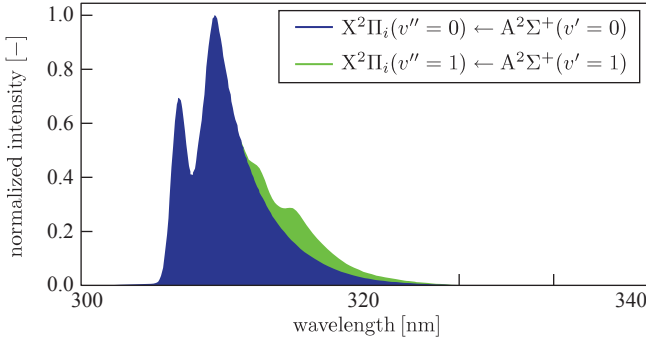
Figure 2.12: The emission of $\Delta v = 0$ band of OH*, which can be considered as the superposition of the $v'' = 0 \leftarrow v' = 0$ and $v'' = 1 \leftarrow v' = 1$ transitions [58]. The spectrum is computed with the software *LIFBASE* [56].

Thus, the chemiluminescence intensity of the $\Delta v = 0$ emission band can be calculated as:

$$i_{\text{OH}^*,\Delta v=0} = N_0 A_{0 \to 0} + N_1 A_{1 \to 1} \tag{2.26}$$

Since the temperature and thus the relative amounts of the radicals in the two vibrational states are usually not known, and the Einstein coefficients $A_{0 \to 0}$ and $A_{1 \to 1}$ are not identical[11], Eq. (2.26) cannot be inverted to calculate the number of radicals $N = N_0 + N_1$ from the chemiluminescence signal. However, since the number of radicals in the $v' = 0$ state is approximately one order of magnitude larger than in the $v' = 1$ state, and since $A_{0 \to 0}$ and $A_{1 \to 1}$ are of the same order of magnitude, it is possible to approximate $A_{1 \to 1} \approx A_{0 \to 0}$. With this approximation the number of OH* radicals is directly proportional to the integral chemiluminescence signal of the $\Delta v = 0$ transition band:

$$N = N_0 + N_1 \approx \frac{i_{\text{OH}^*,\Delta v=0}}{A_{0 \to 0}} \tag{2.27}$$

The error e of this approximation can be estimated as:

$$e = 1 - \left(\frac{1}{N_0 + N_1} \cdot \left(N_0 \frac{A_{0 \to 0}}{A_{0 \to 0}} + N_1 \frac{A_{1 \to 1}}{A_{0 \to 0}} \right) \right) \tag{2.28}$$

Figure 2.13 shows this error as a function of flame temperature.

It can be seen that the error increases with increasing flame temperature. e is approximately 5% for a non-preheated, stoichiometric methane-air flame, and approximately 6% for a non-preheated, stoichiometric hydrogen-air flame. For flame temperatures usually found in modern combustion systems the error is typically less than 3%. Thus, the integral emission of the $\Delta v = 0$ band is a good approximation for the total number of OH* radicals.

Analogously, based on a steady state balance for the vibrational state $v' = 1$, and the approximations and simplifications made before, it can be easily shown that the number of radicals in vibrational state $v' = 1$ can be obtained from the chemiluminescence signal of the $\Delta v = 1$ band:

---

11 $A_{0 \to 0} = 1.451 \cdot 10^6 \text{s}^{-1}$, $A_{1 \to 1} = 0.8595 \cdot 10^6 \text{s}^{-1}$ [57].
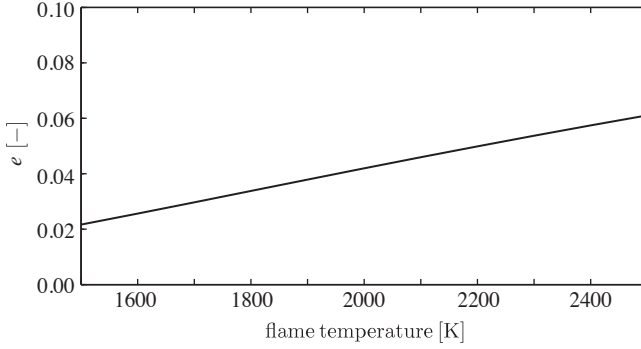
Figure 2.13: The error e made when the chemiluminescence of the $\Delta v = 0$ transitions is assumed to be a representative measure for the number of OH* radicals. The maximum error is made for the highest flame temperature. For temperatures usually found in gas turbines it is approximately 3%.

$$N_1 = \frac{i_{OH^*,\Delta v=1}}{A_{1\rightarrow 0}} \tag{2.29}$$

with $A_{1\rightarrow 0} = 0.4643 \cdot 10^6 \mathrm{s}^{-1}$ [57]. The number of radicals in $v' = 0$ state can then be calculated as:

$$N_0 = N - N_1 = \frac{i_{OH^*,\Delta v=0}}{A_{0\rightarrow 0}} - \frac{i_{OH^*,\Delta v=1}}{A_{1\rightarrow 0}} \tag{2.30}$$

Check of assumed Boltzmann distribution for the production rate ratio (Eq. (2.21))

With these results for the number of OH* radicals in vibrational states $v' = 0$ and $v' = 1$ (Eq. (2.27) and Eq. (2.30)), the above made assumption of a Boltzmann distribution for the production rate ratio $\dot{N}_{1,\text{source}}/\dot{N}_{0,\text{source}}$ can be checked indirectly: Based on measured spectra of a premixed, non-preheated, atmospheric methane-air flame with different equivalence ratios, the ratio of radicals in vibrational states $v' = 0$ and $v' = 1$ is obtained from the integral chemiluminescence intensities of the $\Delta v = 0$ and $\Delta v = 1$ vibrational bands:

$$\frac{N_1}{N_0} = \frac{i_{OH^*,\Delta v=1}/A_{1\to0}}{i_{OH^*,\Delta v=0}/A_{0\to0} - i_{OH^*,\Delta v=1}/A_{1\to0}} \tag{2.31}$$

Figure 2.14 shows ratio N_1/N_0 obtained from the experimental data in comparison with the ratio obtained from Eq. (2.22), assuming a Boltzmann distribution for the ratio $\dot{N}_{1,source}/\dot{N}_{0,source}$. For the calculation of the Boltzmann distribution it was assumed that OH^* is predominately produced in a region of the flame where the temperature is approximately 90% of the maximum flame temperature. This assumption is based on the counterflow calculations described in Sec. 6.3.
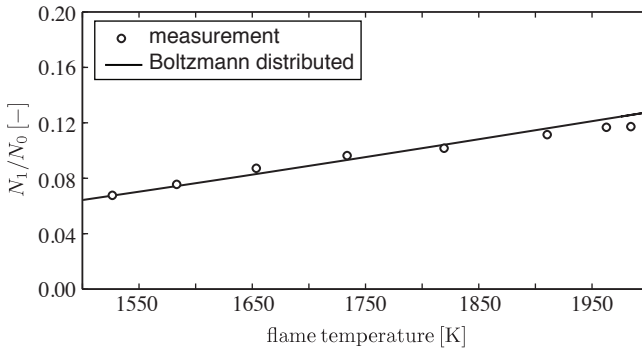
Figure 2.14: Comparison of the ratio of OH^* radicals in vibrational states $v' = 0$ and $v' = 1$ obtained from the Boltzmann distribution (Eq. (2.22)) with measurements.

The measurements are in good agreement with the Boltzmann distribution. Thus, it can be concluded that the ratio N_1/N_0 can be accurately modeled by Eq. (2.22). This also means that by solving Eq. (2.22) for the temperature T, chemiluminescence can be used to measure the local temperature of the flame.

2.3.2 $CO_2{}^*$ chemiluminescence

In flames of carbonaceous fuel, a broadband CO_2^* chemiluminescence is superimposed to the OH^* emissions. Each measurement in the wavelength range of OH^* contains a certain signal from CO_2^* chemiluminescence (Fig. 2.15). The CO_2^* contribution can be of similar or even higher intensity than that from the radical [53].

Thus, a measurement signal including the signal from CO_2^* is no characteristic measure for the number of electronically excited radicals. In order to obtain a representative measurement signal, the CO_2^* contribution must be eliminated from the measurement.

Section 4.3.2 will show the application of the experimental considerations discussed in this section to bandpass filtered measurement data. The result is a representative measure for the number of electronically excited radicals recovered from bandpass filtered measurements with high spatial resolution. These measurements are the basis for the comparison of OH^* chemiluminescence with heat release rate in this study.
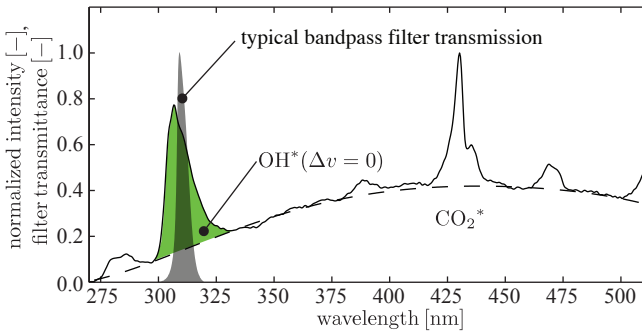
Figure 2.15: A typical chemiluminescence spectrum of a methane-air flame. The OH^* emissions are superimposed with the emissions from CO_2^*. A typical bandpass filtered measurement cannot distinguish between OH^* and CO_2^* chemiluminescence. In general, a measurement in the wavelength range of OH^* is not representative of the number of electronically excited OH radicals.

3 Basics of turbulence and turbulence-flame interaction

This chapter gives an introduction to turbulence, premixed combustion, and turbulence-chemistry interaction as far as they are relevant for this work. Sections 3.1 and 3.2 provide the basics and definitions of turbulent flows. This is followed by the fundamentals of premixed combustion in Sec. 3.3. The flamelet concept, the interaction of turbulence and combustion, and the turbulence induced flame straining are described in Sec. 3.4.

3.1 Turbulence

The term *turbulence* or *turbulent flow* characterizes a fluid mechanical regime in which the properties of the flow are fluctuating stochastically around a mean value (Fig. 3.1).
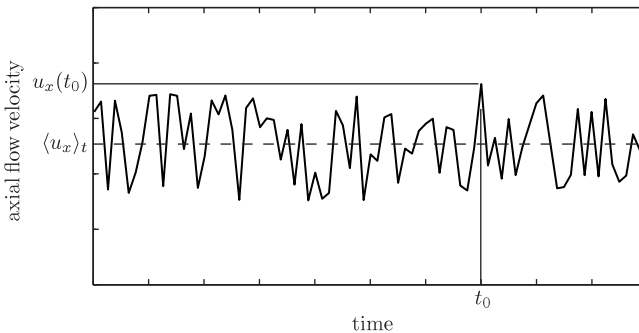
Figure 3.1: Typical time series of the axial component of the flow velocity at a fixed position $\vec{x}$ in a turbulent flow field.

Each flow property, such as the axial component of the flow velocity $u_x(\vec{x}, t)$, can be written as the sum of the average over a period of time $\langle u_x(\vec{x}) \rangle_t$ and the instantaneous deviations from this time average:

$$u_x(\vec{x}, t) = \langle u_x(\vec{x}) \rangle_t + u'_x(\vec{x}, t) \tag{3.1}$$

Commonly, the intensity of the turbulence is given as the *rms*[1] value of the fluctuation of a characteristic flow property. The rms value of the axial velocity component for instance, is defined as:

$$u'_{x,\text{rms}}(\vec{x}) = \langle u'^2_x(\vec{x}, t) \rangle_t^{0.5} \tag{3.2}$$

The turbulent velocity fluctuations in the flow are generated by shear in the mean flow, i.e. by velocity gradients perpendicular to the mean flow [83]. The *Reynolds number* Re is used to characterize a flow as laminar or turbulent. This dimensionless number is the ratio of inertial forces $\rho \langle u \rangle_t^2 / L$ and viscous forces $\mu \langle u \rangle_t / L^2$ [80]:

$$\text{Re} = \frac{\frac{\rho \langle u \rangle_t^2}{L}}{\frac{\mu \langle u \rangle_t}{L^2}} = \frac{\rho \langle u \rangle_t L}{\mu} = \frac{\langle u \rangle_t L}{\nu} \tag{3.3}$$

where ρ is the density of the fluid, $\langle u \rangle_t$ the mean flow velocity, and L a characteristic flow length scale. μ and ν are the dynamic and kinematic viscosities.

3.2 Turbulent energy cascade and length scales

An important characteristic of turbulent flows is the formation of eddies, which is also caused by the presence of shear in the mean flow. The initial eddies are of the size of the flow scale L and are commonly characterized by the *integral length scale of turbulence* l_t. l_t is defined as the integral of the two-point correlation function $R_{u_i u_i}(r_i)$, normalized by $u'^2_{i,\text{rms}}$ [73][2]:

---

1 root mean square

2 A Reynolds number calculated from the integral length scale and the rms value of the velocity fluctuation $\text{Re}_t = u'_{\text{rms}} l_t / \nu$ is called *turbulent Reynolds number*. The transition from laminar to turbulent flows occurs at $\text{Re}_t \approx 1$, with $\text{Re}_t > 1$ indicating turbulent flows, and $\text{Re}_t < 1$ indicating laminar flows.

$$l_t(\vec{x}) = \int\limits_{r_i=0}^{\infty} \frac{R_{u_i u_i}(\vec{x}, r_i)}{u_{i,\text{rms}}'^2(\vec{x})} dr_i = \int\limits_{r_i=0}^{\infty} \frac{\langle u_i(\vec{x})\, u_i(\vec{x} + \vec{e}_i\, r_i)\rangle_t}{u_{i,\text{rms}}'^2(\vec{x})} dr_i \qquad (3.4)$$

With r_i being an arbitrary spatial coordinate and $\vec{e}_i$ the unit vector pointing in the direction of r_i.

Large eddies are unstable and break up into smaller eddies, with their kinetic energy being transferred to smaller eddies. This process is repeated many times transferring the kinetic energy successively to smaller and smaller eddies until a minimum size is reached. The kinetic energy of these eddies is then dissipated by molecular viscosity. The breakup process forming smaller eddies from larger eddies is inviscid, i.e. the total kinetic energy of the initial eddies is passed through different sizes of eddies until the energy is dissipated by the smallest eddies [73]. Since the motion of the smallest eddies is dominated by viscosity, their size can be estimated by a dimensional analysis of the dissipation rate of turbulent kinetic energy ε and the kinematic viscosity ν:

$$l_\eta = \left(\frac{\nu^3}{\varepsilon} \right)^{1/4} \text{ with } [l_\eta] = \left(\frac{(\text{m}^2/\text{s})^3}{\text{m}^2/\text{s}^3} \right)^{1/4} = \text{m} \qquad (3.5)$$

l_η is the *Kolmogorov length scale*, named after the mathematician who first deduced this length scale [46][3].

In 1935, Taylor showed that the dissipation rate of turbulent kinetic energy ε can be calculated from the rms value of the velocity fluctuation and a newly introduced length scale, the so-called Taylor length scale l_λ [82]:

$$\varepsilon = 15\,\nu\, \frac{u_{x,\text{rms}}'^2}{l_\lambda^2} \qquad (3.6)$$

l_λ can be obtained geometrically by constructing a parabola, which osculates[4] the normalized two-point correlation function at $r_i = 0$. The intersection of the parabola with the r_i-axis defines the Taylor length scale l_λ [73]. Figure 3.2 shows a sketch of the geometrical construction of l_λ.

---

3   First published in Russian in *Dokl. Akad. Nauk SSSR* (1941) 30(4).
4   Two functions are called to osculate at a point *P* when they have the same value there and also the same derivatives, up to order 2.
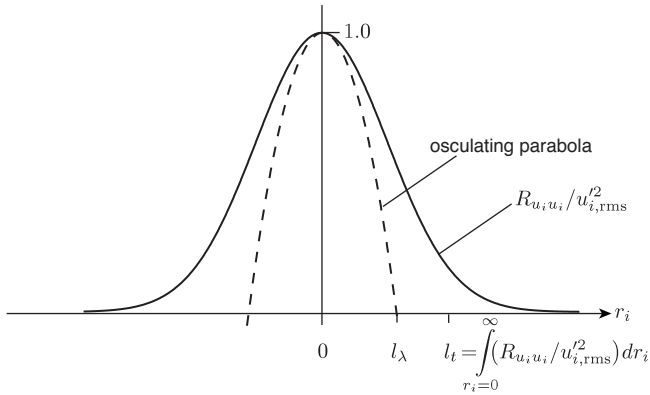
Figure 3.2: Sketch of the two-point correlation function and the parabola defining the Taylor length scale.

In general, the large eddies of a flow are anisotropic. Their geometry is determined by the mean flow field and the boundary conditions. However, the directional properties of the large eddies are lost by the breakup process forming smaller eddies. As a consequence, the small scale turbulent motions are isotropic and the statistics of this small scale turbulent motion have a universal form, which is well-defined by the dissipation rate of turbulent kinetic energy ε and the kinematic viscosity ν [46]. Eddies in a turbulent flow can be divided into three size ranges [73]:

- *Energy containing range*
  The largest, anisotropic eddies form the energy containing range. These are the initial eddies, which are produced by the shear of the mean flow.

- *Inertial subrange*
  In the inertial subrange, viscous effects are negligible. The energy of the larger eddies is transferred to smaller eddies.

- *Dissipation range*
  In the dissipation range effects of viscosity become increasingly important. The turbulent kinetic energy is finally dissipated completely. The smallest eddies in the dissipation range are of the size l_η.

Figure 3.3 shows a schematic spectrum of the turbulent kinetic energy with all relevant size ranges and energy transfer processes as discussed above [73].
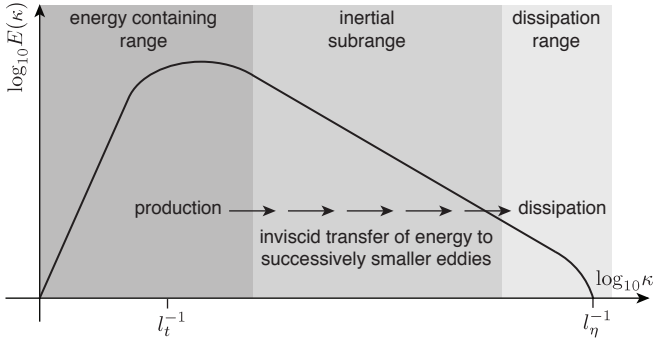
Figure 3.3: Sketch of the turbulent Energy spectrum $E(\kappa)$ as a function of the wavenumber of the eddies $\kappa = l^{-1}$ [73].

All turbulent length scales l are associated with a turbulent time scale τ, which is the typical turn-over time of an eddy of size l, and a characteristic velocity scale v defined as $v = l/\tau$. The Kolmogorov time scale τ_η and velocity v_η are important parameters in the strain rate model which will be introduced in Ch. 6. They are defined as

$$v_\eta = (\varepsilon v)^{1/4} \qquad (3.7)$$

and

$$\tau_\eta = \left(\frac{v}{\varepsilon}\right)^{1/2}. \qquad (3.8)$$

3.3 Premixed combustion

In premixed combustion, oxidizer and fuel are completely mixed before combustion occurs. If the equivalence ratio of the mixture is within the flammability limits and a heat source is supplied, the mixture ignites and a flame front propagates through the mixture. Typically, a chemical equilibrium is reached quickly downstream of the flame (burnt state), while the gas upstream of the flame remains in the unburnt state. Therefore, the flame can be interpreted as a heat source, separating the two stable states of the mixture, burnt and unburnt [69]. For lean hydrocarbon-air mixtures the overall reaction equation reads:

$$
\begin{aligned}
C_nH_m + \frac{1}{\phi}\left(n + \frac{m}{4}\right)\left(O_2 + \frac{79}{21}N_2\right) &\longrightarrow \\
nCO_2 + \frac{m}{2}H_2O + \left(\frac{1}{\phi} - 1\right)\left(n + \frac{m}{4}\right)\left(O_2 + \frac{79}{21}N_2\right) + \frac{79}{21}\left(n + \frac{m}{4}\right)N_2 &
\end{aligned}
\tag{3.9}
$$
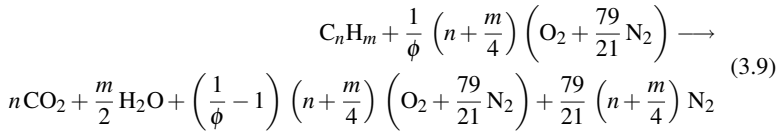
ϕ is the equivalence ratio, defined as the ratio of the fuel-to-oxidizer ratio of the mixture to the stoichiometric fuel-to-oxidizer ratio.

The speed with which an undisturbed flame propagates normal to itself into quiescent products is the laminar flame speed u_l. The maximum achievable combustion temperature for complete oxidation of the fuel without any loss of heat is the adiabatic flame temperature T_{ad}. Both, u_l and T_{ad}, are functions of the fuel and the equivalence ratio.

An undisturbed flame can be treated as a one-dimensional problem introducing a flame coordinate as shown in Fig. 3.4. The flame can be divided in four zones, as described by Peters [69]:

- *Preheat zone*
  The preheat zone is chemically inactive and has the thickness l_f. The products are heated to ignition temperature by heat conduction from the burnt gases. An approximation of the thickness of the preheat zone can be obtained by a comparison of the heat conduction from the flame into the unburnt gases, represented by the thermal diffusivity a, with the undisturbed propagation speed of the flame, represented by the laminar flame speed u_l:

$$
l_f = \frac{a}{u_l}
\tag{3.10}
$$
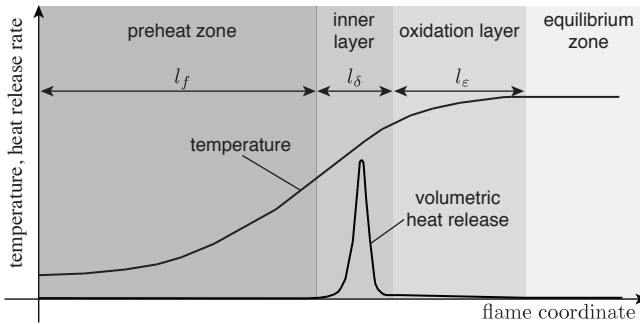
Figure 3.4: Internal structure of a premixed flame [69].

- *Inner Layer*
  Most of the fuel is consumed and radicals are formed by chain-branching reactions in the inner layer, releasing almost all of the heat produced by the flame. A simple estimate for an atmospheric methane-air flame with a preheat zone thickness of l_f gives a thickness of the inner layer l_δ of:

$$l_\delta \approx 0.1 l_f \qquad (3.11)$$

- *Oxidation Layer*
  In the oxidation layer - thickness l_ε - CO produced in the inner layer is oxidized to CO_2 and the maximum combustion temperature is reached.

$$l_\varepsilon \approx 3 l_\delta \qquad (3.12)$$

- *Equilibrium zone*
  All chemical species have reached an equilibrium in this zone. There is no heat release in the equilibrium zone.

The thickness of the entire flame is commonly approximated by the thickness of the preheat zone l_f.

3.4 Turbulence-flame interaction

A premixed flame is influenced by turbulence in the unburnt mixture ahead of the flame. To estimate the impact of turbulence on combustion, the laminar flame speed u_l and the flame thickness l_f are compared with the characteristic turbulence intensity u'_{rms} and the integral length scale of turbulence l_t [69].
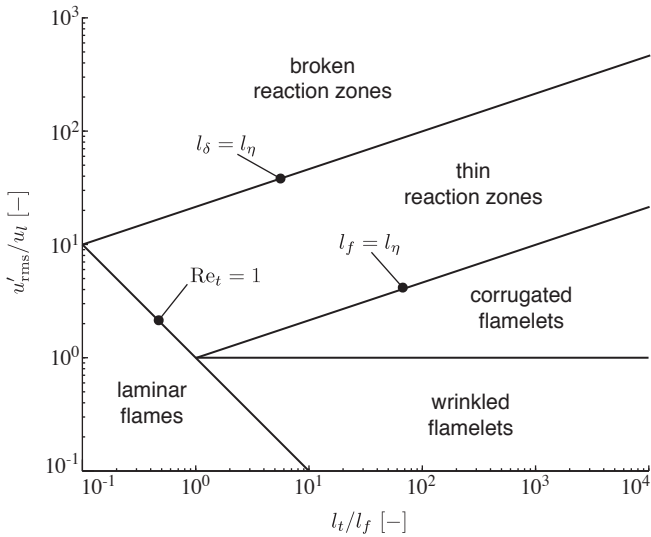
Figure 3.5: Regime diagram for turbulent premixed combustion [69].

3.4.1 Flame regimes

Based on the characteristic quantities for combustion and turbulence, flames can be divided into five regimes (Fig. 3.5) [69]. The classification of these regimes is based on the comparison of the thickness of the different flame layers with the size of the smallest eddies.

- *Laminar flames*
  A region with $Re_t < 1$ refers to laminar flames. In this region the turbulent fluctuations are so small that the flame propagation is not influenced by them at all.

- *Wrinkled flamelet regime*
  In the wrinkled flamelet regime the turbulent velocity fluctuations are smaller than the laminar propagation speed of the flame. Therefore, the laminar flame speed remains the dominant parameter for the flame propagation. The flame front is wrinkled but the laminar one-dimensional structure described in Sec. 3.3 remains unaffected by turbulence.

- *Corrugated flamelets*
  In the corrugated flamelets regime the flame front is strongly wrinkled by turbulence. However, the size of the smallest eddies is still larger than the flame thickness. Therefore, the eddies cannot penetrate the inner flame structure and thus cannot influence the combustion process. The flame remains locally laminar and one-dimensional, but the reacting surface of the flame is significantly enlarged.

- *Thin reaction zone*
  In the thin reaction zone regime the smallest eddies are smaller than the thickness of the flame's preheat zone, but larger than the thickness of the flame's inner layer. The diffusion of heat and radicals from the inner layer to the preheat zone is increased by turbulence, but the chemical reactions in the inner layer itself remain uninfluenced by turbulence.

- *Broken reaction zone*
  In the broken reaction zone regime, eddies can enter the inner layer of the flame. This causes the reaction to break down locally because of excessive heat loss to the preheat zone. The heat loss causes a temperature drop and a subsequent loss of radicals which can extinguish the flame locally.

The wrinkled flamelet regime, the corrugated flamelets regime, and the thin reaction zone regime are commonly called *flamelet regime*, in which a locally laminar flame front and an one-dimensional flame structure can be assumed. A turbulent flame in these regimes can be described as an ensemble of laminar flamelets with locally one-dimensional structure. This *flamelet concept* is widely used in combustion research to describe turbulent flames [69].

3.4.2 Flame straining

As described in Sec. 3.4.1, increasing turbulence intensity results in a stronger wrinkled flame. As a consequence, the effective flame surface of a turbulent flame is larger than that of a laminar flame [68]. Another important impact of turbulence on a flame is the *straining* of the flame front. The correlation between turbulence and straining is explained next and deduced from the basic properties of turbulent flows:

The velocity gradient tensor of a turbulent flow can be split in a symmetric and an antisymmetric part [79]:

$$\frac{\partial u_i}{\partial x_j} = 0.5 \left(\frac{\partial u_i}{\partial x_j} + \frac{\partial u_j}{\partial x_i} \right) + 0.5 \left(\frac{\partial u_i}{\partial x_j} - \frac{\partial u_j}{\partial x_i} \right) = S_{ij} - \Omega_{ij} \tag{3.13}$$

The symmetric part S_{ij} is the fluid dynamic strain-rate tensor of the turbulent flow and the antisymmetric part Ω_{ij} is the rotation rate tensor, which also describes the formation of eddies. Equation (3.13) shows that each eddy in a turbulent flow is accompanied by a straining structure. Figure 3.6 shows how an isolated counter rotating vortex pair and its associated straining structures affect an initially undisturbed flame front. The propagation of the flame is from top to bottom. A detailed analysis of this flame-turbulence interaction is given by Steinberg and Driscoll [79]:

At t_0 the flame front is uninfluenced by the vortices and straining structures. At t_1 the flame front propagates over the leading strain structure and a positive strain rate is imposed to the flame front resulting in a longer but flat flame front. This is depicted in Fig. 3.6 by a longer bold line in the flame front. At t_2 the strained flame is wrinkled by the eddies and a cusp is formed in the flame front. At t_3 negative strain is imposed to the flame by the trailing strain structure. The interaction of turbulence and flame typically attenuates the turbulence during the interaction [79]. As a consequence, the negative strain imposed on the flame by the trailing strain structure and the positive strain imposed by the leading structure do not compensate each other. Steinberg and Driscoll showed in their study that the contribution of the trailing strain structure is small compared to the positive strain imposed by the leading structure. Thus, net positive strain rate is imposed on the flame by the interaction with the eddies and the associated straining structures, resulting in an increased flame surface.

In addition to the *straining* of the flame, which is caused by the turbulence of the flow, also the propagation of a non-flat flame normal to itself entails a change
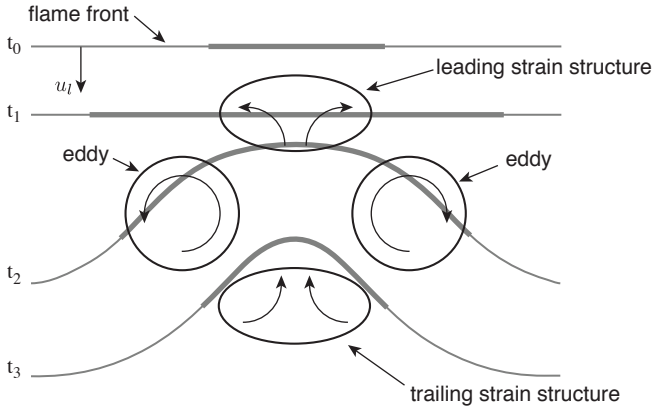
Figure 3.6: Schematic of the interaction of an initially undisturbed flame front with an iso-
lated counter rotating vortex pair and its associated straining structures [79]. The
bold part of the flame front illustrates a representative flame front element.

of flame surface. The rate of flame surface change due to the propagation of the
flame is called *curvature*. The sum of *strain* and *curvature* is the *stretch rate s*
and can be interpreted as the change of flame surface with time. It was shown by
Candel and Poinsot in 1990 that the stretch rate s of a flame surface element δA_f
can be written as [14]

$$s = \frac{1}{\delta A_f} \frac{D\left(\delta A_f\right)}{Dt} = \underbrace{\left(-\vec{n} \cdot \left(\vec{n} \cdot \vec{\nabla}\right) \vec{u}_f + \vec{\nabla} \cdot \vec{u}_f\right)}_{a_t} + \underbrace{s_l \vec{\nabla} \cdot \vec{n}}_{\kappa_c} \qquad (3.14)$$

with $\vec{n}$ being the flame surface normal vector, pointing into the reactants, $\vec{u}_f$ the
velocity vector at the flame element surface, and s_l the propagation speed of the
flame[5]. The first two terms on the right side of Eq. (3.14) describe the influence of
velocity gradients on the flame surface element. Those are the tangential strain a_t
imposed on the flame. The third term represents the curvature rate κ_c. In highly
turbulent flames the curvature effects are much smaller than the tangential straining

---

5   Note that s_l is in general not identical to the laminar flame speed because of the strechting of the flame.

and can be neglected [12]. With this approximation and substituting Eq. (3.13) in Eq. (3.14) the flame stretch can be written as[6]

$$s \approx a_t = -\vec{n} \cdot \left(\vec{n} \cdot (S_{ij})_f \right) + \nabla \cdot \vec{u}_f = \left(\delta_{ij} - n_i n_j \right) (S_{ij})_f \qquad (3.15)$$

The change in flame surface area due to tangential strain alters the heat and mass transfer processes at the flame front and, as a consequence, the rate at which reactants are consumed by the flame and the heat lost to the reactants by the reaction zone. At sufficiently high strain rates $a_t > a_q$ these effects can cause the flame to be locally quenched. This effect is equivalent to the breakup of the reaction zone and the extinction of the flame described for the broken reaction zone regime.

---

6 $\vec{n} \cdot (\vec{n} \cdot \Omega_{ij}) = 0$ due to the antisymmetry of the rotation tensor.

4 Experimental setup and measurement techniques

This chapter introduces the test rig, measurement techniques, and data evaluation procedures. The characteristics of the test rig, the burner, and the investigated operation points are discussed first. Then the optical measurement techniques are presented. In the last subsection, the data evaluation procedures and the flame parameters derived from the measurements are explained.

The emphasis of this chapter is on chemiluminescence measurement and data evaluation procedures and how a representative chemiluminescence signal can be obtained with high spatial resolution. In Sec. 4.3.2 the realization of the experimental considerations introduced in Sec. 2.3 is shown. Additionally, all wavelength dependent and non-linear effects of the measurement hardware are discussed in this chapter. The developed chemiluminescence measurement and data evaluation procedures are of crucial importance for this study. They are necessary to determine what information can be obtained about turbulent flame heat release rate from chemiluminescence (Ch. 5), and to develop a correction method, allowing to determine heat release rate from chemiluminescence by taking all identified non-linear effects into account (Ch. 6).

4.1 Test rig

The investigated flame in this study is a turbulent swirl flame at atmospheric pressure. Turbulent swirl flames are found in gas turbines and aircraft engines and are of outstanding importance in technical applications.

The fuel used is natural gas with a methane content of approximately 98%. Fuel and air are externally premixed in a static mixer to avoid mixture fluctuations in the burner. The mass flows of fuel and air are adjusted by thermal mass flow controllers. Control parameters are the equivalence ratio and the thermal power of the flame. The thermal power P_{th} can be adjusted between 10 kW and 120 kW, the equivalence ratio ϕ between 0.5 and 1.25. The premixed mixture is injected into the plenum. A plate made of sintered metal[1] is used to uniformly distribute

---

1 The porosity of the plate is 0.46, the pore diameter 30 μm. This is sufficiently small to quench propagating flames [85].

the mixture over the plenum cross section. Furthermore, the sintered metal plate quenches the flame in case of a flashback and prevents propagation of the flame into the feed pipe of the plenum.

The burner used in this study is the so-called TD^1 burner, which was first described by Fischer [25]. The modular burner consists of a tangential swirler, a conical nozzle, and a cylindric center body. This geometry stabilizes the flame by the formation of an inner recirculation zone, which is caused by the cross-sectional jump at the nozzle exit and the swirled flow. The center body reduces the flashback tendency of the burner by prohibiting the inner recirculation zone from penetrating into the burner. The flame stabilizes at the inner shear layer between the recirculation zone and the fresh mixture, where the reactants and the burnt gases are quickly mixed by the turbulent transport processes and the fresh mixture reaches ignition conditions (Fig. 4.1).
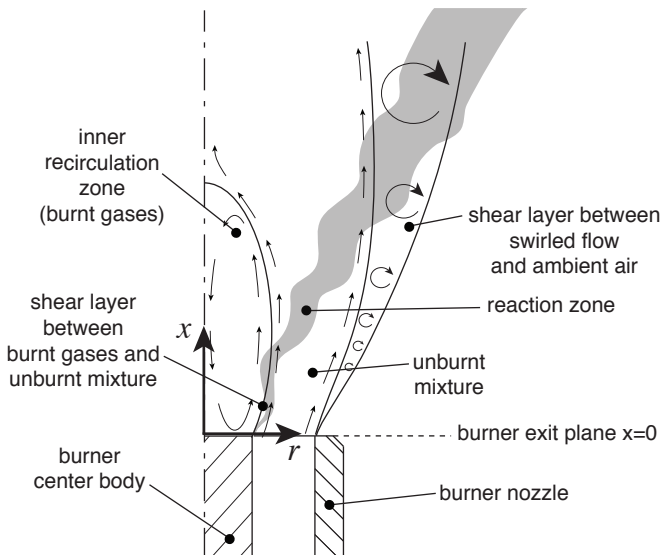
Figure 4.1: Sketch of the flow field at the burner exit.

The inner diameter of the nozzle is $D = 40\,mm$, the diameter of the center body is $d = 16\,mm$. The swirl number can be adjusted by partially blocking the tangential slits of the swirler, but was held constant at 0.55 in this study [88]. The lean blow off limit of the burner in this configuration is $\phi_{min} = 0.56$. Test rig and the burner are shown schematically in Fig. 4.2.
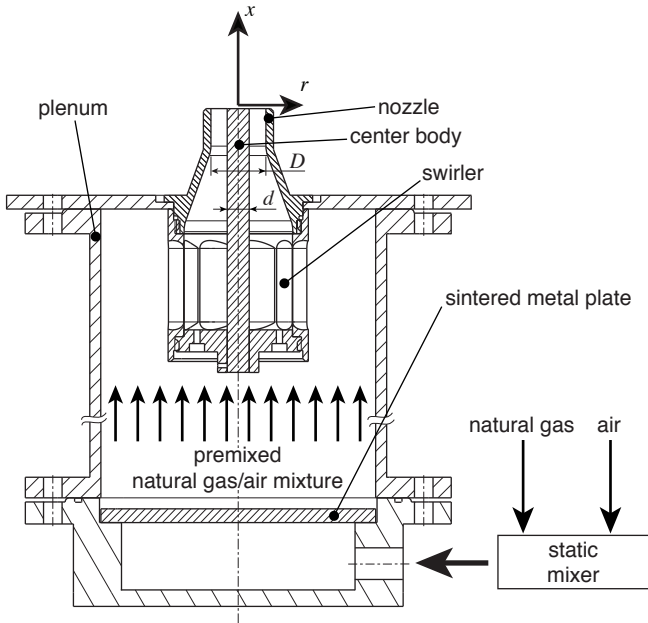
Figure 4.2: Sketch of the test rig.

In the present study, the fuel mass flow is equivalent to $P_{th} = 60\,kW$, and the equivalence ratio is varied from $\phi = 0.63$, which is close to the lean blow off limit of the burner, to $\phi = 1.11$. The Reynolds number in the burner nozzle ranges from 25,600 ($\phi = 1.11$) to 43,600 ($\phi = 0.63$). The test rig is operated with a non-preheated air-fuel mixture. Figure 4.3 shows the investigated operation points plotted in a flame regime diagram. All investigated flames lie within the thin reaction zone regime and can be described by the flamelet model (Sec. 3.4.1).
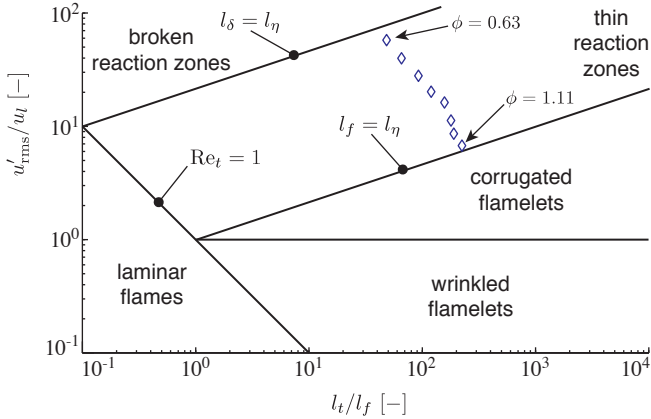
Figure 4.3: Flame regime diagram. The diamonds indicate the investigated flames. All flames lie within the thin reaction zone regime. u'_{rms} and l_t are the average values of the reaction zone obtained from PIV measurements (Sec. 4.3.3), u_l and l_f are calculated from relations found in literature, e.g. Turns [85], as functions of the equivalence ratio.

The flame is burning unconfined without a combustion chamber. This causes a non-constant equivalence ratio. As shown by Wäsle et at. [90], the axial mass flow downstream of the burner exit increases linearly due to turbulent admixing of ambient air in the shear layer between the swirled flow and the ambient air (Fig. 4.4).

As a consequence, the mixture becomes leaner with increasing axial distance from the burner nozzle. The ambient air entrainment takes place in the outer shear layer, but the flame stabilizes at the inner recirculation zone. Thus, the dilution of the mixture does not affect the flame close to the burner exit. Starting from axial distances of approximately $x/D = 0.5$, the flame burns the diluted mixture. The local equivalence ratio decreases with increasing axial distance as expected from the increasing mass flow (Fig. 4.5). This flame property is used to study the influence of equivalence ratio gradients in partially premixed flames, or to mimic admixing of air in confined gas turbine flames leading to mixture gradients.
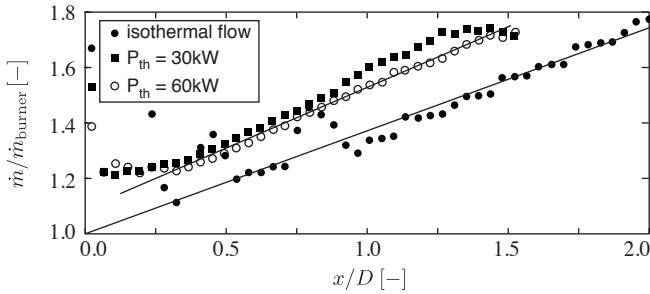
Figure 4.4: Increase in axial mass flow downstream of the burner nozzle due to ambient air entrainment, as measured by Wäsle at el. via Particle Image Velocimetry [90].
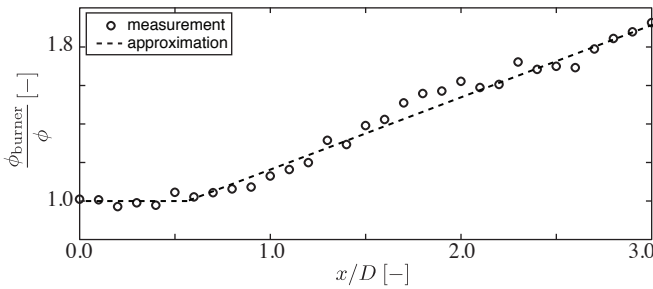
Figure 4.5: Radially averaged equivalence ratio in the flame mid plane of an unconfined flame, measured via the OH*/CH* chemiluminescence ratio. The equivalence ratio stays constant until an axial distance of approximately $0.5D$ is reached. Then, the flame reaches the diluted mixture and $\phi_{\text{burner}}/\phi$ increases linearly. The equivalence ratios shown are normalized with the equivalence ratio in the burner exit plane ϕ_{burner} [53].

4.2 Measurement techniques

In this section, the measurement techniques are described. This study focusses on chemiluminescence, which is measured spectrally resolved with a spectrometer

as well as bandpass filtered with image intensified cameras. All wavelength dependent and non-linear effects of the optical measurement hardware are discussed. The consideration of these effects is of crucial importance for measuring representative chemiluminescence signals.

The time resolved velocity of the flow is measured via *Particle Image Velocimetry* (PIV). Additionally, the instantaneous flame front is measured via *Planar Laser Induced Fluorescence* of the hydroxyl radical (OH-PLIF).

4.2.1 Spectrally resolved chemiluminescence

Spectrally resolved chemiluminescence measurements are acquired with an *Acton Research Cooperation* imaging spectrometer *SpectraPro 275*. The spectrometer is a Czerny-Turner type with in-line optical path. The focal length of the spectrometer is 275mm with an aperture ratio of 1:3.8. An UV camera lens (*Nikkor-UV*) with a focal length of 105mm and a maximum aperture of 1:4.5 is used to project the flame on the bilaterally adjustable slit assembly of the spectrometer. The slit assembly is used to tailor the light of the flame projection that enters the spectrometer. The slit width can be adjusted between 10μm and 3.0mm by an external micrometer. It is set to 10μm for all measurements in this study. The height of the slit is 8.5mm. The focal plane of the spectrometer lies 19mm beyond the housing, which allows for easy positioning of detection devices. The spectrometer has three diffraction gratings with 150g/mm, 600g/mm, and 2400g/mm (g/mm = grooves per millimeter). The 150g/mm grating is used to record the complete flame spectrum with a spectral resolution of approximately 1nm in a single image. The other gratings are used to achieve higher spectral resolution in selected subranges of the flame spectrum. The 150g/mm and 600g/mm gratings have a blaze wavelength of 500nm and an optimum wavelength range from 330nm to 750nm. The 2400g/mm grating is a holographic grating and has an optimum wavelength rage from 200nm to 600nm [1].

An image intensified high speed camera, type *Photron Fastcam Ultima APX I^2*, is attached to the spectrometer to record the spectra. The CMOS (complementary metal oxide semiconductor) sensor of this camera has a maximum resolution of 1024x1024 pixel at a frame rate of 2000 frames per second, and a fiber optically coupled image intensifier. The pixel size is $17x17\mu$m^2 [71]. The quantum efficiency of the image intensifier's photo cathode is better than 10% between 210nm and 550nm. Figure 4.6 shows a sketch of the spectrometer setup.
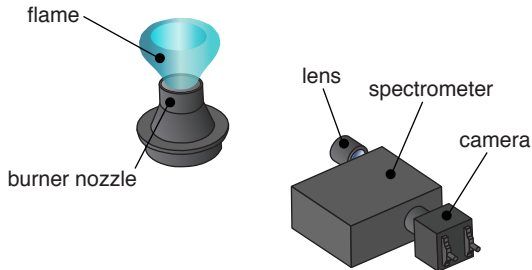
Figure 4.6: Sketch of the spectrometer setup.

Only the spectra of first diffracted order are of interest in this study. However, the larger wavelength of the spectrum of first diffracted order are superimposed by the shorter wavelength of the spectrum of second diffracted order (Fig. 4.7). The superposition of both spectra is recorded by the camera. Thus, the camera images show a distorted spectrum.
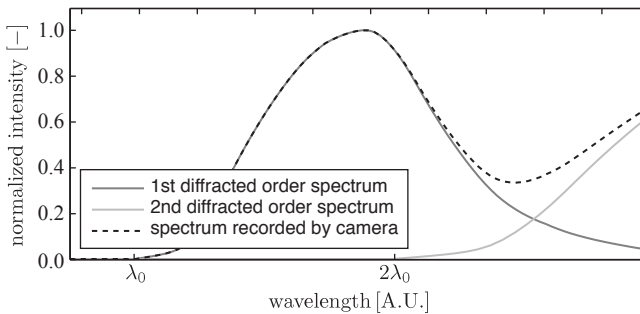
Figure 4.7: Diffraction spectrum of the spectrometer. The spectra of first and second diffracted orders are shown as well as the superposition of these spectra which would be recorded by the camera.

The shortest observable chemiluminescence wavelength with this setup is 275nm (Fig. 2.1). Thus, the interference of different order diffraction spectra only

matters for wavelengths larger than 550nm. In order to reduce the intensities from second order diffracted spectra, wavelengths larger than 550nm are measured with a long-pass edge filter with a cut-on wavelength of 550nm. This filter removes the intensities from second order diffracted spectra from the measured spectra.

The combination of UV-lens, grating, image intensifier, and CMOS sensor results in an unknown, wavelength dependent sensitivity of the spectrometer setup. In order to measure reliable data, this wavelength dependent sensitivity must be known and considered. This is achieved by a calibration. The spectrum of a halogen lamp is measured and compared with the reference spectrum of the lamp. The reference spectrum is obtained from a calibration measurement provided by the manufacturer. From this, a wavelength dependent calibration factor can be obtained and subsequently applied to all spectrometer measurements. Figure 4.8 shows the reference spectrum of the calibration lamp, the measured spectrum, and the resulting wavelength dependent calibration factor.
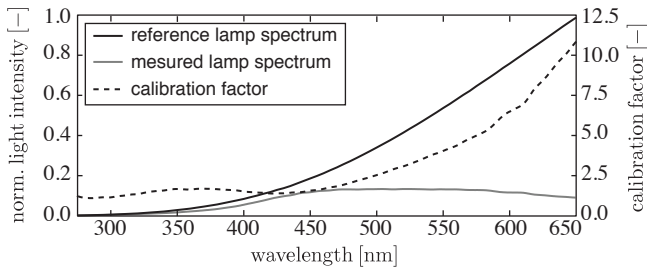
Figure 4.8: Reference and measured emission spectra of the calibration lamp. Additionally, the resulting wavelength dependent calibration factor is shown.

A typical measured spectrum is an image recorded by the camera. The exact wavelengths corresponding to the pixels of the image are obtained by an additional calibration measurement. For this, the spectrum of a mercury arc lamp is measured (Fig. 4.9).

Since the exact wavelength of the mercury emission lines are known, the pixel-scale of the images can be converted to a nm-scale. In Tab. 4.1 the pixel count of the identified mercury lines and the corresponding wavelengths for the spectrum shown in Fig. 4.9 are specified. The wavelengths are taken from McLennan et al. [60] and Sansonetti et al. [77].
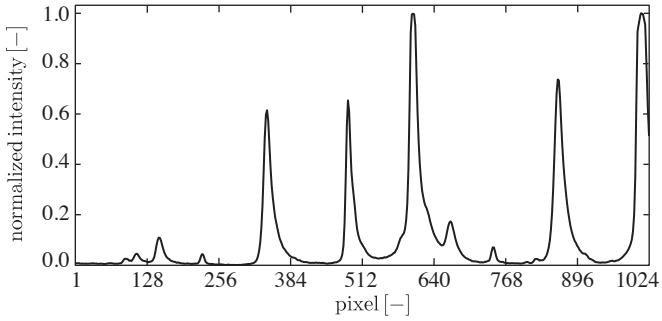
Figure 4.9: Spectrum of the mercury lamp used for wavelength calibration.

pixel count [-]	wavelength [nm]	reference
105	296.7282	Sansonetti et al. [77]
125	302.1503	Sansonetti et al. [77]
163	312.9691	Sansonetti et al. [77]
239	334.1485	Sansonetti et al. [77]
353	365.7793	Sansonetti et al. [77]
495	406.2201	Sansonetti et al. [77]
609	435.8334	Sansonetti et al. [77]
675	456.324	McLennan et al. [60]
863	506.61	McLennan et al. [60]
1011	546.0749	Sansonetti et al. [77]

Table 4.1: Pixel count of the identified mercury lines with their corresponding wavelength [60, 77].

The resulting conversion rule to obtain the nm-scale from the pixel-scale of the image is shown in Fig. 4.10.
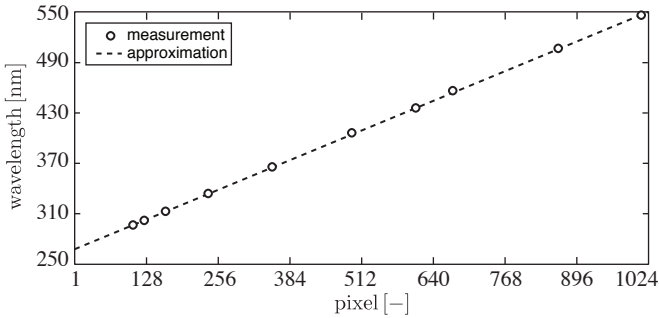
Figure 4.10: Conversion rule of pixel-scale and nm-scale of the spectrometer measurements.

4.2.2 Bandpass filtered chemiluminescence

Bandpass filtered chemiluminescence signals are detected with two *Photron Fast-cam ultima APX I²* high speed cameras with fiber optically coupled image intensifiers and silica glass camera lenses. The *Cerco Sodern* lenses have a focal a length of 45mm and a maximum aperture of 1:1.8. The resolution of the CMOS sensor of the cameras is 1024x1024 pixels for frame rates up to 2000 frames per second. The wavelength dependent quantum efficiency of the image intensifiers is provided by the manufacturer and considered in all measurements. Three bandpass filters are used in this study for chemiluminescence measurements:

- The chemiluminescence of the $\Delta v = 0$ transition of OH^* with superimposed CO_2^* background is measured with an interference filter with a maximum transmission of 16.57% at 309.65nm and a full width at half maximum (FWHM) of 10.2nm.

- Chemiluminescence of CH^* with superimposed CO_2^* background emissions is measured with an interference filter with a maximum transmission of 48.63% at 431.39nm and a FWHM of 10.6nm.

- A third interference filter with a maximum transmission of 68.18% at 456.42nm and a FWHM of 2.4nm is used. This filter transmits in a wavelength range in which only CO_2^* is emitting chemiluminescence.

The two cameras are used simultaneously, positioned on opposite sides of the flame facing each other to record two chemiluminescence signals at the same time[2]. One camera is running at a frame rate of 1kHz and acting as the master camera. The slave camera is synchronized to the master camera. The external trigger signal, which is set manually by the user, is passed from the master camera to the slave camera. Additionally, an external frequency generator, running at 125Hz, is used to mark every eighth frame. This marking function is a special feature of the cameras and is used to check the synchronization of the cameras. Figure 4.11 shows a sketch of the camera setup.
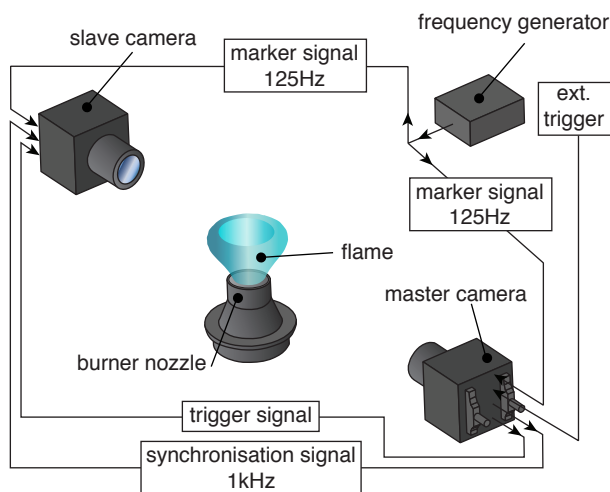
Figure 4.11: The setup of the two chemiluminescence cameras.

For a simultaneous measurement of two different chemiluminescence signals, the image intensifiers of the two cameras are typically operated with different am-

---

2   OH* and CH* are measured one after each other. In Sec. 4.3.2 it will be shown that in order to obtain a representative measurement signal for OH* or CH*, the chemiluminescence in the wavelength range of the radical must be measured simultaneously with the chemiluminescence at around 456nm. Since only two cameras are available in this study, two measurements in succession are necessary to obtain the chemiluminescence of OH* and CH*. All details of the data acquisition and evaluation procedure are given in Sec. 4.3.2.

plification factors (gain settings). This is done because the chemiluminescence signals have different intensities in the two observed wavelength ranges. Although the cameras and image intensifiers are technically identical, the quantum efficiency of the two image intensifiers is not, due to the different deterioration states of the intensifiers because of their different ages. To account for this effect, a calibration measurement is done. Both cameras are positioned opposite to each other at identical distance from the burner axis. On the burner axis a light emitting diode is placed and recorded with both cameras at all image intensifier gain settings. The exposure time of the CMOS sensor is gated to get a constant camera signal for all gain settings. Since the light emission of the LED is constant, the gain dependent quantum efficiencies of the image intensifiers can be determined and considered in the measurements of the flame chemiluminescence. This is necessary to get quantitatively comparable intensities from simultaneous measurements with two cameras. Figure 4.12 shows the intensities recorded by the two cameras as a function of the image intensifier gain setting.
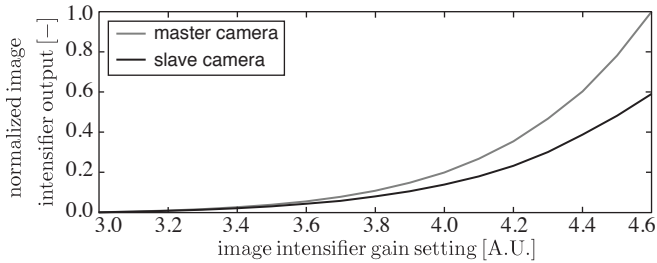
Figure 4.12: Quantum efficiencies of the cameras as a function of the image intensifier gain setting.

Chemiluminescence measurements are always line-of-sight integrated because of the low optical density of the flame. As a consequence, there is no spatial information normal to the camera detection plane. However, in case of time-averaged rotationally symmetric flames, such as the flames investigated in this study, the local time-averaged intensity in the flame mid-plane can be reconstructed from a time-averaged measurement using a deconvolution algorithm [22]. Absorption of chemiluminescence within the flame is not considered, as it was shown to be negligible in atmospheric flames [13, 43].

Additionally, the non-linear response of the CMOS sensor to the incident light intensity has to be considered in all camera measurements. The firmware of the camera automatically applies a gamma correction factor of 0.7 to all recorded images. Therefore, a gamma correction of 1.3 is applied to all images in the post processing. After this correction, the intensities shown by the chemiluminescence images scale linearly with the incident light intensity.

4.2.3 Velocity

The velocity field of the reacting flow is measured with Particle Image Velocimetry (PIV). Only a brief overview on this measurement technique is presented here, details are given by e.g. Raffel et al. [74]. The measurement setup is shown in Fig. 4.13. To capture the motion of the fluid, the flow is seeded with a tracer. This idea is based on experiments of Ludwig Prandtl in 1904, who used a dye to visualize the flow of water. The tracer can consist of particles added to the flow or particles contained in the fluid such as, for instance, bubbles in a two-phase flow. However, care must be taken to choose appropriate tracer particles, because the particles must closely follow the flow without any time lag in order to get reliable information about the fluid motion.

The particles are illuminated with two laser pulses to visualize and capture the tracer motion with a camera recording the light scattered by the particles. The laser beam is widened into a light sheet with appropriate optics to illuminate a plane of the flow field. The camera is positioned perpendicular to the light sheet to capture the undistorted, planar distribution of the tracer particles in a two-dimensional cross section of the flow field. The velocity of the flow field is then reconstructed from the particle distribution of two consecutive images by a statistical analysis: A cross correlation of the particle distribution of the two images gives the local displacements of the particles $\Delta \vec{s}(\vec{x})$. The local velocity of the particles - and of the flow - is calculated from the displacement vector and the time Δt between two laser pulses:

$$\vec{u}(\vec{x}) = \frac{\Delta \vec{s}(\vec{x})}{\Delta t} \tag{4.1}$$

PIV is a laser optical measurement technique which does not require the placement of probes within the measurement volume. Thus, it is non-invasive and can provide velocity data also from high temperature flows like flames, where probes
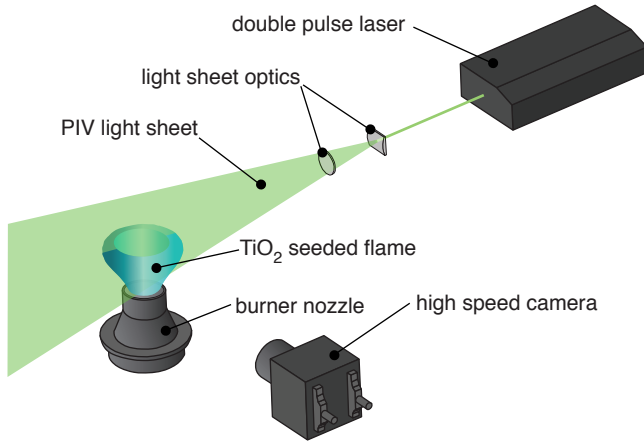
Figure 4.13: Setup of the Particle Image Velocimetry measurement.

might be destroyed by the heat. PIV is capable of providing instantaneous velocity information of a complete two-dimensional cross section of the flow field with a single measurement. This makes PIV well suited for flows with large scale structures like turbulent flames.

The laser system used in this study is a high repetition rate *NewWave Pegasus* double cavity laser. This frequency doubled neodymium-doped yttrium lithium fluoride (Nd:YLF) laser emits at 527nm with 10mJ per pulse. The pulse width is 110ns, with a repetition rate of the double pulses of 1kHz. The illuminated height of the flow field is four burner exit diameters. Depending on the maximum flow velocity, the time delay between the two laser pulses is adjusted between $15\mu s$ and $30\mu s$[3].

The detection camera is a *Photron FASTCAM-ultima APX* high speed CMOS camera. The camera has a maximum resolution of 1024x1024 pixel (dynamic range 10bit) at frame rates up to of 2kHz. The camera has 2.6GB memory, which is sufficient to record 1s at a frame rate of 2kHz and maximum resolution. Camera

---

3 Guidelines on how to choose the appropriate time delay between the laser pulses are given by Raffel et al. [74].

and laser system are synchronized and triggered by an external synchronization unit. The trigger scheme is shown in Fig. 4.14.
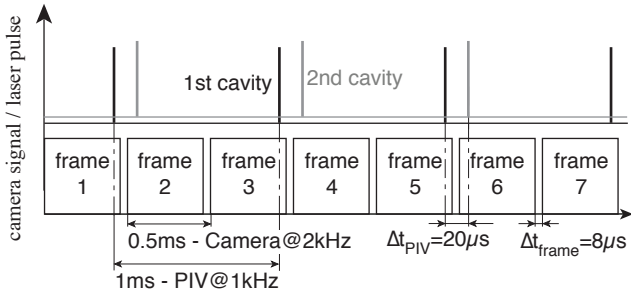
Figure 4.14: Timing of the PIV system. The lasers are running at a repetition rate of 1kHz, the camera at 2kHz. The time delay between the single frames is 8μs, between the two laser pulses 20μs.

The laser pulses of the first cavity are triggered at the end of odd-numbered frames, the pulses of the second cavity at the beginning of even-numbered frames. The time delay between the laser pulses is chosen short enough in order to be able to analyze particle motion with the cross correlation method even for high flow velocities.

The camera is running at a frame rate of 2kHz to obtain velocity fields every 1ms. The camera uses an 85mm focal length lens with a maximum aperture of 1:1.4. The aperture was closed to 1:5.6 during the experiments to increase the depth of focus. To reduce disturbing signals from the chemiluminescence of the flame, an interference filter with a center wavelength of 532nm is used. The maximum transmission of the filter is 90%, the FWHM is 20.2nm. The transmittance at the wavelength of the laser (527nm) is approximately 77%.

Titanium dioxide (TiO_2) particles with 0.3μm diameter are used as tracer particles. The particles are admixed to the air-fuel mixture in the plenum and follow the flow without any relevant time lag [47]. The high temperature resistance of TiO_2 allows to measure the velocity field of stoichiometric flames. Moreover, TiO_2 is non-toxic and can be released to the environment without aftertreatment of the exhaust gases.

4.2.4 Flame front

In order to track the instationary flame front, planar laser induced fluorescence of the hydroxyl radical (OH-PLIF) is used. The hydroxyl radical is an intermediate product of combustion and shows a sudden increase in its concentration in the reaction zone. The boundary between burnt and unburnt gases can be detected from the largest gradient of the hydroxyl radical concentration [23]. To visualize the hydroxyl concentration the radicals are excited from ground state to the first electronically excited state with a narrow band laser. The excited radicals are subject to the same energy transfer processes discussed in Sec. 2.1.3. Figure 4.15 shows schematically the laser induced excitation process of the $X^2\Pi_i(v'' = 0) \rightarrow A^2\Sigma^+(v' = 1)$ transition and the subsequent energy transfer processes.
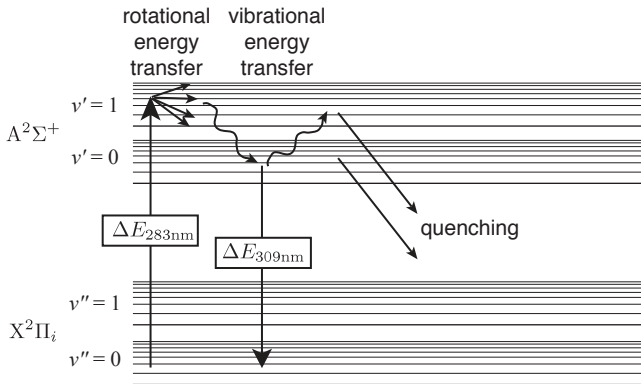
Figure 4.15: Schematic of the energy transfer processes of Laser Induced Fluorescence.

For the excitation of the radicals a frequency doubled *Lambda Physik Scanmate 1* dye laser, pumped with a *Lambda Physik Starline* neodymium-doped yttrium aluminum garnet (Nd:YAG) laser is used. The frequency doubled pump laser (532nm) is operated at a repetition rate of 1kHz. The pulse energy is 5mJ, the pulse duration 10ns. The pumped dye is Rhodamin 6G, which has a high absorption between 510nm and 550nm and emits broadband between 555nm and 585nm with a quantum conversion rate of approximately 32% [11]. The dye laser selects the 565.850nm line from the emission spectrum and converts

it to 282.925nm by a second harmonic generator to excite the $Q_1(6)$ line of the $X^2\Pi_i(v'' = 0) \to A^2\Sigma^+(v' = 1)$ transition. This excitation wavelength was empirically determined to be most suitable within this study [91]. The pulse energy after frequency shift and doubling (532nm $\to$ 565.850nm $\to$ 282.925nm) is approximately 100μJ. The UV-laser beam is then widened with a light sheet optics to illuminate a planar section of the flow field. The height of the light sheet is four times the diameter of the burner exit. Figure 4.16 shows a sketch of the experimental setup.
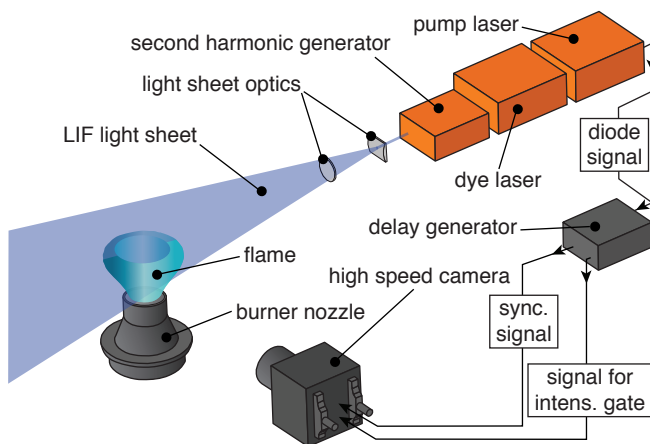
Figure 4.16: Setup of the planar Laser Induced Fluorescence measurement of OH radicals.

Due to the vibrational energy transfer processes within the excited state, the laser excited OH radicals predominantly emit light around 309nm. The detection camera is identical to that used in the the chemiluminescence setup and it is synchronized with the diodes of the pump laser with a delay of 204.2μs. To separate the laser induced fluorescence from the laser light, a bandpass filter *BrightLine HV 320/40* is used. This filter is transmitting light with 320$\pm$20nm at an average transmission rate of 76%. Since this filter is also transmitting chemiluminescence, the separation of laser induced fluorescence and chemiluminescence is achieved by a short gating of the image intensifier. The gate time is 200ns. In this way it

is achieved that the very short but high intensity laser induced fluorescence is not superimposed by the low intensity but continuous chemiluminescence signal.

4.3 Data evaluation procedures

4.3.1 Spectrometer measurements

The spectral characteristics of the different chemiluminescence species and the equivalence ratio dependence of the intensities are evaluated using the spectrometer measurements. For this measurements, the flame is confined with a quartz cylinder with an inner diameter of 158mm to avoid entrainment of ambient air and, as a consequence, to have a flame with no equivalence ratio gradients. For each measurement, 2048 spectra with an exposure time of 1ms are averaged to reduce the noise of the image intensified camera. The thermal power of the flame is set to 60kW. Flame spectra of eight equivalence ratios, ranging from 1.11 to 0.63, are recorded.

The broadband CO_2^* emissions are fitted with a 5th order polynomial. The polynomial is found to be self similar for all investigated equivalence ratios. Also, the shape of the $X^2\Pi_i \leftarrow A^2\Sigma^+(\Delta v = 0)$ OH* transition and $X^2\Pi \leftarrow A^2\Delta(\Delta v = 0)$ CH* transition are approximately self similar in the investigated equivalence ratio range[4]. Figure 4.17 shows the comparison of a model spectrum constructed from the self similar functions and a measured spectrum.

The equivalence ratio dependent ratio of OH* and CH* intensities also is obtained from the spectrometer measurements. The $\Delta v = 0$ transition of OH* and CH* around 309nm and 431nm are spectrally integrated and the ratio of the intensities is calculated. It is found that the OH*/CH* ratio has a monotonic dependence on equivalence ratio within the investigated equivalence ratio range (Fig. 4.18). This is in accordance with results published by, for instance, Haber [31], Panoutsos et al. [65], and Guyot et al. [30] (Sec. 2.2.2). The OH*/CH* ratio increases by more than a factor of ten when doubling the equivalence ratio. As noted in Sec. 2.2.4, this makes the OH*/CH* ratio a very robust measure for the equivalence ratio.

---

4 The shapes of the radical transitions change slightly with flame temperature due to the temperature dependent population of the different rotational states. However, the changes are small within the temperature range investigated in this study and can be neglected.
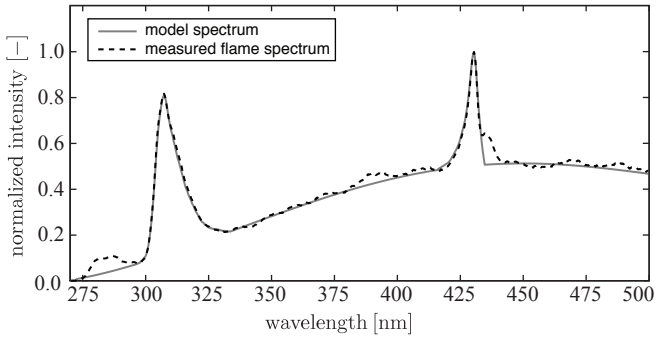
Figure 4.17: Comparison of a model spectrum, constructed from the determined self similar functions for OH^*, CH^*, and CO_2^* chemiluminescence with the measured spectrum of a lean methane-air flame.
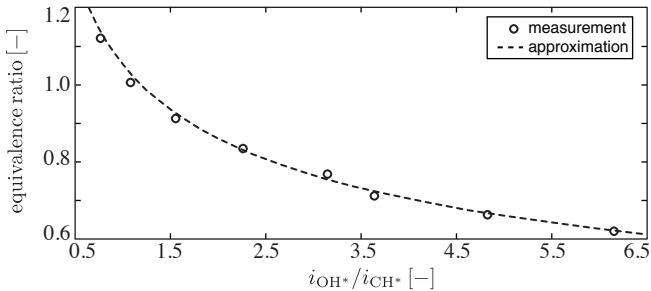
Figure 4.18: The dependence of the OH^*/CH^* chemiluminescence ratio on the equivalence ratio.

4.3.2 Bandpass filtered chemiluminescence and local equivalence ratio

As discussed in Sec. 2.3.1 and Sec. 2.3.2, a bandpass filtered measurement in the wavelength range of OH^* or CH^* is not representative for the number of electronically excited radicals. Each measurement signal contains a certain amount of

CO_2^* chemiluminescence. In addition, not the complete chemiluminescence band is transmitted by typical bandpass filters. This is illustrated in Fig. 4.19. The figure shows a typical chemiluminescence spectrum with narrowband emissions from the radicals superimposed by the broadband emissions from CO_2^*. The signals to be obtained from the measurements and the transmission curves of the used bandpass filters are also shown.
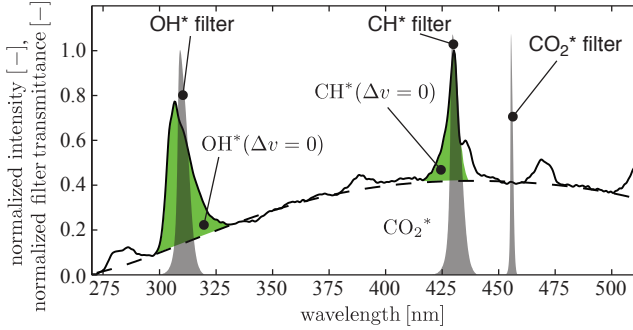
Figure 4.19: Typical chemiluminescence spectrum of an atmospheric turbulent methane-air flame. The dashed line is an approximation for the broadband emission from CO_2^*. The highlighted areas represent signals of interest from OH^* and CH^*. Additionally, the transmission curves of the used bandpass filters are shown.

The chemiluminescence from CO_2^* and the radicals can be written as the product of self-similar functions described in Sec. 4.3.1 and specific proportionality constants. The bandpass filtered measurement signal of OH^* can be written as:

$$S_{\text{BP,310nm}} = \int\limits_0^\infty \Big(\big(C_{OH^*} F_{OH^*}(\lambda) + C_{CO_2^*} F_{CO_2^*}(\lambda) \big) \, T_{\text{BP,310nm}}(\lambda) \Big) d\lambda \qquad (4.2)$$

Here, $S_{\text{BP,310nm}}$ denotes the bandpass filtered measurement signal at around 310 nm and $T_{\text{BP,310nm}}(\lambda)$ the corresponding bandpass filter transmittance. $F(\lambda)$ denotes approximation of OH^* and CO_2^* with self-similar functions, and C the corresponding proportionality factors. λ is the wavelength.

The self-similar functions $F(\lambda)$ are obtained from the spectrometer measurements described before, the bandpass filter transmittance $T(\lambda)$ is provided by the

manufacturer. The proportionality factors C_{OH^*} and $C_{CO_2^*}$ have to be calculated. $C_{CO_2^*}$ can be obtained from a second bandpass filtered measurement in a wavelength range in which only CO_2^* is emitting light. Such wavelength ranges can be found between the $a^3\Pi_h(v'=0) \leftarrow d^3\Pi_g(v''=2)$ and the $a^3\Pi_h(v'=2) \leftarrow d^3\Pi_g(v''=3)$ transitions of C_2^* at 438 nm and 476 nm. A bandpass filtered measurement at around 456 nm can be written as:

$$S_{BP,456nm} = \int_0^\infty C_{CO_2^*} F_{CO_2^*}(\lambda) T_{BP,456nm}(\lambda) \, d\lambda \tag{4.3}$$

$C_{CO_2^*}$ can be obtained from this second measurement signal by solving Eq. (4.3) numerically. The constant C_{OH^*} can then be calculated from Eq. (4.2). The OH* chemiluminescence intensity i_{OH^*} is given by:

$$i_{OH^*} = \int_0^\infty C_{OH^*} F_{OH^*}(\lambda) \, d\lambda \tag{4.4}$$

In order to obtain the necessary measurement data to calculate the chemiluminescence intensity of OH*, bandpass filtered signals around 310 nm and 456 nm are recorded simultaneously as described in Sec. 4.2.2. For each pixel of each image pair, the instantaneous OH* chemiluminescence of the flame is calculated. For every measurement 2048 of such image pairs are captured. The resulting OH* chemiluminescence intensities are averaged and deconvoluted to obtain the spatially resolved OH* intensities in the flame mid-plane [22].

The described data evaluation procedure is a non-linear operation. Thus, it is important that the procedure is applied to instantaneous - i.e. non averaged - measurement data, since the chemiluminescence intensities are fluctuating due to the turbulent character of the flame. The application of the procedure to time-averaged measurement data would lead to an erroneous result. As a consequence, it is necessary that the chemiluminescence signals at around 310 nm and 456 nm are captured simultaneously[5].

---

5 Due to the line-of-sight character of chemiluminescence measurements, instantaneous measurement signals only represent the intensities integrated spatially in direction perpendicular to the camera detection plane (Sec. 4.2.2). Thus, even by application of the presented data evaluation procedure to instantaneous measurement signals, a certain error is made. Since a three-dimensionally spatially resolved measurement of chemiluminescence is not possible in general, this error cannot be avoided. However, the presented data evaluation procedure is the best available approximation for a representative OH* measurement and minimizes all error sources as far as possible.

The chemiluminescence from CH* is measured and calculated analogously after the OH* measurement. These intensities are representative measures for the time-averaged number of electronically excited OH* and CH* radicals in the flame mid-plane. The necessity for this complex measurement and data evaluation procedure becomes obvious by comparing bandpass filtered chemiluminescence signals with intensities measured according to the procedure presented here (Sec. 5.3.2).

Additionally, the ratio of the OH* and CH* intensities in the flame mid-plane is calculated and the local, two-dimensional spatially resolved equivalence ratio in the flame mid-plane is obtained from the calibration curve shown in Fig. 4.18.

4.3.3 Time resolved velocities and turbulent flow properties

The image pairs recorded by the PIV camera are analyzed with the commercial software *VidPIV 4.6* by *ILA* [42]. A four-step adaptive cross-correlation with an 8x8 pixel interrogation area size and 4 pixel separation is applied. This results in 259x259 instantaneous velocity vectors with a spatial resolution of approximately 1 mm. For each operation point, 1024 image pairs are analyzed. From these data, the macroscopic turbulence properties of the reacting flow can be calculated, i.e. the spatially resolved rms value of the turbulent velocity fluctuation $u'_{i,\mathrm{rms}}$ (Eq. (3.2)) and the integral length scale of turbulence l_t (Eq. (3.4)).

However, calculation of the turbulent length scale from Eq. (3.4) is problematic, because the spatial resolution of the velocity measurement is similar to the integral length scale. Thus, integration of Eq. (3.4) based on experimental data would result in great uncertainties. This problem can be solved by using an analytical expression for the normalized two-point correlation instead [37]:

$$\frac{R_{u_i u_i}(\vec{x}, r_i)}{u'^2_{i,\mathrm{rms}}(\vec{x})} = \exp\left(-\frac{\pi}{4}\left(\frac{r_i}{l_t(\vec{x})}\right)^2\right) \tag{4.5}$$

The integral length scale can be determined reliably by fitting the experimental data with this exponential function with $l_t(\vec{x})$ as the only free parameter. Figure 4.20 shows a measured two-point correlation with the corresponding fit and the integral length scale of turbulence determined with this approach.

A direct determination of the Taylor length scale from PIV data is not possible. The spatial resolution of the PIV measurement is too low to determine the slope and curvature of the two-point correlation function accurately enough. Thus, the
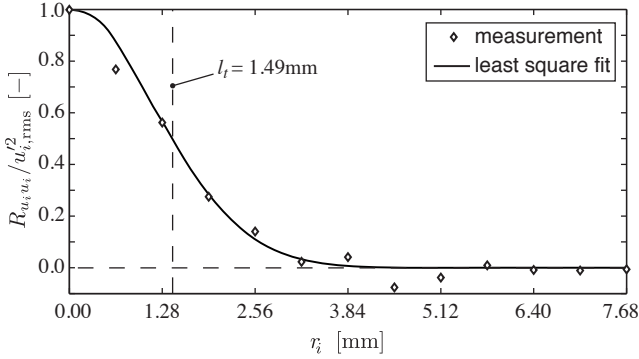
Figure 4.20: Measured two-point correlation fitted with the exponential function defined in Eq. (4.5) and the integral length scale l_t. The integral length scale of 1.49 mm is determined reliably from velocity vectors with 0.64 mm spatial separation.

Taylor length scale is estimated from the integral length scale based on previous studies found in literature and outlined in the next paragraph:

In 1935 Taylor [82] investigated grid generated turbulence. With Constant Temperature Anemometer (CTA) measurements he obtained the relation $l_\lambda \approx 0.5 l_t$. Girimaji and Pope [28] obtained the integral length scale and the Taylor length scale from direct numerical simulation (DNS) of isotropic turbulence. They determined a range from $l_\lambda = 0.33 l_t$ to $l_\lambda = 0.5 l_t$, depending on the Reynolds-number of the turbulent flow. Steinberg and Driscoll [79] characterized the Taylor length scale with laser doppler velocimetry (LDV) in 2009 and obtained $l_\lambda \approx 0.63 l_t$. Based on the above results, the Taylor length scale is approximated with $l_\lambda = 0.5 l_t$ in this study.

4.3.4 Flame front detection and reaction progress of combustion

The instantaneous flame front is determined from the LIF images by detecting the steepest gradient in the OH concentration field [23]. The used flame front detection algorithm follows closely the algorithms of Winkler [91] and Konle [48]. Thus, only a brief outline of the algorithm is given here. Details can be found in both references.
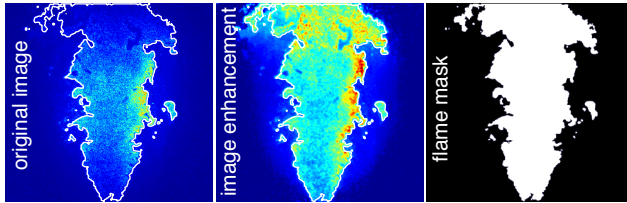
Figure 4.21: Example for the flame front detection procedure. The left image is a raw image captured with the LIF camera. In the middle an enhanced image after the correction of the Gaussian laser beam profile and the divergent light sheet is shown. On the right side the mask of the flame obtained by applying threshold criteria to the enhanced image is shown. In the original and enhanced images the detected flame front is shown as a white line.

The images are processed with a radial averaging filter with a radius of five pixel to reduce the noise from the image intensifier. The image intensity is adjusted to account for the Gaussian intensity profile of the laser beam and the intensity drop in radial direction of the flame due to a divergent light sheet. Then, a local threshold algorithm is used to create a bit mask of the flame from the images with *1* indicating burnt gases and *0* unburnt mixture. The contour of the binarized image is the boundary between burnt and unburnt gases and corresponds to the flame front (Fig. 4.21). For each operation point, 2048 LIF images are evaluated. The resulting bit masks are averaged to obtain the time-averaged reaction progress of combustion *c*. *c* can be interpreted as a dimensionless temperature of an adiabatic flame [85]:

$$c = \frac{T - T_{\mathrm{unburnt}}}{T_{\mathrm{ad}} - T_{\mathrm{unburnt}}} \tag{4.6}$$

Here, T is the temperature, T_{ad} the adiabatic flame temperature, and T_{unburnt} the temperature of the unburnt mixture. For the unconfined flames with equivalence ratio gradients investigated in this study, the local flame temperature can also be calculated from the reaction progress of combustion. In this case the local equivalence ratio, which is measured via the two-dimensionally spatially resolved OH^*/CH^* chemiluminescence ratio in the flame mid-plane, has to be taken into account in order to obtain the local, equivalence ratio dependent adiabatic flame temperature:

$$T(c, \phi) = c \left(T_{\text{ad}}(\phi) - T_{\text{unburnt}} \right) + T_{\text{unburnt}} \tag{4.7}$$

The adiabatic flame temperature T_{ad} can be obtained from literature, e.g. Turns [85], as function of the local equivalence ratio. Thus, the measured reaction progress of combustion can be used to determine the local time-averaged temperature of the flame. Further details on the relevance of the reaction progress of combustion are given, for instance, by Turns [85].

5 Heat release rate measurements

In the last chapter all relevant measurement techniques and data evaluation procedures were introduced. In particular, a method to obtain representative chemiluminescence measurements was presented. With this chemiluminescence measurement method and a precise heat release rate measurement procedure, which is introduced in this chapter and used as a reference, it is investigated what information on the turbulent flame heat release rate can be obtained from chemiluminescence.

The measurement and data evaluation procedure introduced in this chapter is capable of determining the local heat release rate of the flame quantitatively. Based on the first law of thermodynamics, this technique assumes that the local net heat release rate of the flame is balanced by the increase of the fluid's sensible enthalpy due to combustion. For evaluation of this energy balance, measurement data from chemiluminescence, PIV, and OH-PLIF are required. Due to the complexity of this reference method in terms of experimental effort, it is hardly applicable to experimental setups close to technical application. However, the technique is capable of providing the quantitative heat release rate of the laboratory flames investigated in this study and thus can be used to validate chemiluminescence.

Firstly, the theoretical background of the heat release measurement technique is given. Since the required experimental input parameters cannot be acquired simultaneously, the procedure is based on time-averaged quantities. Secondly, the results of the reference technique are discussed and checked for plausibility. In the last section, the obtained heat release distributions are compared with chemiluminescence distributions and the applicability of chemiluminescence measurements to characterization of the local heat release rate of turbulent flames is discussed.

5.1 Theoretical background

The flame in this study can be described as an open, stationary system with constant pressure and reaction (Fig. 5.1).
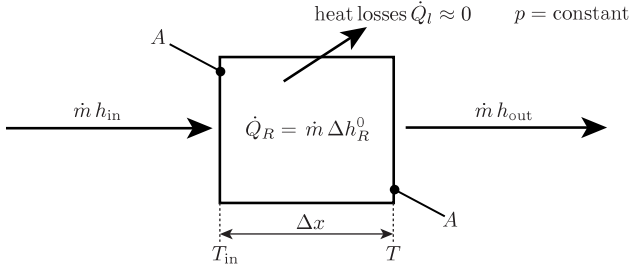
Figure 5.1: Energy balance of a finite flame volume. Heat losses are negligible in this study [54]. The heat release rate of the flame $\dot{Q}_R$ is balanced with the enthalpy of combustion $\dot{m}\Delta h_R^0$.

For such a system the first law of thermodynamics reads:

$$\dot{Q}_l \approx 0 = \dot{m}\left(h_{\text{out}} - h_{\text{in}}\right) \tag{5.1}$$

Here, $\dot{Q}_l$ denotes the heat losses of the flame, which are negligible in this study [54], $\dot{m}$ the mass flow over the system boundaries, and h the specific enthalpy. The mass flow at the inlet boundary has the temperature T_{in}, the mass flow at the outlet boundary the temperature T. $\dot{m}_{\text{in}}$ and $\dot{m}_{\text{out}}$ are identical.

The enthalpies h can be calculated from the enthalpies h^0 at defined temperature T_0 and the temperature integral of the isobaric heat capacities c_p:

$$0 = \dot{m}\left(h_{\text{out}}^0 + \int_{T_0}^{T} c_{p,\text{out}}(T)dT - h_{\text{in}}^0 - \int_{T_0}^{T_{\text{in}}} c_{p,\text{in}}(T)dT\right) \tag{5.2}$$

with

$$h_{\text{out}}^0 - h_{\text{in}}^0 = -\Delta h_R^0 \tag{5.3}$$

Δh_R^0 is the specific enthalpy of the reaction and corresponds to the specific heat release rate due to combustion $\dot{Q}_R/\dot{m}$. Substitution of Eq. (5.3) in Eq. (5.2) gives:

$$
\begin{aligned}
\dot{Q}_R &= \dot{m}\,\Delta h_R^0 \\
&= \dot{m}\left(\int_{T_0}^{T} c_{p,\text{out}}(\text{T})d\text{T} - \int_{T_0}^{T_{\text{in}}} c_{p,\text{in}}(\text{T})d\text{T}\right) \\
&= \dot{m}\left(\langle c_{p,\text{out}}\rangle\,(T - T_0) - \langle c_{p,\text{in}}\rangle\,(T_{\text{in}} - T_0)\right)
\end{aligned}
\tag{5.4}
$$

The reference temperature is set as the temperature at the inlet boundary:

$$
T_0 \equiv T_{\text{in}}
\tag{5.5}
$$

This simplifies Eq. (5.4):

$$
\dot{Q}_R = \dot{m}\,\langle c_{p,\text{out}}\rangle\,(T - T_{\text{in}})
\tag{5.6}
$$

The mass flow can be expressed as the product of fluid velocity u, fluid density ρ, and the boundary area A:

$$
\dot{Q}_R = \rho\,A\,u\,\langle c_{p,\text{out}}\rangle\,(T - T_{\text{in}})
\tag{5.7}
$$

For an infinitely small volume, the heat release rate $\dot{Q}_R$ can be written as the product of the volumetric heat release rate $\dot{q}_{\text{net}}$ and a differential volume dV, and the temperature difference $T - T_{\text{in}}$ as a differential temperature increment dT:

$$
\dot{q}_{\text{net}}\,dV = \rho\,A\,u\,\langle c_{p,\text{out}}\rangle\,dT
\tag{5.8}
$$

Equation (5.8) can be interpreted as an energy balance between the increase in the fluid's sensible enthalpy due to the chemical reaction and the net heat release rate of the flame. For a constant boundary area A, the differential volume dV can be written as:

$$
dV = A\,dx
\tag{5.9}
$$

Furthermore, in an infinitely thin volume the density ρ, the heat capacity $\langle c_{p,\text{out}} \rangle$, and the velocity u can be approximated as constants. Substitution of Eq. (5.9) in Eq. (5.8) gives:

$$\dot{q}_{\text{net}} = \rho \langle c_{p,\text{out}} \rangle u \frac{dT}{dx} \tag{5.10}$$

A similar equation was derived by Boineau et al. from a simplified energy equation in the context of combustion noise studies [9]. Equation (5.10) describes an one-dimensional problem. Since the flow is not one-dimensional in the present study, the gradient of the temperature in direction of the flow has to be considered:

$$\dot{q}_{\text{net}} = \rho \langle c_{p,\text{out}} \rangle \vec{u} \cdot \vec{\nabla} T \tag{5.11}$$

The density and the heat capacity of the fluid are functions of the fluid itself, which can be described by the equivalence ratio ϕ and the time averaged reaction progress of combustion c. Since the flame is described on a time-averaged basis, the progress variable c is necessary to take partial combustion into account. The temperature of the fluid can be estimated from the adiabatic flame temperature which is derived from *Chemkin* calculations [45] as a function of the local equivalence ratio. Again the time-averaged reaction progress variable is used to take partial combustion into account (Eq. 4.7 in Sec. 4.3.4):

$$T(\phi, c) = T_{\text{unburnt}} + c \left(T_{\text{ad}}(\phi) - T_{\text{unburnt}} \right) \tag{5.12}$$

T_{unburnt} is the temperature of the unburnt mixture, which is identical to the ambient air temperature[1]. The volumetric heat release rate of the flame is calculated as:

$$\dot{q}_{\text{net}} = \rho(\phi, c) \langle c_{p,\text{out}}(\phi, c) \rangle \vec{u} \cdot \vec{\nabla} T(\phi, c) \tag{5.13}$$

The required input parameters for Eq. (5.13) are the equivalence ratio, the reaction progress of combustion, and the flow velocity. These quantities are obtained from the measurement techniques and data evaluation described in Sec. 4.2 and Sec. 4.3. Figure 5.2 shows a simplified schematic of the presented heat release rate measurement technique.

---

1 The derived equations are explicitly applicable to the flames investigated in this study with entrainment of ambient air and equivalence ratio gradients.
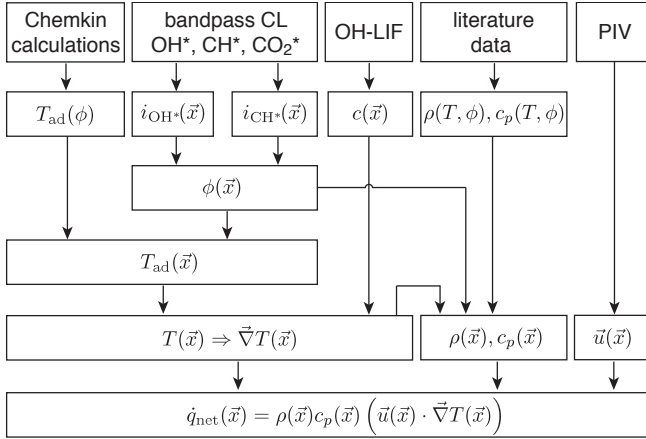
Figure 5.2: Simplified schematic of the presented heat release rate measurement technique.

5.2 Results and plausibility check

As an example for all investigated equivalence ratios, Fig. 5.3 shows the heat release rate in the flame mid plane of the $\phi = 0.91$ operating point.

5.2.1 Integral heat release rate

As a first plausibility check of the reference technique, the obtained heat release rates are spatially integrated. Then, the integral heat release of the flames is compared to the heat release expected for the given fuel-flow rate (Fig. 5.4). The integral heat release of the $\phi = 1.11$ operation point matches the expected value of 60kW well. However, with decreasing equivalence ratio a decreasing integral heat release is observed, despite the constant fuel mass flow.

This can be explained with the entrainment of ambient air in the flame. As shown in Sec. 4.1, the dilution of the mixture starts to affect the flame at about $0.5D$ downstream of the burner nozzle. Starting at this distance, the equivalence ratio decreases with increasing axial distance. As a consequence, the ignition condition of the mixture degrades strongly with increasing distance from the burner exit. In
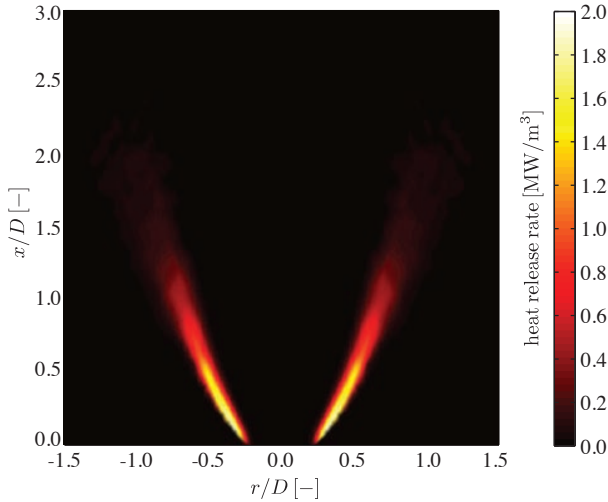
Figure 5.3: Time averaged heat release rate in the flame mid-plane of the $\phi = 0.91$ operation point.

the shear layer between the swirled flow and the ambient air an increasing fraction of the mixture is not burnt because of the intense dilution with ambient air. Due to the radial distance to the burner axis, the unburnt mixture cannot be recirculated, resulting in a decreasing integral heat release.

This effect was also shown by Hoffmann in 1994 [38]. Hoffmann measured the species concentration profiles in turbulent, swirl stabilized, unconfined flames which are comparable to the flames investigated in this study (Fig. 5.5). Hoffmann showed that due to entrainment of ambient air the local equivalence ratio of the flame is already influenced directly downstream of the burner exit. Starting at axial distances $x/D > 0.5$, the mixture fraction of CH_4 does not reach its undiluted value anymore. Especially in the outer regions of the swirled flow, the lower flammability limit of the mixture is exceeded or the intense dilution of the mixture with ambient air quenches the reaction. Hoffmann's measurements show that in premixed, swirl stabilized, unconfined flames, the fuel is not completely burnt, even for mixtures with near stoichiometric equivalence ratios [38].
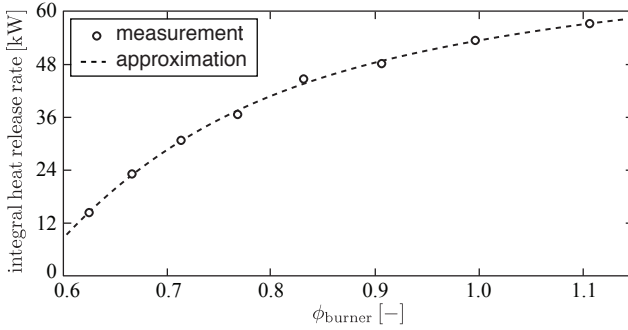
Figure 5.4: Integral heat release rates of the flames. The integral heat release rate decreases with decreasing equivalence ratio, despite a constant fuel mass flow.
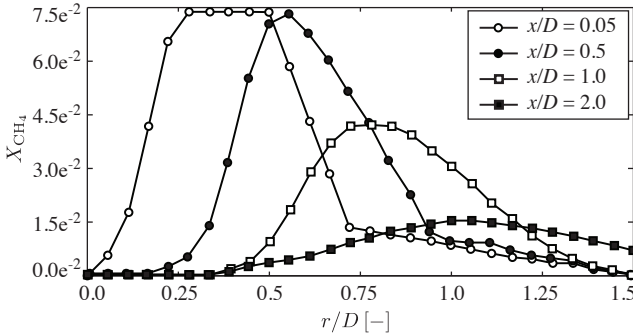
Figure 5.5: Mole fraction profiles of CH_4 in different horizontal planes of the flame investigated by Hoffmann [38]. The swirl number of Hoffmann's burner is 0.8, slightly higher than the swirl number of the burner investigated in this study.

The quenching of combustion in the shear layers can also be seen in the spatial distribution of the time averaged reaction progress of combustion (Fig. 5.6). Close to the burner exit the flame is not influenced by the air entrainment. Further downstream, the reaction is increasingly quenched in the shear layers for leaner equivalence ratios. This can be seen in the smaller flame surface of the leaner flames.
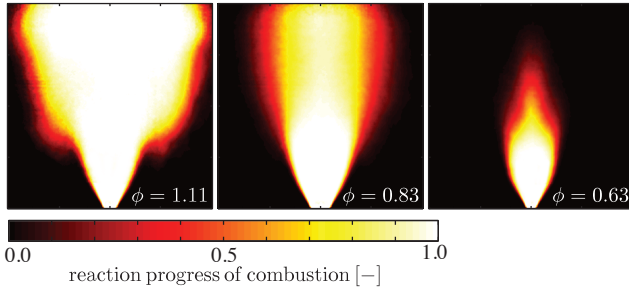
Figure 5.6: Time averaged reaction progress of combustion for burner equivalence ratios of 1.11, 0.83, and 0.63. With decreasing burner equivalence ratio an increasing fraction of the mixture in the shear layer between the swirled flow and the ambient air is not burnt.

5.2.2 Axial heat release rate profiles

In this subsection, the axial heat release rate profiles are discussed and checked for plausibility. Figure 5.7 shows the profiles of the eight investigated equivalence ratios. In this figure three different regimes can be seen:

- For a rich flame ($\phi = 1.11$) the heat release profile is shifted downstream compared with stoichiometric and lean flames. Because of the rich mixture, additional air has to be transported into the flame to reach favorable ignition conditions. This results in a lower heat release near the burner exit.

- For $\phi = 1.0$ to $\phi = 0.71$ the flames show an identical heat release rate up to an axial distance of $0.5D$ downstream of the burner nozzle. Further downstream the heat release distribution is lower for smaller equivalence ratios due to the increased fraction of unburnt fuel.

- The $\phi = 0.67$ and $\phi = 0.63$ flames, which are close to the lean blow-off limit of the burner, show lower heat release rates near the burner exit. This is an indicator for these flames not being properly stabilized any more.

Especially the heat release rates obtained close to the burner exit for the properly stabilized $\phi = 0.71$ to $\phi = 1.0$ flames are in very good agreement with theoretical expectations: The heat release rate is proportional to the volumetric fuel mass flow, which was kept constant for all investigated operation points and is therefore no
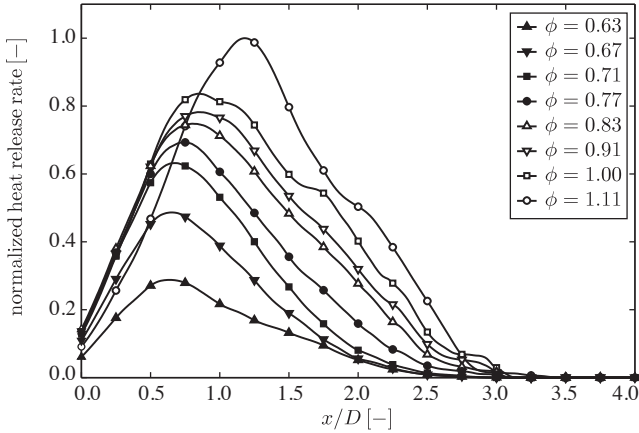
Figure 5.7: Axial heat release profiles of the investigated flames.

function of the equivalence ratio of the undiluted mixture. The determination of identical heat release rates for axial distances up to $0.5D$, which is the region of steepest gradients in the flame, clearly demonstrates the potential of the reference technique. At axial distances $x/D > 0.5$ the dilution of the mixture due to ambient air entrainment becomes increasingly important and the heat release rate decreases as shown by Hoffmann [38]. As can be seen in Fig. 5.7, there is no heat release at axial distances larger than three burner nozzle diameters.

It can be concluded that the results obtained with the reference technique are reasonable and in good agreement with theoretical expectations and previous studies. Furthermore, the reference method is capable of measuring the heat release rate quantitatively. This is a milestone compared to measurement techniques like heat release imaging which are purely qualitative. Therefore, it can be concluded that the reference technique can be used to assess the applicability of chemiluminescence measurements as an indication for heat release rate.

5.3 Comparison with chemiluminescence

In this section a comparison of chemiluminescence and heat release rate is presented. The influence of the CO_2^* contribution in bandpass filtered signals is also shown by comparing bandpass filtered chemiluminescence with chemiluminescence measured as described in Sec. 2.3 and the data evaluation described in Sec. 4.3.2.

5.3.1 Comparison of integral chemiluminescence and heat release rate

In Fig. 5.8 the normalized integral values of heat release and chemiluminescence intensities are shown. The solid lines show the heat release rate and bandpass filtered chemiluminescence data, the dashed lines show representative measurements for the number of OH* and CH* radicals.
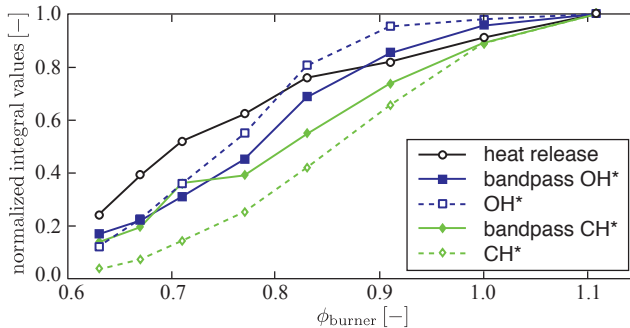
Figure 5.8: Comparison of the integral chemiluminescence intensities and the heat release of the flame. The solid lines show the heat release rate and bandpass filtered chemiluminescence data, the dashed lines show representative measurements for the number of OH* and CH* radicals. All variables are normalized by their maximum value.

It can be seen from Fig. 5.8 that all investigated chemiluminescence signals and the heat release rate are monotonically decreasing with decreasing burner equivalence ratio. However, the characteristics of the chemiluminescence signals are

more complex than those of the heat release rate: While the slope of the heat release rate curve is monotonically decreasing with increasing equivalence ratio, the slopes of the chemiluminescence curves increase at first and then decrease with increasing equivalence ratio with an inflection point in between. This can be explained with the fact that for the flames investigated in this study a change of the equivalence ratio also changes the integral heat release of the flame (Sec. 5.2.1). Thus, the effects from the change of the equivalence ratio and from the simultaneously changing integral heat release on chemiluminescence intensity interfere with each other. This results in the observed complex characteristics. As a consequence, no direct proportionality between any chemiluminescence signal and the heat release can be observed. However, with an empirically determined calibration, an integral chemiluminescence signal can be correlated with the integral heat release rate. It can also be seen from Fig. 5.8 that the CO_2^* contributions in bandpass filtered measurements have little influence on the curves of integral chemiluminescence intensities.

5.3.2 Comparison of axial profiles

Figure 5.9 shows the axial profiles of the chemiluminescence intensities and the heat release rate for the $\phi = 0.83$ operation point. The main characteristics of these profiles and the conclusions drawn for this equivalence ratio are identical for all equivalence ratios investigated in this study. Therefore, only the $\phi = 0.83$ plot is shown here. The corresponding plots of the other equivalence ratios can be found in the Appendix (Fig. A.1 to Fig. A.8).

The influence of the CO_2^* contribution in the bandpass filtered signals can be seen clearly from the normalized chemiluminescence profiles: Close to the burner exit ($x/D < 0.5$) and at axial distances $x/D > 3.0$ the CO_2^* contribution strongly distorts the shape of the chemiluminescence intensities in the bandpass filtered measurements. The relative CO_2^* contribution in the bandpass filtered signals at axial distances $x/D < 0.5$ and $x/D > 3.0$ is higher than at axial distances between $0.5 < x/D < 3.0$. Close to the burner exit and at high axial distances almost the complete bandpass filtered signals consists of CO_2^* chemiluminescence. As a consequence, substantial errors are introduced when bandpass filtered chemiluminescence signals are interpreted as a representative measure for the number of electronically excited radicals.

The CO_2^* contribution corrected CH^* signal is the best approximation of the heat release distribution, even though a significant downstream shift remains. However,
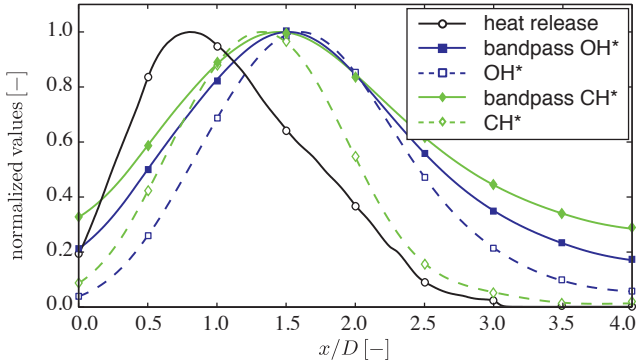
Figure 5.9: Comparison of the axial chemiluminescence profiles of bandpass filtered and CO_2^* contribution corrected OH^* and CH^* with the heat release profile of the flame. The solid lines show the heat release rate and bandpass filtered chemiluminescence data, the dashed lines show representative measurements for the number of OH^* and CH^* radicals

this observation cannot be generalized, as this effect is caused by the ambient air entrainment into the flame: CH^* chemiluminescence exhibits a stronger sensitivity on the equivalence ratio than OH^* with lower intensities for leaner equivalence ratios[2]. Thus, the equivalence ratio gradient in the flame causes the lower intense CH^* signal at axial distances $x/D > 1.5$ compared with OH^*. In constant equivalence ratio flames, a stronger CH^* signal at high axial distances is expected. As a consequence it can be concluded that all chemiluminescence signals indicate a too long flame.

The downstream shift of the chemiluminescence signals in Fig. 5.9 compared with the heat release is of critical importance. Since the equivalence ratio is almost constant near the burner exit (Fig. 4.5), this effect cannot be caused by ambient air entrainment. The shift can be explained with the local turbulence intensities in the flame.

For the flames under investigation in this study the turbulence in the reaction zone is high near the burner exit ($x/D < 1$). With increasing axial distance from

---

2   The measurement of the equivalence ratio via the OH^*/CH^* chemiluminescence ratio is based on this characteristics of OH^* and CH^* (see also Fig. 4.18).
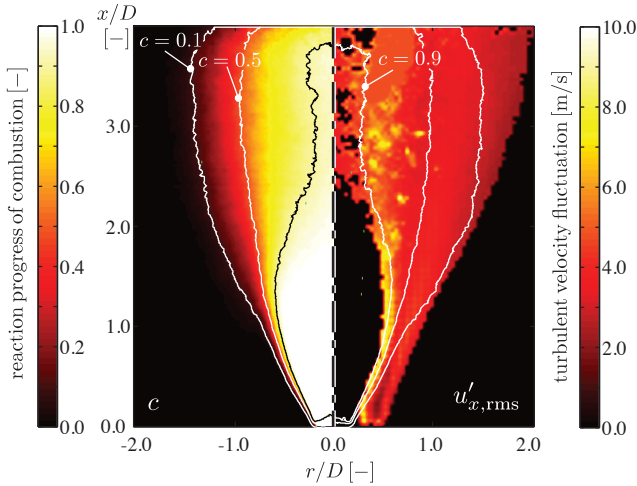
Figure 5.10: Comparison of the reaction progress of combustion (left) and the turbulence intensity (right). The contours indicate a reaction progress of 0.1, 0.5, and 0.9. The main fraction of the heat release rate occurs in between the $c = 0.1$ and $c = 0.9$ contours.

the burner exit the turbulence in the reaction zone decreases. The left part of Fig. 5.10 shows the reaction progress of combustion as an indicator for the reaction zone and the right part the rms value of the axial velocity fluctuation as indication for the local turbulence. The contour lines indicate a reaction progress of 0.1, 0.5, and 0.9. The area between the $c = 0.1$ and $c = 0.9$ contour represents the time averaged reaction zone of the flame.

For $x/D < 1$, the three contours are close together in a region of high turbulence. Further downstream, the reaction zone becomes wider with lower turbulence in between the contour lines. It was shown by John and Summerfield [43], Hurle et al. [40], and Ayoola et al. [6] that high turbulence reduces chemiluminescence intensities significantly (Sec. 2.2). Thus it can be concluded that the observed downstream shift of chemiluminescence compared with heat release is due to a reduction of chemiluminescence intensity caused by high turbulence in the region close to the burner exit.

The findings in this section are identical for all investigated equivalence ratios. Therefore it can be concluded that the observed shift between heat release distribution and chemiluminescence distribution is independent of the equivalence ratio and the integral heat release rate of the flame. This indicates that a similar downstream shift of chemiluminescence compared with heat release has also to be expected in confined, adiabatic flames without mixture gradients.

5.3.3 Flame length

In many applications a characteristic value of the chemiluminescence profile is used as the measure for flame length. In thermoacoustic studies, e.g. [3], the flame length is used to calculate the delay time between a flow perturbation in the burner exit plane and the response of the flame, assuming that the perturbation is transported convectively into the flame. Therefore, the flame length is an important parameter for such studies. The most common definitions of the flame length are:

- The location of the maximum emission $x(i_{max})$

- The balance point of the profile x_{bp}, defined as:

$$x_{bp} = \frac{\int\limits_0^\infty (x \cdot i(x))\, dx}{\int\limits_0^\infty i(x)\, dx} \qquad (5.14)$$

- The distance $x_{0.9}$ at which 90% of the integral chemiluminescence intensity has been emitted. $x_{0.9}$ is defined as:

$$x_{0.9} := x\Big|_{\int\limits_0^x i(x)\, dx = 0.9 \int\limits_0^\infty i(x)\, dx} \qquad (5.15)$$

Figure 5.11 shows the dependency of $x(i_{max})$ on the burner equivalence ratio, and the comparison of $x(i_{max})$ for the different chemiluminescence signals with the corresponding value for the heat release rate profile $x(\dot{q}_{max})$.

Because of the turbulence caused reduction of chemiluminescence intensity near the burner exit, the flame length obtained from the chemiluminescence profiles is longer than the actual flame length indicated by the heat release rate. The chemiluminescence based flame length overestimates the flame length by a factor of about
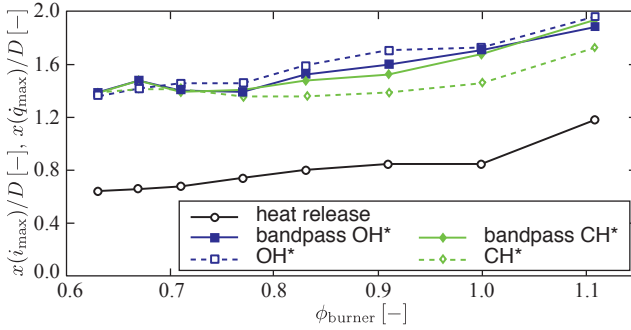
Figure 5.11: Comparison of the locations of maximum emission. The flame length indicated by chemiluminescence signals is longer than the flame length obtained from the heat release rate.

two. It can be seen that the CO_2^* contributions in the bandpass filtered measurements have little effect on the locations of the maximum emission.

Similar findings are obtained for other definitions of the flame length. Figure 5.12 shows the balance points of the axial chemiluminescence and heat release profiles. The results for $x_{0.9}$ are shown in Fig. 5.13.

It can be seen that for all definitions of the flame length the heat release rate shows a monotonic increase with increasing equivalence ratio. This cannot be seen in the chemiluminescence signals. Especially in the range of small equivalence ratios, the flame lengths determined from chemiluminescence show no clear trend. Even though the flame lengths obtained from the representative chemiluminescence signals seem to be a better estimate for the flame length, it has to be emphasized that no chemiluminescence signal gives an accurate approximation of the actual flame length.

As pointed out before, similar discrepancies between a chemiluminescence based estimate of the flame length and the actual flame length have also to be expected for confined, adiabatic flames without mixture gradients. In other words, no reliable information on the flame length can be obtained from chemiluminescence measurements of turbulent swirl stabilized flames.
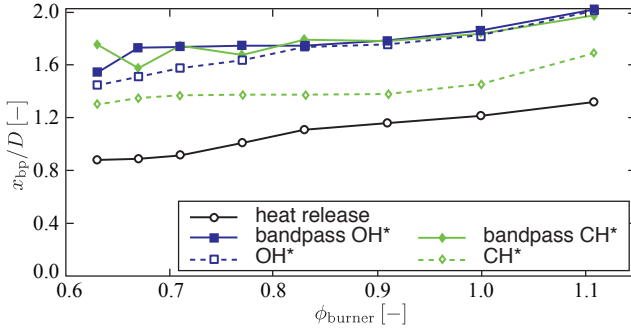
Figure 5.12: Comparison of the balance points of the axial profiles.
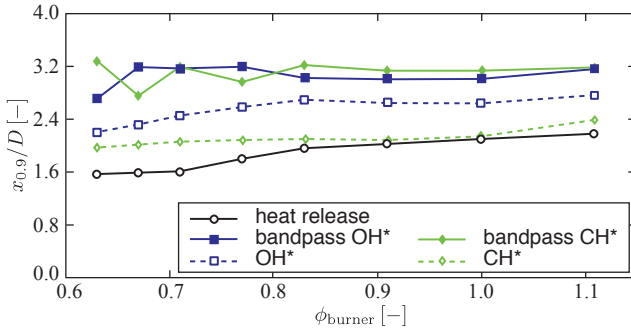
Figure 5.13: Comparison of $x_{0.9}$ as defined in Eq. (5.15).

5.4 Conclusions and implications for further studies

It has been shown that no reliable information on the local heat release rate of turbulent flames can be obtained from chemiluminescence measurements. Even though chemiluminescence can be used to monitor the integral heat release of turbulent flames if an empiric correlation between chemiluminescence and heat release can be obtained, the spatial distribution of the heat release rate cannot be

captured by chemiluminescence. Furthermore, flame lengths obtained from chemiluminescence indicate a too long flame.

The reason for these discrepancies in the spatial distributions of chemiluminescence and heat release rate is the non-constant turbulence intensity in the reaction zone. Close to the burner exit the turbulence is strongest and the chemiluminescence intensity is reduced more strongly than the heat release rate in this region of the flame. Further downstream the turbulence decreases, resulting in higher chemiluminescence intensities there. As a consequence, the chemiluminescence intensities are shifted downstream compared to the heat release profile. The findings on the impact of turbulence on chemiluminescence intensities shown in this chapter are in accordance with results reported by e.g. John and Summerfield [43], Hurle et al. [40], Ayoola et al. [6].

Thus, the influence of turbulence on chemiluminescence intensities (and heat release rate) must be taken into account in order to get reliable information on heat release from chemiluminescence. Otherwise no useful information can be obtained.

6 Strain rate correction method

In Ch. 5 it was shown that the local heat release rate of a turbulent flame is not represented by any chemiluminescence signal. The reason for this is the high turbulence intensity close to the burner exit. The turbulence reduces the chemiluminescence intensity more strongly than the heat release rate and, as a consequence, the chemiluminescence distribution of the flame is shifted downstream compared with the heat release rate. On the basis of this result, a correction method is developed in this chapter to account for the impact of turbulence on chemiluminescence intensities. For the first time, the local heat release rate of a turbulent flame can be determined reliably from OH* chemiluminescence by using this correction method.

It was shown in Sec. 3.4.2 that turbulence affects a flame through straining of the flame front. Furthermore, it was shown in Sec. 4.1 that the turbulent flames under investigation in this study can be described according to the flamelet concept as an ensemble of locally one-dimensional laminar flames. In this chapter, a model based strain rate correction method accounting for the non-linear dependencies of heat release rate and chemiluminescence intensity on strain rate is introduced. Measured OH* intensities are corrected to exhibit heat release rate proportional intensities. The correction method consists of two parts. The first, fluid mechanical part describes statistically the strain rates imposed on a flame by turbulence. The second, reaction kinetics part accounts for the effect of strain on heat release rate and chemiluminescence intensity.

In the first sections of this chapter it is shown how the strain rate imposed on the flame can be measured and modeled. Thereafter, the influence of strain on heat release rate and chemiluminescence intensity is quantified with simulations of strained counterflow flames. After that, both parts of the correction method are coupled to calculate heat release rate proportional chemiluminescence intensities from measured OH* signals. The last section shows additional counterflow simulations to investigate the impact of strain on preheated flames, flames at elevated pressure, and alternative fuel flames. The deficits of the reaction mechanism used in this study is shown there. Additionally, the applicability of the presented method to diffusion flames is briefly discussed.

6.1 Strain rate measurement and modeling

6.1.1 Direct measurement

As shown in Sec. 3.4.2, the tangential strain rate a_t can be calculated from the flame surface normal vector $\vec{n}$ and the flow velocity at the flame front $\vec{u}_f$:

$$a_t = -\vec{n} \cdot \left(\vec{n} \cdot \vec{\nabla} \right) \vec{u}_f + \vec{\nabla} \cdot \vec{u}_f \tag{6.1}$$

The flame front normal vector can be calculated from the flame front detected via OH-PLIF. The velocity at the flame front can be measured using PIV. If both measurement techniques are used simultaneously and are synchronized, with the OH-PLIF laser pulse centered in between the two PIV laser pulses, all necessary information for the calculation of the strain rate are obtained. Details of the simultaneous use of PIV and OH-PLIF are given by Winkler [91] and Konle [48]. Figure 6.1 shows a typical result of simultaneous PIV/OH-PLIF measurements. The background image is scattered laser light from the PIV tracer particles. The contour indicates the flame front obtained from the OH-PLIF, the red vectors indicate the flow velocity at the flame front, and the green vectors indicate the flame front normal vectors, pointing towards the reactants.

The direct measurement of flame strain based on simultaneous PIV/OH-PLIF measurements is reported in several studies, e.g. Donbar et al. 2001 [21], Sinibaldi et al. 2003 [78], Konle 2005 [47], and Hertweck 2009 [35]. However, in the work of Hertweck it was shown that the direct measurement of the strain rates is not applicable for the flames under investigation in this study for two reasons: Firstly, the planar measurement techniques OH-PLIF and PIV only provide the required measures in two dimensions. The contribution from the third dimension, which cannot be neglected in turbulent flames, is lost. Therefore, the measured strain rates are too low to represent the actual tangential strain rate of the flame. Secondly, the spatial resolution of the velocity measurement is too low to provide accurate information about the velocity gradients at the flame front[1].

---

1 As flame straining is caused by the small scale eddies, the velocity gradient of these eddies have to be resolved in order to provide accurate information about flame strain. A typical size of a Taylor scale eddy in the present study is 0.5mm. To resolve the velocity gradient of such an eddy reliably, a PIV measurement with spatial resolution in the range of 0.1mm would be necessary, but cannot be achieved with the available PIV hardware.
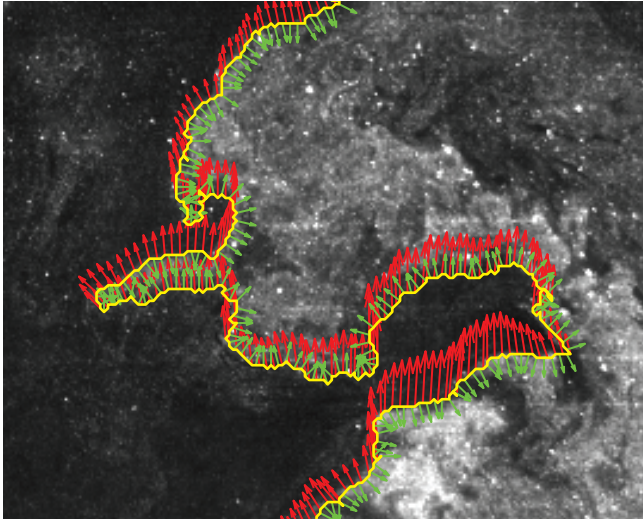
Figure 6.1: Flame front and velocity field obtained from a simultaneous PIV/OH-PLIF measurement. The background image is the mie scattering image of the PIV measurement, the yellow contour is the flame front determined from OH-PLIF. The vectors indicate the flame front normal direction and the velocity at the flame front.

6.1.2 Modeling

Since a direct measurement of flame strain rate is not possible, a statistical strain rate model developed by Pope and coworkers used in this study. The strain rate model was reported by Yeung et al. in 1990 [92].

The model is based on the direct numerical simulation (DNS) of constant-property, homogeneous, isotropic turbulence. The velocity field in the computational domain was artificially forced to obtain statistically stationary turbulence. Surfaces were defined in the computational domain, and the fluid particles representing these surfaces were tracked to obtain the time series of velocity gradients on the surfaces. The velocity gradients were then used to calculate the statistics of strain rate in the tangential plane of the predefined surfaces. The Taylor scale

Reynolds number $\text{Re}_\lambda{}^2$ of the simulations ranged from 38 to 93. It was shown by Yeung and Pope [93] that the spectral characteristics of the small turbulent scales of the simulations were in good agreement with those of grid generated turbulence measured in wind tunnels. All further details of the simulation are given by Yeung and Pope [94].

As shown by Yeung at al. [92], the strain rate statistics are a function of the propagation speed of the investigated surfaces. It was demonstrated that the strain rates of a slowly propagating surface are well represented by the strain rate distribution of a *material surface*, and the strain rates of a rapidly propagating surface by the strain rate distribution of a *randomly oriented surface*[3]. Furthermore, it was shown by Yeung et al. [92] that the probability density function (pdf) of the strain rate shows no significant Reynolds number dependence when the Kolmogorov time scale τ_η is used for normalization. Further it was shown that the strain rate distributions can be approximated very accurately with Gaussian functions. Figure 6.2 shows the pdfs obtained by Yeung et al. [92].

The mean strain rate of a randomly oriented surface $\langle \alpha_t \rangle$ is zero, whereas a material surface has a positive mean strain rate $\langle a_t \rangle = 0.280/\tau_\eta$. The standard deviation of the strain rate distribution for randomly oriented and material surfaces are $\sigma_\alpha = 0.257/\tau_\eta$ and $\sigma_a = 0.342/\tau_\eta$. The parameters of the Gaussian approximations are summarized in Tab. 6.1.

Re_λ	$\langle a_t \rangle \cdot \tau_\eta$	$\sigma_a \cdot \tau_\eta$	$\langle \alpha_t \rangle \cdot \tau_\eta$	$\sigma_\alpha \cdot \tau_\eta$
38	0.287	0.344	0	0.257
63	0.275	0.345	0	0.255
90	0.273	0.339	0	0.257
93	0.283	0.341	0	0.257
average	0.280	0.342	0	0.257

Table 6.1: Parameters of the gaussian descriptions of the strain rate pdfs obtained by Yeung et al. [92]. $\langle a \rangle$ and σ_a refer to a material surface, $\langle \alpha \rangle$ and σ_α to a randomly oriented surface.

---

2 $\text{Re}_\lambda = (u'_{\text{rms}} l_\lambda)/\nu$

3 A material surface is a surface which does not propagate by itself, it is only passively convected by turbulence. A randomly oriented surface propagates uninfluenced by turbulence [92].
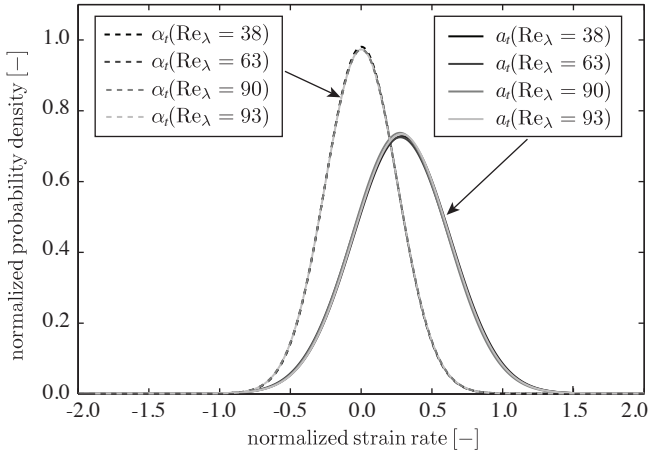
Figure 6.2: Strain rate probability density functions obtained from the DNS of Yeung et al. [92] (calculated from the values given in [92] and shown in Tab. 6.1). a_t denominates the strain rates of a material surface, α_t the strain rates of a randomly oriented surface.

6.2 Applicability of the Pope model to turbulent flames

A simulation of constant property, homogeneous, isotropic turbulence is a very limiting approximation for a turbulent flame. Thus, it has to be discussed whether the statistical strain rate distribution reported by Yeung et al. [92] can be used to describe the straining of (partially) premixed flames. Further, it must be investigated whether flamelets can be described as material or randomly oriented surfaces.

6.2.1 Constant property, homogeneous flow

In a turbulent flame the properties of the fluid are not constant (Sec. 3.1). Density, temperature, and the fluid composition are spatially and temporally changing due to the combustion process. Also, the flow cannot be considered homogeneous. However, in accordance with Pope [72] and Bradley et al. [12], the turbulence ahead of a premixed flame causes the main contribution to flame straining. Thus,

the statistical strain rate distributions can be calculated from the turbulence of the unburnt mixture into which the flame propagates. The premixed, unburnt mixture can be assumed to be a constant property, homogeneous flow.

Furthermore, the applicability of the strain rate model for isotropic turbulent flames is shown by Bradley et al. [12]. Bradley et al. used the strain rate pdfs of Yeung et al. [92] to predict turbulent burning velocities in fan stirred bombs and compared these with experimental data. The predicted and measured velocities were in very good agreement. This is a very strong indicator for the validity of the strain rate model for premixed combustion processes.

Another indicator for the validity of the strain rate model of Yeung et al. [92] for premixed combustion processes was given in 1998 by Chen and Im [15]. Comparable to the work of Yeung et al. [92], strain rates probabilities were obtained from two-dimensional DNS of premixed, unsteady methane-air flames with a detailed C_1 mechanism for the methane oxidation. Stoichiometric and lean mixtures were investigated. The results of Chen and Im [15] are in good agreement with those from Yeung et al. [92].

It can be concluded that although the strain rate distributions presented by Yeung et al. [92] were obtained from simulations of a non-reacting flow, the pdfs reliably describe the straining of isotropic turbulent flames.

6.2.2 Isotropic turbulence

Superimposed to a mean flow velocity, turbulence is in general anisotropic (Sec. 3.2). Thus it has to be discussed, whether a turbulence model assuming isotropic turbulence can be applied to the flames under investigation in this study. This is done by analyzing the statistics of the turbulent velocity fluctuations. In isotropic turbulence the time-averaged product of orthogonal components of the velocity fluctuation equals zero [69]:

$$\langle u_i' u_j' \rangle_t = 0, \; i \neq j \tag{6.2}$$

The right side of Fig. 6.3 shows the time-averaged product of the radial and axial components of the velocity fluctuation $\langle u_x' u_r' \rangle_t$. For comparison, $\langle u_x' u_x' \rangle_t$ is shown on the left side.

It can be seen that Eq. (6.2) is not exactly satisfied in the flow field of the flame, the time averaged product of the radial and axial velocity fluctuation does not
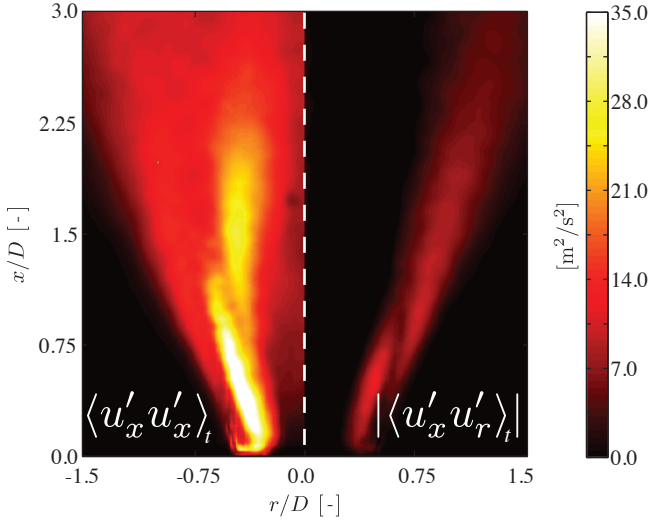
Figure 6.3: Comparison of the time-averaged product of radial and axial components of the velocity fluctuation (right) with $\langle u_x'^2 \rangle_t$ (left).

equal zero. However, since the absolute value of $\langle u_x' u_r' \rangle_t$ is significantly lower than $\langle u_x' u_x' \rangle_t$, the turbulence in the flame can be approximated as isotropic. Other criteria for the isotropy of the turbulence, like $\langle u_i' u_i' \rangle_t = \langle u_j' u_j' \rangle_t$, $i \neq j$ and the independence of the integral length scale on direction, show comparable results and lead to the same conclusions. Moreover, the velocity fluctuations shown in Fig. 6.3 and the other checked criteria are only characteristic for the macroscopic appearance of turbulence. However, the main contribution to flame strain is not caused by the macroscopic turbulence of the flow field, but by the small scale turbulence. As discussed in Sec. 3.2 - based on Kolmogorov's hypothesis of local isotropy - the small scale turbulence can be considered to be isotropic in any case [46]. Thus, the condition of isotropic turbulence is satisfied for the relevant length scales and, as a consequence, the strain rate pdfs proposed by Yeung et al. [92] can be used to describe the straining of the flames under investigation in this study.

6.2.3 Material and randomly oriented surface

In Sec. 6.1.2 is was shown that the strain rate probability density functions are different for material and randomly oriented surfaces. Thus, the turbulent flamelet must be characterized as material or randomly oriented surface in order to choose the appropriate strain rate distribution from the model of Yeung et al [92].

Per definition a material surface does not propagate by itself, it is only passively convected by turbulence [92]. In contrast to a material surface, a randomly oriented surface is propagating independently from turbulence. As a first approximation, a flamelet is propagating with the laminar flame speed in the turbulent flow [92]. On the one hand, the propagation with the laminar flame speed is an indicator for a randomly oriented surface. On the other hand, the flamelet is convected and reorientated by the turbulence, indicating a material surface. Yeung et al. discussed this question in great detail [92]. In their work they analyzed under which circumstances a propagating surface, which is initially coincident to a material surface, remains close enough to the material surface to be considered a material surface itself. Since the Kolmogorov length scale underestimates the smallest turbulent scales by approximately one order of magnitude [72], a distance $z < 5 l_\eta$ after $\Delta t = 16\,\tau_\eta$ between the material surface and the propagating surface was defined as criterion to separate material surfaces from randomly oriented ones. Yeung et al. deduced that this criterion for the approximation of a propagating surface as material surface is easily fulfilled, if the propagation velocity w and the Kolmogorov velocity v_η satisfy $w/v_\eta \ll 1$. Yeung et al. postulated that a flamelet can be considered as a material surface, if the laminar flame speed u_l is smaller than the Kolmogorov velocity v_η.

Bradley et al. investigated the transition of the strain rate distributions between material surfaces and randomly oriented surfaces in more detail [12]. They found that the strain rate distributions show a continuous transition between those of randomly oriented and material surfaces. Based on this result they defined empirically determined exponential functions for $\langle a_t \rangle$ and σ_a to take this transition into account. The only variable in the exponential functions is the ratio of laminar flame speed and Kolmogorov velocity u_l/v_η:

$$\langle a_t \rangle = \left(0.279 \exp\left(-5.123 \cdot 10^{-2} \left(\frac{u_l}{v_\eta} \right)^2 \right) \right) \tau_\eta^{-1} \tag{6.3}$$

$$\sigma_a = \left(0.2582 + 8.262 \cdot 10^{-2} \exp\left(-5.123 \cdot 10^{-2} \left(\frac{u_l}{v_\eta} \right)^2 \right) \right) \tau_\eta^{-1} \tag{6.4}$$

Figure 6.4 shows the average strain rate $\langle a_t \rangle$ and the rms-value σ_a of the strain rate distribution as a function of the ratio of laminar flame speed and Kolmogorov velocity. The solid lines are the functions defined by Bradley et al. [12] and shown in Eq. (6.3) and (6.4), the dashed lines are the values for material and randomly oriented surfaces given by Yeung et al. [92] (Tab. 6.1). It can be seen that the values from Yeung et al. are asymptotes of the functions defined by Bradley and coworkers. Further it can be seen that the criterion $u_l < v_\eta$ defined by Yeung et al. for the approximation of flames as material surfaces is reproduced by Bradley et al. [12].
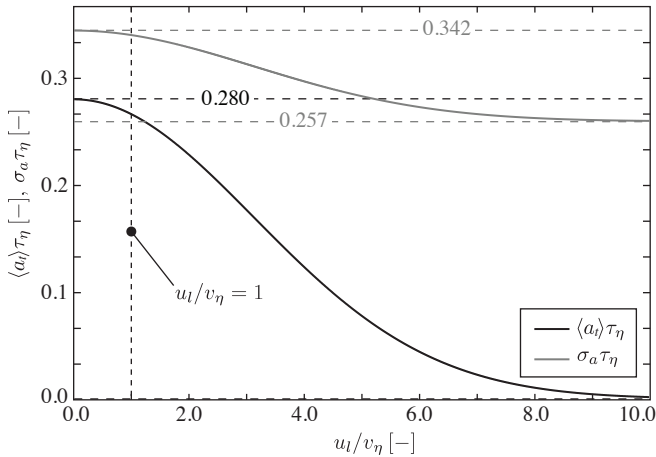
Figure 6.4: Dependency of the average strain rates and rms-values of the strain distributions on the ratio of laminar flame speed and Kolmogorov velocity [12].

The Kolmogorov velocity can be calculated from the PIV measurements (Sec. 3.2 and 4.3.3). The laminar flame speed is a function of the local equivalence ratio, which is obtained from the chemiluminescence measurements. The dependency of the laminar flame speed on equivalence ratio is known from literature (e.g. Turns [85]). Figure 6.5 shows the Kolmogorov velocity (left) for a 60 kW, stoichiometric flame in comparison with the local laminar flame speed (right).

As the thermal power of the flame is kept constant in this study, the lean flames correspond to larger air mass flows and thus higher flow velocities compared with
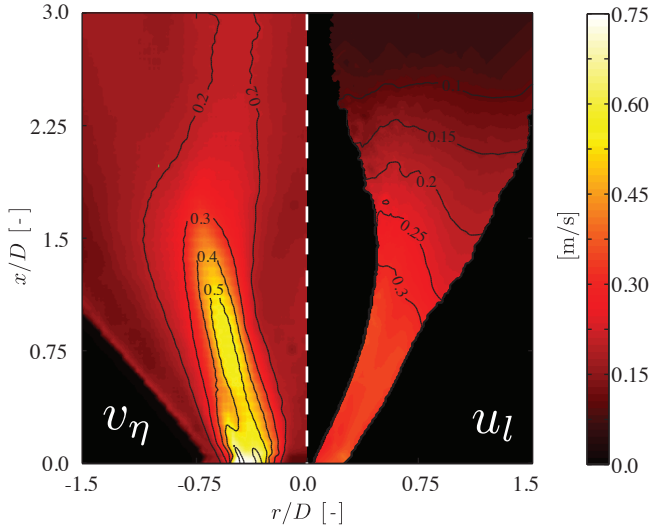
Figure 6.5: Comparison of the Kolmogorov velocity v_η (left) and laminar flame speed u_l (right). The laminar flame speed is obtained from the local equivalence ratio in the flame mid-plane, which is measured via the OH*/CH* chemiluminescence ratio, and a correlation between equivalence ratio and laminar flame speed proposed by Turns [85]. Thus, the laminar flame speed can be determined only in regions where chemiluminescence is emitted, whereas the Kolmogorov velocity, determined from PIV measurement, can be calculated in the complete flame mid-plane.

the stoichiometric flame. This results in increasing values of $u'_{x,\mathrm{rms}}$ with decreasing equivalence ratio, whereas the Taylor length scale shows no significant equivalence dependency. Thus, the Kolmogorov velocities increase with decreasing equivalence ratio, whereas the laminar flame speed is decreasing with decreasing equivalence ratio [85]. Since the condition $v_\eta > u_l$ for material surfaces is already satisfied for the stoichiometric flame, all lean flames under investigation in this study can be considered as material surfaces.

6.2.4 Summary of strain rate model

In the previous sections it was shown that for the considered flames the strain rate model proposed by Yeung et al. [92] can be applied. The assumptions of a constant property, homogeneous flow and isotropic turbulence were checked and discussed. Further, it was shown that the strain rate distribution of the flames is a function of the ratio of laminar flame speed and Kolmogorov velocity. As a consequence, the statistical distribution $p(\vec{x}, a_t)$ of the strain rate a_t of the flames can be approximated as

$$p(\vec{x}, a_t) = \frac{1}{\sqrt{2\pi}\,\sigma_a(\vec{x})} \exp\left(-\frac{1}{2} \left(\frac{a_t - \langle a_t \rangle(\vec{x})}{\sigma_a(\vec{x})} \right)^2 \right) \tag{6.5}$$

with

$$\langle a_t \rangle = \left(0.279 \exp\left(-5.123 \cdot 10^{-2} \left(\frac{u_l(\vec{x})}{v_\eta(\vec{x})} \right)^2 \right) \right) \tau_\eta^{-1}(\vec{x}) \tag{6.6}$$

$$\sigma_a = \left(0.2582 + 8.262 \cdot 10^{-2} \exp\left(-5.123 \cdot 10^{-2} \left(\frac{u_l(\vec{x})}{v_\eta(\vec{x})} \right)^2 \right) \right) \tau_\eta^{-1}(\vec{x}) \tag{6.7}$$

and the Kolmogorov velocity (Eq. (3.7)) and time scale (Eq. (3.2)), as defined in Sec. 3.8 [46]:

$$\tau_\eta(\vec{x}) = \left(15 \frac{u_{x,\mathrm{rms}}'^2(\vec{x})}{l_\lambda^2(\vec{x})} \right)^{-0.5} \tag{6.8}$$

$$v_\eta = \left(15 v^2 \frac{u_{x,\mathrm{rms}}'^2(\vec{x})}{l_\lambda^2(\vec{x})} \right)^{0.25} \tag{6.9}$$

Since the flames under investigation in this study are characterized as material surfaces, the values for the mean strain rate $\langle a_t \rangle$ and the standard deviation of the distribution σ_a can be approximated with the values shown in Tab 6.1. Thus, in this study the strain rate pdf is calculated as

$$p(\vec{x}, a) = \frac{\tau_\eta(\vec{x})}{\sqrt{2\pi}\,0.342} \exp\left(-\frac{1}{2} \left(\frac{a\,\tau_\eta(\vec{x}) - 0.280}{0.342} \right)^2 \right) \tag{6.10}$$

The Taylor length scale l_λ and the rms-vale of the turbulent velocity fluctuation $u'^2_{x,\text{rms}}$ are the only required input parameters for the evaluation of the strain rate pdfs and are obtained from PIV measurements (Sec. 4.3.3).

As an example, Fig. 6.6 shows the average strain rate and the rms-value of the strain rate pdf for the $\phi = 0.91$ operation point. It can be seen that maximum strain of $20{,}000 \text{s}^{-1}$ can occur. This is about twice as high as the highest strain rates which were directly measured by Hertweck [35] for the identical flame. The strain rates are high near the burner exit and decrease with increasing axial distance. At axial distances $x > 1.5D$ the strain rates are significantly lower than close to the burner exit. This is consistent with the results of Sec. 5.3, where the turbulence intensity was found to be highest near the burner exit and to decrease significantly at axial distances $x > 1.5D$.
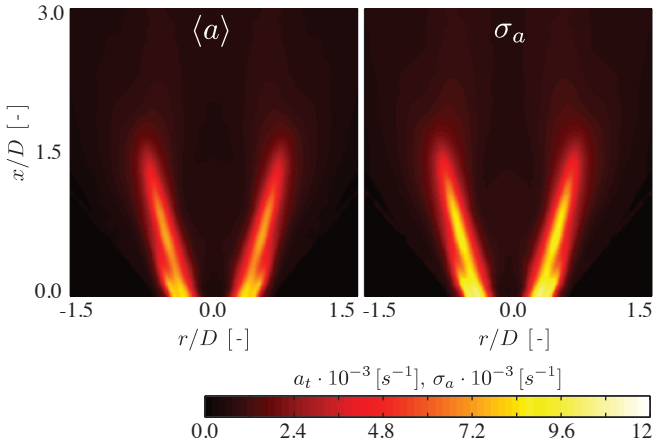
Figure 6.6: The average value and the rms-value of the strain rate distributions in the flame mid-plane of the $\phi = 0.91$ operation point. The maximum strain rates, estimated as $a_{\max} \approx \langle a \rangle + 2\sigma_a$, exceed values of $20{,}000 \text{ s}^{-1}$.

6.3 Counterflow flame calculations

In Sec. 6.1 and Sec. 6.2, the first part of the strain rate correction method, the fluid mechanical part, has been introduced and discussed for its applicability in this study. In this section the second part of the correction method, the influence of strain on heat release rate and chemiluminescence intensity, is presented.

The non-linear effect of strain on chemiluminescence intensity and heat release rate has to be taken into account in order to obtain reliable heat release rate information from OH* measurements. However, this effect is hardly accessible by experiments. Thus, numerical simulations of one-dimensional counterflow flames with detailed chemistry are done to obtain the relationship between strain rate, OH* intensities, and volumetric heat release rate.

6.3.1 Numerical setup

Counterflow flame simulations have developed into an important tool in combustion research over the past decades. The simulated laminar flames have an approximately one-dimensional character. Thus, only a single line of the flow field has to be simulated, which allows that even complex reaction kinetics can be calculated with moderate computational effort [85]. Counterflow flame simulations also offer the opportunity to get insight into combustion processes which are hardly observable by experiment. Typically, counterflow flame simulations are used to obtain flamelet libraries, which are used to describe turbulent flames in the flamelet regime (Sec. 3.4.1) as an ensemble of laminar flamelets. Since this study investigates (partially) premixed flames, only premixed counterflow simulations are considered.

The flow field of a counterflow simulation is formed by two opposed jets which form a stagnation plane in between. The exact location of the stagnation plane depends on the individual inertial momentum fluxes of the jets. Two different setups are possible:

- Two jets of premixed unburnt gases with a twin flame in between, commonly denoted as fresh-to-fresh setup.

- One jet of unburnt mixture opposed to a jet of hot products, called fresh-to-burnt setup. For this case, a single flame stabilizes on the side of the unburnt mixture.

The fresh-to-burnt setup is chosen in the present study, because it is, compared with the fresh-to-fresh setup, the more realistic description for premixed and partially premixed flamelets [12]. Figure 6.7 shows the counterflow setup used in this study.
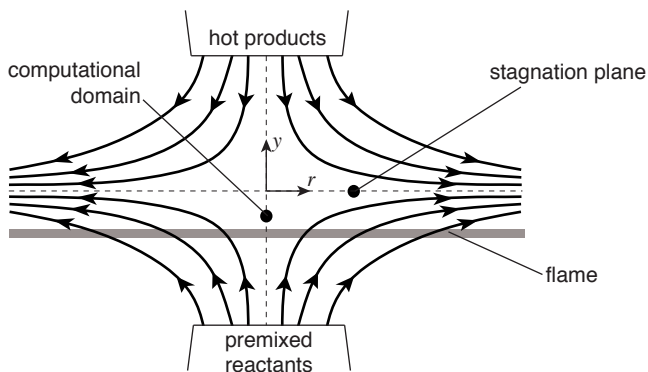
Figure 6.7: Schematic of a typical premixed, fresh-to-burnt counterflow setup.

The flame is one-dimensional and flat with dependencies only in y-direction. Thus, only the symmetry line $r = 0$ of the flow field is simulated. In this study the commercial software *COSILAB 3* by *Rotexo-SoftPredict* is used. All details about this software, e.g. the numerical methods, can be found in [75].

The simulation is done in a fully infinite domain with the strain rate as parameter. The flow velocities of the two opposed jets are automatically adjusted by the simulation software to match the user defined flame strain rate. The used reaction mechanism was recently developed by Kathrotia et al. [44] and consists of 69 species and 496 reactions[4]. Hydrocarbons up to C_4H_{10} are included. Additionally, the known formation and predominant deactivation reactions of OH^*, CH^*, and C_2^* are included. However, only OH^* chemiluminescence is considered in the simulations. The complete reaction mechanism is shown in the Appendix (App. C).

---

4   The reaction mechanism is based on the C_1-C_4 mechanism developed by Heghes [34]. The chemiluminescence sub-mechanism was added to this mechanism by Kathrotia et al. [44].

Nine equivalence ratios ranging from $\phi = 0.56$ to $\phi = 1.0$ and 18 strain rates ranging from $a_t = 500\text{s}^{-1}$ to $a_t = 20,000\text{s}^{-1}$ are simulated. Boundary condition on the fresh gas side are the volume fractions of O_2, N_2 and CH_4, corresponding to the equivalence ratio of the flame, and the unburnt temperature of the mixture. On the burnt side, the boundary conditions impose zero gradients for the volume fractions of all species and the temperature.

For each case an initial solution is calculated with a C_1-mechanism with 16 species and 46 reactions. Then, the more detailed mechanism of Kathrotia et al. is used. The simulations are started in unsteady mode with an initial time step of $\Delta t = 10^{-8}\text{s}$. The time step size is gradually increased to a maximum of $\Delta t_{\max} = 10^3\text{s}$. After $t = 10^4\text{s}$ the simulations are stopped and used as initial solutions for the final, stationary calculations.

Figure 6.8 shows a result of a counterflow flame simulation. For clarity only the profiles of temperature T, volumetric heat release rate $\dot{q}$, and mass fractions of methane Y_{CH_4} and electronically excited hydroxyl Y_{OH^*} are shown. The left boundary of the computational domain corresponds to burnt gases, the right boundary to fresh mixture.
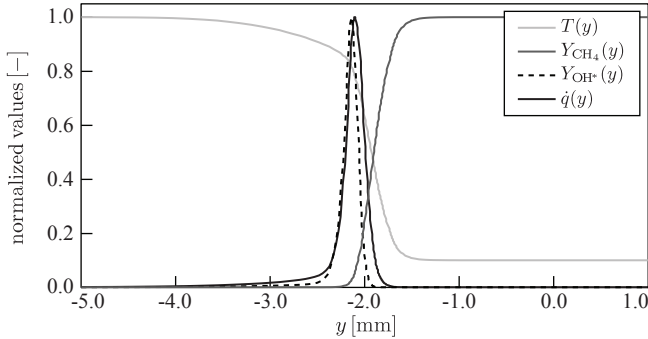
Figure 6.8: Result of a counterflow flame simulation. Only the profiles of temperature T, volumetric heat release rate $\dot{q}$, and the mass fractions of methane Y_{CH_4} and electronically excited hydroxyl Y_{OH^*} are shown.

6.3.2 Data processing

From the simulations, the profiles of the volumetric heat release rate $\dot{q}_y$ and the mole fraction of OH* $X_{\text{OH}^*,y}$ are extracted. $X_{\text{OH}^*,y}$ is directly proportional to the volumetric OH* intensity $i_{\text{OH}^*,y}$, with the Einstein coefficient of spontaneous emission as proportionality factor, because collisional quenching of OH* radicals is explicitly taken into account by the reaction mechanism. From these quantities the strain rate and equivalence ratio dependent proportionality factor $C(a_t, \phi)$ between heat release rate and OH* intensity is defined:

$$C(a_t, \phi) = \frac{\dot{q}(a_t, \phi)}{i_{\text{OH}^*}(a_t, \phi)} = \frac{\int\limits_{-\infty}^{\infty} \dot{q}_y(a_t, \phi, y)dy}{\int\limits_{-\infty}^{\infty} i_{\text{OH}^*,y}(a_t, \phi, y)dy} \tag{6.11}$$

A flamelet cannot experience arbitrary strain rates. Above a certain value $a_q(\phi)$ depending on the equivalence ratio, combustion will be quenched (Sec. 3.4.2). For symmetric (fresh-to-fresh configuration) counterflow flames it was shown in several studies that the heat release profile of the flame hardly changes with strain rate, until the quenching strain rate is reached. Above the quenching strain rate there is no heat release. For fresh-to-burnt counterflow flames the heat release rate profiles change in a more gradual way with increasing strain rate [12]. Figure 6.9 shows the heat release rate of a $\phi = 0.91$ flame as a function of the strain rate.

Since the heat release rate is tending asymptotically to zero for large strain rates, it is convenient to define a quenching strain rate above which the heat release rate is negligibly small compared with the unstrained value and can be approximated as zero. This reduces the number of necessary counterflow flame simulations significantly. A suitable quenching criterion in the present study is the strain rate, for which the integral heat release rate of the flame drops below two percent of the unstrained value[5].

The result of the counterflow flame calculations is a lookup table for the proportionality factor between heat release rate and OH* intensity with strain rate and equivalence ratio as parameters. Values between the calculated data points are interpolated bicubically, values above the quenching strain rate are not taken

---

[5] During the development of the correction method, also values of five percent and one percent of the unstrained heat release rate were tested as quenching criteria. The effect of the variation of the quenching criterion on the results of the presented correction method was negligible.
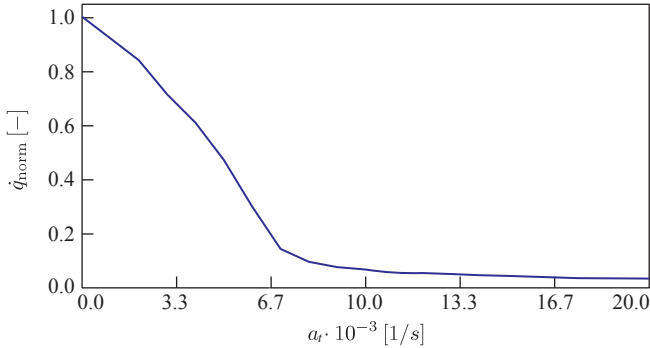
Figure 6.9: Heat release rate of the simulated $\phi = 0.91$ flame as function of the strain rate. The heat release rate is decreasing gradually with increasing strain rate. No clear quenching criterion can be identified. Thus, quenching is assumed when the heat release rate drops below 2% of the unstrained value.

into account. The calculated and interpolated lookup tables for non-preheated, atmospheric methane-air flames are shown in Fig. 6.10[6]. In the interpolated lookup table also the quenching strain rate is plotted.

6.4 OH* chemiluminescence correction and results

In this section the statistical strain rate distributions obtained from the model of Yeung et al. [92] and the PIV measurements (Sec. 6.2) are linked to the lookup table from the one-dimensional counterflow simulations (Sec. 6.3). The purpose is to obtain a correction factor which accounts for the non-linear relationships between OH* intensity, heat release rate, and strain rate. Such a factor can be interpreted as a representative, strain rate distribution averaged proportionality factor between OH* intensity and heat release rate.

---

6   Please note that in all lookup tables shown in this study, the reciprocal of $C(a_t, \phi)$ is plotted. This is done to improve the clarity of the plots in the range of small strain rates.
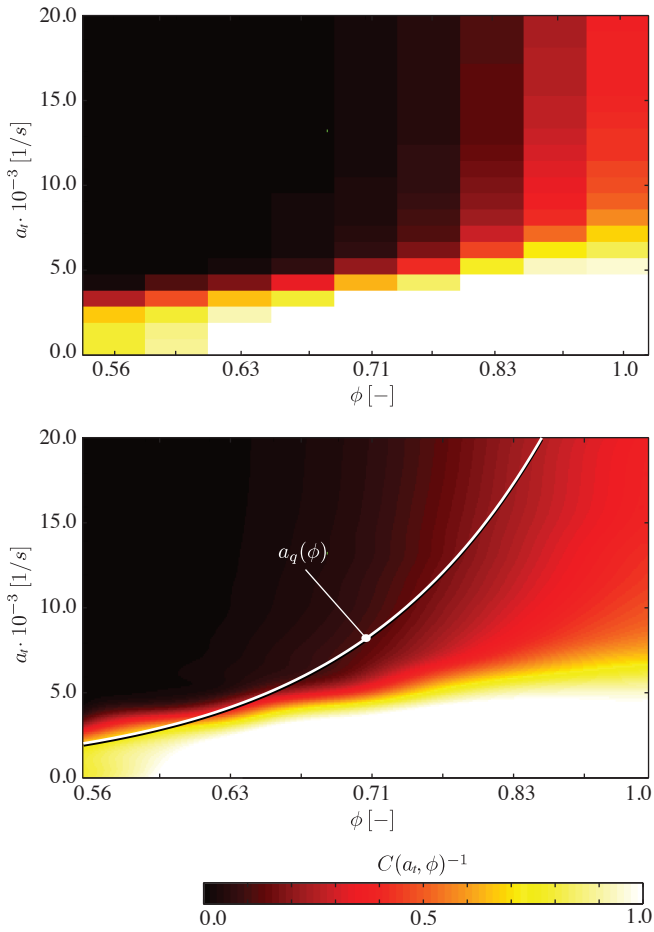
Figure 6.10: Lookup table obtained from the counterflow simulations (top) and the bicubi-
cally interpolated lookup table (bottom). In the interpolated lookup table also
the quenching strain rate, obtained from the 2% criterion, is shown.

6.4.1 Evaluation of strain rate pdfs

The strain rate distribution (Eq. (6.5)) is evaluated at each point of the flame mid-plane. The Kolmogorov time scale is calculated from the PIV measurements. It can be seen easily that approximately 20.6 percent of the obtained strain rates are negative (Fig. 6.2). Negative strain rates are very difficult to access by both experiment and simulation. Thus, for negative strain rates the values of $C(a_t, \phi)$ are approximated with the unstrained value following Bradley et al. [12].

The representative, strain rate averaged proportionality factor $\langle C(\phi) \rangle_a$ between the time averaged heat release rate and chemiluminescence intensity is calculated as:

$$\langle C(\phi(\vec{x}), \vec{x}) \rangle_a = \frac{\int\limits_{-\infty}^{a_q(\phi(\vec{x}))} C(a_t, \phi) p(\vec{x}, a_t) da_t}{\int\limits_{-\infty}^{a_q(\phi(\vec{x}))} p(\vec{x}, a_t) da_t} \tag{6.12}$$

The numerator of the right side of Eq. (6.12) is the strain rate distribution weighted average of the proportionality factor. Since $C(a_t, \phi)$ is only considered for strain rates smaller than the quenching criterion $a_q(\phi)$, the integral is evaluated in the limits $-\infty$ and $a_q(\phi)$. The denominator accounts for this clipping of the Gaussian distribution by re-normalizing the numerator with the integral of all probabilities between $-\infty$ and $a_q(\phi)$. Thus, $\langle C(\phi) \rangle_a$ represents the strain rate distribution averaged proportionality factor between measured OH* chemiluminescence intensity and heat release rate for all unquenched states of the flame. Quenched states must not be taken into account in the proportionality factor, because they do not contribute any heat release rate and chemiluminescence intensity.

6.4.2 Results

The calculated proportionality factor $\langle C \rangle_a$ correlates the measured, time-averaged OH* intensity i_{OH^*} with the time-averaged heat release rate $\langle \dot{q} \rangle_t$ of the flame:

$$\langle C \rangle_a \langle i_{OH^*} \rangle_t \sim \langle \dot{q} \rangle_t \tag{6.13}$$

Since the measured OH* intensities are no quantitative photon count of the light emission of the flame, but a relative measurement signal, the corrected OH* intensities are only proportional to the heat release rate. If the integral heat release rate of the flame is known, for example from the burnt fuel mass flow[7], the obtained corrected chemiluminescence intensities can be scaled accordingly to match this value.

Figure 6.11 shows the result of the correction procedure for the $\phi = 0.77$ operation point. In the upper part of the figure the heat release rate, measured with the energy balance method described in Ch. 5, is shown on the left side. In the middle the measured OH* chemiluminescence intensities, and on the right side the strain rate corrected OH* intensities are shown.

It can be clearly seen that the correction method shifts the intensities closer to the burner exit, which results in a more compact flame with high heat release rates at the burner exit. The corrected intensities are thus a good approximation for the heat release distribution of the flame.

This becomes even more obvious, when the intensities are integrated in radial direction to obtain the one-dimensional axial profiles (Fig. 6.11, lower part). It can be seen that the axial profile of the corrected OH* intensities is in very good agreement with the real heat release profile. For this reason it can be concluded that the corrected OH* intensities are a much better mapping of the heat release rate distribution of the flame than the commonly used uncorrected OH* intensities.

The $\phi = 0.77$ operation point is representative for all six investigated lean operation points ($\phi = 0.63$ - $\phi = 0.91$). For all lean operation points, the correction procedure results in more compact flames and a very good agreement of the one-dimensional profiles.

However, the method fails for the stoichiometric operation point (Fig. 6.12). Only a slight upstream shift of the chemiluminescence intensity due to the correction procedure can be observed.

The reason for this failure is not clear but might be linked in the reaction mechanism. The rate coefficients of the OH* reactions embedded in the mechanism are

---

7   For unconfined flames, like the ones investigated in this study, this is not possible in general, because the burnt fuel mass flow is not known due to the ambient air entrainment and the associated incomplete combustion of the fuel. However, in technical applications it can be assumed that the complete fuel mass flow is burnt. Then the described scaling to obtain quantitative local heat release rates can be done.
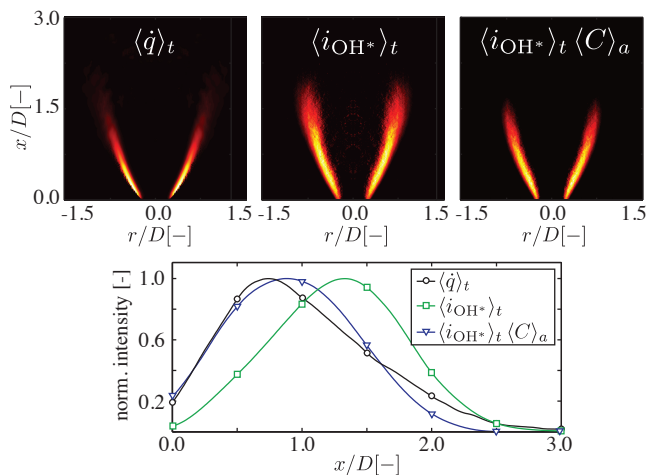
Figure 6.11: Result of the intensity correction procedure for the $\phi = 0.77$ operation point. In the upper part the intensity distributions in the flame mid-plane are shown. On the left side the heat release rate, in the middle the measured OH* intensities and on the right side the corrected, heat release rate proportional OH* intensities are shown. The lower part shows the corresponding axial profiles.

deduced from literature values. While the reaction rates of the quenching reactions are well understood [81], Kathrotia et al. [44] reported difficulties in selecting proper rate coefficients for the formation reactions. The rate coefficients of the formation reactions reported in different studies scatter by two to three orders of magnitude. This is an indicator for the complex nature of the formation reactions. Apparently, not the complete equivalence ratio range (rich, stoichiometric, and lean flames) can be treated with a single set of coefficients. This is also indicated in the study of Najm et al. [61] where it was found that the fraction of carbon being oxidized in the side paths leading to chemiluminescence is dependent on the equivalence ratio (Sec. 2.2). Moreover, it was shown in Sec. 2.2.3 that besides precise reaction rate coefficients for the chemiluminescence reactions, also the ability of a reaction mechanism to correctly predict the concentration of CH radicals, which are the most important OH* precursor, is of crucial importance for a correct prediction of OH* intensities. In methane fueled flames, CH radicals are mainly formed
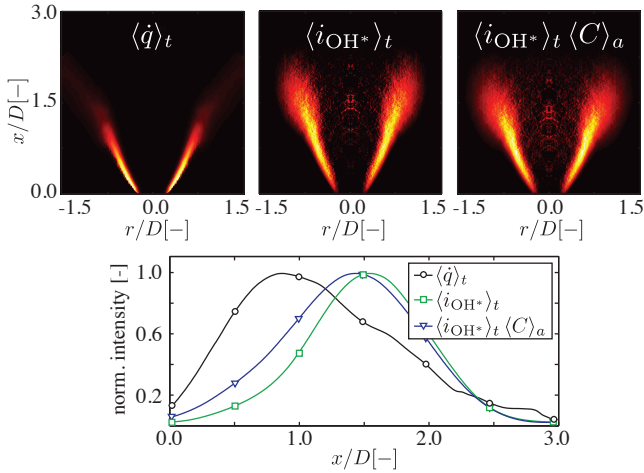
Figure 6.12: Result of the intensity correction procedure for the $\phi = 1.0$ operation point. In the upper part the intensity distributions in the flame mid-plane are shown. On the left hand side the heat release rate, in the middle the measured OH* intensities and on the right hand side the corrected, heat release rate proportional OH* intensities are shown. The lower part shows the corresponding axial profiles.

by the oxidation of C_2 hydrocarbons, which were formed by the recombination of two methyl radicals [34]. It was shown in the work of Heghes [34] that the crucial reactions for the formation of CH radicals are equivalence ratio sensitive and not well represented by the reaction mechanism.

The results of all investigated operation points are presented in the Appendix (Fig. B.1 to Fig. B.7).

6.5 Conclusions

The corrected chemiluminescence intensities of all investigated lean flames are in very good agreement with the heat release rate distributions of the flames. The corrected OH* intensities obtained with the presented correction method are a significantly better approximation for the spatially resolved heat release rate of lean

turbulent flames than the commonly used uncorrected OH* intensities. The presented method represents a significant improvement for heat release rate measurements in the lean flame regime, which is of outstanding technical relevance for low emission combustion techniques.

The proposed method is based on a statistical strain rate model, evaluated with time resolved PIV measurements, and one-dimensional counterflow flame simulations. The simulations are used to obtain the basic relationship between heat release rate, strain rate and OH* chemiluminescence intensity. The only required experimental input are the measured OH* intensities and the velocity field of the flow. Thus, the presented method is universal and can be applied to a wide range of flame studies with moderate effort. Since the method is statistical in character, all required experimental input parameters can be acquired sequentially. The proposed method is explicitly applicable to experimental setups close to technical application, where experimentally more complex measurement techniques like heat release imaging or the reference technique described in Ch. 5 cannot be applied. Accurate heat release rate distributions are obtained for lean premixed and partially premixed flames. The method can be enhanced easily to capture the influence of fuel variations (for example H_2 enriched fuels), preheating temperature, or pressure by appropriate counterflow flame simulations. The results of such simulation are shown in Sec. 6.6. Also additional effects like equivalence ratio fluctuations can easily be taken into account. Then a joint pdf of strain rate and equivalence ratio has to be evaluated in order to calculate the representative proportionality factor between OH* intensity and heat release rate. A schematic overview of the presented correction method is shown in the summary of this work (Fig. 7.1).

The presented method is currently limited to premixed and partially premixed flames. The application to diffusion flames is briefly discussed in Sec. 6.6.5.

6.6 Additional counterflow flame simulations and diffusion flames

So far, the impact of turbulence on the chemiluminescence intensity was only investigated for non-preheated, atmospheric, methane-air flames. To check whether the presented strain rate correction method must be applied to other flames as well, additional counterflow flame simulation were performed. Preheat temperature, pressure influence, and alternative fuels were considered. This section also illustrates further limitations stemming from the reaction mechanism.

6.6.1 Preheat temperature

The lookup table obtained from the counterflow flame calculations for an atmospheric methane-air flame with variable preheating is shown in Fig. 6.13. The equivalence ratio is constant $\phi = 0.71$, and the preheating temperature is varied from 300K to 700K. Flames with strain rates from $500s^{-1}$ to $40,000s^{-1}$ are simulated.

It can be seen that the quenching strain rate a_q increases approximately linearly with preheating temperature. This can be explained with the higher reactivity of preheated mixtures. Further it can be seen that the values of $C(a_t, T_{\text{preheat}})^{-1}$ are shifted to higher values with increasing preheat temperature. The influence of straining on the proportionality constant is strong throughout the investigated preheat temperature range. Thus, the strain rate correction method must also be applied to the chemiluminescence signals of preheated flames in order to obtain reliable information about the local heat release rate.

6.6.2 Hydrogen flames

The lookup table for a non-preheated, atmospheric hydrogen-air flame is shown in Fig. 6.14. The equivalence ratio is varied from $\phi = 0.33$ to $\phi = 1.0$, and the strain rate is varied from $500s^{-1}$ to $50,000s^{-1}$.

It can be seen that the quenching strain rate a_q is much higher than the one observed for non-preheated methane-air flames. The quenching strain rate of near stoichiometric hydrogen-air flames is hardly reachable. Like for methane flames, $C(a_t, \phi)^{-1}$ is highest for near stoichiometric mixtures and low strain rates, and is decreasing for both increasing strain rate and decreasing equivalence ratio. As observed for methane flames, the dependency of $C(a_t, \phi)^{-1}$ on strain rate is stronger than on equivalence ratio. Also for hydrogen flames it can be seen that the proportionality factor between OH* intensity and heat release rate varies significantly within the investigated equivalence ratio range with strain rate. Again, the strain rate correction method must be applied to hydrogen flames in order to obtain reliable information about the local heat release rate.

6.6.3 Elevated pressure

Also counterflow flame simulations of non-preheated methane-air flames at elevated pressure were performed. However, the reaction mechanism is not capable to
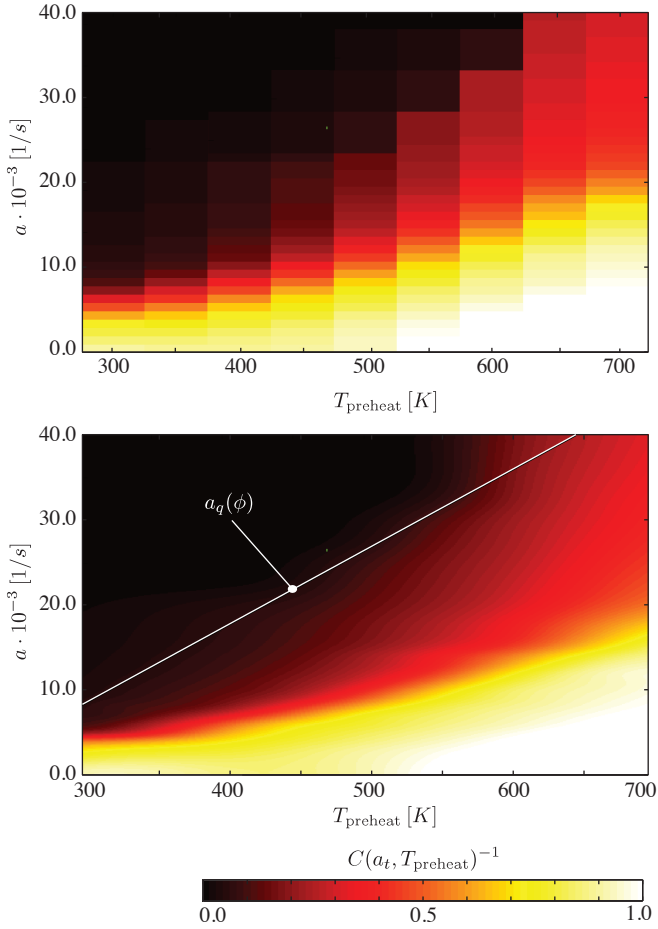
Figure 6.13: Lookup table obtained from the preheated counterflow simulations (top) and the bicubically interpolated lookup table (bottom). In the interpolated lookup table also the quenching strain rate, obtained from the 2% criterion, is shown.
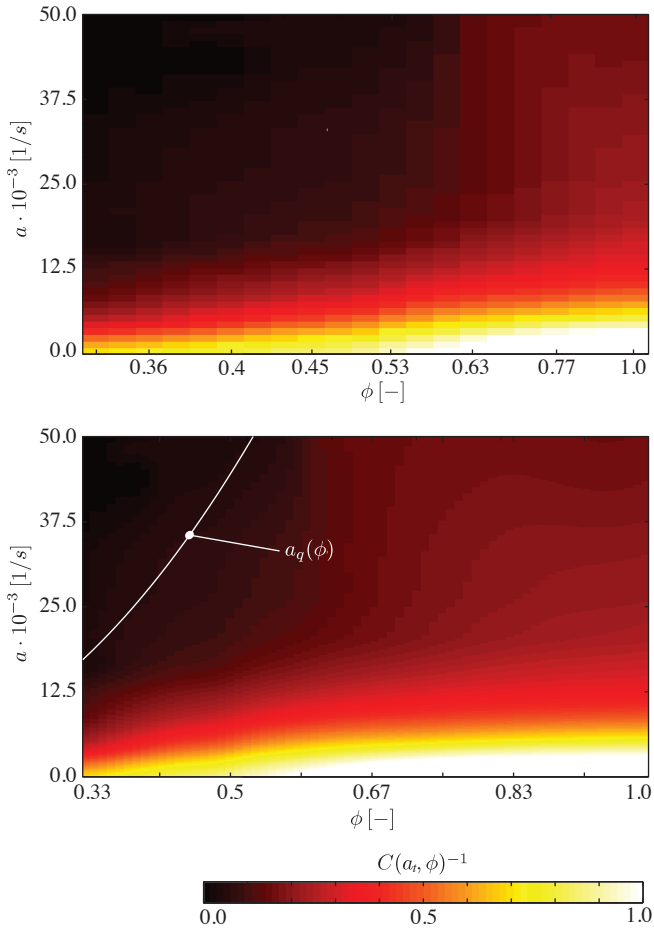
Figure 6.14: Lookup table obtained from the counterflow simulations of hydrogen-air flames (top) and the bicubically interpolated lookup table (bottom). In the interpolated lookup table also the quenching strain rate, obtained from the 2% criterion, is shown.

provide accurate OH* intensities at pressures higher than 1bar. Figure 6.15 shows the OH* intensities obtained from the counterflow simulations in comparison with experimental data. The shown intensities are normalized with the intensity for atmospheric pressure. The fuel mass flow is increasing linearly with pressure for both experiment and simulation.
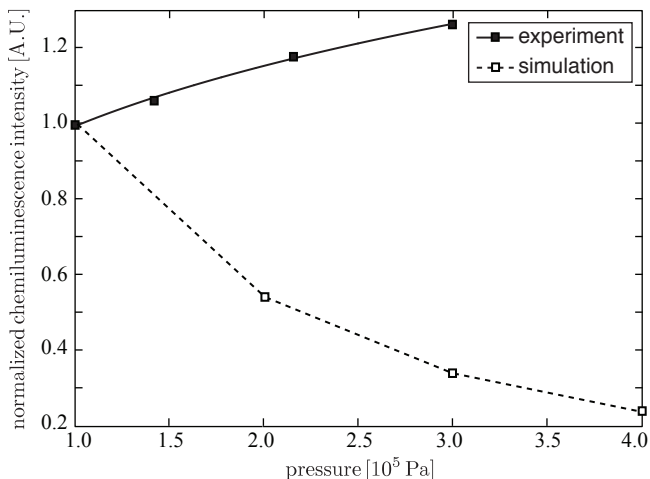
Figure 6.15: Comparison of OH* intensities obtained from the counterflow simulations and experiment for elevated pressures. The fuel mass flow is increasing linearly with pressure. Experimental data from Lauer [52].

The experimental data show a non-linear increase of the OH* intensities with pressure. Comparable results were reported by e.g. Higgins et al. [36] (Sec. 2.2). In contrast to the experimental data, the counterflow simulations predict decreasing OH* intensities with increasing pressure. This erroneous result of the counterflow simulation is not surprising, since the chemiluminescence sub-mechanism of Kathrotia et al. [44] was developed and validated for atmospheric and low-pressure flames only. A pressure dependence of the OH* reactions is not included in the reaction mechanism. Moreover, the rate coefficients for the chemiluminescence formation and deactivation reactions are known to be very sensitive on pressure (e.g. [20], [70]). Additionally, also the reaction rate coefficients of reactions forming

the important OH* precursor CH are validated for atmospheric and low-pressure flames only. No pressure dependence of the important CH formation reactions is included in the reaction mechanism.

To calculate a reliable lookup table for flames at elevated pressure, an improved reaction mechanism is necessary[8]. The most important aspects which must be addressed in order to obtain a reliable OH* reaction mechanism for elevated pressure are:

- The influence of pressure on all OH* formation reactions.

- The influence of pressure on the formation of OH* precursor species, e.g. CH radicals.

- The influence of pressure on the concentration of collisional quenchers, especially atomic hydrogen, which is the most effective collisional quencher [44].

- The influence of pressure on the rate coefficients of the collisional quenching reactions.

So far no reliable information on these aspects is available in literature.

6.6.4 Propane and syngas flames

The lookup table for a non-preheated, atmospheric propane-air flame is shown in Fig. 6.16. The equivalence ratio is varied from $\phi = 0.5$ to $\phi = 1.0$, and the strain rate is varied from $500s^{-1}$ to $40,000s^{-1}$.

The simulations predict increasing values of $C(a_t, \phi)^{-1}$ with increasing strain rate. In other words, the heat release rate is predicted to be quenched more strongly than the OH* intensity with increasing strain rate. This is inverse to the observations made for methane and hydrogen flames, but can be explained by analysing the reaction mechanism: In propane flames, C_2 hydrocarbons, which form the important OH* precursor CH, are not formed exclusively by the recombination of methyl radicals (like it is done in methane flames) but also by chain branching-reactions from propane. Furthermore, the chain-branching reactions form additional methyl radicals. Thus, the concentration of important OH* precursor species

---

8   The determination of rate coefficients of the OH* formation reaction in hydrogen flames at elevated pressure is an important topic of current research, e.g. [70].
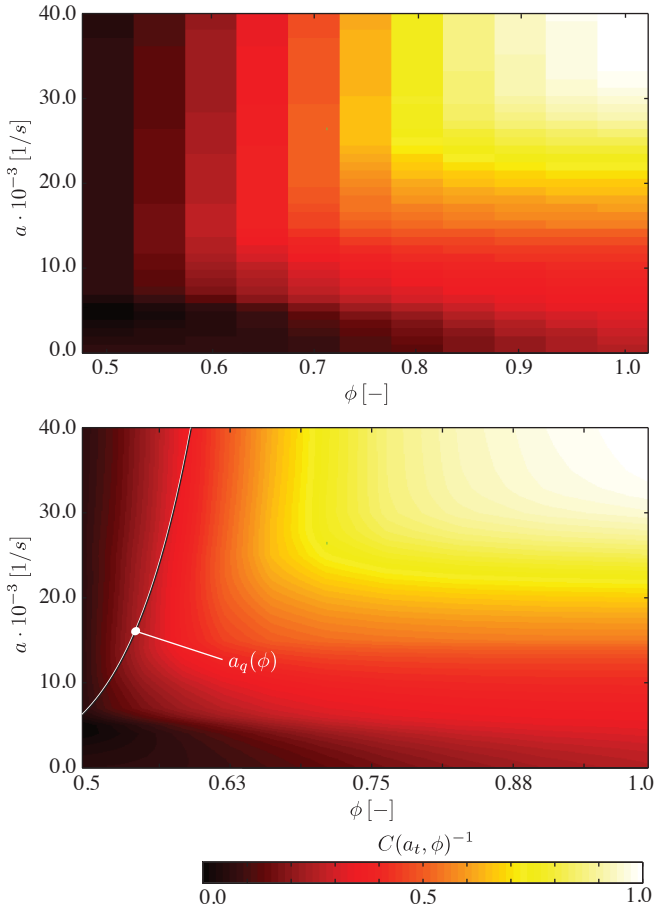
Figure 6.16: Lookup table obtained from the counterflow simulations of propane-air flames (top) and the bicubically interpolated lookup table (bottom). In the interpolated lookup table also the quenching strain rate, obtained from the 2% criterion, is shown.

is linked with the overall reaction rate in an over-proportional way. As a consequence, the OH* intensity is predicted to be quenched less strongly than the heat release rate with increasing strain rate.

However, the simulation result is contrary to experimental data obtained from propane-air flames [43, 41, 64], although the chemiluminescence sub-mechanism showed reasonable results for the other simulated atmospheric flames, and the underlying C_1-C_4 mechanism was validated for propane flames. This indicates that important aspects of the chemiluminescence kinetics are not fully understood yet and are not captured in the reaction mechanism. Anyway, it has to be concluded that it was not possible to predict the OH* intensities of propane-air flames reliably in this study using the reaction mechanism proposed by Kathrotia et al. [44].

Also syngas-air flames (fuel composition 50% CO and 50% H_2) were simulated. However, also for these flames no satisfactory results could be obtained.

6.6.5 Diffusion flames

In contrast to premixed flames, fuel and oxidizer must be mixed before combustion can occur in diffusion flames. The mixing processes are based on diffusion, with the diffusion processes typically being much slower than the combustion processes. Thus, the diffusion rate is the combustion rate limiting factor [69]. Therefore, the impact of turbulence on diffusion flames must be described differently compared to premixed flames. In a premixed flame, the main impact of turbulence on the flame is straining of the flame front. In non-premixed flames, also the diffusion processes prior to combustion are affected by turbulence. This effect is not captured by the model based correction method presented in this study.

In the work of Yeung et al. [92] the impact of straining on diffusion flames was discussed. A joint pdf of strain rate a_t and scalar dissipation rate χ_0 was shown (Fig. 6.17). This pdf could be used to describe the effect of turbulence on the diffusion processes of non-premixed flames. In this case, simulations of strained non-premixed counterflow flames must be performed. For each strain rate a set of simulations with varying diffusion rates for fuel and oxidizer, which can be described as functions of the scalar dissipation rate [69], are necessary. From this set of counterflow simulations an adopted proportionality factor between OH* intensity and heat release rate $\langle C \rangle_{a,\chi}$ can be calculated. $\langle C \rangle_{a,\chi}$ can then be used to correct measured OH* intensities of a diffusion flame in a way comparable to the presented correction procedure for premixed flames. Like for premixed flames, the
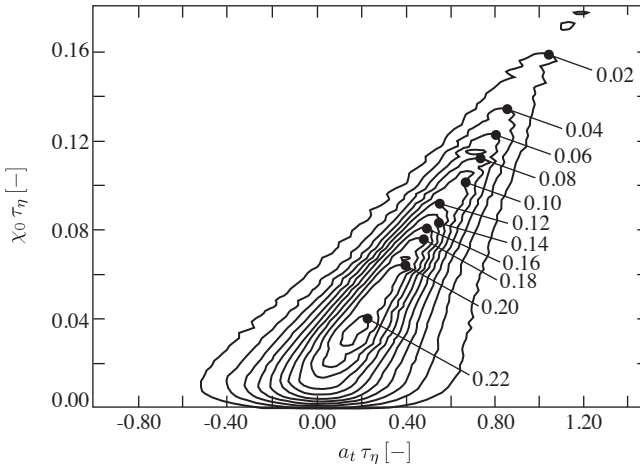
Figure 6.17: Joint pdf of tangential strain rate a_t and scalar dissipation rate χ_0 published by Yeung et al. [92]. Both strain rate and scalar dissipation rate are normalized with the Kolmogorov time scale.

only experimental input parameter for the evaluation of the joint pdf between strain rate and scalar dissipation rate is the Kolmogorov time scale. Thus, no additional experimental input is necessary for the diffusion flame correction method (Fig. 7.1).

However, Yeung et al. note that their approach to obtain the joint pdf of tangential strain rate and scalar dissipation rate involves several simplification. As a consequence, this pdf is most probable only a limiting approximation for the influence of turbulence induced straining on diffusion flames [92]. As this approach was not further developed in this study it must be concluded that the presented strain rate correction method cannot be applied to diffusion flames.

7 Summary and conclusions

7.1 Summary

The utilization of chemiluminescence as a measure for heat release rate in technical applications was investigated.

The heat release distribution of the flame is the most important parameter for the understanding and the prediction of unstable combustion states, such as thermo-acoustic instabilities, pulsed combustion, and flame flashback due to combustion induced vortex breakdown. Also in other research fields such as combustion noise the knowledge of the spatially resolved heat release rate is very important. The direct measurement of the local heat release rate of turbulent flames is difficult because existing measurement techniques are too complex to be applied to technical flames. As a consequence, the light emission of the flame, the chemiluminescence, is commonly used as an indirect measure for heat release rate. The chemiluminescence spectrum of a hydrocarbon flame consists of the emissions from the radicals OH^*, CH^*, and C_2^*, and from the molecule CO_2^*. The radicals emit light in narrow spectral bands. These emissions are superimposed by the broadband emissions from CO_2^*.

For laminar premixed flames the applicability of chemiluminescence as an indirect measure for integral heat release was proven in many experimental and theoretical studies. Most authors consistently report a linear increase of the integral chemiluminescence intensity with increasing fuel-flow rate. Moreover, it was shown that in laminar flames the spatially resolved OH^* chemiluminescence is a good approximation for the local heat release rate of the flame. But for turbulent flames the correlation between chemiluminescence and heat release is more complicated and a direct proportionality between chemiluminescence and heat release rate cannot be expected a priori. Therefore, the determination of heat release rate from OH^* emissions of (partially) premixed turbulent flames was investigated.

Firstly, a measurement and data evaluation procedure to determine a representative measure for the number of electronically excited OH^* radicals was developed. The integral chemiluminescence from the $X^2\Pi_i \leftarrow A^2\Sigma^*(\Delta v = 0)$ transition

between 300nm and 325nm was identified to be such a representative measure. To recover this chemiluminescence signal from bandpass filtered measurements with high spatial resolution, two simultaneous bandpass filtered measurements at around 307nm and 456nm are necessary. Only then the contribution of CO_2^* chemiluminescence in the bandpass filtered signal at around 307nm can be accounted for. It was found that this correction is of crucial importance, because the CO_2^* contribution strongly distorts the local chemiluminescence intensities derived from traditionally bandpass filtered measurements. Additionally, all wavelength dependencies and non-linear characteristics of the measurement hardware were taken into account to obtain measurement signals that scale linearly with the incident light intensity.

Secondly, for validation means, the time-averaged, spatially resolved heat release rate had to be measured by a precise reference method. A new measurement and data evaluation procedure was developed for this purpose. The local net heat release rate of the flame was calculated from the increase of the fluid's sensible enthalpy due to combustion based on the first law of thermodynamics. Input parameters from chemiluminescence, PIV, and OH-PLIF measurements were necessary to evaluate the energy balance. Thus, the developed reference method is hardly applicable to technical flames, but could be used to assess the capability of chemiluminescence as a measure for heat release rate. The comparison of chemiluminescence and heat release rate showed that the integral heat release rate can be obtained from the integral chemiluminescence of the turbulent flame, if an empiric calibration can be obtained. However, it was also shown that the local heat release rate of the turbulent flame is not properly represented by any chemiluminescence signal. Large errors are made when chemiluminescence is interpreted as measure for the local heat release rate. This is due to the non-constant turbulence intensity in the reaction zone of the flame. Close to the burner exit, where turbulence is strongest, chemiluminescence is quenched more strongly than heat release rate, resulting in a downstream shift of chemiluminescence intensities compared with the heat release rate. These findings are not limited to the flames under investigation in this study, but have to be expected for turbulent flames in general.

Thirdly, the effect of turbulence on OH^* intensity and heat release rate was taken into account in a model to correct measured OH^* signals in a way that they exhibit heat release rate proportional intensities. The correction method is based on a statistical model describing the pdfs of turbulence induced straining of flamelets. This strain rate model was coupled with simulations of strained counterflow flames to account for the impact of strain on OH^* intensities and heat release rate. A representative, strain rate distribution averaged proportionality factor between mea-

126

sured OH* intensity and heat release rate was obtained and used to calculate heat release rate proportional intensities from measured OH* signals. For lean flames, the corrected OH* intensities are in very good agreement with the heat release rate distribution determined with the reference method. Figure 7.1 shows a simplified schematic of the presented correction method.
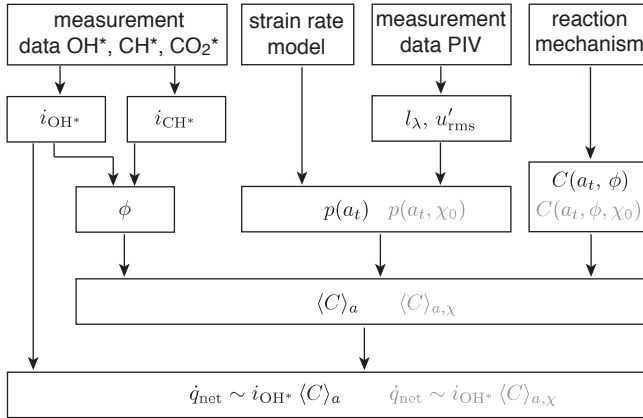
Figure 7.1: Simplified schematic of the strain rate correction method for premixed flames. Differences for the briefly sketched correction method for diffusion flames are depicted in gray color.

7.2 Conclusion

With the presented correction method, it is possible to obtain reliable information on the spatially resolved heat release rate of premixed turbulent flames from chemiluminescence measurements. In general, the correction method is universal and can be applied to a wide range of flames. However, the quality of the used reaction mechanism limits the applicability of the method to atmospheric methane-air and hydrogen-air flames. Also the treatment of diffusion flames is not included in the presented correction method. Only a brief sketch for a diffusion flame correction method was shown. Therefore, the enhancement of the reaction mechanism

for elevated pressure and other hydrocarbon fuel, as well as the development and validation of the correction method for diffusion flames are important aspects for further research.

It was shown that the integral chemiluminescence intensity can be used to monitor the integral heat release rate of flames. Moreover, it was shown that for this purpose simple bandpass filtered measurements are sufficient. The simultaneous measurement of two wavelength ranges to account for the CO_2^* contribution in bandpass filtered signals is not necessary. For example, this is especially important for the measurement of flame transfer functions, which is commonly done during the development process of new gas turbine combustors. Therefore, it was shown that the commonly applied method for measuring flame transfer functions with photomultiplier, bandpass filter, and CTA probe gives reliable results.

However, when information on the spatially resolved heat release rate is necessary, simple bandpass filtered measurements cannot be used. Then the correction of CO_2^* contributions and the impact of strain on the chemiluminescence intensities is required. An example for such a situation is the measurement of the convective time delay between a velocity fluctuation in a burner and the response of the flame, which represents a very important parameter for the thermoacoustic characterization of premixed flames. With the presented strain rate correction method such information can be obtained reliably with moderate experimental effort.

Bibliography

[1] Acton Research Corporation, Spectroscopy Instruments GmbH. *SpectraPro 0.275 meter digital scanning monochromator - Operating Instructions*, 1988.

[2] International Energy Agency. *World enery outlook 2009*. Organization for Economic Cooperation & Development, 2009.

[3] P. Alemela. *Measurement and scaling of acoustic transfer matrices of premixed swirl flames*. PhD thesis, Technische Universität München, 2009.

[4] M. Auer, C. Gebauer, K. Mösl, C. Hirsch, and T. Sattelmayer. Feedback of combustion instabilities on the injection of gaseous fuel. *ASME Journal of Engineering for Gas Turbines and Power*, 127:748–754, 2005.

[5] M. Auer, C. Hirsch, and T. Sattelmayer. Influence of the interaction of equivalence ratio and mass flow fluctuation on flame dynamics. In *Proceedings of the ASME Turbo Expo*, 2005.

[6] B. Ayoola, R. Balachandran, J. Frank, E. Mastorakos, and C. Kaminski. Spatially resolved heat release rate measurements in turbulent premixed flames. *Combustion and Flame*, 144:1–16, 2006.

[7] R. Balachandran, B. Ayoola, C. Kaminski, A. Dowling, and E. Mastorakos. Experimental investigation of the nonlinear response of turbulent premixed flames to imposed inlet velocity oscillations. *Combustion and Flame*, 143:37–55, 2005.

[8] K. Becker, D. Haaks, and T. Tatarczyk. The natural lifetime of OH $(^2\Sigma^+, v = 0, N = 2, J = 3/2)$ and its quenching by atomic hydrogen. *Chemical Physics Letters*, 25/4:564–567, 1974.

[9] P. Boineau, Y. Gervais, and V. Morice. An aerothermoacoustic model for computation of sound radiated by turbulent flames. In *Proceedings of the International Congress on Noise Control Engineering*, 1996.

[10] U. Bonne, T. Grewer, and H. Wagner. Messungen in der Reaktionszone von Wasserstoff-Sauerstoff- und Methan-Sauerstoff-Flammen. *Zeitschrift für physikalische Chemie Neue Folge*, 26:93–110, 1960.

[11] U. Brackmann. *Lambdachrome laser dyes, 3rd edition*. Lambda Physik, 2000.

[12] D. Bradley, A. Lau, and M. Lawes. Flame stretch rate as a determinant of turbulent burning velocity. *Philosophical Transactions of the Royal Society of London, Series A*, 338:359–387, 1992.

[13] H. Büchner. *Experimentelle und theoretische Untersuchungen der Entstehungsmechanismen selbsterregter Druckschwingungen in technischen Vormisch-Verbrennungssystemen*. PhD thesis, Universität Fridericiana Karlsruhe (T.H.), 1992.

[14] S. Candel and T. Poinsot. Flame stretch and the balance equation for the flame area. *Combustion Science and Technology*, 70(1):1–15, 1990.

[15] J. Chen and H. Im. Correlation of flame speed with stretch in turbulent premixed methane/air flames. *Symposium (International) on Combustion*, 27:819–826, 1998.

[16] T. Clark. Studies of OH, CO, CH and C_2 radiation from laminar and turbulent propane-air and ethylene-air flames - NACA Technical Note 4266. Technical report, National Advisory Committee for Aeronautics, Lewis Flight Propulsion Laboratory Cleveland, Ohio, 1958.

[17] T. Clark and D. Bittker. *A study of the radiation from laminar and turbulent open propane-air flames as a function of flame area, equivalence ratio, and fuel flow rate*. National Advisory Committee for Aeronautics, Lewis Flight Propulsion Laboratory Cleveland, Ohio, 1954.

[18] C. Copeland, J. Friedman, and M. Renksizbulut. Planar temperature imaging using thermally assisted laser induced fluorescence of OH in a methane-air flame. *Experimental Thermal and Fluid Science*, 31:221–236, 2007.

[19] D. Crosley and G. Smith. Vibrational energy transfer in laser-excited $A^2\Sigma^+$ OH as a flame thermometer. *Applied Optics*, 19/4:517–520, 1980.

[20] N. Donato, B. Hogan, E. Petersen, and F. Güthe. Assessment of current chemiluminescence kinetics models at elevated pressures. In *Proceedings of the Technical Meeting of the Central States Section of The Combustion Institute*, 2010.

[21] J. Donbar, J. Driscoll, and C. Carter. Strain rates measured along the wrinkled flame contour within turbulent non-premixed jet flames. *Combustion and Flame*, 125:1239–1257, 2001.

[22] V. Dribinski, A. Ossadtchi, V. Mandelshtam, and H. Reisler. Reconstruction of abel-transformable images: The gaussian basis-set expansion abel transform method. *Review of Scientific Instruments*, 73:2634–2642, 2002.

[23] A. Eckbreth and W. Sirignano (ed.). *Laser diagnostics for combustion temperature and species*. Gordon and Breach Publishers, 1995. Second edition.

[24] D. Fanaca, P. Alemela, F. Ettner, C. Hirsch, T. Sattelmayer, and B. Schuermans. Determination and comparison of the dynamic characteristics of a perfectly premixed flame in both single and annular combustion chambers. In *Proceedings of ASME Turbo Expo*, 2008.

[25] A. Fischer. *Hybride, thermoakustische Charakterisierung von Drallbrennern*. PhD thesis, Technische Universität München, 2004.

[26] E. Freitag, H. Konle, M. Lauer, C. Hirsch, and T. Sattelmayer. Pressure influence on the flame transfer function of a premixed swirling flame. In *Proceedings of the ASME Turbo Expo*, 2006.

[27] N. Garland and D. Crosley. On the collisional quenching of electronically excited OH, NH and CH in flames. In *21th Symposium (International) on Combustion*, pages 1693–1702, 1986.

[28] S. Girimaji and S. Pope. Material-element deformation in isotropic turbulence. *Journal of Fluid Mechanics*, 220:427–458, 1990.

[29] R. Gordon, A. Masri, and E. Mastorakos. Heat release rate as represented by [OH] x [CH_2O] and its role in autoignition. *Combustion Theory and Modelling*, 13/4:645–670, 2009.

[30] D. Guyot, F. Guethe, B. Schuermans, A. Lacarelle, and O. Paschereit. CH^*/OH^* chemiluminescence response of an atmospheric premixed flame under varying operation conditions. In *Proceedings of ASME Turbo Expo*, 2010.

[31] L. Haber. An investigation into the origin, measurement and application of chemiluminescent light emissions from premixed flames. Master's thesis, Virginia Polytechnic Institute and State University, 2000.

[32] L. Haber, U. Vandsburger, W. Saunders, and V. Khanna. An examination of the relationship between chemiluminescent light emissions and heat release rate under non-adiabatic conditions. In *Proceedings of International Gas Turbine Institute*, 2000.

[33] Y. Hardalupas and M. Orain. Local measurements of the time-dependent heat release rate and equivalence ratio using chemiluminescent emission from a flame. *Combustion and Flame*, 139:188–207, 2004.

[34] C. Heghes. C_1-C_4 *hydrocarbon oxidation mechanism*. PhD thesis, Rupertus Carola Universität Heidelberg, 2006.

[35] M. Hertweck. Charakterisierung der Flammenstreckungsrate von vorgemischten, turbulenten Drallflammen. Master's thesis, Technische Universität München, 2009.

[36] B. Higgins, M. McQuay, F. Lacas, J. Rolon, N. Darabiha, and S. Candel. Systematic measurements of OH chemiluminescence for fuel-lean, high-pressure, premixed, laminar fames. *Fuel*, 80:67–74, 2001.

[37] J. Hinze and B. Clark (ed.). *Turbulence (2nd edition)*. McGraw-Hill, 1975.

[38] S. Hoffmann. *Untersuchung des Stabilisierungsverhaltens und der Stabilitätsgrenzen von Drallflammen mit innerer Rückströmzone*. PhD thesis, Universität Fridericiana Karlsruhe (TH), 1994.

[39] P. Hogan and D. Davis. OH lifetime measurements of several K levels in the $v' = 1$ manifold of the $^2\Sigma^+$ electronic state: Excitation via a tunable UV laser. *Chemical Physics Letters*, 29/4:555–557, 1974.

[40] I. Hurle, R. Price, T. Sugden, and A. Thomas. Sound emission from open turbulent premixed flames. *Proceedings of Royal Society*, 303:409–427, 1968.

[41] Y. Ikeda, A. Nishiyama, S. Kim, N. Kawahara, and E. Tomita. Anchor point structure measurements for laminar propane/air and methane/air premixed flames using local chemiluminescence spectra. In *Proceedings of 31th International Symposium on Combustion*, 2006.

[42] ILA - Intelligent Laser Applications GmbH. *Introduction to VidPIV - User Manual*, 2004.

[43] R. John and M. Summerfield. Effect of turbulence on radiation intensity from propane-air flames. *Jet Propulsion*, 27:169–179, 1957.

[44] T. Kathrotia, U. Riedel, and J. Warnatz. A numerical study on the relation of OH*, CH*, and C$_2^*$ chemiluminescence and heat release in premixed methane flames. In *Proceedings of the European combustion Meeting*, 2009.

[45] R. Kee, J. Miller, and T. Jefferson. CHEMKIN: A general-purpose, problem-independent, transportable, fortran chemical kinetics code package - Sandia report SAND80-8003. Technical report, Sandia National Laboratories, 1989.

[46] A. Kolmogorov. The local structure of turbulence in incompressible viscous fluid for very large Reynolds numbers. *Proceedings of Royal Society of London, Series A*, 434:9–13, 1991.

[47] M. Konle. Simultane PIV-LIF-Messungen zur Bestimmung der Flammenstreckungsrate. Master's thesis, Technische Universität München, 2005.

[48] M. Konle. *Verbrennungsinduziertes Wirbelaufplatzen in moderat turbulenten Drallströmungen*. PhD thesis, Technische Universität München, 2010.

[49] M. Konle, F. Kiesewetter, and T. Sattelmayer. Simultaneous high repetition rate PIV-LIF measurements of CIVB driven flashback. *Experiments in Fluids*, 44:529–538, 2008.

[50] M. Konle and T. Sattelmayer. Time scale model for the prediction of the onset of flame flashback driven by combustion induced vortex breakdown. *Journal of Engineering for Gas Turbines and Power*, 132/4:041503/1–6, 2010.

[51] C. Külsheimer and H. Büchner. Combustion dynamics of turbulent swirling flames. *Combustion and Flame*, 131:70–84, 2002.

[52] M. Lauer. Untersuchung des druckabhängigen Verlaufs von Flammentransferfunktionen. Master's thesis, Technische Universität München, 2005.

[53] M. Lauer and T. Sattelmayer. On the adequacy of chemiluminescence as a measure for heat release in turbulent flames with mixture gradients. *Journal of Engineering for Gas Turbines and Power*, 132/6:061502/1–8, 2010.

[54] M. Lauer, M. Zellhuber, C. Aul, and T. Sattelmayer. Determination of the heat release distribution in turbulent flames by a model based correction of OH* chemiluminescence. In *Proceedings of the ASME Turbo Expo*, 2011.

[55] J. Lee and D. Santavicca. Experimental diagnostics for the study of combustion instabilities in lean premixed combustors. *Propulsion and Power*, 19/5:735–750, 2003.

[56] J. Luque and D. Corsley. LIFBASE, Database and spectral simulation for diatomic molecules (v1.6). Technical report, SRI International Report MP-99-009, 1999.

[57] J. Luque and D. Crosley. Transition probabilities in the $A^2\Sigma^+$ - $X^2\Pi_i$ electronic system of OH. *Journal of Chemical Physics*, 109/2:439–448, 1998.

[58] J. Luque and D. Crosley. *LIFBASE (version 1.9) - Database and spectral simulation for OH A-X, OD A-X, NO A-X, B-X, C-X, D-X, CH A-X,*

B-X, C-X, CN B-X, N_2^+ B-X, SiH A-X and CF A-X. SRI International, http://www.sri.com/cem/lifbase, 1999.

[59] T. Mayer-Kuckuk. *Atomphysik - Eine Einführung*. Teubner Stuttgart, 1997. 5th edition.

[60] J. McLennan, A. McLay, and M. Crawford. Spark spectrum of mercury, Hg II. *Proceedings of the Royal Society of Lonon, Series A.*, 823:41–47, 1931.

[61] H. Najm, P. Paul, C. Mueller, and P. Wyckoff. On the adequacy of certain experimental observables as measurements of flame burning rate. *Combustion and Flame*, 113:312–332, 1998.

[62] Y. Neumeier, A. Nabi, A. Arbel, M. Vertzberger, and B. Zinn. Open-loop performance of a fast-response, actively controlled fuel injector actuator. *Journal of Propulsion and Power*, 13/6:705–713, 1997.

[63] V. Nori and J. Seitzman. Chemiluminescence measurements and modeling in syngas, methane and jet-a fueled combustors. In *Proceedings of the 45th AIAA Aerospace Sciences Meeting and Exhibit*, 2007.

[64] M. Orain and Y. Hardalupas. Effect of fuel type on equivalence raio measurements using chemiluminescence in premixed flames. *Comptes Rendus Mechanique*, 338/5:241–254, 2010.

[65] C. Panoutsos, Y. Hardalupas, and A. Taylor. Numerical evaluation of equivalence ratio measurement using OH* and CH* chemiluminescence in premixed and non-premixed methane-air flames. *Combustion and Flame*, 156:273–291, 2009.

[66] P. Paul. Vibrational energy transfer and quenching of OH $A^2\Sigma^+$(v'=1) measured at high temperatures in a shock tube. *Journal of Chemical Physics*, 99:8472–8476, 1995.

[67] P. Paul and N. Najm. Planar laser-induced fluorescence imaging of flame heat release rate. *Symposium (International) on Combustion*, 27:43–50, 1998.

[68] N. Peters. Laminar flamelet concepts in turbulent combustion. *Symposium (International) on Combustion*, 21:1231–1250, 1986.

[69] N. Peters and G. Batchelor (ed.). *Turbulent combustion*. Cambridge University Press, 2000.

[70] E. Petersen, M. Kopp, and N. Donato. Assessment of current chemiluminescence kinetic models at engine conditions. In *Proceedings of the ASME Turbo Expo*, 2011.

[71] Photron Europe Limited. *FASTCAM-ultima APX Hardware Manual*, english version, rev. 1.07 edition, 2004.

[72] S. Pope. Turbulent premixed flames. *Annual Review of Fluid Mechanics*, 19:237–270, 1987.

[73] S. Pope. *Turbulent flows*. Cambridge University Press, 2000.

[74] M. Raffel, C. Willert, and J. Kompenhans. *Particle Image Velocimetry - A practical guide*. Springer Berlin, 1998.

[75] Rotexo-SoftPredict. *Combustion Simulation Laboratory 3 - 1-D and Counterflow Flames*, July 2009.

[76] J.-M. Samaniego, F. Egolfopoulos, and C. Bowman. CO_2^* chemiluminescence in premixed flames. *Combustion Science and Technology*, 109:183–203, 1995.

[77] C. Sansonetti, M. Salit, and J. Reader. Wavelengths of spectral lines in mercury pencil lamps. *Applied Optics*, 35:74–77, 1996.

[78] J. Sinibaldi, J. Driscoll, C. Mueller, J. Donbar, and C. Carter. Propagation speeds and stretch rates measured along wrinkled flames to assess the theory of flame stretch. *Combustion and Flame*, 133:323–334, 2003.

[79] A. Steinberg and J. Driscoll. Straining and wrinkling processes during turbulence-premixed flame interaction measured using temporally-resolved diagnostics. *Combustion and Flame*, 156:2285–2306, 2009.

[80] G. Stokes. On the effect of the internal friction of fluids on the motion of pendulums. *Transactions of the Cambridge Philosophical Society*, 9:8–106, 1851.

[81] M. Tamura, P. Berg, J. Harrington, J. Luque, J. Jeffries, G. Smith, and D. Crosley. Collisional quenching of CH(A), OH(A), and NO(A) in low pressure hydrocarbon flames. *Combustion and Flame*, 114:502–514, 1998.

[82] G. Taylor. Statistical theory of turbulence - I. *Proceedings of Royal Society of London, Series A*, 151:421–444, 1935.

[83] H. Tennekes and J. Lumley. *A first course in turbulence*. The MIT Press, 1987. 11th edition. First edition 1972.

[84] P. Tipler. *Physik*. Spektrum Akademischer Verlag GmbH, 1995. Corrected reprint of first edition 1994.

[85] S. Turns. *An introduction to combustion*. McGraw-Hill, 2000. Second edition.

[86] H. Vogel. *Gerthsen Physik*. Springer Berlin, 1995. 18th edition.

[87] Q. Wang, V. McDonnel, E. Steinthorsson, A. Mansour, and B. Hollon. Correlating flashback tendencies for premixed injection of hydrogen and methane mixtures at elevated temperature and pressure. In *Proceedings of the ASME Turbo Expo*, 2009.

[88] J. Wäsle. *Vorhersage der Lärmemission turbulenter Vormischflammen*. PhD thesis, Technische Universität München, 2007.

[89] J. Wäsle, A. Winkler, M. Lauer, and T. Sattelmayer. Combustion noise modeling using chemiluminescence data as indicator for the heat release distribution. In *Proceedings of European Combustion Meeting*, 2007.

[90] J. Wäsle, A. Winkler, E. Rößle, and T. Sattelmayer. Development of an annular porous burner for the investigation of adiabatic unconfined flames. In *Proceedings of 13th International Symposium on Applications of Laser Techniques to Fluid Mechanics*, 2006.

[91] A. Winkler. *Validierung eines Modells zur Vorhersage turbulenten Verbrennungslärms*. PhD thesis, Technische Universität München, 2007.

[92] P. Yeung, S. Girimaji, and S. Pope. Straining and scalar dissipation on material surfaces in turbulence: Implications for flamelets. *Combustion and Flame*, 79:340–365, 1990.

[93] P. Yeung and S. Pope. An algorithm for tracking fluid particles in numerical simulations of homogeneous turbulence. *Journal of Computational Physics*, 79/2:373–416, 1988.

[94] P. Yeung and S. Pope. Lagrangian statistics from direct numerical simulations of isotropic turbulence. *Journal of Fluid Mechanics*, 207:531–568, 1989.

List of Figures

List of Tables

Appendix A

Heat release measurement results

In Ch. 5 the axial chemiluminescence profiles of bandpass filtered and CO_2^* contribution corrected OH^* and CH^* were compared to the heat release rate profiles obtained with the reference technique. Only the result of the $\phi = 0.83$ operation point was shown, because the characteristics of the profiles and the conclusions drawn for this equivalence ratio were identical for all investigated operation points. For completeness, the results of all eight investigated equivalence ratios are shown here (Fig. A.1 to Fig. A.8).

It can be seen that for all investigated flames all chemiluminescence profiles are shifted downstream compared with the heat release rate. This effect is caused by the the strong turbulence intensity close to the burner exit. In this region, the chemiluminescence intensities are quenched more strongly than the heat release rate by turbulence induced straining of the flamelets. As a consequence, no reliable information about turbulent flame heat release rate can be obtained from any chemiluminescence signal.
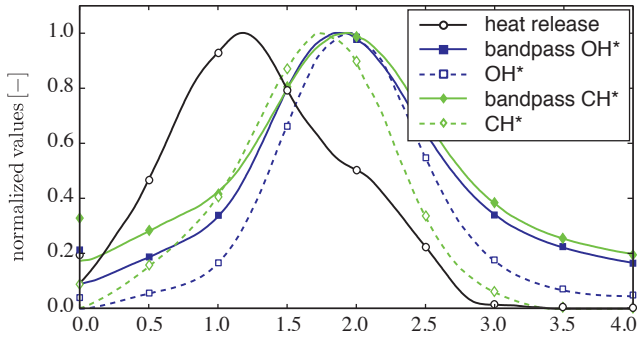
Figure A.1: Comparison of the axial chemiluminescence profiles of bandpass filtered and CO_2* contribution corrected OH* and CH* with the heat release profile of the flame of the $\phi = 1.11$ operation point.
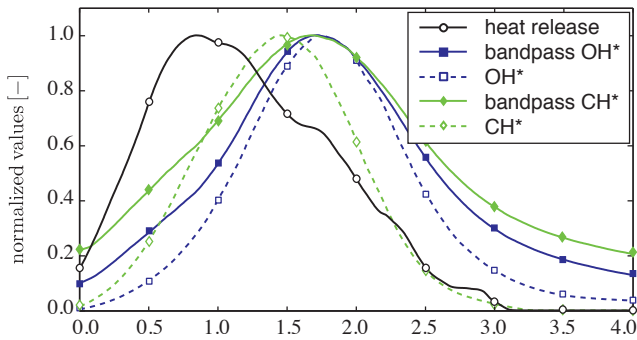
Figure A.2: Comparison of the axial chemiluminescence profiles of bandpass filtered and CO_2* contribution corrected OH* and CH* with the heat release profile of the flame of the $\phi = 1.0$ operation point.
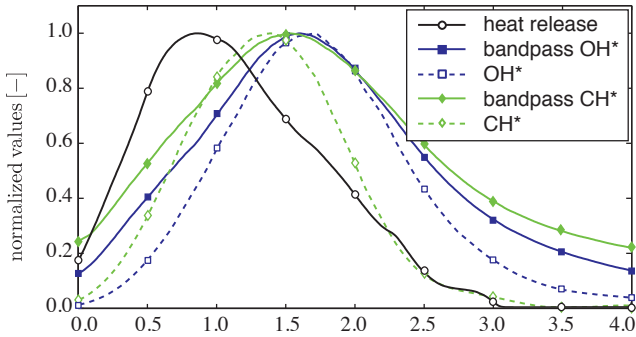
Figure A.3: Comparison of the axial chemiluminescence profiles of bandpass filtered and CO_2* contribution corrected OH* and CH* with the heat release profile of the flame of the $\phi = 0.91$ operation point.
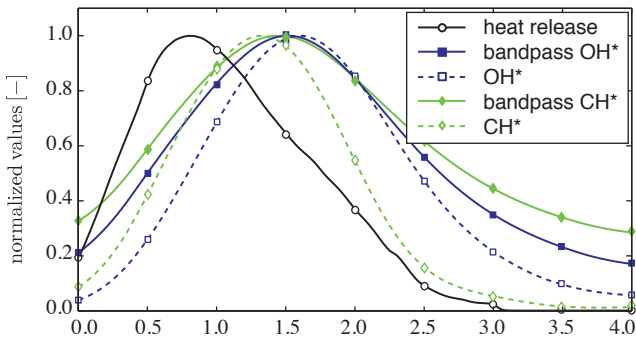
Figure A.4: Comparison of the axial chemiluminescence profiles of bandpass filtered and CO_2* contribution corrected OH* and CH* with the heat release profile of the flame of the $\phi = 0.83$ operation point.
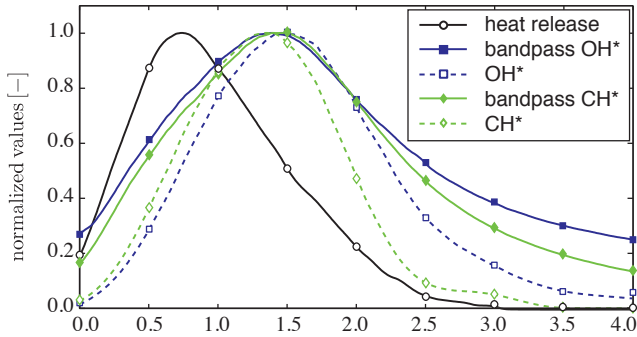
Figure A.5: Comparison of the axial chemiluminescence profiles of bandpass filtered and CO_2* contribution corrected OH* and CH* with the heat release profile of the flame of the $\phi = 0.77$ operation point.
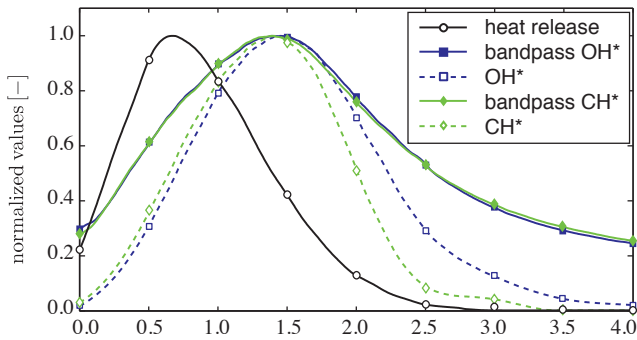
Figure A.6: Comparison of the axial chemiluminescence profiles of bandpass filtered and CO_2* contribution corrected OH* and CH* with the heat release profile of the flame of the $\phi = 0.71$ operation point.
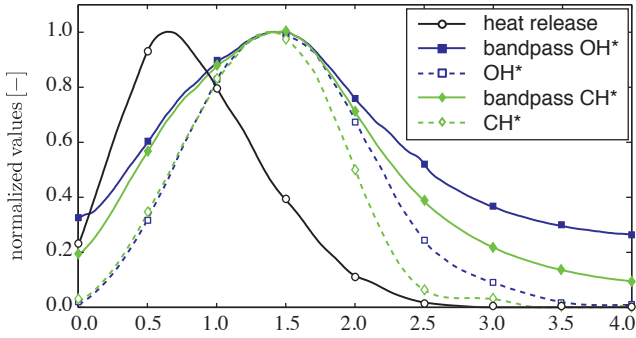
Figure A.7: Comparison of the axial chemiluminescence profiles of bandpass filtered and CO_2^* contribution corrected OH* and CH* with the heat release profile of the flame of the $\phi = 0.67$ operation point.
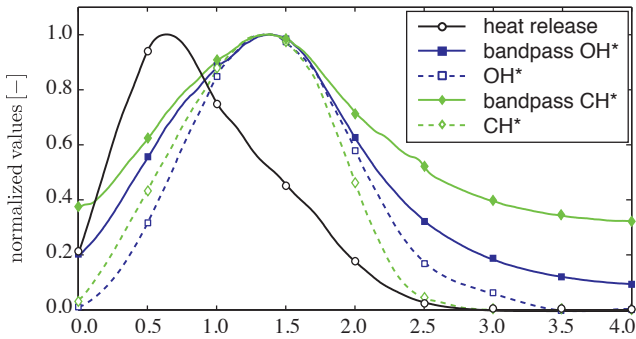
Figure A.8: Comparison of the axial chemiluminescence profiles of bandpass filtered and CO_2^* contribution corrected OH* and CH* with the heat release profile of the flame of the $\phi = 0.63$ operation point.

Appendix B

Results of strain rate correction method

In Ch. 6 the results of the strain rate correction method were only shown for $\phi = 0.77$ and the $\phi = 1.0$ operation points, with the result of the $\phi = 0.77$ operation point being representative for all investigated lean equivalence ratios. For completeness, the results of all seven investigated equivalence ratios are shown here (Fig. B.1 to Fig. B.7).

For all investigated lean flames, the correction method shifts the intensities closer to the burner exit, which results in a more compact flame. The comparison of the axial profiles shows that the corrected OH* intensities are in good agreement with the heat release rate in case of lean equivalence ratios.
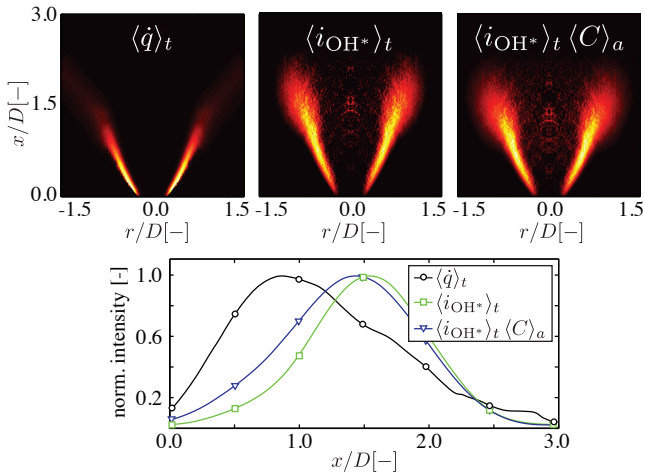
Figure B.1: Result of the intensity correction procedure for the $\phi = 1.0$ operation point. In the upper part the intensity distributions in the flame mid-plane are shown. On the left hand side the heat release rate, in the middle the measured OH*-intensities and on the right hand side the corrected, heat release rate proportional OH*-intensities are shown. The lower part shows the corresponding axial profiles.
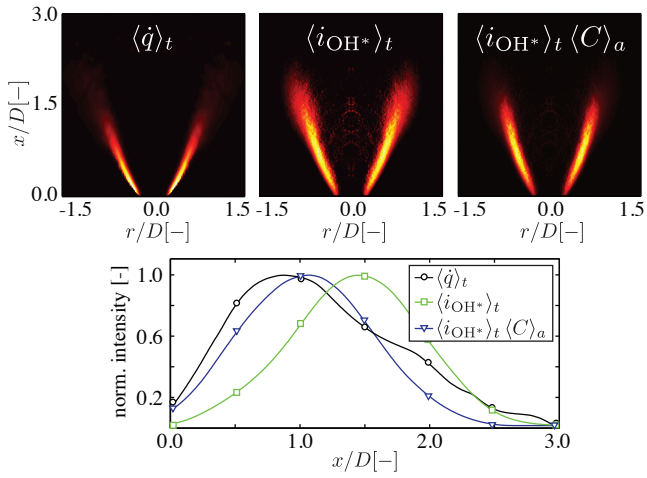
Figure B.2: Result of the intensity correction procedure for the $\phi = 0.91$ operation point.
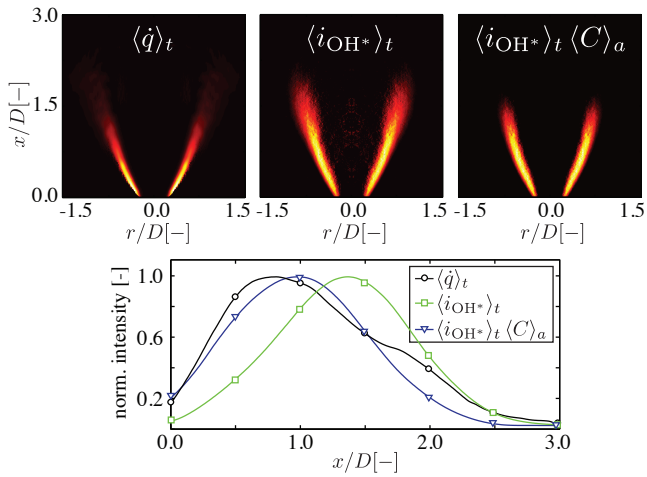
Figure B.3: Result of the intensity correction procedure for the $\phi = 0.83$ operation point.
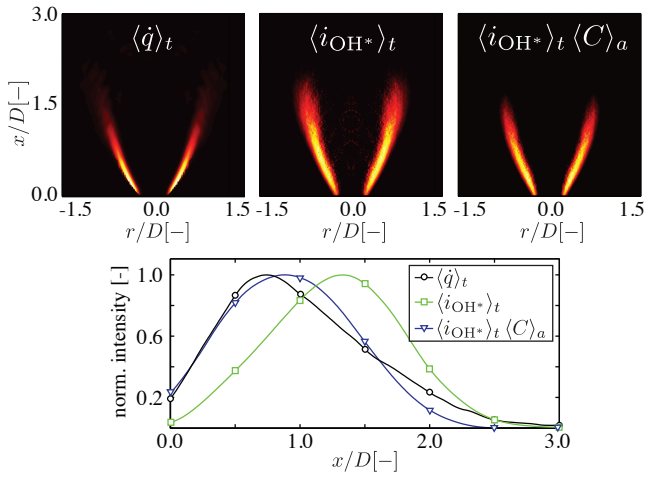
Figure B.4: Result of the intensity correction procedure for the $\phi = 0.77$ operation point.
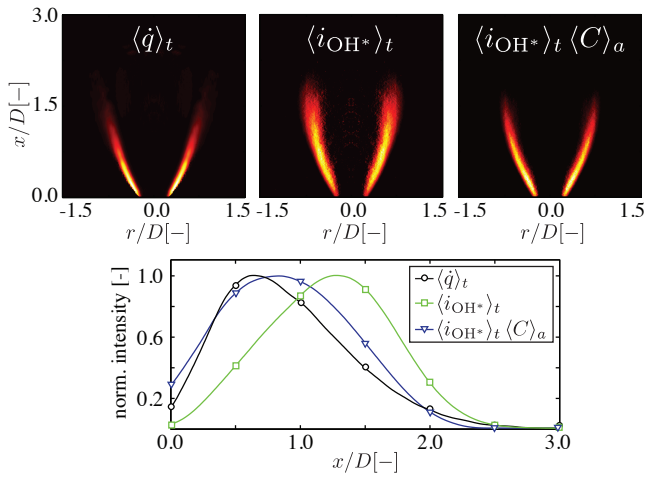
Figure B.5: Result of the intensity correction procedure for the $\phi = 0.71$ operation point.
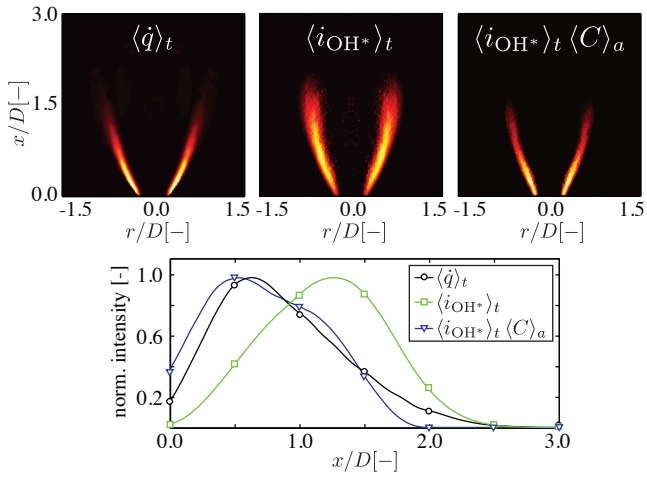
Figure B.6: Result of the intensity correction procedure for the $\phi = 0.67$ operation point.
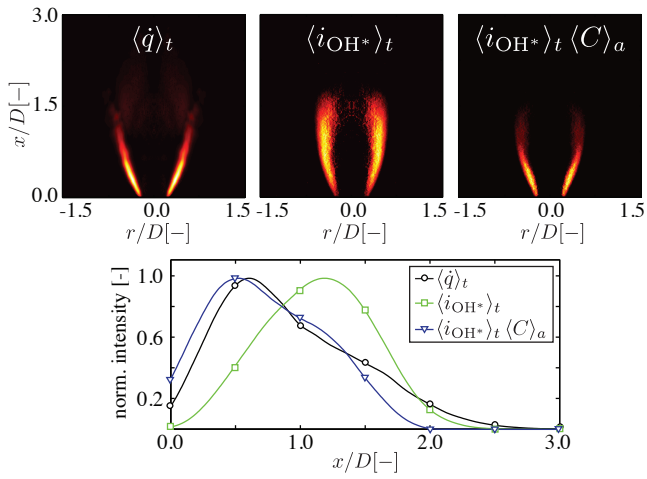
Figure B.7: Result of the intensity correction procedure for the $\phi = 0.63$ operation point.

Appendix C

Reaction mechanism [44]

An important part of the presented strain rate correction method is the reaction mechanism, which is used to obtain the non-linear relationships between OH^* intensity, heat release, and strain rate. The used mechanism, which includes all relevant chemiluminescence formation and deactivation processes, as far as they were known at this time, was developed by Kathrotia et al. [44], based on a C_1-C_4 mechanism which was developed by Heghes [34].

Since the reaction mechanism was still under development during this study, the stage of development which was used is shown here.

C.1 Elements

Element	Symbol	Molar Mass [kg/kmol]
Carbon	C	12,011
Oxygen	O	15,999
Hydrogen	H	1,008
Nitrogen	N	14,007
Argon	Ar	39,948

C.2 Species

C.2.1 Transport database

	Species	Geometry	M [kg/kmol]	ε/k_B [K]	σ [Å]	μ [D]	α [a]	$Z_{rot}\vert_{298K}$
1	Ar	monatomic	39,948	136,500	3,330	0,000	0,000	0,000
2	C	monatomic	12,011	80,000	2,750	0,000	0,000	0,000
3	C-2-C_4H_8	non-linear	47,035	244,000	3,763	0,000	2,650	2,100
4	C_2	linear	24,000	209,000	4,100	0,000	0,000	2,500
5	C_2*	linear	24,000	209,000	4,100	0,000	0,000	2,500
6	C_2H	linear	25,038	209,000	4,100	0,000	0,000	2,500
7	C_2H_2	linear	26,046	209,000	4,100	0,000	0,000	2,500
8	C_2H_3	non-linear	27,054	209,000	4,100	0,000	0,000	2,500
9	C_2H_4	non-linear	28,062	243,000	4,050	0,000	0,000	2,000
10	C_2H_5	non-linear	29,070	246,000	4,320	0,000	0,000	2,000
11	C_2H_5O	non-linear	45,061	417,000	3,690	1,700	0,000	2,000
12	C_2H_5OH	non-linear	46,070	417,000	3,690	1,700	0,000	2,000
13	C_2H_6	non-linear	30,000	246,000	4,320	0,000	0,000	2,000
14	C_2O	linear	39,999	232,400	3,828	0,000	0,000	1,000
15	C_3	linear	36,000	209,000	4,100	0,000	0,000	2,500
16	C_3H	linear	38,057	373,300	4,424	0,000	0,000	1,000
17	C_3H_2	linear	38,057	373,300	4,424	0,000	0,000	1,000
18	C_3H_3	linear	39,065	373,300	4,424	0,000	0,000	1,000
19	p-C_3H_4	linear	40,073	373,300	4,424	0,000	0,000	1,000
20	a-C_3H_5	linear	40,073	373,300	4,424	0,000	0,000	1,000

21	C_3H_6	non-linear	42,089	373,300	4,424	0,000	0,000	1,000
22	C_3H_8	non-linear	44,105	266,800	4,982	0,000	0,000	1,000
23	C_4H_{10}	non-linear	58,132	531,400	4,687	0,000	0,000	1,000
24	C_4H_2	linear	50,068	357,000	5,180	0,000	0,000	1,000
25	C_4H_6	non-linear	54,100	357,000	5,176	0,000	0,000	1,000
26	C_4H_7	non-linear	55,108	266,800	4,982	0,000	0,000	1,000
27	CH	linear	13,019	80,000	2,750	0,000	0,000	0,000
28	$CH*$	linear	13,019	80,000	2,750	0,000	0,000	0,000
29	CH_2CH_2OH	non-linear	45,061	417,000	3,690	1,700	0,000	2,000
30	CH_2HCO	non-linear	43,046	436,000	3,970	0,000	0,000	2,000
31	CH_2CO	non-linear	42,038	436,000	3,970	0,000	0,000	2,000
32	CH_2O	non-linear	30,026	498,000	3,590	0,000	0,000	2,000
33	CH_2OH	non-linear	31,034	417,000	3,690	1,700	0,000	2,000
34	CH_3	non-linear	15,035	141,400	3,746	0,000	0,000	13,000
35	CH_3HCO	non-linear	44,054	436,000	3,970	0,000	0,000	2,000
36	CH_3CHOH	non-linear	45,061	417,000	3,690	1,700	0,000	2,000
37	CH_3CO	non-linear	43,046	436,000	3,970	0,000	0,000	2,000
38	CH_3O	non-linear	31,035	417,000	3,690	1,700	0,000	2,000
39	CH_3O_2	non-linear	47,035	244,000	3,763	0,000	2,650	2,100
40	CH_3O_2H	non-linear	48,042	417,000	3,690	1,700	0,000	2,000
41	CH_3OH	non-linear	32,043	417,000	3,690	1,700	0,000	2,000
42	CH_4	non-linear	16,043	141,400	3,746	0,000	2,600	13,000
43	HCO	non-linear	29,018	498,000	3,590	0,000	0,000	0,000
44	CO	linear	28,010	98,100	3,650	0,000	1,950	1,800
45	CO_2	linear	44,010	244,000	3,763	0,000	2,650	2,100

46	H	monatomic	1,008	145,000	2,050	0,000	0,000	0,000
47	H_2	linear	2,016	38,000	2,920	0,000	0,790	280,000
48	H_2O	non-linear	18,015	572,400	2,605	1,844	0,000	2,100
49	H_2O_2	non-linear	34,015	107,400	3,458	0,000	0,000	3,800
50	HCCO	non-linear	41,030	436,000	3,970	0,000	0,000	2,000
51	HO_2	non-linear	33,007	107,400	3,458	0,000	0,000	3,800
52	iso-C_3H_7	non-linear	43,097	266,800	4,982	0,000	0,000	1,000
53	iso-C_4H_7	non-linear	55,108	266,800	4,982	0,000	0,000	1,000
54	iso-C_4H_8	non-linear	56,116	357,000	5,176	0,000	0,000	1,000
55	iso-C_4H_9	non-linear	57,124	357,000	5,176	0,000	0,000	1,000
56	iso-C_4H_{10}	non-linear	58,132	330,100	5,278	0,000	0,000	1,000
57	n-C_3H_7	non-linear	43,097	266,800	4,982	0,000	0,000	1,000
58	N_2	linear	28,014	97,530	3,621	0,000	1,760	4,000
59	O	monatomic	15,999	80,000	2,750	0,000	0,000	0,000
60	O_2	linear	31,999	107,400	3,458	0,000	1,600	3,800
61	OH	linear	17,007	80,000	2,750	0,000	0,000	0,000
62	OH*	linear	17,007	80,000	2,750	0,000	0,000	0,000
63	1-C_4H_8	non-linear	56,116	357,000	5,176	0,000	0,000	1,000
64	1-CH_2	linear	14,027	141,400	3,746	0,000	0,000	13,000
65	p-C_4H_9	non-linear	57,124	357,000	5,176	0,000	0,000	1,000
66	s-C_4H_9	non-linear	57,124	357,000	5,176	0,000	0,000	1,000
67	tert-C_4H_9	non-linear	57,124	357,000	5,176	0,000	0,000	1,000
68	3-CH_2	linear	14,027	141,400	3,746	0,000	0,000	13,000
69	2-C_4H_8	non-linear	56,116	357,000	5,176	0,000	0,000	1,000

C.2.2 NASA polynomial coefficients for the low temperature limit

No.	Species	T [K]	a_1	a_2	a_3	a_4	a_5	a_6	a_7
1	Ar	300	0.02500000e2	0.000000000e0	0.000000000e0	0.0000000e0	0.000000000e0	-0.0745375e04	0.04366000e2
2	C	300	0.02498584e2	0.08085776e-3	-0.02697697e-5	0.03040729e-8	-0.01106518e-12	0.0854587e6	0.04753459e2
3	C-2-C₄H₈	300	0.24108791e1	0.25147773e-1	0.98473047e-5	-0.22716758e-7	0.86585895e-11	-0.27758694e4	0.1484535e2
4	C₂	200	-1.96261001e0	5.76822247e-2	-1.58039636e-4	1.72462711e-7	-6.57913199e-11	9.82538219e4	2.33201223e1
5	C₂*	200	-1.96261001e0	5.76822247e-2	-1.58039636e-4	1.72462711e-7	-6.57913199e-11	1.31640879e5	2.33201223e1
6	C₂H	300	0.03050667e2	0.06051674e-1	-0.04956634e-4	0.02804159e-7	-0.08193332e-11	0.06630011e6	0.05954361e2
7	C₂H₂	300	0.02013556e2	0.15190446e-1	-0.16161893e-4	0.09078992e-7	-0.01912746e-10	0.02612444e6	0.08805378e2
8	C₂H₃	300	0.02459276e2	0.07371476e-1	0.02109872e-4	-0.13216421e-8	-0.11847838e-11	0.03335225e6	0.1155620e2
9	C₂H₄	300	-0.08614880e1	0.02796164e0	-0.03388677e-3	0.02785152e-6	-0.09737879e-10	0.05573046e5	0.02421148e3
10	C₂H₅	300	0.02690701e2	0.08719133e-1	0.04419838e-4	0.09338703e-8	-0.03927773e-10	0.1287040e4	0.1218319e2
11	C₂H₆	300	0.0690457e1	0.02951397e0	-0.02245116e-3	0.10110602e-7	-0.02044100e-10	-0.1599918e4	0.02130229e3
12	C₂H₅OH	200	0.48586957e1	-0.37401726e-2	0.69555378e-4	-0.88654790e-7	0.35168835e-10	-0.29996132e5	0.4801845e1
13	C₂H₆	300	0.1462538e1	0.1549467e-1	0.05780967e-4	-0.12578319e-7	0.04586267e-10	-0.1123917e5	0.1443229e2
14	C₂O	200	2.86278214e0	1.19701204e-2	-1.80851222e-5	1.52777730e-8	-5.20063163e-12	4.51328492e4	8.89759099e0
15	C₃	200	0.54328396e1	-0.44675438e-2	0.14932148e-4	-0.14795314e-7	0.50142111e-11	0.99495722e5	-0.15872071e1
16	C₃H	300	3.34917187e0	1.65826262e-2	-2.77115653e-5	2.51382364e-8	-8.85285352e-12	8.49863168e4	6.80362439e0
17	C₃H₂	150	3.16671400e0	2.48257200e-2	-4.59163700e-5	4.26801900e-8	-1.48215200e-11	6.35042100e4	8.69446400e0
18	C₃H₂	300	0.25097322e1	0.17103866e-1	-0.45710858e-5	-0.82841574e-8	0.54362287e-11	0.37040680e5	0.11011264e2
19	p-C₃H₄	300	-0.02131968e1	0.03355871e0	-0.03880478e-3	0.02745833e-6	-0.08690044e-10	0.02163048e6	0.02029393e3
20	a-C₃H₅	200	0.37878186e1	0.94851495e-2	0.24231843e-4	-0.36557902e-7	0.14858341e-10	0.18635957e5	0.78287037e1
21	C₃H₆	300	0.14933071e1	0.02092517e0	0.04486794e-4	-0.16689121e-7	0.07158146e-10	0.1074826e4	0.16145340e2
22	C₃H₈	300	0.08969208e1	0.02668898e0	0.05431425e-4	-0.02126000e-6	0.09243330e-10	-0.1395491e5	0.1935533e3
23	C₄H₁₀	300	-0.02256611e2	0.05881732e0	-0.04525782e-3	0.02037115e-6	-0.04079458e-10	-0.01760233e6	0.03329595e3
24	C₄H₆	300	0.04005191e2	0.01981000e0	-0.09865877e-4	-0.06635158e-7	0.06077413e-10	0.0542406e5	0.01845756e2
25	C₄H₆	300	0.03197108e2	0.02025591e0	0.06501092e-4	-0.16584423e-7	0.06400282e-10	0.1571520e5	0.09989566e2
26	C₄H₇	300	0.9278151e1	-0.2956305e-1	0.1632866e-3	-0.2000576e-6	0.7934605e-10	0.196381e5	-0.1296653e2
27	CH	300	0.03200202e2	0.02027875e-1	-0.05134431e-4	0.05733890e-7	-0.01955553e-10	0.0704525e6	0.03331587e2
28	CH*	200	3.47250101e0	4.26443626e-4	-1.95181794e-6	3.51755043e-9	-1.60436174e-12	1.04334869e5	1.44795533e0
29	CH₃CH₂OH	300	0.14019508e1	0.21543175e-1	-0.22326512e-5	-0.14464092e-7	0.80488420e-11	-0.38464519e4	0.19135818e2
30	CH₂HCO	300	0.03409062e2	0.1073857e-1	0.01891492e-4	-0.07158583e-7	0.02867385e-10	0.15214766e4	0.09558829e2
31	CH₂CO	300	0.02974979e2	0.12118712e-1	-0.02345045e-4	-0.04646685e-7	0.03905649e-10	-0.07632636e5	0.08673553e2
32	CH₂O	300	0.1652731e1	0.1263143e-1	-0.01888168e-3	0.02050031e-6	-0.08413237e-10	-0.1486540e5	0.1378482e2
33	CH₂OH	250	0.02862623e2	0.1001527e-1	-0.06528543e-5	0.05138539e-7	-0.02246041e-10	-0.0334967e5	0.1039793e2
34	CH₃	300	0.02430442e2	0.11124099e-2	-0.01680220e-4	0.16218288e-7	-0.05864952e-10	0.1642378e5	0.06789794e2
35	CH₃HCO	300	0.02505695e2	0.13369907e-1	0.04671953e-4	-0.11281401e-7	0.04263566e-10	-0.02124588e6	0.1350887e2
36	CH₃CHOH	300	0.1419398e1	0.02870643e0	-0.02373820e-3	0.11488865e-7	-0.02391420e-10	-0.0863871e5	0.01844256e3
37	CH₃O	300	0.03125278e2	0.09778220e-1	-0.04521448e-4	-0.09009462e-7	0.03193717e-10	0.04108507e5	0.1122885e2
38	CH₃O	300	0.02106204e2	0.07216595e-1	0.05338472e-4	-0.07377656e-7	0.02075610e-10	0.09786011e4	0.1315217e2
39	CH₃O₂	300	0.20986499e1	0.15786357e-1	0.75683261e-7	-0.11274587e-7	0.56665133e-11	0.20695879e4	0.15007068e2
40	CH₃O₂H	298	0.27586279e1	0.18150526e-1	-0.40892298e-5	-0.68391987e-8	0.44307016e-11	-0.17986394e5	0.13071986e2

No.	Species	T [K]	a_1	a_2	a_3	a_4	a_5	a_6	a_7
41	CH_3OH	300	0.02660115e2	0.07341508e-1	0.071170050e-4	-0.08793194e-7	0.023905570e-10	-0.025335348e6	0.1232631e2
42	CH_4	300	0.07787415e1	0.0174768e0	-0.02783409e-3	0.03049078e-6	-0.12239307e-10	-0.098252296e5	0.1372219e2
43	HCO	300	0.02898929e2	0.0619914e-1	-0.09623084e-4	0.10898249e-7	-0.0457548Se-10	0.041599226e5	0.0898361e2
44	CO	300	0.03626451e2	0.15119409e-2	-0.038881755e-4	0.05581944e-7	-0.0247495le-10	-0.143105369e5	0.04848897e2
45	CO_2	300	0.02275724e2	0.09922072e-1	-0.01409113e-4	0.06806680e-7	-0.02117280e-10	-0.048373146e6	0.1018488e2
46	H	300	0.02500000e2	0.0000000e0	0.0000000e0	0.0000000e0	0.0000000e0	0.025471626e6	-0.0460117e1
47	H_2	300	0.03298124e2	0.08249441e-2	-0.08143015e-5	-0.09475434e-9	0.04134872e-1	-0.101252069e4	-0.0329409e2
48	H_2O	300	0.03386842e2	0.03474983e-1	-0.06354696e-4	0.069068581e-7	-0.025065886e-10	-0.030208116e6	0.0290232e2
49	H_2O_2	300	0.03388753e2	0.06569926e-1	-0.14850125e-6	-0.04625805e-7	0.02471514e-10	-0.017663146e6	0.0678536e2
50	$HCCO$	300	0.05047965e2	0.04453478e-1	0.02268282e-5	-0.14820945e-8	0.022590741e-11	0.019658916e6	0.04818439e1
51	HO_2	300	0.02979966e2	0.04999669e-1	-0.03790997e-4	0.02354192e-7	-0.08089024e-11	0.01762273e4	0.09222724e2
52	$iso\text{-}C_3H_7$	300	0.01713399e2	0.0254261e0	0.15808083e-5	-0.01821286e-6	0.08827710e-10	0.0753580e5	0.1297900e2
53	$iso\text{-}C_4H_7$	298	-0.34391326e1	0.67889035e-1	-0.92118162e-4	0.75423011e-7	-0.25411345e-10	0.1327801e5	0.3795642e2
54	$iso\text{-}C_4H_8$	300	0.26471405e1	0.25902957e-1	0.819851354e-5	-0.22193259e-7	0.88958580e-11	-0.03730694e4	0.1268955e2
55	$iso\text{-}C_4H_9$	200	3.54885235e0	1.78747638e-2	5.00782825e-5	-7.94475071e-8	3.3580234e-11	4.740158e3	1.118493e2
56	$iso\text{-}C_4H_{10}$	300	0.5455901Ge0	0.37825324e-1	0.56197796e-5	-0.30570963e-7	0.14058456e-10	-0.18034047e5	0.2112960e2
57	$n\text{-}C_3H_7$	300	0.01922586e2	0.02347892e0	0.01810249e-4	-0.017783265e-6	0.08582996e-10	0.0971328e5	0.1399271e2
58	N_2	300	0.03298677e2	0.140823404e-2	-0.039063222e-4	0.05641515e-7	-0.02444854e-10	-0.020899e4	0.0395037e2
59	O	300	0.02946428e2	-0.16381665e-2	0.02421031e-4	-0.16028431e-8	0.03890696e-1	0.02914764e6	0.0296399e2
60	O_2	300	0.03212936e2	0.11274864e-1	-0.05756150e-5	0.13138773e-8	-0.08768554e-11	-0.10062490e4	0.0603473e2
61	OH	300	0.03637206e2	0.01850910e-2	-0.16761640e-5	0.02387202e-7	-0.08431442e-11	0.0360678e5	0.1358860e2
62	OH^*	200	3.46084428e0	5.01872172e-4	-2.00254474e-6	3.18901984e-9	-1.35451838e-12	5.0734946e4	1.7397641e0
63	$1\text{-}C_4H_8$	300	0.11811380e1	0.30853380e-1	0.508655247e-5	-0.24654888e-7	0.11110193e-10	-0.17904004e4	0.2106246e2
64	$1\text{-}CH_2$	300	0.03971265e2	-0.01699008e-2	0.10253689e-5	0.02492550e-7	-0.019811266e-10	0.04989367e6	0.05753207e0
65	$p\text{-}C_4H_9$	298	0.22069454e1	0.32849152e-1	0.34258574e-5	-0.24451637e-7	0.11456845e-10	0.5896281e4	0.1716966e2
66	$s\text{-}C_4H_9$	300	0.69567555e0	0.33100396e-1	0.63189173e-5	-0.27052078e-7	0.1200780e-10	0.68517148e4	0.2627072e2
67	$tert\text{-}C_4H_9$	200	6.87327133e0	-1.85146306e-2	1.30560116e-4	-1.50832755e-7	5.65358282e-11	4.10958938e3	2.3001660e-1
68	$3\text{-}CH_2$	250	0.03762237e2	0.11598191e-2	0.02489585e-5	0.08800843e-9	-0.07332435e-11	0.045367906e6	0.017125772
69	$2\text{-}C_4H_8$	300	0.12594252e1	0.27808424e-1	0.87013932e-5	-0.24402058e-7	0.98977710e-11	-0.29647742e4	0.2050112e2

C.2.3 NASA polynomial coefficients for the high temperature limit

No.	Species	T [K]	a_1	a_2	a_3	a_4	a_5	a_6	a_7
1	Ar	5000	0.0250000e2	0.0000000e0	0.0000000e0	0.0000000e0	0.0000000e0	-0.07453750e4	0.04366000e2
2	C	5000	0.0260208fe2	-0.01787081e-2	0.09087041e-6	-0.11499333e-10	0.033108444e-14	0.0854215e6	0.04195177e2
3	$C=2\text{-}C_4H_8$	5000	0.1109738Se1	0.355425578e-1	-0.164817t03e-4	0.34412202e-8	-0.264114468e-12	-0.26507607e4	0.1935351e62
4	C_2	6000	4.12492246e0	1.08348338e-4	1.572523585e-7	-4.240468288e-11	3.250593373e-15	9.81882961e4	7.97432262e-1
5	C_2^*	6000	4.12492246e0	1.08348338e-4	1.572523585e-7	-4.240468288e-11	3.250593373e-15	1.31575887e5	7.97432262e-1
6	C_2H	5000	0.04427688e2	0.0221626te-1	-0.06048952e-5	0.0988251te-9	-0.0735179te-13	0.0659041Se6	-0.1199441Se1
7	C_2H_2	5000	0.0443677Ce2	0.0537603te-1	-0.0191281te-4	0.03286379e-8	-0.0215670te-12	0.0256676e6	-0.0280037Se2

#	Species								
8	C_2H_3	5000	0.0593346e2	0.0401774e-1	-0.03966739e-5	-0.1441266e-9	0.02378643e-12	0.03185434e6	-0.08530313e2
9	C_2H_4	5000	0.0352841e2	0.1148518e-1	-0.04418385e-4	0.0784460e-8	-0.05266848e-12	0.0442828e5	0.02230389e2
10	C_2H_5	5000	0.0719049e2	0.0648407e-1	-0.0642806e-5	-0.0234787e-8	0.0388087e-12	0.1067454e5	-0.1478089e2
11	C_2H_4O	4000	0.1187114e2	0.0539041e-1	-0.04990159e-5	-0.0239595e-8	0.0425545e-12	-0.0595045e5	-0.0399465e3
12	C_2H_5OH	6000	0.6562436e1	0.1520422e-1	-0.5389679e-5	0.8622501e-9	-0.5128978e-13	-0.3152562e5	-0.9473020e1
13	C_2H_6	5000	0.0482593e2	0.1384042e-1	-0.04557258e-4	0.067249e-8	-0.0359816e-12	-0.1271779e5	-0.05239506e2
14	C_2O	5000	5.4246837e0	1.8539394e-3	-5.1793295e-7	6.7764623e-11	-3.5331523e-15	4.4536390e4	-3.6960840e0
15	C_3	6000	0.4803577e1	0.2145112e-2	-0.1072920e-5	0.2607352e-9	-0.2016319e-13	0.9939654e5	0.3893698e0
16	C_3H_2	6000	6.1418449e0	3.3966101e-3	-1.2191544e-6	1.9778283e-10	-1.1831280e-14	8.4422575e4	-6.4448011e0
17	C_3H_2	4000	7.67098100e0	2.74874900e-3	-4.37094300e-7	-6.45559000e-11	-1.66388700e-14	6.25972200e4	-1.23689000e1
18	C_3H_3	5000	0.8091625e1	0.3737285e-2	0.1388647e-5	-0.122986e-8	0.206815e-12	0.3543779e5	-0.1820446e2
19	$p\text{-}C_3H_4$	5000	0.0572914e2	0.1236804e-1	-0.0480562e-4	0.08601e-8	-0.0581280e-12	0.0201298e6	-0.0944866e2
20	$a\text{-}C_3H_5$	6000	0.6547473e1	0.1313531e-1	-0.4783389e-5	0.7719592e-9	-0.4619368e-13	0.1728232e5	-0.9274537e1
21	C_3H_6	5000	0.0673225e2	0.1490833e-1	-0.04994899e-4	0.0721202e-8	-0.0376260e-12	-0.0923570e4	-0.1331334e2
22	C_3H_8	5000	0.0752521e2	0.0188903e0	-0.0628392e-4	0.0919373e-8	-0.0481241e-12	-0.1646454e5	-0.0178439e3
23	C_4H_{10}	4000	0.0199878e3	0.1037280e0	-0.0961081e-4	-0.0462301e-8	0.0820282e-12	-0.0262555e6	-0.0883790e3
24	C_4H_6	6000	0.0903140e2	0.0604725e0	-0.0194878e-4	0.0275486e-8	-0.1385608e-12	0.0529473e5	-0.0238506e3
25	C_4H_6	5000	0.0804583e2	0.1648525e-1	-0.0552222e-4	0.0812359e-8	-0.0429507e-12	0.1370130e5	-0.0180045e3
26	C_4H_7	3000	0.544006e1	0.274460e-1	-0.1365496e-4	0.334035e-8	-0.329005e-12	0.190371e5	-0.287596e1
27	CH	5000	0.0219622e2	0.0234038e-1	-0.07058201e-5	0.0900758e-9	-0.0385504e-13	0.0708672e6	0.0917837e2
28	CH^*	6000	2.7822075e0	1.4724675e-3	-4.6343622e-7	7.3273602e-11	-4.1970540e-15	1.0454706e5	5.1742101e0
29	CH_3CH_2OH	5000	0.7594401e1	0.9329339e-2	-0.3030385e-5	0.4321631e-9	-0.2197003e-13	-0.5772785e5	-0.1396873e2
30	CH_2HCO	5000	0.0597567e2	0.0813059e-1	-0.02743624e-4	0.04070304e-8	-0.02176017e-12	0.0490321e4	-0.05045251e2
31	CH_3CO	5000	0.0603881e2	0.05800484e-1	-0.01920953e-4	0.02793484e-8	-0.1458676e-13	-0.0888340e5	-0.0765758e2
32	CH_2O	5000	0.0295560e2	0.0668132e-1	-0.02628954e-4	0.0473715e-8	-0.03212517e-12	-0.1532030e5	0.0691257e2
33	CH_2OH	4000	0.0632752e2	0.0360832e0	-0.03201547e-4	-0.01939875e-8	0.035097e-12	-0.0447450e5	-0.0832936e2
34	CH_3	5000	0.02844051e2	0.06137974e-1	-0.02230345e-4	0.03785161e-8	-0.02452159e-12	0.1643780e5	0.05452697e2
35	CH_2HCO	5000	0.0586865e2	0.1079424e-1	-0.03643530e-4	0.04856684e-8	-0.02896844e-12	-0.0226456e6	-0.0601294e2
36	CH_3CHOH	4000	0.1161148e2	0.0517311e-1	-0.04856684e-5	0.0220289e-8	-0.0450342e-12	-0.1248810e5	-0.0368821e3
37	CH_3CO	5000	0.0561227e2	0.0844988e-1	-0.0285414e-4	0.0428376e-8	-0.0226840e-12	-0.0518786e5	-0.0327494e2
38	CH_3O	3000	0.0377079e2	0.07871497e-1	-0.02656384e-4	0.03894443e-8	-0.02112616e-12	0.1278325e3	0.0292957e2
39	CH_3O_2	5000	0.0668129e1	0.08005727e-2	-0.27188507e-5	0.40631365e-9	-0.21927725e-13	0.5262185e3	-0.09423847e1
40	CH_3O_2H	5000	0.6649994e1	0.1035146e-1	-0.3352410e-5	0.5364535e-9	-0.3394975e-13	-0.1923234e5	-0.7792626e1
41	CH_3OH	5000	0.0402906e2	0.0993769e-1	-0.03050254e-4	0.04358793e-8	-0.0222472e-12	-0.0261579e6	0.0237819e2
42	CH_4	5000	0.0168347e2	0.1023723e-1	-0.03875128e-4	0.0637855e-8	-0.0450343e-12	-0.1008078e5	0.0962339e2
43	HCO	5000	0.0355727e2	0.03345572e-1	-0.01330060e-4	0.02470572e-8	-0.0171385e-12	0.0391632e5	0.0555529e2
44	CO	5000	0.03025078e2	0.1442685e-2	-0.0563087e-5	0.1018581e-9	-0.0691095e-13	-0.1426835e5	0.0610821e2
45	CO_2	5000	0.0445346e2	0.0314014e0	-0.1278410e-4	0.0239399e-8	-0.1669033e-13	-0.0489669e6	-0.0955395e1
46	H	5000	0.0250000e2	0.000000e0	0.000000e0	0.000000e0	0.000000e0	0.0254716e6	-0.0460117e1
47	H_2	5000	0.02991423e2	0.07000644e-2	-0.0563338e-6	-0.09231578e-10	0.15827519e-14	-0.0835030e4	-0.13551101e1
48	H_2O	5000	0.0267214e2	0.03056293e-1	-0.0873020e-5	0.1200996e-9	-0.0639161e-13	-0.0298992e6	0.0686281e2
49	H_2O_2	5000	0.0457316e2	0.0433613e-1	-0.1474688e-5	0.0234890e-8	-0.1431653e-13	-0.0180069e6	0.0501136e1
50	$HCCO$	4000	0.0675807e2	0.0200040e0	-0.02027607e-4	-0.1041318e-9	0.0190151e-12	0.0190151e6	-0.0907126e2
51	HO_2	5000	0.0407219e2	0.02131296e-1	-0.05308145e-5	0.06112269e-9	-0.02841164e-13	-0.1579727e3	0.0347602e2

52	iso-C$_3$H$_7$	5000	0.0806336e2	0.15744876e-1	-0.05182391e-4	0.07477245e-8	-0.03854422e-12	0.0531387e5	-0.0192646e3
53	iso-C$_3$H$_7$	5000	0.9065617e1	0.1947774e-1	-0.73385554e-1	0.1286373e-8	-0.85601393e-13	0.10187909e5	-0.24022063e2
54	iso-C$_4$H$_8$	5000	0.4460947e1	0.29611487e-1	-0.1307719e-2	0.26571934e-8	-0.20134713e-12	-0.50066758e4	0.10803180e1
55	iso-C$_4$H$_9$	6000	9.4304060e0	2.342713349e-2	-8.5359182e-6	1.39748355e-9	-8.4405745e-14	2.14214862e3	-2.42207994e1
56	iso-C$_4$H$_{10}$	5000	0.1084125e2	0.23317061e-1	-0.77685427e-5	0.11348074e-8	-0.59397203e-13	-0.21728570e5	-0.35915939e2
57	n-C$_3$H$_7$	5000	0.07978129e2	0.1576113e-1	-0.05173243e-4	0.07443892e-8	-0.0382497e-12	0.07579402e5	-0.0193611e3
58	N$_2$	5000	0.029296640e2	0.14879768e-2	-0.05684760e-5	0.1009703e-9	-0.0675335e-13	-0.09227977e4	0.0598052e2
59	O	5000	0.02542059e2	-0.02755061e-3	-0.031028030e-7	0.04551067e-10	-0.0436805e-14	0.0292308e6	0.049203080e2
60	O$_2$	5000	0.03697578e2	0.06135197e-2	-0.12588420e-6	0.01775281e-9	-0.11364354e-14	-0.1233930e4	0.03189165e2
61	OH	5000	0.02882730e2	0.10139743e-2	-0.02276877e-5	0.02174683e-9	-0.05126305e-14	0.0388688e5	0.055957122e2
62	OH*	6000	2.7558292e0	1.39848756e-3	-4.19428493e-7	6.3345328e-11	-3.56042218e-15	5.0975175e4	5.62581429e0
63	1-C$_4$H$_8$	5000	0.2053584e1	0.34350507e-1	-0.15883197e-4	0.3308966e-8	-0.25361045e-12	-0.21397231e4	0.15543201e2
64	1-CH$_2$	4000	0.03552888e2	0.020066788e-1	-0.0191411e-5	-0.11046733e-9	0.02021349e-12	0.0498497e6	0.016865702
65	p-C$_4$H$_9$	5000	0.901141239e1	0.239854498e-1	-0.89440655e-5	0.15295127e-8	-0.98013882e-13	0.3459904e4	-0.20575729e2
66	s-C$_4$H$_9$	5000	0.94282923e1	0.2191845e-1	-0.72831863e-5	0.10622090e-8	-0.55580591e-13	0.3630092e4	-0.22419800e2
67	tert-C$_4$H$_9$	6000	6.6307465e0	2.5935374e-2	-9.3716311e-6	1.51845890e-9	-9.1119086e-14	2.0086132e3	-9.20581440e0
68	3-CH$_2$	4000	0.03636407e2	0.0193056e-1	-0.01687016e-5	-0.10098994e-9	0.01808256e-12	0.0453413e6	0.021565602
69	3-C$_4$H$_8$	5000	0.827976760	0.35864539e-1	-0.16634498e-4	0.34732759e-8	-0.26657398e-12	-0.30521033e4	0.21342545e2

C.3 Reactions

H$_2$-O$_2$ reactions

No.	Reaction	Factor	Exponent	ΔE_A [kJ/mol]
1	$O_2 + H \rightleftharpoons OH + O$	$2,0650 \cdot 10^{14}$	$-9,7000 \cdot 10^{-2}$	$6,2853 \cdot 10^1$
2	$H_2 + O \rightleftharpoons OH + H$	$3,8180 \cdot 10^{12}$	$0,0000 \cdot 10^0$	$3,3256 \cdot 10^1$
3	$H_2 + O \rightleftharpoons OH + H$	$1,025 \cdot 10^{15}$	$0,000 \cdot 10^0$	$8,2300 \cdot 10^1$
4	$H_2 + OH \rightleftharpoons H_2O + H$	$2,1680 \cdot 10^8$	$1,5200 \cdot 10^0$	$1,4466 \cdot 10^1$
5	$OH + OH \rightleftharpoons H_2O + O$	$3,3480 \cdot 10^4$	$2,4200 \cdot 10^0$	$-8,0640 \cdot 10^0$
6	$H + H + M \rightleftharpoons H_2 + M$	$1,0150 \cdot 10^{17}$	$-6,0000 \cdot 10^{-1}$	$0,0000 \cdot 10^0$
7	$O + O + M \rightleftharpoons O_2 + M$	$5,4000 \cdot 10^{13}$	$0,0000 \cdot 10^0$	$-7,4000 \cdot 10^0$
8	$H + OH + M \rightleftharpoons H_2O + M$	$5,5600 \cdot 10^{22}$	$-2,0000 \cdot 10^0$	$0,0000 \cdot 10^0$

HO$_2$ reactions

No.	Reaction	Factor	Exponent	ΔE_A [kJ/mol]
9	H$+$O$_2$$+$M $\rightleftharpoons$ HO$_2$$+$M	$1,7460 \cdot 10^{17}$	$0,0000 \cdot 10^{0}$	$0,0000 \cdot 10^{0}$
10	HO$_2$$+$H $\rightleftharpoons$ OH$+$OH	$4,4570 \cdot 10^{14}$	$0,0000 \cdot 10^{0}$	$5,8190 \cdot 10^{0}$
11	HO$_2$$+$H $\rightleftharpoons$ H$_2$$+O_2$	$1,0540 \cdot 10^{14}$	$0,0000 \cdot 10^{0}$	$8,5630 \cdot 10^{0}$
12	HO$_2$$+$H $\rightleftharpoons$ H$_2$O$+$O	$1,4450 \cdot 10^{12}$	$0,0000 \cdot 10^{0}$	$0,0000 \cdot 10^{0}$
13	HO$_2$$+$O $\rightleftharpoons$ OH$+$O$_2$	$1,6260 \cdot 10^{13}$	$0,0000 \cdot 10^{0}$	$-1,8620 \cdot 10^{0}$
14	HO$_2$$+$OH $\rightleftharpoons$ H$_2$O$+$O$_2$	$9,2750 \cdot 10^{15}$	$0,0000 \cdot 10^{0}$	$7,3246 \cdot 10^{1}$

H$_2$O$_2$ reactions

No.	Reaction	Factor	Exponent	ΔE_A [kJ/mol]
15	HO$_2$$+HO_2$ $\rightleftharpoons$ H$_2$O$_2$$+O_2$	$4,220 \cdot 10^{14}$	$0,000$	$50,140$
16	HO$_2$$+HO_2$ $\rightleftharpoons$ H$_2$O$_2$$+O_2$	$1,3250 \cdot 10^{11}$	$0,0000 \cdot 10^{0}$	$-6,8200 \cdot 10^{0}$
17	OH$+$OH$+$M $\rightleftharpoons$ H$_2$O$_2$$+$M	$1,5660 \cdot 10^{13}$	$0,0000 \cdot 10^{0}$	$0,0000 \cdot 10^{0}$
18	H$_2$O$_2$$+$H $\rightleftharpoons$ H$_2$$+HO_2$	$1,6860 \cdot 10^{12}$	$0,0000 \cdot 10^{0}$	$1,5713 \cdot 10^{1}$
19	H$_2$O$_2$$+$H $\rightleftharpoons$ H$_2$O$+$OH	$1,0240 \cdot 10^{13}$	$0,0000 \cdot 10^{0}$	$1,4970 \cdot 10^{1}$
20	H$_2$O$_2$$+$O $\rightleftharpoons$ OH$+$HO$_2$	$4,2160 \cdot 10^{11}$	$0,0000 \cdot 10^{0}$	$1,6628 \cdot 10^{1}$
21	H$_2$O$_2$$+$O $\rightleftharpoons$ H$_2$O$+$O$_2$	$4,2160 \cdot 10^{11}$	$0,0000 \cdot 10^{0}$	$1,6628 \cdot 10^{1}$
22	H$_2$O$_2$$+$OH $\rightleftharpoons$ H$_2$O$+$HO$_2$	$1,6400 \cdot 10^{18}$	$0,0000 \cdot 10^{0}$	$1,2305 \cdot 10^{2}$
23	H$_2$O$_2$$+$OH $\rightleftharpoons$ H$_2$O$+$HO$_2$	$1,9200 \cdot 10^{12}$	$0,0000 \cdot 10^{0}$	$1,7870 \cdot 10^{0}$

CO reactions

No.	Reaction	Factor	Exponent	ΔE_A [kJ/mol]
24	$CO+O+M \rightleftharpoons CO_2+M$	$1,5400 \cdot 10^{15}$	$0,0000 \cdot 10^{0}$	$1,2560 \cdot 10^{1}$
25	$CO+OH \rightleftharpoons CO_2+H$	$1,0050 \cdot 10^{13}$	$0,0000 \cdot 10^{0}$	$6,6927 \cdot 10^{1}$
26	$CO+OH \rightleftharpoons CO_2+H$	$9,034 \cdot 10^{11}$	$0,0000 \cdot 10^{0}$	$1,9120 \cdot 10^{1}$
27	$CO+OH \rightleftharpoons CO_2+H$	$1,0120 \cdot 10^{11}$	$0,0000 \cdot 10^{0}$	$2,4900 \cdot 10^{-1}$
28	$CO+HO_2 \rightleftharpoons CO_2+OH$	$1,5000 \cdot 10^{14}$	$0,0000 \cdot 10^{0}$	$9,8700 \cdot 10^{1}$
29	$CO+O_2 \rightleftharpoons CO_2+O$	$2,5000 \cdot 10^{12}$	$0,0000 \cdot 10^{0}$	$2,0000 \cdot 10^{2}$

C reactions

No.	Reaction	Factor	Exponent	ΔE_A [kJ/mol]
30	$CH+H \rightleftharpoons C+H_2$	$5,0000 \cdot 10^{14}$	$0,0000 \cdot 10^{0}$	$0,0000 \cdot 10^{0}$
31	$C+O_2 \rightleftharpoons CO+O$	$6,0230 \cdot 10^{13}$	$0,0000 \cdot 10^{0}$	$2,6600 \cdot 10^{0}$

CH reactions

No.	Reaction	Factor	Exponent	ΔE_A [kJ/mol]
32	$CH+O \rightleftharpoons CO+H$	$4,0000 \cdot 10^{13}$	$0,0000 \cdot 10^{0}$	$0,0000 \cdot 10^{0}$
33	$CH+OH \rightleftharpoons HCO+H$	$3,0000 \cdot 10^{13}$	$0,0000 \cdot 10^{0}$	$0,0000 \cdot 10^{0}$
34	$CH+O_2 \rightleftharpoons HCO+O$	$1,6860 \cdot 10^{13}$	$0,0000 \cdot 10^{0}$	$0,0000 \cdot 10^{0}$

35	$CH+CO+M \rightleftharpoons HCCO+M$	$1,0240 \cdot 10^{15}$	$-4,0000 \cdot 10^{-1}$	$0,0000 \cdot 10^{0}$
36	$CH+CO_2 \rightleftharpoons HCO+CO$	$6,3840 \cdot 10^{7}$	$1,5100 \cdot 10^{0}$	$-2,9930 \cdot 10^{0}$
37	$CH+H_2O \rightleftharpoons CH_2O+H$	$4,5770 \cdot 10^{16}$	$-1,4200 \cdot 10^{0}$	$0,0000 \cdot 10^{0}$
38	$CH+H_2O \rightleftharpoons 3-CH_2+OH$	$4,5770 \cdot 10^{16}$	$-1,4200 \cdot 10^{0}$	$0,0000 \cdot 10^{0}$

CHO reactions

No.	Reaction	Factor	Exponent	ΔE_A [kJ/mol]
39	$HCO+M \rightleftharpoons CO+H+M$	$1,1350 \cdot 10^{14}$	$0,0000 \cdot 10^{0}$	$6,5015 \cdot 10^{1}$
40	$HCO+H \rightleftharpoons CO+H_2$	$9,0340 \cdot 10^{13}$	$0,0000 \cdot 10^{0}$	$0,0000 \cdot 10^{0}$
41	$HCO+O \rightleftharpoons CO+OH$	$3,0110 \cdot 10^{13}$	$0,0000 \cdot 10^{0}$	$0,0000 \cdot 10^{0}$
42	$HCO+O \rightleftharpoons CO_2+H$	$3,0110 \cdot 10^{13}$	$0,0000 \cdot 10^{0}$	$0,0000 \cdot 10^{0}$
43	$HCO+OH \rightleftharpoons CO+H_2O$	$1,0840 \cdot 10^{14}$	$0,0000 \cdot 10^{0}$	$0,0000 \cdot 10^{0}$
44	$HCO+O_2 \rightleftharpoons CO+HO_2$	$7,5880 \cdot 10^{12}$	$0,0000 \cdot 10^{0}$	$1,6960 \cdot 10^{0}$
45	$HCO+HCO \rightleftharpoons CH_2O+CO$	$3,0000 \cdot 10^{13}$	$0,0000 \cdot 10^{0}$	$0,0000 \cdot 10^{0}$

CH$_2$ reactions

No.	Reaction	Factor	Exponent	ΔE_A [kJ/mol]
46	$3-CH_2+H \rightleftharpoons CH+H_2$	$1,2040 \cdot 10^{14}$	$0,0000 \cdot 10^{0}$	$0,0000 \cdot 10^{0}$
47	$3-CH_2+O \rightarrow CO+H+H$	$1,2280 \cdot 10^{14}$	$0,0000 \cdot 10^{0}$	$2,2440 \cdot 10^{0}$
48	$3-CH_2+O \rightleftharpoons CO+H_2$	$8,1910 \cdot 10^{13}$	$0,0000 \cdot 10^{0}$	$2,2440 \cdot 10^{0}$

No.	Reaction	Factor	Exponent	ΔE_A [kJ/mol]
49	$3-CH_2+O_2 \rightleftharpoons CO+OH+H$	$1,8060 \cdot 10^{12}$	$0,0000 \cdot 10^{0}$	$0,0000 \cdot 10^{0}$
50	$3-CH_2+O_2 \rightleftharpoons CO_2+H_2$	$1,8060 \cdot 10^{12}$	$0,0000 \cdot 10^{0}$	$0,0000 \cdot 10^{0}$
51	$3-CH_2+3-CH_2 \rightleftharpoons C_2H_2+H_2$	$1,8060 \cdot 10^{14}$	$0,0000 \cdot 10^{0}$	$4,9884 \cdot 10^{1}$
52	$3-CH_2+3-CH_2 \rightleftharpoons C_2H_2+H+H$	$1,6260 \cdot 10^{15}$	$0,0000 \cdot 10^{0}$	$4,9884 \cdot 10^{1}$
53	$3-CH_2+CH_3 \rightleftharpoons C_2H_4+H$	$7,2270 \cdot 10^{13}$	$0,0000 \cdot 10^{0}$	$0,0000 \cdot 10^{0}$
54	$1-CH_2+M \rightleftharpoons 3-CH_2+M$	$6,0230 \cdot 10^{12}$	$0,0000 \cdot 10^{0}$	$0,0000 \cdot 10^{0}$
55	$1-CH_2+H_2 \rightleftharpoons CH_3+H$	$1,2600 \cdot 10^{16}$	$-5,6000 \cdot 10^{-1}$	$6,6500 \cdot 10^{1}$
56	$1-CH_2+O_2 \rightleftharpoons CO+OH+H$	$3,1000 \cdot 10^{13}$	$0,0000 \cdot 10^{0}$	$0,0000 \cdot 10^{0}$

CH$_2$O reactions

No.	Reaction	Factor	Exponent	ΔE_A [kJ/mol]
57	$CH_2O+M \rightleftharpoons HCO+H+M$	$4,8720 \cdot 10^{15}$	$0,0000 \cdot 10^{0}$	$3,1635 \cdot 10^{2}$
58	$CH_2O+M \rightleftharpoons CO+H_2+M$	$2,8300 \cdot 10^{15}$	$0,0000 \cdot 10^{0}$	$2,6696 \cdot 10^{2}$
59	$CH_2O+H \rightleftharpoons HCO+H_2$	$4,0950 \cdot 10^{8}$	$1,4700 \cdot 10^{0}$	$1,0226 \cdot 10^{1}$
60	$CH_2O+O \rightleftharpoons HCO+OH$	$4,1550 \cdot 10^{11}$	$5,7000 \cdot 10^{-1}$	$1,1556 \cdot 10^{1}$
61	$CH_2O+OH \rightleftharpoons HCO+H_2O$	$1,3910 \cdot 10^{13}$	$0,0000 \cdot 10^{0}$	$2,5270 \cdot 10^{0}$
62	$CH_2O+HO_2 \rightleftharpoons HCO+H_2O_2$	$4,0950 \cdot 10^{4}$	$2,5000 \cdot 10^{0}$	$4,2734 \cdot 10^{1}$
63	$CH_2O+O_2 \rightleftharpoons HCO+HO_2$	$2,4390 \cdot 10^{5}$	$2,5000 \cdot 10^{0}$	$1,5256 \cdot 10^{2}$
64	$CH_2O+CH_3 \rightleftharpoons HCO+CH_4$	$3,1920 \cdot 10^{1}$	$3,360 \cdot 10^{0}$	$1,8041 \cdot 10^{1}$

CH₂OH reactions

No.	Reaction	Factor	Exponent	ΔE_A [kJ/mol]
65	$CH_2OH + M \rightleftharpoons CH_2O + H + M$	$2,8000 \cdot 10^{14}$	$-7,3000 \cdot 10^{-1}$	$1,3731 \cdot 10^{2}$
66	$CH_2OH + H \rightleftharpoons CH_2O + H_2$	$2,4450 \cdot 10^{13}$	$0,0000 \cdot 10^{0}$	$0,0000 \cdot 10^{0}$
67	$CH_2OH + H \rightleftharpoons CH_3 + OH$	$1,0480 \cdot 10^{13}$	$0,0000 \cdot 10^{0}$	$0,0000 \cdot 10^{0}$
68	$CH_2OH + O_2 \rightleftharpoons CH_2O + HO_2$	$2,8910 \cdot 10^{16}$	$-1,5000 \cdot 10^{0}$	$0,0000 \cdot 10^{0}$
69	$CH_2OH + O_2 \rightleftharpoons CH_2O + HO_2$	$7,2270 \cdot 10^{13}$	$0,0000 \cdot 10^{0}$	$1,5630 \cdot 10^{1}$

CH₃ reactions

No.	Reaction	Factor	Exponent	ΔE_A [kJ/mol]
70	$CH_3 + M \rightleftharpoons 3 - CH_2 + H + M$	$2,9220 \cdot 10^{16}$	$0,0000 \cdot 10^{0}$	$3,7900 \cdot 10^{2}$
71	$CH_3 + M \rightleftharpoons CH + H_2 + M$	$1,8920 \cdot 10^{16}$	$0,0000 \cdot 10^{0}$	$3,5584 \cdot 10^{2}$
72	$CH_3 + O \rightleftharpoons CH_2O + H$	$6,7450 \cdot 10^{13}$	$0,0000 \cdot 10^{0}$	$0,0000 \cdot 10^{0}$
73	$CH_3 + OH \rightarrow CH_3O + H$	$1,2040 \cdot 10^{10}$	$0,0000 \cdot 10^{0}$	$5,8114 \cdot 10^{1}$
74	$CH_3 + OH \rightleftharpoons 1 - CH_2 + H_2O$	$3,0000 \cdot 10^{13}$	$0,0000 \cdot 10^{0}$	$1,1640 \cdot 10^{1}$
75	$CH_3 + OH + M \rightleftharpoons CH_3OH + M$	$4,3360 \cdot 10^{15}$	$-7,9000 \cdot 10^{-1}$	$0,0000 \cdot 10^{0}$
76	$CH_3 + HO_2 \rightleftharpoons CH_3O + OH$	$1,6000 \cdot 10^{13}$	$0,0000 \cdot 10^{0}$	$0,0000 \cdot 10^{0}$
77	$CH_3 + O_2 \rightleftharpoons CH_2O + OH$	$6,8600 \cdot 10^{1}$	$2,8600 \cdot 10^{0}$	$4,0870 \cdot 10^{1}$
78	$CH_3 + O_2 \rightarrow O + CH_3O$	$6,0800 \cdot 10^{7}$	$1,5400 \cdot 10^{0}$	$1,1644 \cdot 10^{2}$
79	$CH_3 + O_2 + M \rightleftharpoons CH_3O_2 + M$	$7,8290 \cdot 10^{8}$	$1,2000 \cdot 10^{0}$	$0,0000 \cdot 10^{0}$
80	$CH_3 + CO + M \rightleftharpoons CH_3CO + M$	$5,0580 \cdot 10^{11}$	$0,0000 \cdot 10^{0}$	$2,8770 \cdot 10^{1}$

No.	Reaction	Factor	Exponent	ΔE_A [kJ/mol]
81	$CH_3 + 1 - CH_2 \rightleftharpoons C_2H_4 + H$	$7,2270 \cdot 10^{13}$	$0,0000 \cdot 10^0$	$0,0000 \cdot 10^0$
82	$CH_3 + CH_3 + M \rightleftharpoons C_2H_6 + M$	$3,6100 \cdot 10^{13}$	$0,0000 \cdot 10^0$	$0,0000 \cdot 10^0$

CH_3O reactions

No.	Reaction	Factor	Exponent	ΔE_A [kJ/mol]
83	$CH_3O + M \rightleftharpoons CH_2O + H + M$	$6,8000 \cdot 10^{13}$	$0,0000 \cdot 10^0$	$1,0949 \cdot 10^2$
84	$CH_3O + H \rightarrow CH_3 + OH$	$1,6260 \cdot 10^{13}$	$0,0000 \cdot 10^0$	$2,4940 \cdot 10^0$
85	$CH_3O + H \rightleftharpoons CH_2O + H_2$	$3,7940 \cdot 10^{13}$	$0,0000 \cdot 10^0$	$2,4940 \cdot 10^0$
86	$CH_3O + O \rightarrow O_2 + CH_3$	$1,1290 \cdot 10^{13}$	$0,0000 \cdot 10^0$	$0,0000 \cdot 10^0$
87	$CH_3O + O \rightleftharpoons OH + CH_2O$	$3,7640 \cdot 10^{12}$	$0,0000 \cdot 10^0$	$0,0000 \cdot 10^0$
88	$CH_3O + OH \rightleftharpoons CH_2O + H_2O$	$1,8100 \cdot 10^{13}$	$0,0000 \cdot 10^0$	$0,0000 \cdot 10^0$
89	$CH_3O + O_2 \rightleftharpoons CH_2O + HO_2$	$2,1680 \cdot 10^{10}$	$0,0000 \cdot 10^0$	$7,3000 \cdot 10^0$
90	$CH_3O + CH_2O \rightleftharpoons CH_3OH + HCO$	$1,1500 \cdot 10^{11}$	$0,0000 \cdot 10^0$	$5,2000 \cdot 10^0$

CH_3O_2 reactions

No.	Reaction	Factor	Exponent	ΔE_A [kJ/mol]
91	$CH_3O_2 + HO_2 \rightleftharpoons CH_3O_2H + O_2$	$2,2760 \cdot 10^{11}$	$0,0000 \cdot 10^0$	$-6,2350 \cdot 10^0$
92	$CH_3O_2 + CH_3 \rightleftharpoons CH_3O + CH_3O$	$1,5000 \cdot 10^{13}$	$0,0000 \cdot 10^0$	$-5,0000 \cdot 10^0$
93	$CH_3O_2 + CH_3O_2 \rightarrow CH_2O + CH_3OH + O_2$	$3,4260 \cdot 10^{10}$	$0,0000 \cdot 10^0$	$-3,2420 \cdot 10^0$
94	$CH_3O_2 + CH_3O_2 \rightarrow CH_3O + CH_3O + O_2$	$2,2880 \cdot 10^{10}$	$0,0000 \cdot 10^0$	$-3,2420 \cdot 10^0$

No.	Reaction	Factor	Exponent	ΔE_A [kJ/mol]
95	$CH_3O_2 + H_2O_2 \rightleftharpoons CH_3O_2H + HO_2$	$2,4000 \cdot 10^{12}$	$0,0000 \cdot 10^{0}$	$4,1800 \cdot 10^{1}$
96	$CH_3O_2 + CH_2O \rightleftharpoons CH_3O_2H + HCO$	$1,3000 \cdot 10^{11}$	$0,0000 \cdot 10^{0}$	$3,7700 \cdot 10^{1}$
97	$CH_3O_2 + CH_4 \rightleftharpoons CH_3O_2H + CH_3$	$1,8100 \cdot 10^{11}$	$0,0000 \cdot 10^{0}$	$7,7800 \cdot 10^{1}$
98	$CH_3O_2 + CH_3OH \rightleftharpoons CH_3O_2H + CH_2OH$	$1,8100 \cdot 10^{11}$	$0,0000 \cdot 10^{0}$	$5,7700 \cdot 10^{1}$

CH$_4$ reactions

No.	Reaction	Factor	Exponent	ΔE_A [kJ/mol]
99	$CH_4 + M \rightleftharpoons CH_3 + H + M$	$2,4600 \cdot 10^{16}$	$0,0000 \cdot 10^{0}$	$4,3900 \cdot 10^{2}$
100	$CH_4 + H \rightleftharpoons H_2 + CH_3$	$6,1430 \cdot 10^{5}$	$2,5000 \cdot 10^{0}$	$4,0115 \cdot 10^{1}$
101	$CH_4 + O \rightleftharpoons OH + CH_3$	$4,3960 \cdot 10^{5}$	$2,5000 \cdot 10^{0}$	$2,7519 \cdot 10^{1}$
102	$CH_4 + OH \rightleftharpoons H_2O + CH_3$	$1,3670 \cdot 10^{6}$	$2,1800 \cdot 10^{0}$	$1,1223 \cdot 10^{1}$
103	$CH_4 + HO_2 \rightleftharpoons H_2O_2 + CH_3$	$4,6970 \cdot 10^{4}$	$2,5000 \cdot 10^{0}$	$8,7879 \cdot 10^{1}$
104	$CH_4 + O_2 \rightleftharpoons CH_3 + HO_2$	$4,8780 \cdot 10^{5}$	$2,5000 \cdot 10^{0}$	$2,1924 \cdot 10^{2}$
105	$CH_4 + CH \rightleftharpoons C_2H_4 + H$	$1,3250 \cdot 10^{16}$	$-9,4000 \cdot 10^{-1}$	$2,4100 \cdot 10^{-1}$
106	$CH_4 + 3 - CH_2 \rightleftharpoons CH_3 + CH_3$	$8,4000 \cdot 10^{12}$	$0,0000 \cdot 10^{0}$	$-2,0780 \cdot 10^{0}$

CH$_3$OH reactions

No.	Reaction	Factor	Exponent	ΔE_A [kJ/mol]
107	$CH_3OH + H \rightleftharpoons CH_2OH + H_2$	$2,7460 \cdot 10^{9}$	$1,2400 \cdot 10^{0}$	$1,8789 \cdot 10^{1}$
108	$CH_3OH + H \rightleftharpoons CH_3O + H_2$	$6,8660 \cdot 10^{8}$	$1,2400 \cdot 10^{0}$	$1,8789 \cdot 10^{1}$

No.	Reaction	Factor	Exponent	ΔE_A [kJ/mol]
109	$CH_3OH + O \rightleftharpoons CH_2OH + OH$	$1,9750 \cdot 10^{13}$	$0,0000 \cdot 10^0$	$2,2198 \cdot 10^1$
110	$CH_3OH + O \rightleftharpoons CH_3O + OH$	$4,9380 \cdot 10^{12}$	$0,0000 \cdot 10^0$	$2,2198 \cdot 10^1$
111	$CH_3OH + OH \rightleftharpoons CH_2OH + H_2O$	$5,2730 \cdot 10^6$	$1,9200 \cdot 10^0$	$-1,1970 \cdot 10^0$
112	$CH_3OH + OH \rightleftharpoons CH_3O + H_2O$	$9,3000 \cdot 10^5$	$1,9200 \cdot 10^0$	$-1,1970 \cdot 10^0$
113	$CH_3OH + HO_2 \rightleftharpoons CH_2OH + H_2O_2$	$6,2000 \cdot 10^{12}$	$0,0000 \cdot 10^0$	$8,1100 \cdot 10^1$
114	$CH_3OH + O_2 \rightleftharpoons HO_2 + CH_2OH$	$2,0500 \cdot 10^{13}$	$0,0000 \cdot 10^0$	$1,8910 \cdot 10^2$
115	$CH_3OH + CH_3 \rightleftharpoons CH_4 + CH_2OH$	$9,9370 \cdot 10^0$	$3,4500 \cdot 10^0$	$3,3422 \cdot 10^1$
116	$CH_3OH + CH_3 \rightleftharpoons CH_4 + CH_3O$	$2,0170 \cdot 10^1$	$3,4500 \cdot 10^0$	$3,3422 \cdot 10^1$
117	$CH_3OH + CH_3O \rightleftharpoons CH_2OH + CH_3OH$	$1,5000 \cdot 10^{12}$	$0,0000 \cdot 10^0$	$2,9300 \cdot 10^1$
118	$CH_3OH + CH_2O \rightarrow CH_3O + CH_3O$	$1,5300 \cdot 10^{12}$	$0,0000 \cdot 10^0$	$3,3320 \cdot 10^2$

CH$_3$O$_2$H reactions

No.	Reaction	Factor	Exponent	ΔE_A [kJ/mol]
119	$CH_3O_2H \rightleftharpoons CH_3O + OH$	$6,0000 \cdot 10^{14}$	$0,0000 \cdot 10^0$	$1,7710 \cdot 10^2$
120	$CH_3O_2H + O \rightleftharpoons OH + CH_3O_2$	$2,4690 \cdot 10^{13}$	$0,0000 \cdot 10^0$	$1,9953 \cdot 10^1$
121	$CH_3O_2H + OH \rightleftharpoons H_2O + CH_3O_2$	$1,0840 \cdot 10^{12}$	$0,0000 \cdot 10^0$	$-1,8290 \cdot 10^0$

C$_2$H reactions

No.	Reaction	Factor	Exponent	ΔE_A [kJ/mol]
122	$C_2H + O \rightleftharpoons CO + CH$	$5,9620 \cdot 10^{13}$	$0,0000 \cdot 10^0$	$0,0000 \cdot 10^0$

123	$C_2H + O_2 \rightleftharpoons HCO + CO$	$1,0000 \cdot 10^{15}$	$-3,5000 \cdot 10^{-1}$	$0,0000 \cdot 10^{0}$
124	$C_2H + O_2 \rightleftharpoons H + CO + CO$	$2,9200 \cdot 10^{15}$	$-3,5000 \cdot 10^{-1}$	$0,0000 \cdot 10^{0}$
125	$C_2H + O_2 \rightleftharpoons CO_2 + CH$	$8,1500 \cdot 10^{12}$	$-3,5000 \cdot 10^{-1}$	$0,0000 \cdot 10^{0}$
126	$C_2H + O_2 \rightleftharpoons HCCO + O$	$8,1500 \cdot 10^{12}$	$-3,5000 \cdot 10^{-1}$	$0,0000 \cdot 10^{0}$
127	$C_2H + CH_4 \rightleftharpoons C_2H_2 + CH_3$	$2,1680 \cdot 10^{10}$	$9,4000 \cdot 10^{-1}$	$2,7260 \cdot 10^{0}$

HCCO reactions

No.	Reaction	Factor	Exponent	ΔE_A [kJ/mol]
128	$HCCO + H \rightleftharpoons 3 - CH_2 + CO$	$1,0600 \cdot 10^{13}$	$0,0000 \cdot 10^{0}$	$0,0000 \cdot 10^{0}$
129	$HCCO + O \rightarrow CO + CO + H$	$1,5270 \cdot 10^{14}$	$0,0000 \cdot 10^{0}$	$0,0000 \cdot 10^{0}$
130	$HCCO + 3 - CH_2 \rightleftharpoons C_2H_3 + CO$	$3,0000 \cdot 10^{13}$	$0,0000 \cdot 10^{0}$	$0,0000 \cdot 10^{0}$

C$_2$H$_2$ reactions

No.	Reaction	Factor	Exponent	ΔE_A [kJ/mol]
131	$C_2H_2 + M \rightleftharpoons C_2H + H + M$	$3,6000 \cdot 10^{16}$	$0,0000 \cdot 10^{0}$	$4,4600 \cdot 10^{2}$
132	$C_2H_2 + H \rightleftharpoons C_2H + H_2$	$1,0100 \cdot 10^{10}$	$1,6400 \cdot 10^{0}$	$1,2679 \cdot 10^{2}$
133	$C_2H_2 + O \rightleftharpoons 3 - CH_2 + CO$	$1,4800 \cdot 10^{8}$	$1,4000 \cdot 10^{0}$	$9,2280 \cdot 10^{0}$
134	$C_2H_2 + O \rightleftharpoons HCCO + H$	$9,3950 \cdot 10^{8}$	$1,4000 \cdot 10^{0}$	$9,2280 \cdot 10^{0}$
135	$C_2H_2 + OH \rightleftharpoons H_2O + C_2H$	$6,4200 \cdot 10^{14}$	$0,0000 \cdot 10^{0}$	$5,6540 \cdot 10^{1}$
136	$C_2H_2 + O_2 \rightleftharpoons HCCO + OH$	$5,0000 \cdot 10^{7}$	$1,5000 \cdot 10^{0}$	$1,2600 \cdot 10^{2}$

| 137 | $C_2H_2 + C_2H \rightleftharpoons C_4H_2 + H$ | $7,8290 \cdot 10^{13}$ | $0,0000 \cdot 10^{0}$ | $0,0000 \cdot 10^{0}$ |

CH$_2$CO reactions

No.	Reaction	Factor	Exponent	ΔE_A [kJ/mol]
138	$CH_2CO + M \rightleftharpoons 3 - CH_2 + CO + M$	$1,0000 \cdot 10^{16}$	$0,0000 \cdot 10^{0}$	$2,4800 \cdot 10^{2}$
139	$CH_2CO + H \rightleftharpoons CH_3 + CO$	$3,2520 \cdot 10^{10}$	$8,5000 \cdot 10^{-1}$	$1,1889 \cdot 10^{1}$
140	$CH_2CO + O \rightleftharpoons CH_2O + CO$	$3,6130 \cdot 10^{11}$	$0,0000 \cdot 10^{0}$	$5,6530 \cdot 10^{0}$
141	$CH_2CO + O \rightarrow HCO + H + CO$	$1,8060 \cdot 10^{11}$	$0,0000 \cdot 10^{0}$	$5,6530 \cdot 10^{0}$
142	$CH_2CO + O \rightleftharpoons HCO + HCO$	$1,8060 \cdot 10^{11}$	$0,0000 \cdot 10^{0}$	$5,6530 \cdot 10^{0}$
143	$CH_2CO + OH \rightleftharpoons CH_3 + CO_2$	$6,2390 \cdot 10^{11}$	$0,0000 \cdot 10^{0}$	$4,2400 \cdot 10^{0}$
144	$CH_2CO + OH \rightleftharpoons CH_2O + HCO$	$3,3700 \cdot 10^{10}$	$0,0000 \cdot 10^{0}$	$4,2400 \cdot 10^{0}$

C$_2$H$_3$ reactions

No.	Reaction	Factor	Exponent	ΔE_A [kJ/mol]
145	$C_2H_3 + M \rightleftharpoons C_2H_2 + H + M$	$7,8000 \cdot 10^{8}$	$1,6200 \cdot 10^{0}$	$1,5506 \cdot 10^{2}$
146	$C_2H_3 + H \rightleftharpoons C_2H_2 + H_2$	$4,2160 \cdot 10^{13}$	$0,0000 \cdot 10^{0}$	$0,0000 \cdot 10^{0}$
147	$C_2H_3 + O \rightleftharpoons C_2H_2 + OH$	$3,0110 \cdot 10^{13}$	$0,0000 \cdot 10^{0}$	$0,0000 \cdot 10^{0}$
148	$C_2H_3 + O \rightleftharpoons CH_3 + CO$	$3,0110 \cdot 10^{13}$	$0,0000 \cdot 10^{0}$	$0,0000 \cdot 10^{0}$
149	$C_2H_3 + O \rightleftharpoons HCO + 3 - CH_2$	$3,0110 \cdot 10^{13}$	$0,0000 \cdot 10^{0}$	$0,0000 \cdot 10^{0}$
150	$C_2H_3 + OH \rightleftharpoons C_2H_2 + H_2O$	$5,0000 \cdot 10^{12}$	$0,0000 \cdot 10^{0}$	$0,0000 \cdot 10^{0}$

No.	Reaction	Factor	Exponent	ΔE_A [kJ/mol]
151	$C_2H_3 + O_2 \rightleftharpoons CH_2O + HCO$	$7,7080 \cdot 10^{12}$	$0,0000 \cdot 10^0$	$-9,9700 \cdot 10^{-1}$
152	$C_2H_3 + O_2 \rightleftharpoons CH_2HCO + O$	$8,1490 \cdot 10^{12}$	$0,0000 \cdot 10^0$	$-1,0390 \cdot 10^0$
153	$C_2H_3 + O_2 \rightleftharpoons C_2H_2 + HO_2$	$4,6500 \cdot 10^{11}$	$0,0000 \cdot 10^0$	$-1,0390 \cdot 10^0$

CH$_3$CO reactions

No.	Reaction	Factor	Exponent	ΔE_A [kJ/mol]
154	$CH_3CO + H \rightleftharpoons CH_2CO + H_2$	$2,0000 \cdot 10^{13}$	$0,0000 \cdot 10^0$	$0,0000 \cdot 10^0$

CH$_2$CHO reactions

No.	Reaction	Factor	Exponent	ΔE_A [kJ/mol]
155	$CH_2HCO + H \rightleftharpoons CH_2CO + H_2$	$2,0000 \cdot 10^{13}$	$0,0000 \cdot 10^0$	$0,0000 \cdot 10^0$

C$_2$H$_4$ reactions

No.	Reaction	Factor	Exponent	ΔE_A [kJ/mol]
156	$C_2H_4 + M \rightleftharpoons C_2H_2 + H_2 + M$	$2,9200 \cdot 10^{17}$	$1,0000 \cdot 10^0$	$3,2749 \cdot 10^2$
157	$C_2H_4 + M \rightleftharpoons C_2H_3 + H + M$	$7,3990 \cdot 10^{17}$	$0,0000 \cdot 10^0$	$4,0406 \cdot 10^2$
158	$C_2H_4 + H + M \rightarrow C_2H_5 + M$	$3,9750 \cdot 10^9$	$1,2800 \cdot 10^0$	$5,4000 \cdot 10^0$
159	$C_2H_4 + H \rightleftharpoons C_2H_3 + H_2$	$2,3480 \cdot 10^2$	$3,6200 \cdot 10^0$	$4,7140 \cdot 10^1$

No.	Reaction	Factor	Exponent	ΔE_A [kJ/mol]
160	$C_2H_4 + O \rightleftharpoons CH_2HCO + H$	$4,7430 \cdot 10^6$	$1,8800 \cdot 10^0$	$7,6400 \cdot 10^{-1}$
161	$C_2H_4 + O \rightleftharpoons HCO + CH_3$	$8,1310 \cdot 10^6$	$1,8800 \cdot 10^0$	$7,6400 \cdot 10^{-1}$
162	$C_2H_4 + O \rightleftharpoons CH_2CO + H_2$	$6,7700 \cdot 10^5$	$1,8800 \cdot 10^0$	$7,6400 \cdot 10^{-1}$
163	$C_2H_4 + OH \rightleftharpoons C_2H_3 + H_2O$	$6,4800 \cdot 10^{12}$	$0,0000 \cdot 10^0$	$2,4900 \cdot 10^1$
164	$C_2H_4 + CH \rightleftharpoons p - C_3H_4 + H$	$1,3250 \cdot 10^{14}$	$0,0000 \cdot 10^0$	$-1,4400 \cdot 10^0$
165	$C_2H_4 + 1 - CH_2 \rightleftharpoons C_3H_6$	$7,2400 \cdot 10^{13}$	$0,0000 \cdot 10^0$	$0,0000 \cdot 10^0$
166	$C_2H_4 + CH_3 \rightleftharpoons C_2H_3 + CH_4$	$6,0230 \cdot 10^7$	$1,5600 \cdot 10^0$	$6,9600 \cdot 10^1$

CH$_3$CHO reactions

No.	Reaction	Factor	Exponent	ΔE_A [kJ/mol]
167	$CH_3HCO + M \rightleftharpoons CH_3 + HCO + M$	$2,1000 \cdot 10^{16}$	$0,0000 \cdot 10^0$	$3,4200 \cdot 10^2$
168	$CH_3HCO + H \rightleftharpoons CH_3CO + H_2$	$2,0470 \cdot 10^9$	$1,1600 \cdot 10^0$	$1,0059 \cdot 10^1$
169	$CH_3HCO + H \rightleftharpoons CH_2HCO + H_2$	$2,0470 \cdot 10^9$	$1,1600 \cdot 10^0$	$1,0059 \cdot 10^1$
170	$CH_3HCO + O \rightleftharpoons CH_3CO + OH$	$5,2580 \cdot 10^{12}$	$0,0000 \cdot 10^0$	$7,6000 \cdot 10^0$
171	$CH_3HCO + O \rightleftharpoons CH_2HCO + OH$	$5,8420 \cdot 10^{11}$	$0,0000 \cdot 10^0$	$7,6000 \cdot 10^0$
172	$CH_3HCO + OH \rightleftharpoons CH_3CO + H_2O$	$2,6880 \cdot 10^8$	$1,3500 \cdot 10^0$	$-6,5840 \cdot 10^0$
173	$CH_3HCO + OH \rightleftharpoons CH_2HCO + H_2O$	$2,0230 \cdot 10^7$	$1,3500 \cdot 10^0$	$-6,5840 \cdot 10^0$
174	$CH_3HCO + HO_2 \rightleftharpoons CH_3CO + H_2O_2$	$4,0950 \cdot 10^4$	$2,5000 \cdot 10^0$	$4,2692 \cdot 10^1$
175	$CH_3HCO + O_2 \rightleftharpoons CH_3CO + HO_2$	$1,2040 \cdot 10^5$	$2,5000 \cdot 10^0$	$1,5713 \cdot 10^2$
176	$CH_3HCO + 3 - CH_2 \rightleftharpoons CH_3CO + CH_3$	$2,5000 \cdot 10^{12}$	$0,0000 \cdot 10^0$	$1,5900 \cdot 10^1$
177	$CH_3HCO + CH_3 \rightleftharpoons CH_3CO + CH_4$	$3,4930E - 010$	$6,2100 \cdot 10^0$	$6,8170 \cdot 10^0$

C$_2$H$_5$ reactions

No.	Reaction	Factor	Exponent	ΔE_A [kJ/mol]
178	$C_2H_5 + M \rightarrow C_2H_4 + H + M$	$4,1000 \cdot 10^{13}$	$0,0000 \cdot 10^0$	$1,6680 \cdot 10^2$
179	$C_2H_5 + H \rightleftharpoons CH_3 + CH_3$	$4,2160 \cdot 10^{13}$	$0,0000 \cdot 10^0$	$0,0000 \cdot 10^0$
180	$C_2H_5 + O \rightleftharpoons CH_3HCO + H$	$5,3200 \cdot 10^{13}$	$0,0000 \cdot 10^0$	$0,0000 \cdot 10^0$
181	$C_2H_5 + O \rightleftharpoons CH_2O + CH_3$	$3,9750 \cdot 10^{13}$	$0,0000 \cdot 10^0$	$0,0000 \cdot 10^0$
182	$C_2H_5 + O_2 \rightleftharpoons C_2H_4 + HO_2$	$2,4100 \cdot 10^{10}$	$0,0000 \cdot 10^0$	$0,0000 \cdot 10^0$
183	$C_2H_5 + CH_3 \rightleftharpoons C_2H_4 + CH_4$	$9,0340 \cdot 10^{11}$	$0,0000 \cdot 10^0$	$0,0000 \cdot 10^0$
184	$C_2H_5 + C_2H_5 \rightleftharpoons C_2H_4 + C_2H_6$	$1,4000 \cdot 10^{12}$	$0,0000 \cdot 10^0$	$0,0000 \cdot 10^0$

C$_2$H$_5$O reactions

No.	Reaction	Factor	Exponent	ΔE_A [kJ/mol]
185	$C_2H_5O \rightleftharpoons CH_3HCO + H$	$2,0000 \cdot 10^{14}$	$0,0000 \cdot 10^0$	$9,7000 \cdot 10^1$
186	$C_2H_5O \rightleftharpoons CH_2O + CH_3$	$8,0000 \cdot 10^{13}$	$0,0000 \cdot 10^0$	$9,0000 \cdot 10^1$
187	$C_2H_5O + H \rightleftharpoons CH_3HCO + H_2$	$1,0000 \cdot 10^{14}$	$0,0000 \cdot 10^0$	$0,0000 \cdot 10^0$
188	$C_2H_5O + O \rightleftharpoons CH_3HCO + OH$	$1,2100 \cdot 10^{14}$	$0,0000 \cdot 10^0$	$0,0000 \cdot 10^0$
189	$C_2H_5O + OH \rightleftharpoons CH_3HCO + H_2O$	$1,0000 \cdot 10^{14}$	$0,0000 \cdot 10^0$	$0,0000 \cdot 10^0$
190	$C_2H_5O + O_2 \rightleftharpoons CH_3HCO + HO_2$	$6,0000 \cdot 10^{10}$	$0,0000 \cdot 10^0$	$7,0000 \cdot 10^0$

CH$_3$CHOH reactions

No.	Reaction	Factor	Exponent	ΔE_A [kJ/mol]
191	CH$_3$CHOH $\rightleftharpoons$ CH$_3$HCO + H	$1,0000 \cdot 10^{14}$	$0,0000 \cdot 10^{0}$	$1,0500 \cdot 10^{2}$
192	CH$_3$CHOH + H $\rightleftharpoons$ CH$_3$HCO + H$_2$	$3,0000 \cdot 10^{13}$	$0,0000 \cdot 10^{0}$	$0,0000 \cdot 10^{0}$
193	CH$_3$CHOH + O $\rightleftharpoons$ CH$_3$HCO + OH	$1,2000 \cdot 10^{14}$	$0,0000 \cdot 10^{0}$	$0,0000 \cdot 10^{0}$
194	CH$_3$CHOH + OH $\rightleftharpoons$ CH$_3$HCO + H$_2$O	$1,5100 \cdot 10^{13}$	$0,0000 \cdot 10^{0}$	$0,0000 \cdot 10^{0}$
195	CH$_3$CHOH + O$_2$ $\rightleftharpoons$ CH$_3$HCO + HO$_2$	$8,4320 \cdot 10^{15}$	$-1,2000 \cdot 10^{0}$	$0,0000 \cdot 10^{0}$
196	CH$_3$CHOH + O$_2$ $\rightleftharpoons$ CH$_3$HCO + HO$_2$	$4,8180 \cdot 10^{14}$	$0,0000 \cdot 10^{0}$	$2,0100 \cdot 10^{1}$

CH$_2$CH$_2$OH reactions

No.	Reaction	Factor	Exponent	ΔE_A [kJ/mol]
197	CH$_2$CH$_2$OH $\rightleftharpoons$ C$_2$H$_4$ + OH	$1,0000 \cdot 10^{14}$	$0,0000 \cdot 10^{0}$	$1,4000 \cdot 10^{2}$
198	CH$_2$CH$_2$OH + H $\rightleftharpoons$ CH$_3$HCO + H$_2$	$5,0000 \cdot 10^{13}$	$0,0000 \cdot 10^{0}$	$0,0000 \cdot 10^{0}$

C$_2$H$_5$OH reactions

No.	Reaction	Factor	Exponent	ΔE_A [kJ/mol]
199	C$_2$H$_5$OH $\rightleftharpoons$ CH$_3$ + CH$_2$OH	$3,1000 \cdot 10^{15}$	$0,0000 \cdot 10^{0}$	$3,3720 \cdot 10^{2}$
200	C$_2$H$_5$OH $\rightleftharpoons$ C$_2$H$_5$ + OH	$5,0000 \cdot 10^{16}$	$0,0000 \cdot 10^{0}$	$3,8160 \cdot 10^{2}$
201	C$_2$H$_5$OH $\rightleftharpoons$ C$_2$H$_4$ + H$_2$O	$1,0000 \cdot 10^{14}$	$0,0000 \cdot 10^{0}$	$3,2090 \cdot 10^{2}$

No.	Reaction	Factor	Exponent	ΔE_A [kJ/mol]
202	$C_2H_5OH + H \rightleftharpoons CH_3CHOH + H_2$	$4,4000 \cdot 10^{12}$	$0,0000 \cdot 10^0$	$1,9100 \cdot 10^1$
203	$C_2H_5OH + H \rightleftharpoons C_2H_5 + H_2O$	$5,9000 \cdot 10^{11}$	$0,0000 \cdot 10^0$	$1,4400 \cdot 10^1$
204	$C_2H_5OH + O \rightleftharpoons CH_3CHOH + OH$	$5,4200 \cdot 10^5$	$2,5000 \cdot 10^0$	$7,7320 \cdot 10^0$
205	$C_2H_5OH + O \rightleftharpoons C_2H_5O + OH$	$3,0100 \cdot 10^4$	$2,5000 \cdot 10^0$	$7,7320 \cdot 10^0$
206	$C_2H_5OH + O \rightleftharpoons CH_2CH_2OH + OH$	$3,0100 \cdot 10^4$	$2,5000 \cdot 10^0$	$7,7320 \cdot 10^0$
207	$C_2H_5OH + OH \rightleftharpoons CH_3CHOH + H_2O$	$2,1400 \cdot 10^7$	$1,7800 \cdot 10^0$	$-3,5330 \cdot 10^0$
208	$C_2H_5OH + OH \rightleftharpoons C_2H_5O + H_2O$	$9,0300 \cdot 10^5$	$1,7800 \cdot 10^0$	$-3,5330 \cdot 10^0$
209	$C_2H_5OH + OH \rightleftharpoons CH_2CH_2OH + H_2O$	$1,1280 \cdot 10^6$	$1,7800 \cdot 10^0$	$-3,5330 \cdot 10^0$
210	$C_2H_5OH + HO_2 \rightleftharpoons CH_3CHOH + H_2O_2$	$6,3000 \cdot 10^{12}$	$0,0000 \cdot 10^0$	$8,1100 \cdot 10^1$
211	$C_2H_5OH + CH_3 \rightleftharpoons CH_3CHOH + CH_4$	$4,6970 \cdot 10^{11}$	$0,0000 \cdot 10^0$	$4,0572 \cdot 10^1$
212	$C_2H_5OH + CH_3 \rightleftharpoons CH_2CH_2OH + CH_4$	$3,6130 \cdot 10^{10}$	$0,0000 \cdot 10^0$	$3,9907 \cdot 10^1$
213	$C_2H_5OH + CH_3 \rightleftharpoons C_2H_5O + CH_4$	$9,0340 \cdot 10^{10}$	$0,0000 \cdot 10^0$	$3,9325 \cdot 10^1$
214	$C_2H_5OH + CH_3O \rightleftharpoons CH_3CHOH + CH_3OH$	$2,0000 \cdot 10^{11}$	$0,0000 \cdot 10^0$	$2,9300 \cdot 10^1$
215	$C_2H_5OH + CH_2O \rightleftharpoons C_2H_5O + CH_3O$	$1,5300 \cdot 10^{12}$	$0,0000 \cdot 10^0$	$3,3320 \cdot 10^2$
216	$C_2H_5OH + C_2H_5O \rightleftharpoons C_2H_5OH + CH_3CHOH$	$2,0000 \cdot 10^{11}$	$0,0000 \cdot 10^0$	$2,9300 \cdot 10^1$

C_2H_6 reactions

No.	Reaction	Factor	Exponent	ΔE_A [kJ/mol]
217	$C_2H_6 + H \rightleftharpoons C_2H_5 + H_2$	$9,8170 \cdot 10^{13}$	$0,0000 \cdot 10^0$	$3,8577 \cdot 10^1$
218	$C_2H_6 + O \rightleftharpoons C_2H_5 + OH$	$1,0000 \cdot 10^9$	$1,5000 \cdot 10^0$	$2,4400 \cdot 10^1$
219	$C_2H_6 + OH \rightleftharpoons C_2H_5 + H_2O$	$9,1540 \cdot 10^6$	$2,0000 \cdot 10^0$	$4,1570 \cdot 10^0$
220	$C_2H_6 + HO_2 \rightleftharpoons C_2H_5 + H_2O_2$	$1,1020 \cdot 10^5$	$2,5000 \cdot 10^0$	$7,0502 \cdot 10^1$

221	$C_2H_6 + O_2 \rightleftharpoons C_2H_5 + HO_2$	$7,2870 \cdot 10^5$	$2,5000 \cdot 10^0$	$2,0569 \cdot 10^2$
222	$C_2H_6 + 3 - CH_2 \rightleftharpoons C_2H_5 + CH_3$	$2,2000 \cdot 10^{13}$	$0,0000 \cdot 10^0$	$3,6300 \cdot 10^1$
223	$C_2H_6 + CH_3 \rightleftharpoons C_2H_5 + CH_4$	$5,6010 \cdot 10^{10}$	$0,0000 \cdot 10^0$	$3,9408 \cdot 10^1$
224	$C_2H_6 + CH_3 \rightleftharpoons C_2H_5 + CH_4$	$8,4320 \cdot 10^{14}$	$0,0000 \cdot 10^0$	$9,3116 \cdot 10^1$
225	$C_2H_6 + CH \rightleftharpoons C_2H_4 + CH_3$	$1,0840 \cdot 10^{14}$	$0,0000 \cdot 10^0$	$-1,1000 \cdot 10^0$

C$_3$H$_2$ reactions

No.	Reaction	Factor	Exponent	ΔE_A [kJ/mol]
226	$C_3H_2 + O_2 \rightleftharpoons HCO + HCCO$	$1,0000 \cdot 10^{13}$	$0,0000 \cdot 10^0$	$0,0000 \cdot 10^0$

C$_3$H$_3$ reactions

No.	Reaction	Factor	Exponent	ΔE_A [kJ/mol]
227	$C_3H_3 + OH \rightleftharpoons C_3H_2 + H_2O$	$2,0000 \cdot 10^{13}$	$0,0000 \cdot 10^0$	$0,0000 \cdot 10^0$
228	$C_3H_3 + O \rightarrow CO + C_2H_3$	$3,8000 \cdot 10^{13}$	$0,0000 \cdot 10^0$	$0,0000 \cdot 10^0$
229	$C_3H_3 + O_2 \rightarrow HCCO + CH_2O$	$6,0000 \cdot 10^{12}$	$0,0000 \cdot 10^0$	$0,0000 \cdot 10^0$

C$_3$H$_4$ reactions

No.	Reaction	Factor	Exponent	ΔE_A [kJ/mol]
230	$p-C_3H_4 + O \rightleftharpoons CH_2O + C_2H_2$	$1,0000 \cdot 10^{12}$	$0,0000 \cdot 10^{0}$	$0,0000 \cdot 10^{0}$
231	$p-C_3H_4 + O \rightleftharpoons HCO + C_2H_3$	$1,0000 \cdot 10^{12}$	$0,0000 \cdot 10^{0}$	$0,0000 \cdot 10^{0}$
232	$p-C_3H_4 + OH \rightleftharpoons CH_2O + C_2H_3$	$1,0000 \cdot 10^{12}$	$0,0000 \cdot 10^{0}$	$0,0000 \cdot 10^{0}$
233	$p-C_3H_4 + OH \rightleftharpoons HCO + C_2H_4$	$1,0000 \cdot 10^{12}$	$0,0000 \cdot 10^{0}$	$0,0000 \cdot 10^{0}$
234	$p-C_3H_4 + M \rightleftharpoons H + C_3H_3 + M$	$1,0000 \cdot 10^{17}$	$0,0000 \cdot 10^{0}$	$2,9300 \cdot 10^{2}$
235	$p-C_3H_4 + H \rightleftharpoons CH_3 + C_2H_2$	$2,0000 \cdot 10^{13}$	$0,0000 \cdot 10^{0}$	$1,0000 \cdot 10^{1}$
236	$p-C_3H_4 + H \rightleftharpoons H_2 + C_3H_3$	$1,0000 \cdot 10^{12}$	$0,0000 \cdot 10^{0}$	$6,3000 \cdot 10^{0}$
237	$p-C_3H_4 + C_2H \rightleftharpoons C_2H_2 + C_3H_3$	$1,0000 \cdot 10^{13}$	$0,0000 \cdot 10^{0}$	$0,0000 \cdot 10^{0}$
238	$p-C_3H_4 + CH_3 \rightleftharpoons C_3H_3 + CH_4$	$2,0000 \cdot 10^{12}$	$0,0000 \cdot 10^{0}$	$3,2200 \cdot 10^{1}$

C$_3$H$_5$ reactions

No.	Reaction	Factor	Exponent	ΔE_A [kJ/mol]
239	$a-C_3H_5 \rightleftharpoons p-C_3H_4 + H$	$3,9800 \cdot 10^{13}$	$0,0000 \cdot 10^{0}$	$2,9310 \cdot 10^{2}$
240	$a-C_3H_5 + H \rightleftharpoons p-C_3H_4 + H_2$	$1,8060 \cdot 10^{13}$	$0,0000 \cdot 10^{0}$	$0,0000 \cdot 10^{0}$
241	$a-C_3H_5 + O_2 \rightleftharpoons p-C_3H_4 + HO_2$	$1,0230 \cdot 10^{12}$	$0,0000 \cdot 10^{0}$	$9,4780 \cdot 10^{1}$
242	$a-C_3H_5 + OH \rightleftharpoons p-C_3H_4 + H_2O$	$6,0230 \cdot 10^{12}$	$0,0000 \cdot 10^{0}$	$0,0000 \cdot 10^{0}$
243	$C_3H_6 + O_2 \rightleftharpoons a-C_3H_5 + HO_2$	$1,9000 \cdot 10^{12}$	$0,0000 \cdot 10^{0}$	$1,6380 \cdot 10^{2}$
244	$a-C_3H_5 + CH_3 \rightleftharpoons p-C_3H_4 + CH_4$	$3,6140 \cdot 10^{11}$	$0,0000 \cdot 10^{0}$	$0,0000 \cdot 10^{0}$
245	$a-C_3H_5 + a-C_3H_5 \rightleftharpoons C_3H_6 + p-C_3H_4$	$6,0230 \cdot 10^{10}$	$0,0000 \cdot 10^{0}$	$0,0000 \cdot 10^{0}$
246	$CH_3 + C_2H_2 \rightleftharpoons a-C_3H_5$	$6,0000 \cdot 10^{11}$	$0,0000 \cdot 10^{0}$	$3,2400 \cdot 10^{1}$

C$_3$H$_6$ reactions

No.	Reaction	Factor	Exponent	ΔE_A [kJ/mol]
247	$C_3H_6 \rightleftharpoons a-C_3H_5+H$	$1{,}0000 \cdot 10^{13}$	$0{,}0000 \cdot 10^0$	$3{,}2600 \cdot 10^2$
248	$C_3H_6 \rightleftharpoons C_2H_3+CH_3$	$1{,}1000 \cdot 10^{21}$	$-1{,}2000 \cdot 10^0$	$4{,}0880 \cdot 10^2$
249	$H+C_3H_6 \rightleftharpoons a-C_3H_5+H_2$	$5{,}0000 \cdot 10^{12}$	$0{,}0000 \cdot 10^0$	$6{,}3000 \cdot 10^0$
250	$C_3H_6+O \rightleftharpoons C_2H_4+CH_2O$	$5{,}9000 \cdot 10^{13}$	$0{,}0000 \cdot 10^0$	$2{,}1000 \cdot 10^1$
251	$C_3H_6+O \rightleftharpoons C_2H_5+HCO$	$3{,}6000 \cdot 10^{12}$	$0{,}0000 \cdot 10^0$	$0{,}0000 \cdot 10^0$
252	$C_3H_6+O \rightleftharpoons CH_3+CH_3CO$	$5{,}0000 \cdot 10^{12}$	$0{,}0000 \cdot 10^0$	$2{,}5000 \cdot 10^0$
253	$C_3H_6+OH \rightleftharpoons C_2H_5+CH_2O$	$7{,}9000 \cdot 10^{12}$	$0{,}0000 \cdot 10^0$	$0{,}0000 \cdot 10^0$
254	$C_3H_6+OH \rightleftharpoons CH_3+CH_3HCO$	$5{,}1000 \cdot 10^{12}$	$0{,}0000 \cdot 10^0$	$0{,}0000 \cdot 10^0$
255	$C_3H_6+OH \rightleftharpoons a-C_3H_5+H_2O$	$4{,}0000 \cdot 10^{12}$	$0{,}0000 \cdot 10^0$	$0{,}0000 \cdot 10^0$
256	$CH_3+C_3H_6 \rightleftharpoons CH_4+a-C_3H_5$	$8{,}9100 \cdot 10^{10}$	$0{,}0000 \cdot 10^0$	$3{,}5600 \cdot 10^1$
257	$C_3H_6+C_2H_5 \rightleftharpoons a-C_3H_5+C_2H_6$	$1{,}0000 \cdot 10^{11}$	$0{,}0000 \cdot 10^0$	$3{,}8500 \cdot 10^1$

n-C$_3$H$_7$ reactions

No.	Reaction	Factor	Exponent	ΔE_A [kJ/mol]
258	$n-C_3H_7 \rightleftharpoons CH_3+C_2H_4$	$9{,}6000 \cdot 10^{13}$	$0{,}0000 \cdot 10^0$	$1{,}2980 \cdot 10^2$
259	$n-C_3H_7 \rightleftharpoons H+C_3H_6$	$1{,}2500 \cdot 10^{14}$	$0{,}0000 \cdot 10^0$	$1{,}5490 \cdot 10^2$
260	$n-C_3H_7+O_2 \rightleftharpoons C_3H_6+HO_2$	$1{,}0000 \cdot 10^{12}$	$0{,}0000 \cdot 10^0$	$2{,}0900 \cdot 10^1$

iso-C$_3$H$_7$ reactions

No.	Reaction	Factor	Exponent	ΔE_A [kJ/mol]
261	iso $-$ C$_3$H$_7$ $\rightleftharpoons$ H $+$ C$_3$H$_6$	$6,3000 \cdot 10^{13}$	$0,0000 \cdot 10^0$	$1,5450 \cdot 10^2$
262	iso $-$ C$_3$H$_7$ $\rightleftharpoons$ CH$_3$ $+$ C$_2$H$_4$	$2,0000 \cdot 10^{10}$	$0,0000 \cdot 10^0$	$1,2350 \cdot 10^2$
263	iso $-$ C$_3$H$_7$ $+$ O$_2$ $\rightleftharpoons$ C$_3$H$_6$ $+$ HO$_2$	$1,9880 \cdot 10^{10}$	$0,0000 \cdot 10^0$	$-1,0725 \cdot 10^1$

C$_3$H$_8$ reactions

No.	Reaction	Factor	Exponent	ΔE_A [kJ/mol]
264	C$_3$H$_8$ $+$ M $\rightleftharpoons$ CH$_3$ $+$ C$_2$H$_5$ $+$ M	$4,0000 \cdot 10^{23}$	$-1,8700 \cdot 10^0$	$3,7741 \cdot 10^2$
265	H $+$ C$_3$H$_8$ $\rightleftharpoons$ H$_2$ $+$ n $-$ C$_3$H$_7$	$1,3000 \cdot 10^{14}$	$0,0000 \cdot 10^0$	$4,0600 \cdot 10^1$
266	H $+$ C$_3$H$_8$ $\rightleftharpoons$ H$_2$ $+$ iso $-$ C$_3$H$_7$	$1,0000 \cdot 10^{14}$	$0,0000 \cdot 10^0$	$3,4900 \cdot 10^1$
267	C$_3$H$_8$ $+$ O $\rightleftharpoons$ n $-$ C$_3$H$_7$ $+$ OH	$3,0000 \cdot 10^{13}$	$0,0000 \cdot 10^0$	$2,4100 \cdot 10^1$
268	C$_3$H$_8$ $+$ O $\rightleftharpoons$ iso $-$ C$_3$H$_7$ $+$ OH	$2,6000 \cdot 10^{13}$	$0,0000 \cdot 10^0$	$1,8700 \cdot 10^1$
269	C$_3$H$_8$ $+$ OH $\rightleftharpoons$ n $-$ C$_3$H$_7$ $+$ H$_2$O	$3,7000 \cdot 10^{12}$	$0,0000 \cdot 10^0$	$6,9000 \cdot 10^0$
270	C$_3$H$_8$ $+$ OH $\rightleftharpoons$ iso $-$ C$_3$H$_7$ $+$ H$_2$O	$2,8000 \cdot 10^{12}$	$0,0000 \cdot 10^0$	$3,6000 \cdot 10^0$
271	C$_3$H$_8$ $+$ HO$_2$ $\rightarrow$ n $-$ C$_3$H$_7$ $+$ H$_2$O$_2$	$1,1400 \cdot 10^{13}$	$0,0000 \cdot 10^0$	$8,1200 \cdot 10^1$
272	n $-$ C$_3$H$_7$ $+$ H$_2$O$_2$ $\rightarrow$ C$_3$H$_8$ $+$ HO$_2$	$2,3300 \cdot 10^{12}$	$0,0000 \cdot 10^0$	$4,1100 \cdot 10^1$
273	C$_3$H$_8$ $+$ HO$_2$ $\rightarrow$ iso $-$ C$_3$H$_7$ $+$ H$_2$O$_2$	$3,4000 \cdot 10^{12}$	$0,0000 \cdot 10^0$	$7,1200 \cdot 10^1$
274	iso $-$ C$_3$H$_7$ $+$ H$_2$O$_2$ $\rightarrow$ C$_3$H$_8$ $+$ HO$_2$	$4,1600 \cdot 10^{11}$	$0,0000 \cdot 10^0$	$3,1100 \cdot 10^1$
275	CH$_3$ $+$ C$_3$H$_8$ $\rightarrow$ CH$_4$ $+$ n $-$ C$_3$H$_7$	$4,0000 \cdot 10^{11}$	$0,0000 \cdot 10^0$	$3,9800 \cdot 10^1$
276	CH$_4$ $+$ n $-$ C$_3$H$_7$ $\rightarrow$ CH$_3$ $+$ C$_3$H$_8$	$3,1200 \cdot 10^{12}$	$0,0000 \cdot 10^0$	$6,8900 \cdot 10^1$

No.	Reaction	Factor	Exponent	ΔE_A [kJ/mol]
277	$CH_3 + C_3H_8 \rightarrow CH_4 + iso-C_3H_7$	$1,3000 \cdot 10^{12}$	$0,0000 \cdot 10^{0}$	$4,8600 \cdot 10^{1}$
278	$CH_4 + iso-C_3H_7 \rightarrow CH_3 + C_3H_8$	$1,0100 \cdot 10^{13}$	$0,0000 \cdot 10^{0}$	$7,7700 \cdot 10^{1}$
279	$C_3H_8 + O_2 \rightarrow n-C_3H_7 + HO_2$	$2,5200 \cdot 10^{13}$	$0,0000 \cdot 10^{0}$	$2,0520 \cdot 10^{2}$
280	$n-C_3H_7 + HO_2 \rightarrow C_3H_8 + O_2$	$2,0800 \cdot 10^{12}$	$0,0000 \cdot 10^{0}$	$0,0000 \cdot 10^{0}$
281	$C_3H_8 + O_2 \rightarrow iso-C_3H_7 + HO_2$	$2,0000 \cdot 10^{13}$	$0,0000 \cdot 10^{0}$	$1,9930 \cdot 10^{2}$
282	$iso-C_3H_7 + HO_2 \rightarrow C_3H_8 + O_2$	$2,0800 \cdot 10^{12}$	$0,0000 \cdot 10^{0}$	$0,0000 \cdot 10^{0}$
283	$C_3H_8 + CH_3O \rightarrow n-C_3H_7 + CH_3OH$	$3,0000 \cdot 10^{11}$	$0,0000 \cdot 10^{0}$	$2,9300 \cdot 10^{1}$
284	$n-C_3H_7 + CH_3OH \rightarrow C_3H_8 + CH_3O$	$1,2200 \cdot 10^{10}$	$0,0000 \cdot 10^{0}$	$3,8500 \cdot 10^{1}$
285	$C_3H_8 + CH_3O \rightarrow iso-C_3H_7 + CH_3OH$	$3,0000 \cdot 10^{11}$	$0,0000 \cdot 10^{0}$	$2,9300 \cdot 10^{1}$
286	$iso-C_3H_7 + CH_3OH \rightarrow C_3H_8 + CH_3O$	$1,2200 \cdot 10^{10}$	$0,0000 \cdot 10^{0}$	$3,8500 \cdot 10^{1}$

C_4H_2 reactions

No.	Reaction	Factor	Exponent	ΔE_A [kJ/mol]
287	$C_4H_2 + O \rightleftharpoons C_3H_2 + CO$	$7,8900 \cdot 10^{12}$	$0,0000 \cdot 10^{0}$	$5,6400 \cdot 10^{0}$
288	$C_4H_2 + OH \rightleftharpoons C_3H_2 + HCO$	$6,6800 \cdot 10^{12}$	$0,0000 \cdot 10^{0}$	$-1,7100 \cdot 10^{0}$

C_4H_6 reactions

No.	Reaction	Factor	Exponent	ΔE_A [kJ/mol]
287	$C_4H_6 \rightleftharpoons C_2H_3 + C_2H_3$	$4,0300 \cdot 10^{19}$	$-1,0000 \cdot 10^{0}$	$4,1100 \cdot 10^{2}$
288	$C_2H_3 + C_2H_4 \rightleftharpoons C_4H_6 + H$	$7,8300 \cdot 10^{10}$	$0,0000 \cdot 10^{0}$	$0,0000 \cdot 10^{0}$

No.	Reaction	Factor	Exponent	ΔE_A [kJ/mol]
289	$C_4H_6 + O \rightleftharpoons C_2H_4 + CH_2CO$	$1,0000 \cdot 10^{12}$	$0,0000 \cdot 10^{0}$	$0,0000 \cdot 10^{0}$
290	$C_4H_6 + O \rightleftharpoons CH_2O + p - C_3H_4$	$1,0000 \cdot 10^{12}$	$0,0000 \cdot 10^{0}$	$0,0000 \cdot 10^{0}$
291	$C_4H_6 + OH \rightleftharpoons C_2H_5 + CH_2CO$	$1,0000 \cdot 10^{12}$	$0,0000 \cdot 10^{0}$	$0,0000 \cdot 10^{0}$
292	$C_4H_6 + OH \rightleftharpoons CH_2O + a - C_3H_5$	$2,0000 \cdot 10^{12}$	$0,0000 \cdot 10^{0}$	$0,0000 \cdot 10^{0}$
293	$C_4H_6 + OH \rightleftharpoons C_2H_3 + CH_3HCO$	$5,0000 \cdot 10^{12}$	$0,0000 \cdot 10^{0}$	$0,0000 \cdot 10^{0}$

C_4H_7 reactions

No.	Reaction	Factor	Exponent	ΔE_A [kJ/mol]
294	$C_4H_7 \rightleftharpoons C_4H_6 + H$	$1,2000 \cdot 10^{14}$	$0,0000 \cdot 10^{0}$	$2,0640 \cdot 10^{2}$
295	$C_4H_7 \rightleftharpoons C_2H_4 + C_2H_3$	$1,0000 \cdot 10^{11}$	$0,0000 \cdot 10^{0}$	$1,5490 \cdot 10^{2}$
296	$H + C_4H_7 \rightleftharpoons C_4H_6 + H_2$	$3,1600 \cdot 10^{12}$	$0,0000 \cdot 10^{0}$	$0,0000 \cdot 10^{0}$
297	$C_4H_7 + O_2 \rightleftharpoons C_4H_6 + HO_2$	$1,0000 \cdot 10^{11}$	$0,0000 \cdot 10^{0}$	$0,0000 \cdot 10^{0}$
298	$C_4H_7 + C_4H_7 \rightleftharpoons C_4H_6 + 1 - C_4H_8$	$3,1600 \cdot 10^{12}$	$0,0000 \cdot 10^{0}$	$0,0000 \cdot 10^{0}$
299	$C_4H_7 + CH_3 \rightleftharpoons C_4H_6 + CH_4$	$1,0000 \cdot 10^{13}$	$0,0000 \cdot 10^{0}$	$0,0000 \cdot 10^{0}$
300	$C_4H_7 + C_2H_3 \rightleftharpoons C_4H_6 + C_2H_4$	$4,0000 \cdot 10^{12}$	$0,0000 \cdot 10^{0}$	$0,0000 \cdot 10^{0}$
301	$C_4H_7 + C_2H_5 \rightleftharpoons C_4H_6 + C_2H_6$	$4,0000 \cdot 10^{12}$	$0,0000 \cdot 10^{0}$	$0,0000 \cdot 10^{0}$
302	$C_4H_7 + C_2H_5 \rightleftharpoons 1 - C_4H_8 + C_2H_4$	$5,0000 \cdot 10^{11}$	$0,0000 \cdot 10^{0}$	$0,0000 \cdot 10^{0}$
303	$C_4H_7 + C_2H_5 \rightleftharpoons 2 - C_4H_8 + C_2H_4$	$5,0000 \cdot 10^{11}$	$0,0000 \cdot 10^{0}$	$0,0000 \cdot 10^{0}$
304	$C_4H_7 + C_2H_5 \rightleftharpoons C - 2 - C_4H_8 + C_2H_4$	$5,0000 \cdot 10^{11}$	$0,0000 \cdot 10^{0}$	$0,0000 \cdot 10^{0}$
305	$C_4H_7 + a - C_3H_5 \rightleftharpoons C_4H_6 + C_3H_6$	$4,0000 \cdot 10^{13}$	$0,0000 \cdot 10^{0}$	$0,0000 \cdot 10^{0}$

1-C₄H₈ reactions

No.	Reaction	Factor	Exponent	ΔE_A [kJ/mol]
306	$1-C_4H_8 \rightleftharpoons 2-C_4H_8$	$4,0000 \cdot 10^{11}$	$0,0000 \cdot 10^0$	$2,5100 \cdot 10^2$
307	$1-C_4H_8 \rightleftharpoons C-2-C_4H_8$	$4,0000 \cdot 10^{11}$	$0,0000 \cdot 10^0$	$2,5100 \cdot 10^2$
308	$1-C_4H_8 \rightleftharpoons a-C_3H_5+CH_3$	$8,0000 \cdot 10^{16}$	$0,0000 \cdot 10^0$	$3,0740 \cdot 10^2$
309	$1-C_4H_8 \rightleftharpoons C_2H_3+C_2H_5$	$2,0000 \cdot 10^{18}$	$-1,0000 \cdot 10^0$	$4,0520 \cdot 10^2$
310	$1-C_4H_8 \rightleftharpoons H+C_4H_7$	$4,1100 \cdot 10^{18}$	$-1,0000 \cdot 10^0$	$4,0770 \cdot 10^2$
311	$1-C_4H_8+H \rightleftharpoons C_4H_7+H_2$	$5,0000 \cdot 10^{13}$	$0,0000 \cdot 10^0$	$1,6300 \cdot 10^1$
312	$1-C_4H_8+O \rightleftharpoons CH_3HCO+C_2H_4$	$1,2550 \cdot 10^{12}$	$0,0000 \cdot 10^0$	$3,6000 \cdot 10^0$
313	$1-C_4H_8+O \rightleftharpoons CH_3+C_2H_5+CO$	$1,6250 \cdot 10^{13}$	$0,0000 \cdot 10^0$	$3,6000 \cdot 10^0$
314	$1-C_4H_8+O \rightleftharpoons C_3H_6+CH_2O$	$2,5050 \cdot 10^{12}$	$0,0000 \cdot 10^0$	$0,0000 \cdot 10^0$
315	$1-C_4H_8+O \rightleftharpoons C_4H_7+OH$	$1,3000 \cdot 10^{13}$	$0,0000 \cdot 10^0$	$1,8800 \cdot 10^1$
316	$1-C_4H_8+OH \rightleftharpoons CH_3HCO+C_2H_5$	$1,0000 \cdot 10^{11}$	$0,0000 \cdot 10^0$	$0,0000 \cdot 10^0$
317	$1-C_4H_8+OH \rightleftharpoons CH_3+C_2H_6+CO$	$1,0000 \cdot 10^{10}$	$0,0000 \cdot 10^0$	$0,0000 \cdot 10^0$
318	$1-C_4H_8+OH \rightleftharpoons n-C_3H_7+CH_2O$	$6,5000 \cdot 10^{12}$	$0,0000 \cdot 10^0$	$0,0000 \cdot 10^0$
319	$1-C_4H_8+OH \rightleftharpoons C_4H_7+H_2O$	$1,7500 \cdot 10^{13}$	$0,0000 \cdot 10^0$	$2,9100 \cdot 10^1$
320	$1-C_4H_8+CH_3 \rightleftharpoons C_4H_7+CH_4$	$1,0000 \cdot 10^{11}$	$0,0000 \cdot 10^0$	$3,0600 \cdot 10^1$
321	$1-C_4H_8+O_2 \rightleftharpoons C_4H_7+HO_2$	$4,0000 \cdot 10^{12}$	$0,0000 \cdot 10^0$	$1,6740 \cdot 10^2$
322	$1-C_4H_8+HO_2 \rightleftharpoons C_4H_7+H_2O_2$	$1,0000 \cdot 10^{11}$	$0,0000 \cdot 10^0$	$7,1400 \cdot 10^1$
323	$1-C_4H_8+C_2H_5 \rightleftharpoons C_4H_7+C_2H_6$	$1,0000 \cdot 10^{11}$	$0,0000 \cdot 10^0$	$3,3500 \cdot 10^1$
324	$1-C_4H_8+a-C_3H_5 \rightleftharpoons C_4H_7+C_3H_6$	$8,0000 \cdot 10^{10}$	$0,0000 \cdot 10^0$	$5,1900 \cdot 10^1$
325	$1-C_4H_8+C_4H_7 \rightleftharpoons C_4H_7+2-C_4H_8$	$3,9800 \cdot 10^{10}$	$0,0000 \cdot 10^0$	$5,1900 \cdot 10^1$
326	$1-C_4H_8+C_4H_7 \rightleftharpoons C_4H_7+C-2-C_4H_8$	$3,9800 \cdot 10^{10}$	$0,0000 \cdot 10^0$	$5,1900 \cdot 10^1$

2-C$_4$H$_8$ reactions

No.	Reaction	Factor	Exponent	ΔE_A [kJ/mol]
327	$2-C_4H_8 \rightleftharpoons H + C_4H_7$	$4,1100 \cdot 10^{18}$	$-1,0000 \cdot 10^{0}$	$4,0770 \cdot 10^{2}$
328	$2-C_4H_8 \rightleftharpoons CH_3 + a - C_3H_5$	$6,5000 \cdot 10^{14}$	$0,0000 \cdot 10^{0}$	$2,9830 \cdot 10^{2}$
329	$2-C_4H_8 + H \rightleftharpoons C_4H_7 + H_2$	$5,0000 \cdot 10^{12}$	$0,0000 \cdot 10^{0}$	$1,4600 \cdot 10^{1}$
330	$2-C_4H_8 + O \rightleftharpoons C_2H_4 + CH_3HCO$	$1,0000 \cdot 10^{12}$	$0,0000 \cdot 10^{0}$	$0,0000 \cdot 10^{0}$
331	$2-C_4H_8 + O \rightleftharpoons iso - C_3H_7 + HCO$	$6,0300 \cdot 10^{12}$	$0,0000 \cdot 10^{0}$	$0,0000 \cdot 10^{0}$
332	$2-C_4H_8 + OH \rightleftharpoons C_4H_7 + H_2O$	$1,0100 \cdot 10^{14}$	$0,0000 \cdot 10^{0}$	$1,2800 \cdot 10^{1}$
333	$2-C_4H_8 + OH \rightleftharpoons C_2H_5 + CH_3HCO$	$1,5140 \cdot 10^{13}$	$0,0000 \cdot 10^{0}$	$0,0000 \cdot 10^{0}$
334	$2-C_4H_8 + CH_3 \rightleftharpoons C_4H_7 + CH_4$	$1,0000 \cdot 10^{11}$	$0,0000 \cdot 10^{0}$	$3,4300 \cdot 10^{1}$

C-2-C$_4$H$_8$ reactions

No.	Reaction	Factor	Exponent	ΔE_A [kJ/mol]
335	$C-2-C_4H_8 \rightleftharpoons 2 - C_4H_8$	$1,0000 \cdot 10^{13}$	$0,0000 \cdot 10^{0}$	$2,5940 \cdot 10^{2}$
336	$C-2-C_4H_8 \rightleftharpoons C_4H_6 + H_2$	$1,0000 \cdot 10^{13}$	$0,0000 \cdot 10^{0}$	$2,7410 \cdot 10^{2}$
337	$C-2-C_4H_8 \rightleftharpoons C_4H_7 + H$	$4,0740 \cdot 10^{18}$	$-1,0000 \cdot 10^{0}$	$4,0730 \cdot 10^{2}$
338	$C-2-C_4H_8 \rightleftharpoons a - C_3H_5 + CH_3$	$1,2540 \cdot 10^{15}$	$0,0000 \cdot 10^{0}$	$2,9830 \cdot 10^{2}$
339	$C-2-C_4H_8 + H \rightleftharpoons C_4H_7 + H_2$	$1,0000 \cdot 10^{12}$	$0,0000 \cdot 10^{0}$	$1,4600 \cdot 10^{1}$
340	$C-2-C_4H_8 + OH \rightleftharpoons C_4H_7 + H_2O$	$1,2550 \cdot 10^{14}$	$0,0000 \cdot 10^{0}$	$1,2800 \cdot 10^{1}$
341	$C-2-C_4H_8 + OH \rightleftharpoons C_2H_5 + CH_3HCO$	$1,4000 \cdot 10^{13}$	$0,0000 \cdot 10^{0}$	$0,0000 \cdot 10^{0}$
342	$C-2-C_4H_8 + O \rightleftharpoons iso - C_3H_7 + HCO$	$6,0300 \cdot 10^{12}$	$0,0000 \cdot 10^{0}$	$0,0000 \cdot 10^{0}$

| 343 | $C-2-C_4H_8 + O \rightleftharpoons C_2H_4 + CH_3HCO$ | $1,0000 \cdot 10^{12}$ | $0,0000 \cdot 10^0$ | $0,0000 \cdot 10^0$ |
| 344 | $C-2-C_4H_8 + CH_3 \rightleftharpoons C_4H_7 + CH_4$ | $1,0000 \cdot 10^{11}$ | $0,0000 \cdot 10^0$ | $3,4300 \cdot 10^1$ |

p-C$_4$H$_9$ reactions

No.	Reaction	Factor	Exponent	ΔE_A [kJ/mol]
345	$p-C_4H_9 \rightleftharpoons C_2H_5 + C_2H_4$	$2,5000 \cdot 10^{13}$	$0,0000 \cdot 10^0$	$1,2060 \cdot 10^2$
346	$p-C_4H_9 \rightleftharpoons 1-C_4H_8 + H$	$1,2600 \cdot 10^{13}$	$0,0000 \cdot 10^0$	$1,6160 \cdot 10^2$
347	$p-C_4H_9 + O_2 \rightleftharpoons 1-C_4H_8 + HO_2$	$1,0000 \cdot 10^{12}$	$0,0000 \cdot 10^0$	$8,4000 \cdot 10^0$

s-C$_4$H$_9$ reactions

No.	Reaction	Factor	Exponent	ΔE_A [kJ/mol]
348	$s-C_4H_9 \rightleftharpoons 1-C_4H_8 + H$	$2,0000 \cdot 10^{13}$	$0,0000 \cdot 10^0$	$1,6920 \cdot 10^2$
349	$s-C_4H_9 \rightleftharpoons 2-C_4H_8 + H$	$5,0000 \cdot 10^{13}$	$0,0000 \cdot 10^0$	$1,5870 \cdot 10^2$
350	$s-C_4H_9 \rightleftharpoons C-2-C_4H_8 + H$	$5,0000 \cdot 10^{13}$	$0,0000 \cdot 10^0$	$1,5870 \cdot 10^2$
351	$s-C_4H_9 \rightleftharpoons C_3H_6 + CH_3$	$4,0000 \cdot 10^{14}$	$0,0000 \cdot 10^0$	$1,3900 \cdot 10^2$
352	$s-C_4H_9 + O_2 \rightleftharpoons 1-C_4H_8 + HO_2$	$2,0000 \cdot 10^{12}$	$0,0000 \cdot 10^0$	$1,8800 \cdot 10^1$
353	$s-C_4H_9 + O_2 \rightleftharpoons 2-C_4H_8 + HO_2$	$2,0000 \cdot 10^{13}$	$0,0000 \cdot 10^0$	$1,7800 \cdot 10^1$
354	$s-C_4H_9 + O_2 \rightleftharpoons C-2-C_4H_8 + HO_2$	$2,0000 \cdot 10^{13}$	$0,0000 \cdot 10^0$	$1,7800 \cdot 10^1$

C$_4$H$_{10}$ reactions

No.	Reaction	Factor	Exponent	ΔE_A [kJ/mol]
355	$C_2H_5 + C_2H_5 \rightleftharpoons C_4H_{10}$	$8,0000 \cdot 10^{12}$	$0,0000 \cdot 10^0$	$0,0000 \cdot 10^0$
356	$C_4H_{10} \rightarrow n - C_3H_7 + CH_3$	$1,0000 \cdot 10^{17}$	$0,0000 \cdot 10^0$	$3,5760 \cdot 10^2$
357	$n - C_3H_7 + CH_3 \rightarrow C_4H_{10}$	$2,0000 \cdot 10^{13}$	$0,0000 \cdot 10^0$	$0,0000 \cdot 10^0$
358	$C_4H_{10} + H \rightarrow p - C_4H_9 + H_2$	$5,6300 \cdot 10^7$	$2,0000 \cdot 10^0$	$3,2200 \cdot 10^1$
359	$p - C_4H_9 + H_2 \rightarrow C_4H_{10} + H$	$9,1200 \cdot 10^{12}$	$0,0000 \cdot 10^0$	$6,0600 \cdot 10^1$
360	$C_4H_{10} + H \rightarrow s - C_4H_9 + H_2$	$1,7500 \cdot 10^7$	$2,0000 \cdot 10^0$	$2,0900 \cdot 10^1$
361	$s - C_4H_9 + H_2 \rightarrow C_4H_{10} + H$	$1,5400 \cdot 10^{13}$	$0,0000 \cdot 10^0$	$6,5000 \cdot 10^1$
362	$C_4H_{10} + O \rightarrow p - C_4H_9 + OH$	$1,1300 \cdot 10^{14}$	$0,0000 \cdot 10^0$	$3,2900 \cdot 10^1$
363	$p - C_4H_9 + OH \rightarrow C_4H_{10} + O$	$1,4800 \cdot 10^{13}$	$0,0000 \cdot 10^0$	$5,1300 \cdot 10^1$
364	$C_4H_{10} + O \rightarrow s - C_4H_9 + OH$	$5,6200 \cdot 10^{13}$	$0,0000 \cdot 10^0$	$2,1800 \cdot 10^1$
365	$s - C_4H_9 + OH \rightarrow C_4H_{10} + O$	$7,3500 \cdot 10^{12}$	$0,0000 \cdot 10^0$	$4,0200 \cdot 10^1$
366	$C_4H_{10} + OH \rightarrow p - C_4H_9 + H_2O$	$4,1300 \cdot 10^7$	$1,7000 \cdot 10^0$	$3,2000 \cdot 10^0$
367	$p - C_4H_9 + H_2O \rightarrow C_4H_{10} + OH$	$7,1700 \cdot 10^7$	$1,7000 \cdot 10^0$	$9,3300 \cdot 10^1$
368	$C_4H_{10} + OH \rightarrow s - C_4H_9 + H_2O$	$7,2300 \cdot 10^7$	$1,6000 \cdot 10^0$	$-1,0000 \cdot 10^0$
369	$s - C_4H_9 + H_2O \rightarrow C_4H_{10} + OH$	$1,2800 \cdot 10^8$	$1,6000 \cdot 10^0$	$8,9100 \cdot 10^1$
370	$C_4H_{10} + HO_2 \rightarrow p - C_4H_9 + H_2O_2$	$1,1400 \cdot 10^{13}$	$0,0000 \cdot 10^0$	$8,1200 \cdot 10^1$
371	$p - C_4H_9 + H_2O_2 \rightarrow C_4H_{10} + HO_2$	$4,5800 \cdot 10^{12}$	$0,0000 \cdot 10^0$	$4,1100 \cdot 10^1$
372	$C_4H_{10} + HO_2 \rightarrow s - C_4H_9 + H_2O_2$	$6,8000 \cdot 10^{12}$	$0,0000 \cdot 10^0$	$7,1200 \cdot 10^1$
373	$s - C_4H_9 + H_2O_2 \rightarrow C_4H_{10} + HO_2$	$1,6300 \cdot 10^{12}$	$0,0000 \cdot 10^0$	$3,1000 \cdot 10^1$
374	$C_4H_{10} + CH_3 \rightarrow p - C_4H_9 + CH_4$	$1,3000 \cdot 10^{12}$	$0,0000 \cdot 10^0$	$4,8600 \cdot 10^1$
375	$p - C_4H_9 + CH_4 \rightarrow C_4H_{10} + CH_3$	$1,0100 \cdot 10^{13}$	$0,0000 \cdot 10^0$	$7,7700 \cdot 10^1$

No.	Reaction	Factor	Exponent	ΔE_A [kJ/mol]
376	$C_4H_{10} + CH_3 \rightarrow s-C_4H_9 + CH_4$	$8,0000 \cdot 10^{11}$	$0,0000 \cdot 10^0$	$3,9800 \cdot 10^1$
377	$s-C_4H_9 + CH_4 \rightarrow C_4H_{10} + CH_3$	$6,2400 \cdot 10^{12}$	$0,0000 \cdot 10^0$	$6,8900 \cdot 10^1$
378	$C_4H_{10} + O_2 \rightarrow p-C_4H_9 + HO_2$	$2,5000 \cdot 10^{13}$	$0,0000 \cdot 10^0$	$2,0520 \cdot 10^2$
379	$p-C_4H_9 + HO_2 \rightarrow C_4H_{10} + O_2$	$2,5000 \cdot 10^{12}$	$0,0000 \cdot 10^0$	$-9,2000 \cdot 10^0$
380	$C_4H_{10} + O_2 \rightarrow s-C_4H_9 + HO_2$	$4,0000 \cdot 10^{13}$	$0,0000 \cdot 10^0$	$1,9930 \cdot 10^2$
381	$s-C_4H_9 + HO_2 \rightarrow C_4H_{10} + O_2$	$4,0700 \cdot 10^{12}$	$0,0000 \cdot 10^0$	$-1,5200 \cdot 10^1$
382	$C_4H_{10} + CH_3O \rightarrow p-C_4H_9 + CH_3OH$	$3,0000 \cdot 10^{11}$	$0,0000 \cdot 10^0$	$2,9300 \cdot 10^1$
383	$p-C_4H_9 + CH_3OH \rightarrow C_4H_{10} + CH_3O$	$1,2200 \cdot 10^{10}$	$0,0000 \cdot 10^0$	$2,0940 \cdot 10^2$
384	$C_4H_{10} + CH_3O \rightarrow s-C_4H_9 + CH_3OH$	$6,0000 \cdot 10^{11}$	$0,0000 \cdot 10^0$	$2,9300 \cdot 10^1$
385	$s-C_4H_9 + CH_3OH \rightarrow C_4H_{10} + CH_3O$	$2,4400 \cdot 10^{10}$	$0,0000 \cdot 10^0$	$2,0940 \cdot 10^2$

iso-C_4H_7 reactions

No.	Reaction	Factor	Exponent	ΔE_A [kJ/mol]
386	$iso-C_4H_7 \rightleftharpoons p-C_3H_4 + CH_3$	$1,0000 \cdot 10^{13}$	$0,0000 \cdot 10^0$	$2,1360 \cdot 10^2$

iso-C_4H_8 reactions

No.	Reaction	Factor	Exponent	ΔE_A [kJ/mol]
387	$iso-C_4H_8 \rightleftharpoons a-C_3H_5 + CH_3$	$5,0000 \cdot 10^{18}$	$-1,0000 \cdot 10^0$	$3,0740 \cdot 10^2$
388	$iso-C_4H_8 \rightleftharpoons iso-C_4H_7 + H$	$1,0000 \cdot 10^{17}$	$0,0000 \cdot 10^0$	$3,6850 \cdot 10^2$
389	$iso-C_4H_8 + H \rightleftharpoons iso-C_4H_7 + H_2$	$1,0000 \cdot 10^{13}$	$0,0000 \cdot 10^0$	$1,5900 \cdot 10^1$

No.	Reaction	Factor	Exponent	ΔE_A [kJ/mol]
390	$iso-C_4H_8+O \rightleftharpoons iso-C_4H_7+OH$	$2,5000 \cdot 10^5$	$2,6000 \cdot 10^0$	$-4,7000 \cdot 10^0$
391	$iso-C_4H_8+O \rightleftharpoons iso-C_3H_7+HCO$	$7,2300 \cdot 10^5$	$2,3000 \cdot 10^0$	$-4,4000 \cdot 10^0$
392	$iso-C_4H_8+OH \rightleftharpoons iso-C_4H_7+H_2O$	$9,6000 \cdot 10^{12}$	$0,0000 \cdot 10^0$	$5,2000 \cdot 10^0$
393	$iso-C_4H_8+OH \rightleftharpoons iso-C_3H_7+CH_2O$	$1,5000 \cdot 10^{12}$	$0,0000 \cdot 10^0$	$0,0000 \cdot 10^0$
394	$iso-C_4H_8+CH_3 \rightleftharpoons iso-C_4H_7+CH_4$	$6,0300 \cdot 10^{11}$	$0,0000 \cdot 10^0$	$3,7230 \cdot 10^1$

iso-C_4H_9 reactions

No.	Reaction	Factor	Exponent	ΔE_A [kJ/mol]
395	$iso-C_4H_9 \rightleftharpoons C_3H_6+CH_3$	$2,0000 \cdot 10^{13}$	$0,0000 \cdot 10^0$	$1,2534 \cdot 10^2$
396	$iso-C_4H_9 \rightleftharpoons iso-C_4H_8+H$	$1,0000 \cdot 10^{14}$	$0,0000 \cdot 10^0$	$1,5188 \cdot 10^2$
397	$iso-C_4H_9+O_2 \rightleftharpoons iso-C_4H_8+HO_2$	$2,4100 \cdot 10^{10}$	$0,0000 \cdot 10^0$	$0,0000 \cdot 10^0$

tert-C_4H_9 reactions

No.	Reaction	Factor	Exponent	ΔE_A [kJ/mol]
398	$tert-C_4H_9 \rightleftharpoons H+iso-C_4H_8$	$8,3000 \cdot 10^{13}$	$0,0000 \cdot 10^0$	$1,5963 \cdot 10^2$
399	$tert-C_4H_9 \rightleftharpoons C_3H_6+CH_3$	$1,0000 \cdot 10^{16}$	$0,0000 \cdot 10^0$	$1,9300 \cdot 10^2$
400	$tert-C_4H_9+O_2 \rightleftharpoons iso-C_4H_8+HO_2$	$6,0230 \cdot 10^{10}$	$0,0000 \cdot 10^0$	$-1,3219 \cdot 10^1$
401	$tert-C_4H_9+tert-C_4H_9 \rightleftharpoons iso-C_4H_{10} + iso-C_4H_8$	$7,2270 \cdot 10^{16}$	$-1,7300 \cdot 10^0$	$0,0000 \cdot 10^0$

iso-C_4H_{10} reactions

No.	Reaction	Factor	Exponent	ΔE_A [kJ/mol]
402	iso $-$ $C_4H_{10} \rightleftharpoons CH_3 +$ iso $-$ C_3H_7	$1,1000 \cdot 10^{26}$	$-2,6100 \cdot 10^{0}$	$3,7799 \cdot 10^{2}$
403	iso $-$ $C_4H_{10} \rightleftharpoons$ tert $-$ $C_4H_9 +$ H	$1,0000 \cdot 10^{15}$	$0,0000 \cdot 10^{0}$	$3,9070 \cdot 10^{2}$
404	iso $-$ $C_4H_{10} \rightleftharpoons$ iso $-$ $C_4H_9 +$ H	$1,0000 \cdot 10^{15}$	$0,0000 \cdot 10^{0}$	$4,1040 \cdot 10^{2}$
405	iso $-$ $C_4H_{10} +$ H $\rightleftharpoons$ tert $-$ $C_4H_9 + H_2$	$6,0200 \cdot 10^{5}$	$2,4000 \cdot 10^{0}$	$1,0810 \cdot 10^{1}$
406	iso $-$ $C_4H_{10} +$ H $\rightleftharpoons$ iso $-$ $C_4H_9 + H_2$	$1,8100 \cdot 10^{6}$	$2,5400 \cdot 10^{0}$	$2,8270 \cdot 10^{1}$
407	iso $-$ $C_4H_{10} +$ O $\rightleftharpoons$ tert $-$ $C_4H_9 +$ OH	$1,5600 \cdot 10^{5}$	$2,5000 \cdot 10^{0}$	$4,6600 \cdot 10^{0}$
408	iso $-$ $C_4H_{10} +$ O $\rightleftharpoons$ iso $-$ $C_4H_9 +$ OH	$4,2800 \cdot 10^{5}$	$2,5000 \cdot 10^{0}$	$1,5250 \cdot 10^{1}$
409	iso $-$ $C_4H_{10} +$ OH $\rightleftharpoons$ tert $-$ $C_4H_9 + H_2O$	$5,7300 \cdot 10^{10}$	$5,1000 \cdot 10^{-1}$	$2,7000 \cdot 10^{-1}$
410	iso $-$ $C_4H_{10} +$ OH $\rightleftharpoons$ iso $-$ $C_4H_9 + H_2O$	$2,2900 \cdot 10^{8}$	$1,5300 \cdot 10^{0}$	$3,2400 \cdot 10^{0}$
411	iso $-$ $C_4H_{10} + HO_2 \rightleftharpoons$ iso $-$ $C_4H_9 + H_2O_2$	$3,0100 \cdot 10^{4}$	$2,5500 \cdot 10^{0}$	$6,4850 \cdot 10^{1}$
412	iso $-$ $C_4H_{10} + HO_2 \rightleftharpoons$ tert $-$ $C_4H_9 + H_2O_2$	$3,6100 \cdot 10^{3}$	$2,5500 \cdot 10^{0}$	$4,4070 \cdot 10^{1}$
413	iso $-$ $C_4H_{10} + CH_3 \rightleftharpoons$ tert $-$ $C_4H_9 + CH_4$	$9,0400 \cdot 10^{-1}$	$3,4600 \cdot 10^{0}$	$1,9240 \cdot 10^{1}$
414	iso $-$ $C_4H_{10} + CH_3 \rightleftharpoons$ iso $-$ $C_4H_9 + CH_4$	$1,3600 \cdot 10^{0}$	$3,6500 \cdot 10^{0}$	$2,9900 \cdot 10^{1}$
415	iso $-$ $C_4H_{10} + O_2 \rightleftharpoons$ iso $-$ $C_4H_9 + HO_2$	$4,0400 \cdot 10^{13}$	$0,0000 \cdot 10^{0}$	$2,1310 \cdot 10^{2}$
416	iso $-$ $C_4H_{10} + O_2 \rightleftharpoons$ tert $-$ $C_4H_9 + HO_2$	$3,9700 \cdot 10^{13}$	$0,0000 \cdot 10^{0}$	$1,8408 \cdot 10^{2}$
417	iso $-$ $C_4H_{10} + CH_3O_2 \rightleftharpoons$ iso $-$ $C_4H_9 + CH_3O_2H$	$3,0100 \cdot 10^{4}$	$2,5500 \cdot 10^{0}$	$6,4850 \cdot 10^{1}$
418	iso $-$ $C_4H_{10} + CH_3O_2 \rightleftharpoons$ tert $-$ $C_4H_9 + CH_3O_2H$	$3,6100 \cdot 10^{3}$	$2,5500 \cdot 10^{0}$	$4,4070 \cdot 10^{1}$

OH* formation reactions

No.	Reaction	Factor	Exponent	ΔE_A [kJ/mol]
419	$CH+O_2 \rightarrow CO+OH*$	$3,2400 \cdot 10^{14}$	$-0,4000 \cdot 10^{0}$	$1,7000 \cdot 10^{1}$
420	$HCO+O \rightarrow CO+OH*$	$2,8900 \cdot 10^{11}$	$0,0000 \cdot 10^{0}$	$1,9300 \cdot 10^{0}$
421	$H+O+M \rightarrow OH*+M$	$1,2000 \cdot 10^{13}$	$0,0000 \cdot 10^{0}$	$2,9000 \cdot 10^{1}$

OH* deactivation reactions

No.	Reaction	Factor	Exponent	ΔE_A [kJ/mol]
422	$OH* \rightarrow OH$	$1,4500 \cdot 10^{6}$	$0,0000 \cdot 10^{0}$	$0,0000 \cdot 10^{0}$
423	$OH*+O_2 \rightarrow OH+O_2$	$2,1000 \cdot 10^{12}$	$5,0000 \cdot 10^{-1}$	$-2,0200 \cdot 10^{0}$
424	$OH*+H_2O \rightarrow OH+H_2O$	$5,9300 \cdot 10^{12}$	$5,0000 \cdot 10^{-1}$	$-3,6100 \cdot 10^{0}$
425	$OH*+H_2 \rightarrow OH+H_2$	$2,9500 \cdot 10^{12}$	$5,0000 \cdot 10^{-1}$	$-1,8600 \cdot 10^{0}$
426	$OH*+CO_2 \rightarrow OH+CO_2$	$2,7600 \cdot 10^{12}$	$5,0000 \cdot 10^{-1}$	$-4,0600 \cdot 10^{0}$
427	$OH*+CO \rightarrow OH+CO$	$3,2300 \cdot 10^{12}$	$5,0000 \cdot 10^{-1}$	$-3,3000 \cdot 10^{0}$
428	$OH*+CH_4 \rightarrow OH+CH_4$	$3,3600 \cdot 10^{12}$	$5,0000 \cdot 10^{-1}$	$-2,6600 \cdot 10^{0}$
429	$OH*+OH \rightarrow OH+OH$	$6,0100 \cdot 10^{12}$	$5,0000 \cdot 10^{-1}$	$-3,1900 \cdot 10^{0}$
430	$OH*+H \rightarrow OH+H$	$1,3100 \cdot 10^{13}$	$5,0000 \cdot 10^{-1}$	$-7,0000 \cdot 10^{-1}$
431	$OH*+N_2 \rightarrow OH+N_2$	$1,0800 \cdot 10^{11}$	$5,0000 \cdot 10^{-1}$	$-5,1900 \cdot 10^{0}$
432	$OH*+Ar \rightarrow OH+Ar$	$1,6900 \cdot 10^{12}$	$0,0000 \cdot 10^{0}$	$1,7320 \cdot 10^{1}$

CH* formation reactions

No.	Reaction	Factor	Exponent	ΔE_A [kJ·mol]
433	$C_2H + O_2 \rightarrow CO_2 + CH*$	$3,2000 \cdot 10^{11}$	$0,0000 \cdot 10^{0}$	$6,7000 \cdot 10^{0}$
434	$C_2H + O \rightarrow CO + CH*$	$1,4400 \cdot 10^{13}$	$0,0000 \cdot 10^{0}$	$1,8800 \cdot 10^{0}$
435	$C_2 + OH \rightarrow CO + CH*$	$2,0000 \cdot 10^{14}$	$0,0000 \cdot 10^{0}$	$0,0000 \cdot 10^{0}$

CH* deactivation reactions

No.	Reaction	Factor	Exponent	ΔE_A [kJ/mol]
436	$CH* \rightarrow CH$	$1,8600 \cdot 10^{6}$	$0,0000 \cdot 10^{0}$	$0,0000 \cdot 10^{0}$
437	$CH* + O_2 \rightarrow CH + O_2$	$2,4800 \cdot 10^{6}$	$2,1400 \cdot 10^{0}$	$-7,2000 \cdot 10^{0}$
438	$CH* + CO_2 \rightarrow CH + CO_2$	$2,4000 \cdot 10^{-1}$	$4,3000 \cdot 10^{0}$	$-7,1000 \cdot 10^{0}$
439	$CH* + CO \rightarrow CH + CO$	$2,4400 \cdot 10^{12}$	$5,0000 \cdot 10^{-1}$	$0,0000 \cdot 10^{0}$
440	$CH* + CH_4 \rightarrow CH + CH_4$	$1,7300 \cdot 10^{13}$	$0,0000 \cdot 10^{0}$	$7,0000 \cdot 10^{-1}$
441	$CH* + H_2O \rightarrow CH + H_2O$	$5,3000 \cdot 10^{13}$	$0,0000 \cdot 10^{0}$	$0,0000 \cdot 10^{0}$
442	$CH* + H \rightarrow CH + H$	$2,0100 \cdot 10^{14}$	$0,0000 \cdot 10^{0}$	$5,7000 \cdot 10^{0}$
443	$CH* + OH \rightarrow CH + OH$	$7,1300 \cdot 10^{13}$	$0,0000 \cdot 10^{0}$	$5,7000 \cdot 10^{0}$
444	$CH* + H_2 \rightarrow CH + H_2$	$1,4700 \cdot 10^{14}$	$0,0000 \cdot 10^{0}$	$5,7000 \cdot 10^{0}$
445	$CH* + N_2 \rightarrow CH + N_2$	$3,0300 \cdot 10^{2}$	$3,4000 \cdot 10^{0}$	$-1,6000 \cdot 10^{0}$
446	$CH* + Ar \rightarrow CH + Ar$	$3,1300 \cdot 10^{11}$	$0,0000 \cdot 10^{0}$	$0,0000 \cdot 10^{0}$

C$_2^*$ formation reactions

No.	Reaction	Factor	Exponent	ΔE_A [kJ/mol]
447	$1 - CH_2 + C \rightarrow H_2 + C_2*$	$2,4000 \cdot 10^{12}$	$0,0000 \cdot 10^0$	$0,0000 \cdot 10^0$
448	$C_3 + O \rightarrow CO + C_2*$	$5,2000 \cdot 10^{11}$	$0,0000 \cdot 10^0$	$0,0000 \cdot 10^0$

C$_2^*$ deactivation reactions

No.	Reaction	Factor	Exponent	ΔE_A [kJ/mol]
449	$C_2* \rightarrow C_2$	$1,0000 \cdot 10^7$	$0,0000 \cdot 10^0$	$0,0000 \cdot 10^0$
450	$C_2* + O_2 \rightarrow C_2 + O_2$	$4,8000 \cdot 10^{13}$	$0,0000 \cdot 10^0$	$0,0000 \cdot 10^0$
451	$C_2* + CO_2 \rightarrow C_2 + CO_2$	$4,8000 \cdot 10^{13}$	$0,0000 \cdot 10^0$	$0,0000 \cdot 10^0$
452	$C_2* + H_2O \rightarrow C_2 + H_2O$	$4,8000 \cdot 10^{13}$	$0,0000 \cdot 10^0$	$0,0000 \cdot 10^0$
453	$C_2* + N_2 \rightarrow C_2 + N_2$	$4,8000 \cdot 10^{13}$	$0,0000 \cdot 10^0$	$0,0000 \cdot 10^0$
454	$C_2* + CO \rightarrow C_2 + CO$	$4,8000 \cdot 10^{13}$	$0,0000 \cdot 10^0$	$0,0000 \cdot 10^0$
455	$C_2* + CH_4 \rightarrow C_2 + CH_4$	$4,8000 \cdot 10^{13}$	$0,0000 \cdot 10^0$	$0,0000 \cdot 10^0$
456	$C_2* + H \rightarrow C_2 + H$	$4,8000 \cdot 10^{13}$	$0,0000 \cdot 10^0$	$0,0000 \cdot 10^0$
457	$C_2* + H_2 \rightarrow C_2 + H_2$	$4,8000 \cdot 10^{13}$	$0,0000 \cdot 10^0$	$0,0000 \cdot 10^0$
458	$C_2* + OH \rightarrow C_2 + OH$	$4,8000 \cdot 10^{13}$	$0,0000 \cdot 10^0$	$0,0000 \cdot 10^0$
459	$C_2* + Ar \rightarrow C_2 + Ar$	$4,8000 \cdot 10^{13}$	$0,0000 \cdot 10^0$	$0,0000 \cdot 10^0$

C reactions

No.	Reaction	Factor	Exponent	ΔE_A [kJ/mol]
460	$C + H_2 \rightleftharpoons 3 - CH_2$	$1,2410 \cdot 10^{13}$	$0,0000 \cdot 10^0$	$-4,7000 \cdot 10^{-1}$
461	$C + H_2O \rightleftharpoons CO + H_2$	$6,0000 \cdot 10^{11}$	$0,0000 \cdot 10^0$	$0,0000 \cdot 10^0$
462	$C + OH \rightleftharpoons H + CO$	$5,0000 \cdot 10^{13}$	$0,0000 \cdot 10^0$	$0,0000 \cdot 10^0$
463	$C + OH \rightleftharpoons CH + O$	$2,4100 \cdot 10^{14}$	$0,0000 \cdot 10^0$	$9,1000 \cdot 10^1$
464	$C + CH \rightleftharpoons C_2 + H$	$1,0000 \cdot 10^{13}$	$0,0000 \cdot 10^0$	$0,0000 \cdot 10^0$
465	$C + C_2H \rightleftharpoons C_3 + H$	$2,0000 \cdot 10^{16}$	$-1,0000 \cdot 10^0$	$0,0000 \cdot 10^0$
466	$C + 1 - CH_2 \rightleftharpoons C_2 + H_2$	$3,0000 \cdot 10^{12}$	$0,0000 \cdot 10^0$	$0,0000 \cdot 10^0$
467	$C + 3 - CH_2 \rightleftharpoons C_2 + H_2$	$3,0000 \cdot 10^{12}$	$0,0000 \cdot 10^0$	$0,0000 \cdot 10^0$
468	$C + CH_4 \rightleftharpoons C_2H_4$	$1,2050 \cdot 10^9$	$0,0000 \cdot 10^0$	$0,0000 \cdot 10^0$
469	$C + C_2H_2 \rightleftharpoons C_3 + H_2$	$1,6300 \cdot 10^{14}$	$0,0000 \cdot 10^0$	$1,3000 \cdot 10^{-1}$
470	$C + C_2H_4 \rightleftharpoons C_3H_3 + H$	$1,2650 \cdot 10^{14}$	$0,0000 \cdot 10^0$	$0,0000 \cdot 10^0$

C$_2$ reactions

No.	Reaction	Factor	Exponent	ΔE_A [kJ/mol]
471	$C_2 + O \rightleftharpoons CO + C$	$1,0000 \cdot 10^{14}$	$0,0000 \cdot 10^0$	$0,0000 \cdot 10^0$
472	$C_2 + O_2 \rightleftharpoons CO + CO$	$9,0000 \cdot 10^{13}$	$0,0000 \cdot 10^0$	$4,1000 \cdot 10^0$
473	$C_2 + H_2 \rightleftharpoons C_2H + H$	$6,6000 \cdot 10^{13}$	$0,0000 \cdot 10^0$	$3,3260 \cdot 10^1$
474	$C_2 + OH \rightleftharpoons CH + CO$	$5,0000 \cdot 10^{13}$	$0,0000 \cdot 10^0$	$0,0000 \cdot 10^0$
475	$C_2 + OH \rightleftharpoons C_2O + H$	$1,2050 \cdot 10^{13}$	$0,0000 \cdot 10^0$	$0,0000 \cdot 10^0$

No.	Reaction	Factor	Exponent	ΔE_A [kJ/mol]
476	$C_2 + CH_4 \rightleftharpoons C_2H + CH_3$	$3,0000 \cdot 10^{13}$	$0,0000 \cdot 10^0$	$2,4700 \cdot 10^0$
477	$C_2 + C_2H_2 \rightleftharpoons C_2H + C_2H$	$1,0000 \cdot 10^{13}$	$0,0000 \cdot 10^0$	$0,0000 \cdot 10^0$
478	$C_2 + C_2H_4 \rightleftharpoons C_2H + C_2H_3$	$1,0000 \cdot 10^{14}$	$0,0000 \cdot 10^0$	$0,0000 \cdot 10^0$
479	$C_2 + C_2H_6 \rightleftharpoons C_2H + C_2H_5$	$5,0000 \cdot 10^{13}$	$0,0000 \cdot 10^0$	$0,0000 \cdot 10^0$
480	$C_2 + CH \rightleftharpoons C_3 + H$	$2,0000 \cdot 10^{14}$	$0,0000 \cdot 10^0$	$0,0000 \cdot 10^0$

C_2O reactions

No.	Reaction	Factor	Exponent	ΔE_A [kJ/mol]
481	$C_2O + H \rightleftharpoons CH + CO$	$5,0000 \cdot 10^{13}$	$0,0000 \cdot 10^0$	$0,0000 \cdot 10^0$
482	$C_2O + O \rightleftharpoons CO + CO$	$5,0000 \cdot 10^{13}$	$0,0000 \cdot 10^0$	$0,0000 \cdot 10^0$
483	$C_2O + OH \rightleftharpoons CH + CO_2$	$2,0000 \cdot 10^{13}$	$0,0000 \cdot 10^0$	$0,0000 \cdot 10^0$

C_3 reactions

No.	Reaction	Factor	Exponent	ΔE_A [kJ/mol]
484	$C_3 + H_2 \rightleftharpoons C_3H + H$	$4,0000 \cdot 10^5$	$0,0000 \cdot 10^0$	$9,2110 \cdot 10^1$
485	$C_3 + OH \rightleftharpoons CO + C_2H$	$2,0000 \cdot 10^{13}$	$0,0000 \cdot 10^0$	$0,0000 \cdot 10^0$
486	$C_3 + O_2 \rightleftharpoons CO_2 + C_2$	$9,0000 \cdot 10^{11}$	$0,0000 \cdot 10^0$	$4,6060 \cdot 10^1$
487	$C_3 + O \rightleftharpoons CO + C_2$	$1,0000 \cdot 10^{12}$	$0,0000 \cdot 10^0$	$0,0000 \cdot 10^0$

C₂H, C₂H₂, C₂H, C₃H und C₃H₂ reactions

No.	Reaction	Factor	Exponent	ΔE_A [kJ/mol]
488	$C_2H_2 + 3-CH_2 \rightleftharpoons C_3H_3 + H$	$1,2050 \cdot 10^{13}$	$0,0000 \cdot 10^0$	$2,7700 \cdot 10^1$
489	$CH + C_2H_2 \rightleftharpoons C_3H_2 + H$	$2,1080 \cdot 10^{14}$	$0,0000 \cdot 10^0$	$-5,1000 \cdot 10^{-1}$
490	$C_3H_2 + O \rightleftharpoons HCO + C_2H$	$4,0000 \cdot 10^{13}$	$0,0000 \cdot 10^0$	$0,0000 \cdot 10^0$
491	$C_3H_2 + OH \rightleftharpoons HCO + C_2H_2$	$1,0000 \cdot 10^{13}$	$0,0000 \cdot 10^0$	$0,0000 \cdot 10^0$
492	$CH + C_2H \rightleftharpoons C_3H + H$	$5,0000 \cdot 10^{13}$	$0,0000 \cdot 10^0$	$0,0000 \cdot 10^0$
493	$C_3H + H_2 \rightleftharpoons C_3H_2 + H$	$4,0000 \cdot 10^5$	$2,4000 \cdot 10^0$	$4,1870 \cdot 10^0$
494	$C_3H + O \rightleftharpoons CO + C_2H$	$4,0000 \cdot 10^{13}$	$0,0000 \cdot 10^0$	$0,0000 \cdot 10^0$
495	$C_3H + OH \rightleftharpoons CO + C_2H_2$	$2,0000 \cdot 10^{13}$	$0,0000 \cdot 10^0$	$0,0000 \cdot 10^0$
496	$C_3H + O_2 \rightleftharpoons CO + HCCO$	$3,0000 \cdot 10^{13}$	$0,0000 \cdot 10^0$	$0,0000 \cdot 10^0$

C.4 Third-body efficiencies

No.	H_2	H_2O	O_2	Ar	CO	CO_2	C_2H_2
6	1,0	6,5	0,4	0,35	0,75	1,5	3,0
7	1,0	6,5	0,4	0,35	0,75	1,5	3,0
8	1,0	2,55	0,4	0,15	0,75	1,5	3,0
9	1,0	6,5	0,4	0,29	0,75	1,5	3,0
17	1,0	6,5	0,4	0,35	0,75	1,5	3,0
24	1,0	6,5	0,4	0,35	0,75	1,5	3,0
35	1,0	2,55	0,4	0,15	0,75	1,5	3,0

39	1,0	6,5	0,4	0,35	0,75	1,5	3,0
54	1,0	6,5	0,4	0,35	0,75	1,5	3,0
57	1,0	6,5	0,4	0,35	0,75	1,5	3,0
58	1,0	6,5	0,4	0,35	0,75	1,5	3,0
65	1,0	6,5	0,4	0,35	0,75	1,5	3,0
70	1,0	6,5	0,4	0,35	0,75	1,5	3,0
71	1,0	6,5	0,4	0,35	0,75	1,5	3,0
75	1,0	6,5	0,4	0,35	0,75	1,5	3,0
79	1,0	6,5	0,4	0,35	0,75	1,5	3,0
80	1,0	6,5	0,4	0,35	0,75	1,5	3,0
82	1,0	6,5	0,4	0,35	0,75	1,5	3,0
83	1,0	6,5	0,4	0,35	0,75	1,5	3,0
99	1,0	6,5	0,4	0,35	0,75	1,5	0,66
131	1,0	6,5	0,4	0,35	0,75	1,5	3,0
138	1,0	6,5	0,4	0,35	0,75	1,5	3,0
145	1,0	6,5	0,4	0,35	0,75	1,5	3,0
156	1,0	6,5	0,4	0,35	0,75	1,5	3,0
157	1,0	6,5	0,4	0,35	0,75	1,5	3,0
158	1,0	6,5	0,4	0,35	0,75	1,5	3,0
167	1,0	6,5	0,4	0,35	0,75	1,5	3,0
178	1,0	6,5	0,4	0,35	0,75	1,5	3,0
234	1,0	6,5	0,4	0,35	0,75	1,5	3,0
264	1,0	6,5	0,4	0,35	0,75	1,5	3,0
421	1,0	6,5	0,4	0,35	0,75	1,5	0,66

C.5 Pressure dependencies

No.	Factor (low pressure limit)	Exponent (low pressure limit)	ΔE_A [kJ/mol] (low pressure limit)	Troe paramater 1	Troe paramater 2	Troe paramater 3	Troe paramater 4
9	$2.3670 \cdot 10^{19}$	$-1.2000 \cdot 10^{0}$	$0.0000 \cdot 10^{0}$	$0.5000 \cdot 10^{0}$	$0.0000 \cdot 10^{0}$	$0.0000 \cdot 10^{0}$	$0.0000 \cdot 10^{0}$
17	$5.9800 \cdot 10^{19}$	$-0.8000 \cdot 10^{0}$	$0.0000 \cdot 10^{0}$	$0.5000 \cdot 10^{0}$	$0.0000 \cdot 10^{0}$	$0.0000 \cdot 10^{0}$	$0.0000 \cdot 10^{0}$
35	$3.7900 \cdot 10^{0}$	$-2.5000 \cdot 10^{0}$	$0.0000 \cdot 10^{0}$	$0.6000 \cdot 10^{0}$	$0.0000 \cdot 10^{0}$	$0.0000 \cdot 10^{0}$	$0.0000 \cdot 10^{0}$
65	$1.5000 \cdot 10^{34}$	$-5.3900 \cdot 10^{0}$	$1.5146 \cdot 10^{2}$	$9.6000 \cdot 10^{-1}$	$6.7200 \cdot 10^{1}$	$1.8550 \cdot 10^{3}$	$7.5430 \cdot 10^{3}$
75	$1.0980 \cdot 10^{38}$	$-6.2100 \cdot 10^{0}$	$5.5780 \cdot 10^{0}$	$2.5000 \cdot 10^{-1}$	$2.1000 \cdot 10^{2}$	$1.4340 \cdot 10^{3}$	$0.0000 \cdot 10^{0}$
79	$1.5540 \cdot 10^{26}$	$-3.3000 \cdot 10^{0}$	$0.0000 \cdot 10^{0}$	$3.6000 \cdot 10^{-1}$	$0.0000 \cdot 10^{0}$	$0.0000 \cdot 10^{0}$	$0.0000 \cdot 10^{0}$
80	$3.1090 \cdot 10^{14}$	$0.0000 \cdot 10^{0}$	$1.5880 \cdot 10^{1}$	$5.0000 \cdot 10^{-1}$	$0.0000 \cdot 10^{0}$	$0.0000 \cdot 10^{0}$	$0.0000 \cdot 10^{0}$
82	$3.6300 \cdot 10^{41}$	$-7.0000 \cdot 10^{0}$	$1.1600 \cdot 10^{1}$	$6.2000 \cdot 10^{-1}$	$7.3000 \cdot 10^{1}$	$1.1800 \cdot 10^{3}$	$0.0000 \cdot 10^{0}$
83	$4.6600 \cdot 10^{25}$	$-3.0000 \cdot 10^{0}$	$1.0168 \cdot 10^{2}$	$4.5000 \cdot 10^{-1}$	$0.0000 \cdot 10^{0}$	$0.0000 \cdot 10^{0}$	$0.0000 \cdot 10^{0}$
99	$4.6970 \cdot 10^{47}$	$-8.2000 \cdot 10^{0}$	$4.9218 \cdot 10^{2}$	$0.0000 \cdot 10^{0}$	$1.3500 \cdot 10^{3}$	$1.0000 \cdot 10^{0}$	$7834.0 \cdot 10^{3}$
145	$3.2370 \cdot 10^{27}$	$-3.4000 \cdot 10^{0}$	$1.4982 \cdot 10^{2}$	$3.5000 \cdot 10^{-1}$	$0.0000 \cdot 10^{0}$	$0.0000 \cdot 10^{0}$	$0.0000 \cdot 10^{0}$
158	$1.1780 \cdot 10^{19}$	$0.0000 \cdot 10^{0}$	$3.2000 \cdot 10^{0}$	$7.6000 \cdot 10^{-1}$	$4.0000 \cdot 10^{1}$	$1.0250 \cdot 10^{3}$	$0.0000 \cdot 10^{0}$
167	$7.8290 \cdot 10^{17}$	$0.0000 \cdot 10^{0}$	$3.4200 \cdot 10^{2}$	$5.0000 \cdot 10^{-1}$	$0.0000 \cdot 10^{0}$	$0.0000 \cdot 10^{0}$	$0.0000 \cdot 10^{0}$
178	$3.6540 \cdot 10^{18}$	$0.0000 \cdot 10^{0}$	$1.3968 \cdot 10^{2}$	$7.5000 \cdot 10^{-1}$	$9.7000 \cdot 10^{1}$	$1.3790 \cdot 10^{3}$	$0.0000 \cdot 10^{0}$
264	$2.2370 \cdot 10^{19}$	$0.0000 \cdot 10^{0}$	$2.7187 \cdot 10^{2}$	$7.6000 \cdot 10^{-1}$	$1.9460 \cdot 10^{3}$	$3.8000 \cdot 10^{1}$	$0.0000 \cdot 10^{0}$